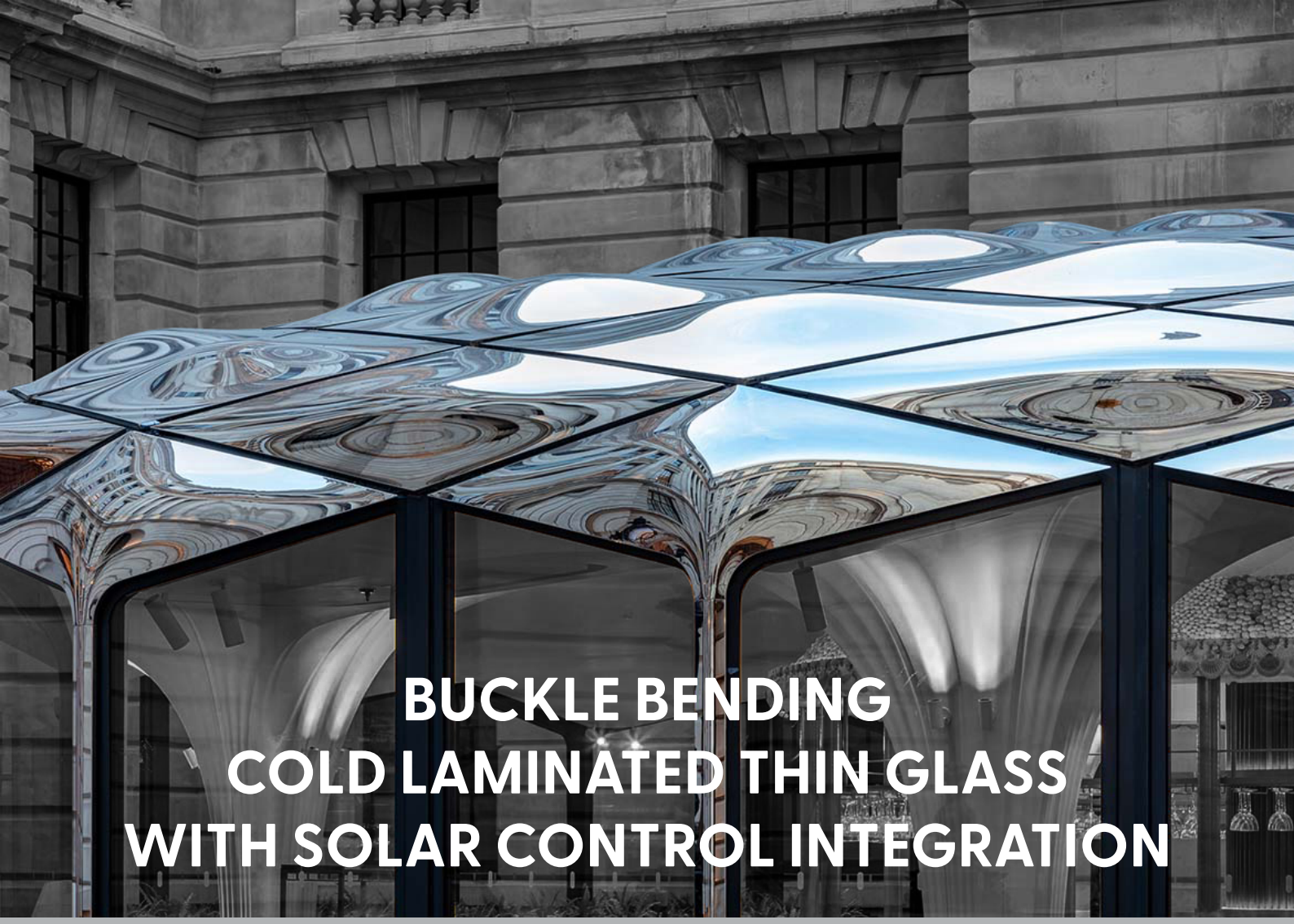

BUCKLE BENDING COLD LAMINATED THIN GLASS WITH SOLAR CONTROL INTEGRATION

MSc in Architecture, Urbanism and Building Sciences
Building Technology Track

Thesis Report

Sanguk Ryu

Supervisor

Prof. Dr. Mauro Overend
Dr. Eleonora Brembilla
Robert Capel (Octatube)

Duration

November, 2024 – July, 2025

Industry Partner

octatube
PILKINGTON
H.B. Fuller | KÖMMERLING
TTEC

TU Delft

ACKNOWLEDGEMENTS

The months spent working on this thesis were truly fulfilling, so engaging that time often seemed to fly. While some say that any thesis, no matter how exciting at first, can eventually become tiresome, I am grateful that my passion endured until the very end.

I would first like to sincerely thank my supervisors, Mauro and Eleonora. Their guidance helped shape my overly ambitious ideas into a coherent direction. Mauro, your enthusiasm for glass inspired me to explore its potential deeply, and your dedication during our meetings pushed my work toward a professional prototype level. Eleonora, thank you for your constant encouragement and for helping me develop greater interest and insight in solar design. Your scientific guidance and warm support, even on short notice, meant a great deal.

I am also deeply grateful to Octatube, where I spent nearly a year. Special thanks to Robert, who provided generous support and valuable input across many areas. I'm also thankful to all my colleagues there who kindly offered help whenever I needed it. In particular, I want to thank Jan de Goede for supervising the manufacturing process and ensuring everything proceeded safely.

To Victor Muñoz Sanz, my thesis committee member, thank you for your time and interest in my work.

Special thanks to Rory Back from Pilkington, who showed great interest in the project and helped with sourcing glass. I'm also grateful to the NSG Japan team for delivering high-quality samples on a tight schedule. Chris Davis and Sebastian Dillinger from H.B. Fuller | Kömmerling provided not only materials and technical advice but also hands-on support during the lamination process. I would also like to thank Tom Therre and Andreas Schwab from TTEC for their valuable assistance with panel lamination and cold bending techniques.

As I reflect on this journey, I am reminded of how many people have supported and shaped this research. I feel truly blessed to have received such generous help. This work would not have been possible without the unwavering love of my wife and my family in Korea, who stood by me through every step.

Above all, I dedicate this thesis to my Heavenly Father. Thank You for calling me to study in a distant land, for giving me clear vision and purpose, and for surrounding me with the right people and opportunities. Your grace has carried me through this journey, and for that, I am deeply grateful.

To all who were part of this journey, thank you.

Sanguk Ryu

ABSTRACT

This research investigates the application of cold-bent thin glass in double-curved roofing, using the OWO Pavilion as a benchmark. To achieve its complex form, a novel cold bending technique—buckle bending—is introduced, inspired by structural buckling behaviour. This method enables smooth, double-curved geometries without heat or moulds by inducing in-plane compression through edge supports. The most effective shape, a sinusoidal half-paraboloid, balances structural efficiency and manufacturability while maintaining curvature levels comparable to single-curved geometries.

A performance-driven solar control strategy is integrated using variable-density ceramic fritting. Frit patterns are optimised based on solar radiation mapping, blocking more sunlight in exposed areas and allowing transparency where needed. To manage computational demands, a staged simulation approach is employed by first optimising on simplified geometries, then applying results to the full surface.

Structurally, the laminated sinusoidal panels show enhanced mid-span stability but their sensitivity under different loading conditions and force directions varies depending on the glass geometry and boundary support configuration. Post-failure performance benefits from the interlayer's viscoelasticity, which stabilises stress over time and retains fragments after fracture. Manufacturing challenges include the unpredictability of brittle failure, the need for precise deformation control, and the complexity of lamination with uncured interlayers like LOCA (Liquid Optically Clear Adhesive).

In conclusion, this research demonstrates how buckle bending enables geometrically expressive, materially efficient, and structurally reliable thin glass applications with integrated solar responsiveness. By combining structural optimisation with solar performance strategies, the study opens new possibilities for architectural glass design by overcoming conventional curvature limitations while contributing to a more sustainable and adaptable built environment.

Keywords:
Thin glass, double-curvature, buckle bending, cold bending, lamination, LOCA, ceramic frit, solar control

Author's Note
All images, figures, and diagrams in this thesis were created by the author unless otherwise stated.
Coverpage image modified from © by Kyungsub Shin. Used with permission.

TABLE OF CONTENTS

I FRAMEWORK 7

1.1 Background 7

1.2 Problem Statement 8

1.3 Objective 9

1.4 Research Questions 11

1.5 Research Limitations 11

1.6 Methodology 12

1.7 Relevance 13

II LITERATURE REVIEW 14

2.1 Introduction 15

2.2 Thin Glass 15

2.2.1 General Glass Manufacturing Process 15

2.2.2 Brittleness of Glass 15

2.2.3 Thermal Tempering 17

2.2.4 Chemical Strengthening 17

2.2.5 Thin Glass 17

2.2.6 Aluminosilicate Hybrid Thin Glass 18

2.3 Cold-Bending 18

2.3.1 Curved Glass 18

2.3.2 Strength and Stiffness 19

2.3.3 Factors Affecting Glass Deformation 20

2.3.4 Thin Plate Theory 21

2.3.5 Developable Surface 21

2.3.6 Single Curvature Deformation 22

2.3.7 Double Curvature Deformation 23

2.3.8 Support Condition 23

2.4 Lamination 24

2.4.1 Post-Breakage Behaviour 24

2.4.2 Lamination Process 25

2.4.3 Behaviour of Different Lamination Types 26

2.4.4 Cold-Lamination-Bending (CLB) 26

2.4.5 Cast in Place (CIP) 28

2.5 Solar Control 28
2.5.1 Transparency 28
2.5.2 Solar Transmittance 29
2.5.3 Solar Control Methods 31
2.5.4 Surface Treatments 32
2.5.5 Frit Pattern 33
2.5.6 Radiation and Geometry 35

III CONCEPTUAL DESIGN 36
3.1 The OWO Pavilion 37
3.2 Design Objectives 38
3.3 Buckle Bending 38
3.4 Buckle Bending Test - Sinusoidal Paraboloid 39
3.5 Buckle Bending Test - Half Sinusoidal Paraboloid 39
3.5.1 Considerations for Manufacturing 40
3.5.2 Materials 41
3.5.3 Testing & Result 41
3.6 Lamination & Solar Control 43
3.7 Discussion 45

IV DESIGN DEVELOPMENT 46
4.1 Structural Design - Single Plate 47
4.1.1 Methodology 47
4.1.2 Finite Element Analysis (FEA) 47
4.1.3 Single Curvature Cold Bending 48
4.1.4 Sinusoidal Single-Curved Cold Buckle Bending 49
4.1.5 Boundary Condition Optimisation - 3 Edge Fixture 51
4.1.6 Boundary Condition Optimisation - 2 Edge Fixture 53
4.1.7 Displacement Step Adjustment 55
4.2 Geometry Design 57
4.2.1 Methodology 58
4.2.2 Continuity 58
4.2.3 Curvature Continuity in Buckling Deformation 59
4.2.4 Cold Bending Distortion 60
4.2.5 Cold Bent Geometry Analysis 60
4.3 Structural Design - Sandwich Panel 61
4.3.1 Methodology 62
4.3.2 Interlayer Application Strategy 62

4.3.3 Interlayer Thickness Calculation 63
4.3.4 Viscoelastic Material 64
4.3.5 Numerical Analysis Setup 65
4.3.6 Load Scenario 67
4.3.7 Creep Behaviour 68
4.3.8 Springback Effect 70
4.4 Solar Design 73
4.4.1 Methodology 73
4.4.2 Simulation Setup 74
4.4.3 Incident Radiation on Roof Surface 75
4.4.4 Roof Meshing 76
4.4.5 Glass Transmission Calculation 76
4.4.6 Optimisation Objective 77
4.4.7 Optimisation Strategy 79
4.4.8 Multi-Objective Optimisation 81
4.5 Discussion 83

V EXPERIMENT-DRVEN DESIGN 87
5.1 Structural Validation Experiment 88
5.1.1 Experiment Preparation 88
5.1.2 Apparatus Setup 89
5.1.3 Numerical Model Setting 91
5.1.4 Stress Relaxation 92
5.1.5 Bending Strength 94
5.1.6 Creep Behaviour 96
5.2 Panel Prototyping 97
5.2.1 LOCA Manufacturing for Curved Geometry 97
5.2.2 Development of Deformation Device 98
5.2.3 Sinusoidal Half Paraboloid Cold Buckling 101
5.2.4 LOCA Cold Buckle Bending Surface Quality 102
5.2.5 Sinusoidal Half Paraboloid Light Reflection 105
5.2.6 LOCA Cold Buckle Bending Spring-back 106
5.3 Solar Design Validation Experiment 107
5.3.1 Experiment Preparation 108
5.3.2 Experiment Setup 110
5.3.3 Light Transmittance Measurement 111
5.3.4 Experiment Result 115
5.4 Discussion 117

VI FINAL DESIGN 122

6.1 Methodology 123
6.2 Unfolding Cold-Bent Geometry 123
6.3 Structural Design - Sinusoidal Half Paraboloid 125
6.4 Structural Design - Sinusoidal Single Curve 126
6.3.1 Cold Lamination Bending 110
6.3.2 Load Test 111
6.5 Solar Design 130
6.6 OWO Pavilion Roof Assembly 132
6.7 Final OWO Pavilion Roof Design 134
6.8 Discussion 135

VII CONCLUSION 137
7.1 Answers to the Research Questions 137
7.2 Discussion and Further Research 140
7.2.1 Scientific and Societal Impact 140
7.2.2 Interpretation of Results and Limitations 140
7.2.3 Future Research Directions 142

REFERENCE 143

APPENDIX 149

I. FRAMEWORK

1.1 Background

Architects have strong interest in using glass in architectural design. They have been fascinated by its ability to flood spaces with natural light and connect interiors with the outside world. In response to the increasing demand, glass technology has advanced rapidly to address its inherent brittleness. Despite its tendency to break instantly without warning, glass remains nearly unrivalled as a transparent construction material. To meet these challenges, advancements in manufacturing have significantly improved its properties—making it stronger, purer, thinner, and allowing for free-form shaping.

To achieve the enhanced properties mentioned above, glass undergoes a highly complex manufacturing process (Figure 1.1). Despite these advancements, most glass used in architecture is produced as flat glass through a process known as the float line. To achieve the free-formed shapes desired by architects, the glass requires bending. This process can be categorized into two main types: thermal bending and cold bending.
Thermal bending allows for the creation of larger curvatures and the realization of complex double-curvature shapes by heating the glass to its softening point and shaping it with moulds. In contrast, cold bending does not require additional thermal processes or moulds, resulting in greater efficiency through reduced material use, minimized waste, and improved sustainability. However, only large radii achievable with cold bending limit its application to shallow shells with small curvature limiting its design application (Fildhuth & Jan, 2012).

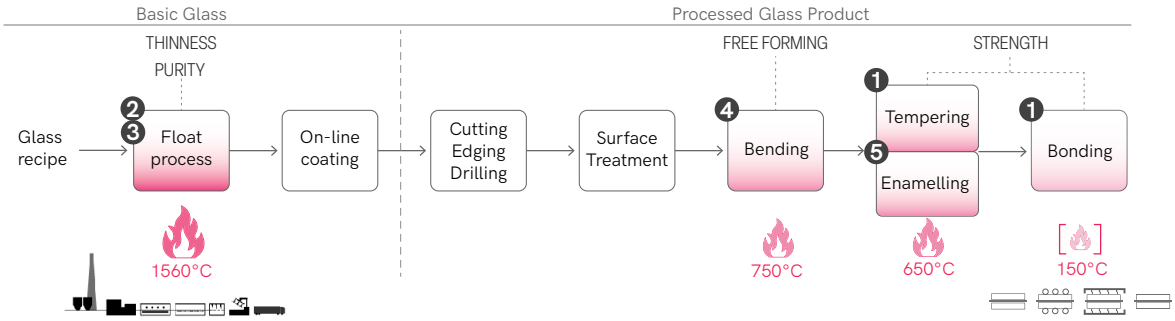

Fig. 1.1 | General float glass manufacturing process
Note. 1: Strength 2: Purity 3: Thinness 4: Free-form 5: Solar control

Architectural trends increasingly demand the use of glass in curvilinear forms to create smooth, free-form façades (Eekhout, 2004). While the manufacturing complexity of double-curved glass has limited its application compared to single-curved glass, double-curved hot-bent glass has been consistently utilized in building façades since the early 2000s. For example, at Prada Aoyama (Herzog & de Meuron, Tokyo, 2003), hot-bent glass was employed for aesthetic and expressive purposes featuring concave and convex

rhombus-shaped paraboloid geometries made with 12 mm hot-bent annealed glass, implemented as insulated glass units (IGUs). At Vakko HQ (REX, Istanbul, 2010), laminated glass was hot-slumped into a three-dimensional X shape, leveraging gravity to achieve the desired form. In this case, the stiffness of the panels, achieved through geometrical deformation, allowed the architect to reduce the thickness of the glass sheets. More recently, at the renovated P & T Engelhornhaus Museum (Architekten BDA, Mannheim, 2023), two layers of 8 mm laminated float glass were hot-bent to create panels resembling a shear buckling deformation shape (Figure 1.2).



Fig. 1.2 | Examples of hot-bent glass designs in buildings
Note. Left: Prada Aoyama, Herzog & de Meuron, Tokyo, 2003 (© Johannes Marburg)
Middle: Vakko HQ, REX, Istanbul, 2010 (© Adrian Betanzos)
Right: P&T Engelhornhaus Museum, Architekten BDA, Mannheim, 2023 (© Glasbau Pritz, Engelskirchen)

1.2 Problem Statement

Thermal bending offers significant design freedom by enabling high curvatures, and supporting continuous repetitive patterns through the use of moulds. However, it is less effective for creating varied geometries, as each unique shape requires a separate mould. Additionally, the hot-forming process can produce unwanted ripple-shaped defects, compromising surface quality. Adding to these limitations, thermal forming has room for further optimization, particularly in enhancing material efficiency.

Brittleness has long been the biggest challenge when using glass as a structural element. Loads acting transversely to the glass plane are typically resisted by bending stiffness. As a result, glass structures often require increased thickness, leading to heavier constructions and greater material usage (Wurm, 2007). However, with the relatively recent development of thin glass products ranging from 0.5 mm to 2 mm in thickness, a completely new realm of possibilities has emerged. Although thin glass is weak against local bending due to its thinness, it possesses a high stress capacity, allowing it to bend easily without breaking. Par-

adoxically, this flexibility, which seems disadvantageous for use as a construction material, can be harnessed to create intentional cold deformations. By cold-bending thin glass into cylindrical geometries, the shape creates stiffness in the membrane and the potential for use as an architectural element (Neugebauer, 2016).
However, examples featuring double-curved shells remain rare, as progress is hindered by fabrication challenges and the complexities involved in analysing the geometric non-linearities inherent in these forms (Van Driel et al., 2022). This leads to the following problem statement:

"Despite the potential of thin glass to achieve both material efficiency and structural stiffness through curving, its application remains limited due to fabrication challenges and the complexities of analysing the geometric non-linearities of double-curved shells."

1.3 Objective

The primary aim of this research is to investigate how thin glass can overcome geometric limitations that have traditionally been unattainable with cold bending. By leveraging the unique properties of thin glass, the study seeks to experimentally identify the range of geometries that can be achieved and applied in architectural design. Furthermore, it introduces an innovative approach for manufacturing double-curved, cold-bent glass tailored for architectural use, taking into account the complexities of the glass production process and the need for compatibility across different manufacturing stages. Lastly, the research proposes strategies to address secondary challenges that arise from areas beyond structural design and fabrication, such as issues related to glass lamination and solar control performance.

Louter et al. (2018) highlighted that while several studies have explored the application of thin glass in architecture, most implementations have been limited to dynamic façades, window units, or indoor partitions. In Table 1.1, the use of glass in buildings requires careful consideration of various design factors, which differ based on its installation location and purpose (Schittich et al., 2007). When applied as a horizontal element, thin glass offers advantages, by revealing its reduced self-weight on the design process, allowing for material reduction and structural efficiency. Therefore for this research utilises thin glass as a roof element.
To define the boundary conditions for applying cold-bent geometry, the sinusoidal double-curved roof of *The OWO Pavilion* is used as a benchmarking model (Figure 1.3). The roof panels of The OWO Pavilion are currently constructed from mirror-polished stainless steel, shaped using hydraulic pressure to create a distinctive smooth form reminiscent of natural water droplets, utilising the elongation properties of the metal, which do not apply to glass. This research aims to replace the existing opaque roof with a lightweight and trans-

Installed angle	Use	Examples
Vertical 80°- 90°	w — vertical glazing	
Inclined 15°- 80°	g, s; w — inclined or overhead glazing	
Inclined 0° -15°	p; g, s; w — horizontal or overhead glazing	

	Very short-term effect		Short-term effect	Medium-term effect		Permanent effect	
	Impact	Wind	Snow	Barrier-load	Foot traffic	Climate load	Self-weight
Vertical glazing	△	●		△		△	
Horizontal and inclined glazing	△	●	●			△	●
Glazing subject to unrestricted foot traffic	●	●	●		●	△	●

Table 1.1 | Typical loads and load durations on glazing types
Note. w indicates window load, g gravity load, s snow load, and p point load. In the table, circles (●) represent significant influence, while triangles (▲) indicate partial or minor influence.

parent cold-bent thin glass, maintaining a similar smooth and unique double curvature. There are two main scenarios to consider when using thin glass as a roofing panel. First, it is crucial to address the risk of cutting or piercing injuries caused by falling glass shards in the event of breakage. Ensuring safety involves developing appropriate protective measures, such as laminating the glass to contain fragments. Second, the large amount of solar energy entering through the roof must be effectively controlled to maintain interior comfort

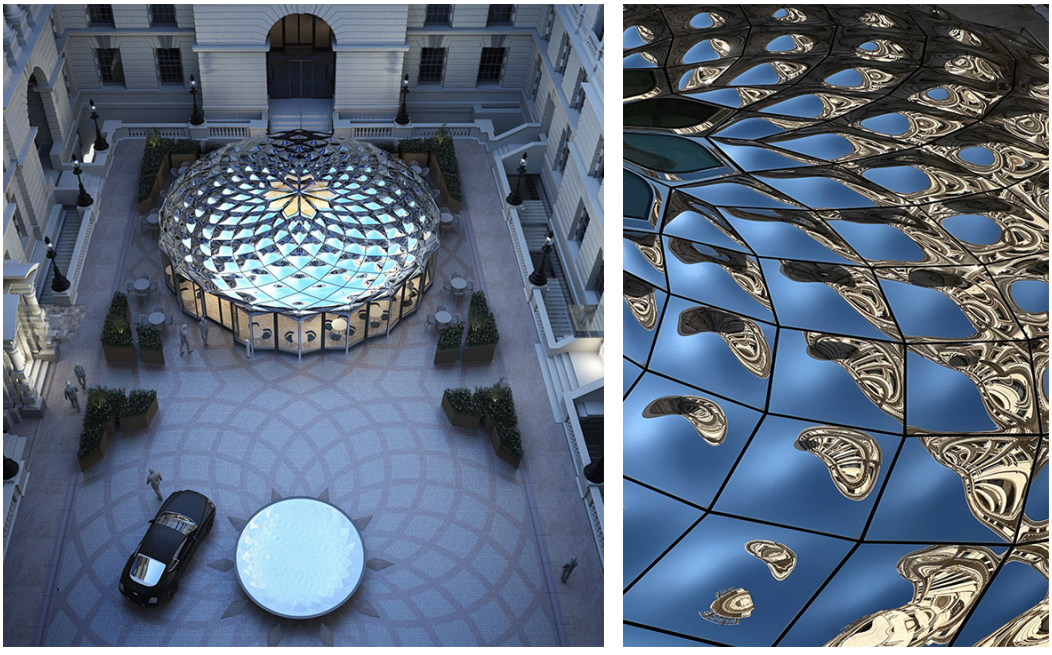

Fig. 1.3 | The OWO Pavilion (Daewhagang Architecture, London, 2023, © Daewhagang Architecture)

and energy efficiency. This requires the integration of strategies such as advanced coatings or shading devices to regulate solar transmittance without compromising the transparency and aesthetics of the glass roof.

1.4 Research Questions

Based on the problem statement, a double-curved cold-bent glass unit with various essential properties must be developed for use as a roofing element. Therefore, the main research question is as follows:

"How can thin glass be cold-bent and laminated into smooth double-curvature forms for architectural applications, while integrating solar control mechanisms?"

This research will also answer the following sub-questions:

1. What kind of deformation methods could be used to create a water-droplet like geometry for thin glass?

2. What is the most effective form driven from the cold-bending process to implement the benchmark roof design?

3. How does the laminated glass panel behave under general load conditions, and what are its post-failure characteristics?

4. How can solar simulations be utilised to design an effective solar transmittance control mechanism for double-curved thin glass?

5. What are the main manufacturing challenges?

1.5 Research Limitations

This research does not aim to develop a fully code-compliant or structurally safe building system using thin glass. Rather, its focus is on exploring new possibilities in cold bending by pushing the material to its geometric and physical limits. The study investigates how the unique flexibility of thin glass can be utilised to achieve forms that would be difficult or impossible with conventional glass. Instead of adhering to standard safety requirements, this research prioritises experimental exploration, aiming to better understand the extreme performance capacities of thin glass and its potential for innovative architectural applications.

1.6 Methodology

Literature Review

Literature review is conducted based on keywords such as *thin glass, cold-bending, lamination,* and *solar control*. This process provides valuable insights that contributed to establishing the foundational knowledge and boundary conditions for the product design. Through this review, research gaps could be found to supplement areas that required further investigation.

Schematic Design

Before directly handling the brittle and challenging material, a more manageable substitute will be used to study cold bending under specific boundary conditions to minimize risks instead of testing with glass. This approach allows for physical verification step to determine whether the form implemented in the benchmarking building can actually be achieved through cold-bending. The process begins with designing a force-application device, to observe how the plate deforms, identify areas of high stress, and gather insights into thin plate's bending behaviour. From the perspective of the overall glass fabrication process, schematic ideation is developed regarding the integration of lamination and ceramic fritting methods.

Numerical Simulation

Finite element method (FEM) and analysis will be conducted based on the actual dimensions of the end-product. Applying the pre-stressed state (cold bending) on the glass is crucial because it affects the glass behaviour. Additionally, this numerical analysis stage allows to simulate the required glass thickness to withstand specific loads, identify areas of maximum stress, and predict potential points of structural failure incorporating the viscoelastic core layer. Detailed design optimisation is carried out by adjusting simulation variables. For solar control simulation, the real climate data for The OWO Pavilion will be applied with the optimized double-curved glass geometry coming from the structural analysis. Solar control design optimisation will be carried out in a way that maximises the transparency of the glass while taking indoor solar radiation as an indicator for indoor comfort.

Manufacturing & Experimental Testing

The validation process to confirm whether the numerical structure analysis conducted is similar to the actual performance will be conducted through a bending test with laminated sandwich panels. The roof panel module, designed at a 1:1 scale similar to that of The OWO Pavilion, is planned to be fabricated and assembled in collaboration with Octatube (cold-bending fixture), Pilkington (thin chemically toughened glass), H.B. Fuller| Kömmerling (lamination material), and TTEC (lamination manufacturing). Through this process, it will be checked whether the conceptual production method can be actually implemented to real world application. Additional qualitative assessment for surface quality and quanti-

tative springback measurement is carried out to evaluate the cold bent product. For solar control mechanism validation, a simplified roof unit is compared with a digital twin model.

Application of Research-Based Design

Based on the findings from the preceding research and experiments, a design proposal for the new OWO Pavilion is developed. The aim is to identify the most feasible design under the given conditions. The proposal reflects both structural and manufacturing considerations.

1.7 Relevance

Scientific Relevance

The study introduces a novel thin glass buckling method for achieving smooth, double-curved geometry that has not been tested before. It also addresses the interdependent nature of thin glass manufacturing by integrating the cold buckle bending process with lamination and ceramic frit patterning into a unified framework. This holistic approach aims to reduce performance inconsistencies, resolve process incompatibilities, and improve production efficiency—challenges that are often overlooked when these components are studied in isolation.

Social Relevance

Thin glass offers a sustainable alternative to conventional materials by reducing resource consumption and enabling lighter, more efficient structures. Its lower weight decreases material use and structural demands, while the cold-bending process avoids the carbon-intensive energy required for thermal forming. Its ability to achieve high-curvature, free double-curved shapes through cold-bending challenges the traditional bending manufacturing approach. This innovation will enable cold-bending to achieve forms previously possible only with hot-bending, allowing architects to realise more diverse and expressive designs in glass.

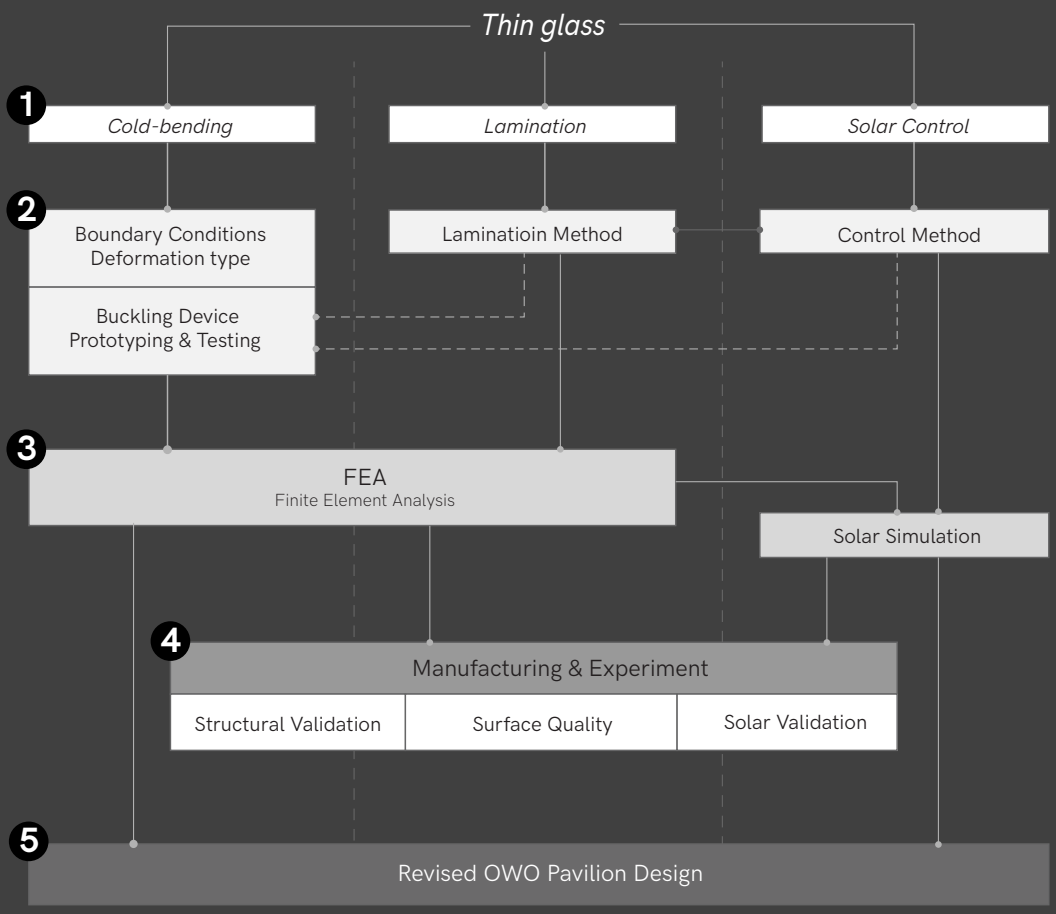

1. LITERATURE REVIEW & BACKGROUND KNOWLEDGE
2. CONCEPTUAL DESIGN
3. DESIGN DEVELOPMENT
4. EXPERIMENTAL VALIDATION
5. FINAL DESIGN

II. LITERATURE REVIEW

2.1 Introduction

The key terms identified through the research question are *thin glass, cold-bent, laminated,* and *solar protection*. Given the complexity of the manufacturing process from raw materials to the final product, these keywords should not be considered in isolation. The specific characteristics of *thin glass* influence all subsequent processes, including cold bending, lamination, and the application of solar protection methods. Therefore, *thin glass* is the primary focus. This research has reviewed relevant research based on the relationships between key terms such as *thin glass-cold bending* and *thin glass-lamination*. Due to limited research specifically on thin glass, studies involving *glass* or *chemically toughened glass* are also considered when necessary.

Although the novelty of this research lies in the cold-bending method and the resulting deformed geometry, subsequent processes such as lamination and solar protection must be carefully coordinated to ensure compatibility. The goal is to identify methodologies that align the requirements of each production stage without compromising performance. At each stage, relevant literature is reviewed with consideration for maintaining high surface quality, in line with the standard established by the benchmark design.

2.2 Thin Glass

2.2.1 General Glass Manufacturing Process

The most important revolution in the industrialisation of glass was the invention of the float glass process in 1957 by Alastair Pilkington. The float process is the most widely used primary manufacturing method, accounting for around 90% of today's flat glass production worldwide. While its major advantages include low cost, superior optical quality, and large pane sizes, the development of many post-processing and refinement technologies over the past 50 years—such as bending, tempering, and laminating—has greatly expanded glass's applications, particularly in the construction industry (Figure 1.1). Structural analysis methods have further enabled glass to be used as a key material in structural building elements (Schittich et al., 2007).

2.2.2 Brittleness of Glass

Construction glass consists of approximately 75% silica (SiO_2), which is abundantly found in the Earth's crust as pure quartz sand, making it commonly referred to as silicate glass. This glass-forming substance is combined with sodium oxide (soda), which acts as a flux, reduc-

ing the transformation temperature to 550 °C and simplifying the manufacturing process. To enhance chemical resistance, calcium oxide (lime) is added as a stabiliser. As the molten mass cools, glass transitions from a liquid to a solid without forming a regular, symmetrical crystal lattice, meaning it lacks crystallinity. As a result, the molecular structure does not allow for dislocations, and there is no plasticity in the material (Veer, 2007). Glass deforms linearly and elastically under increasing load, but when the load exceeds its capacity, it fractures suddenly and without warning, particularly under tensile stress. Being isotropic, glass's properties are uniform regardless of direction or orientation. The modulus of elasticity of glass is 70 GPa, which is about one-third of steel.

Glass surfaces contain numerous microscopic irregularities and defects. When exposed to compressive stress, these surface flaws are compressed, preventing the formation of stress peaks. However, under tensile load, stress peaks form at the notches, leading to stress concentrations at the crack root and eventually causing crack propagation (Figure 2.1a). It means that small flaws on the glass surface are governing the strength of the glass (Nategh et al., 2022). For structural glass applications, tempering (heat strengthening) is essential. It creates a favourable residual stress field with compressive stresses on the surface and tensile stresses in the core, making the glass more resistant to crack propagation. As long as the tensile stress on the surface is smaller than the residual compressive stress, cracks are prevented, ensuring the glass's integrity.

Tempered glass can be broadly categorised into three types: heat-strengthened glass, fully toughened glass, and chemically toughened glass. Heat-strengthened glass has compressive stress on its surface but is not as strong as fully toughened glass. Fully toughened glass, subjected to higher heating and rapid cooling, offers much higher strength. Chemical toughened glass, processed through an ion-exchange method, increases strength by replacing smaller ions with larger ones on the surface. Each type provides distinct advantages based on the application's needs.

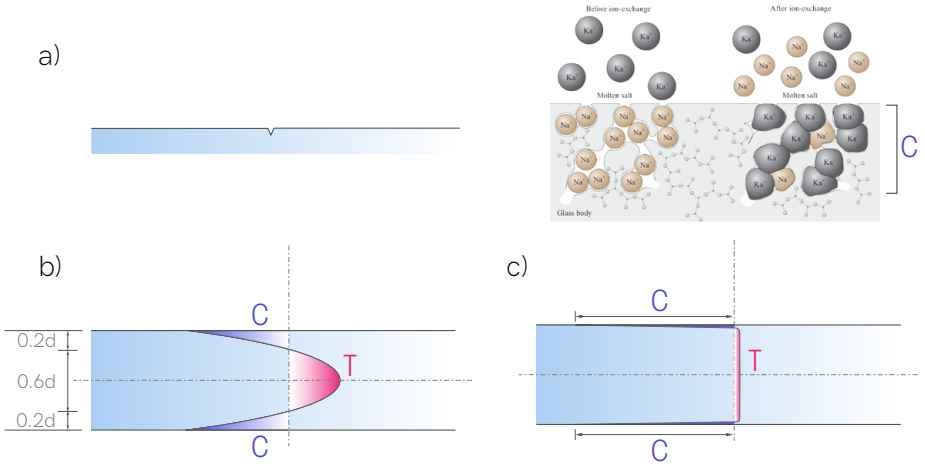

Fig. 2.1 | Different tempering methods of glass
Note. a: Notch on glass surface (Author) b: Thermal pre-stressing stress profile (Author)
c: Chemical toughening mechanism & stress profile (Schittich et al., 2007)

2.2.3 Thermal Tempering

In the thermal tempering process, glass is heated above its transition temperature (650 °C), entering a viscoelastic state. It is then rapidly cooled, taking advantage of the principle that cooling causes material shrinkage. The outer surface cools and solidifies faster than the core, creating a temperature gradient. This allows the surface to enter a compressed state without introducing significant internal stresses. The resulting Gaussian pre-stressing stress profile is illustrated in Figure 2.1b. Thermal tempering is in general not effective when glass is thinner than 3 mm (Fan et al., 2016).

2.2.4 Chemical Strengthening

Chemical strengthening is a thermal, time-dependent ion exchange process (Figure 2.1c) that occurs at the outer surfaces of the glass. The process consists of immersing the glass for a given soak time into a molten salt of potassium nitrate kept at a given temperature (Bartholomew et al. 1980). The soak time varies between 2 and 24 hours and during the process, small ions on the surface get replaced with larger ions. This creates compressive stresses on the surface that are typically much higher than thermally induced residual stresses, but the effect is limited to a very thin layer (Figure 2.1). Generally, as the soak time increases, the depth of layer (DoL), referring to the thickness of the compressive stress region, also increases, resulting in a stronger surface layer.

2.2.5 Thin Glass

Around 2007, smart phones entered the market, using glass thinner than 2 mm that is chemically strengthened for exceptional mechanical properties and flexibility. Often made through the down-drawn process (Figure 2.2), a ribbon of glass is drawn vertically from the furnace and annealed to reduce stress, achieving thickness as low as 25 micrometers. Most such glass is made from aluminosilicate, known for toughness, scratch resistance, and thermal stability (Schott, n.d.). Aluminosilicate glass, like Gorilla Glass, is widely used as durable cover glass in electronics. Its higher density, thermal expansion, and viscosity require higher production temperatures, making it costlier than traditional soda-lime float glass. These higher costs limit its use in architecture, but it remains essential for high-performance applications.

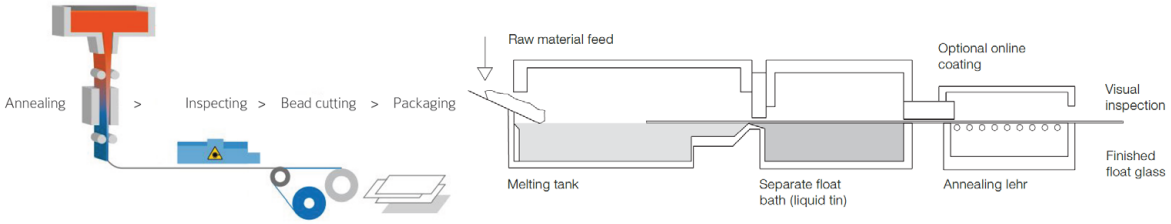

Fig. 2.2 | Down-drawn process & float glass process
Notes. Left: Down-drawn process (Schott, 2014) Right: Float glass process (Schittich, 2007)

2.2.6 Aluminosilicate Hybrid Thin Glass

To use thin glass in architectural applications, chemical toughening (CT) is required for strength while maintaining a thin thickness. Soda-lime glass is generally unsuitable for CT due to its limited strength, durability and Ionic exchange inefficiency. Pure aluminosilicate glass, which requires temperatures up to 1600 °C for production, cannot be processed on float lines, making it economically unfeasible for large glass panels. However, glanova®, a hybrid of soda-lime and aluminosilicate glass made from NSG | Pilkington, provides a cost-effective alternative, lowering the softening temperature while offering chemical properties suitable for CT.

Chemically strengthened glass features surface compression transitioning to core tension at the depth of layer (DoL). Strength depends on surface compression and DoL: flaws above the DoL are harmless, while deeper flaws weaken the glass under core tension. The effectiveness of chemical strengthening is influenced by the alkali-oxide to aluminum oxide ratio, making aluminosilicate glass more responsive than soda-lime glass. The differences in compressive strength and DoL, and the comparison between soda-lime glass and glanova®, are shown in Figure 2.3 (NSG, n.d.).

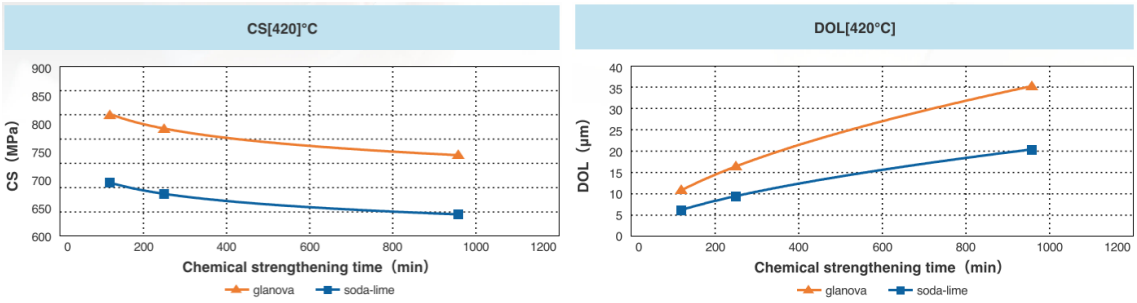

Fig. 2.3 | Chemical strengthening properties of glanova® (NSG n.d.)

Zaccaria et al. (2022) conducted a novel bending test on CT hybrid aluminosilicate thin glass, increasing curvature until fracture using AGC Falcon glass. After 8 hours of chemical strengthening, the glass achieved the best performance with a characteristic bending strength of 230 MPa, significantly exceeding the design characteristic bending strength (f_{gk}) of 150 MPa, as specified in EN 19100-1 (2024).

2.3 Cold Bending

2.3.1 Curved Glass

Also known as bent glass, curved glass has been heated past its softening point and formed into a curved shape, typically by draping it over or into a mould. The glass can be curved along one or both axes. Uni-axial curving is generally achieved through sag bending, where the heated glass is allowed to take on the form of the mould under its own weight. For doubly curved shapes, the glass must be pressed into the mould. For larger bending angles,

chemical tempering may be necessary.

Due to the limitations of hot-bending, which requires the use of moulds, thermal process, and deficient clarity of surface quality, cold-bending methods has been developed. Cold-bending are mostly being done with single curve bending, 1-corner displacement, or twisting techniques to achieve a double curved surface (Bijster et al., 2016). Cold bending induces internal stress in the glass. Unlike hot bending, which allows for viscous deformation and stress relief as the glass cools, cold bending faces limitations in terms of deformation due to the internal stresses that remain. To perform cold bending, tempered glass, which has higher strength than annealed glass, is required. While cold bending does not necessitate moulds or thermal procedures, offering potential savings in materials and construction costs, it requires proper engineering before installation. Therefore, the choice of bending method is typically determined by the building's design and specific circumstances, aiming to maximise the advantages of each method in line with the project's requirements (Fildhuth et al., 2018).

2.3.2 Strength and Stiffness

When using glass in construction, strength and stiffness are distinct yet interconnected properties influenced by different factors. Strength in glass is primarily governed by surface flaws and stress distribution. Microscopic defects or irregularities that act as stress concentrators under tensile stress, significantly reducing glass' apparent strength compared to its theoretical strength. To address this, pre-stressing methods such as thermal or chemical toughening are used to introduce compressive stresses on the surface, which delay or prevent crack initiation and propagation under tensile loads. Additionally, the loading conditions, particularly tensile stresses caused by bending, thermal expansion, or impact, dictate the failure mode, as glass is inherently weakest under tension (Haldimann et al., 2008). The bending strength resistance is calculated based on formula 2.1 from EN 19100-1 (2024).

$$f_{g,d} = k_e \cdot k_{\mathrm{sp}} \cdot \lambda_A \cdot \lambda_l \cdot k_{\mathrm{mod}} \cdot \frac{f_{g,k}}{\gamma_M} + k_p \cdot k_{e,p} \cdot \frac{f_{b,k} - f_{g,k}}{\gamma_p} \qquad (2.1)$$

$f_{g,d}$ Total design bending strength
$f_{g,k}$ Characteristic bending strength of annealed glass
$f_{b,k}$ Characteristic value of glass strength after strengthening treatment
γ_{M} Material partial factor
γ_p Partial factor for pre-stress on the surface
k_e Edge or hole finishing factor
k_{sp} Surface profile factor
k_{mod} Modification factor
λ_A Size effect
λ_l Size effect
k_p Pre-stressing process factor
$k_{e,p}$ Edge or hole pre-stressing factor

In contrast, stiffness is determined by the elastic modulus and geometry of the glass, regardless of failure. The modulus of elasticity for glass is approximately 70 GPa, a fixed property

that does not vary with orientation, as glass is isotropic. Stiffness is also highly dependent on geometry, particularly thickness, as the bending stiffness of glass scales with the cube of its thickness, which can be observed in formula 2.2.

$$D = \frac{E \cdot t^3}{12 \cdot (1 - \nu^2)} \tag{2.2}$$

D Bending stiffness
E Elastic modulus
t Thickness of glass
υ Poisson's ratio

2.3.3 Factors Affecting Glass Deformation

The deformability of glass is influenced by several key factors, with the deformation limit being determined primarily by three variables: thickness, support condition, and pane geometry. Thickness plays a crucial role in defining the material's ability to withstand bending forces; thicker glass tends to have higher stiffness and is less prone to deformation under load. Support conditions, including how the glass is supported on points, along its edges, or throughout its surface, also significantly affect the deform capacity. Fixed or rigid supports can resist more deformation than simply supported edges, as they provide greater restraint against bending, however the peak stresses should be considered near the support. The geometry of the glass pane, particularly its shape and size, further influences how it deforms under applied forces (Nehring & Siebert, 2018). Larger panes with more extensive surface areas are generally more susceptible to bending. The relation between the key factors are shown in Figure 2.4.

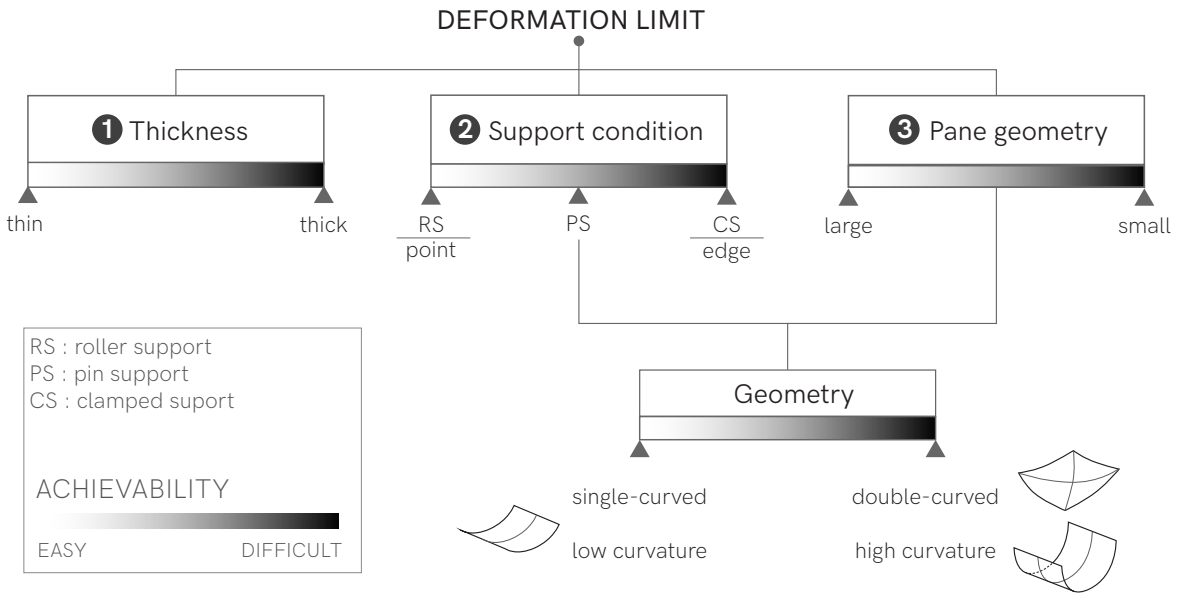

Fig. 2.4 | Factors affecting glass deformation

2.3.4 Thin Plate Theory

In analysing the behaviour of thin plates under normal loading, the classical small-deflection theory (Von Kármán, 1910) has traditionally been used. However, when plates are supported along their boundaries, the load is increasingly carried by middle surface forces, leading to large deformations where the strain-displacement relationship becomes nonlinear. As deformation increases, an additional term must be considered, resulting in a quadratic strain relation. This introduces computational complexity and leads to membrane stiffening, where structural stiffness increases with deformation. Thin plates primarily resist applied loads through their flexural rigidity, acting as cantilevers clamped along one boundary and free along others. In this case, middle surface forces play an insignificant role, allowing the inextensional assumption, where middle surface strains are considered negligible. As a result, the deformed surface remains developable (Mansfield, 1955). Since thin plates naturally resist loads via flexural stiffness, achieving double curvature contradicts this intrinsic behaviour. To induce double curvature, complex boundary and loading conditions, including higher applied forces, are required. Similar to bending paper into a doubly curved shape, significant challenges such as folding and wrinkling arise, making the process inherently difficult.

2.3.5 Developable Surface

According to Mansfield's theory, during deformation, a plate remains in a developable surface, meaning it has zero Gaussian curvature ($K = 0$), which allows the structure to maintain a low-stress state, transferring long-term loads primarily through axial membrane forces while minimising constant bending moments on the surface (Galuppi et al., 2014). Developable surfaces can be flattened onto a plane without stretching, cutting, or deforming, such as cylinders, cones, or tangentially ruled surfaces, making them particularly relevant in shaping thin glass without introducing excessive internal stress (Wang, 2017). Gaussian curvature is mathematically defined as the product of the two principal curvatures (κ_1 and κ_2), expressed as $K = \kappa_1 \times \kappa_2$. If $K=0$, the surface is classified as developable, as seen in cylindrical and conical shapes that can be unrolled into a plane without deformation. If $K>0$, the surface is synclastic, where both principal curvatures are in the same direction, as in spheres and domes, making these surfaces non-developable since they cannot be flattened without stretching. If $K<0$, the surface is anticlastic, meaning the principal curvatures are in opposite directions, as in hyperbolic paraboloids or saddle shapes, which also makes them non-developable. Theoretically, curved structures can support distributed loads through axial stresses in compression and tension; however, as glass is relatively weak in tension, these stresses should be minimised to prevent failure (Weber, 2009). Since monoclastic ($K=0$) surfaces, are developable, they are more suitable for glass structures as they avoid excessive tensile stress and deformation. Conversely, synclastic and anticlastic surfaces require more complex fabrication techniques, making their implementation in glass structures more challenging (Figure 2.5).

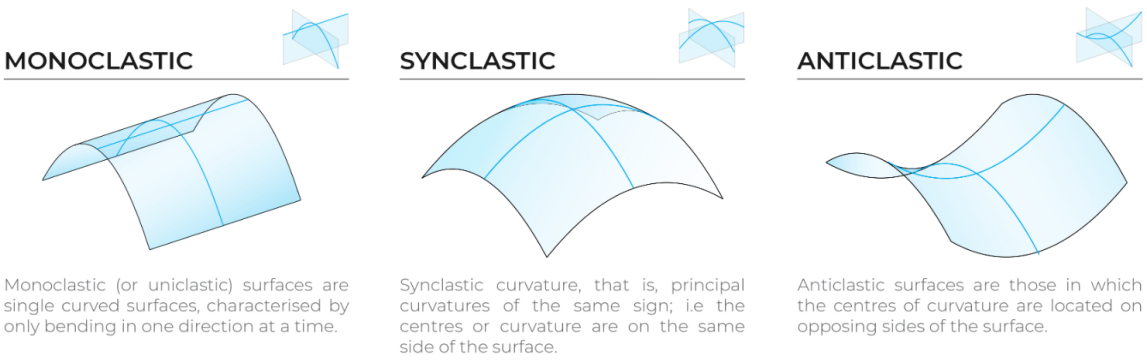

Fig. 2.5 | Different surface types based on curvature (Whitehead, 2018, https://wewanttolearn.wordpress.com/tag/monoclastic/)

2.3.6 Single Curvature Deformation

When deforming a glass plate of given thickness and size into a single curvature, the maximum deflection can be relatively easily calculated using formula 2.3. Galuppi & Riva (2024) conducted numerical and experimental research on this topic. They measured the maximum deflection and stress of a single 0.5 x 1 m, 1.1 mm and 2.1 mm thick Falcon glass under a constant curvature bending condition until failure. In a standard-thickness glass plate, even with a single curvature, the Poisson's effect causes deformation in the perpendicular plane, resulting in a geometry that is not purely monoclastic but double-curved. However, when using thin glass, the effects caused by Poisson's effect are minimal, and experimental results closely align with those predicted by formula 2.3. The 2.1 mm glass proved to be remarkably flexible and capable of endure high stress conditions, achieving curvatures with radii of less than 1 m (Figure 2.6).

$$\varphi = \frac{L}{2\rho_y} = \frac{L}{2}\frac{M}{E^* I_x} \qquad E^* = \frac{E}{1-\nu^2} \tag{2.3}$$

φ	Angle	L'	Final distance between ends
ρ_y	Arc radius	M	Bending moment
v_{max}	Maximum deflection	E^*	Plane strain Young's modulus

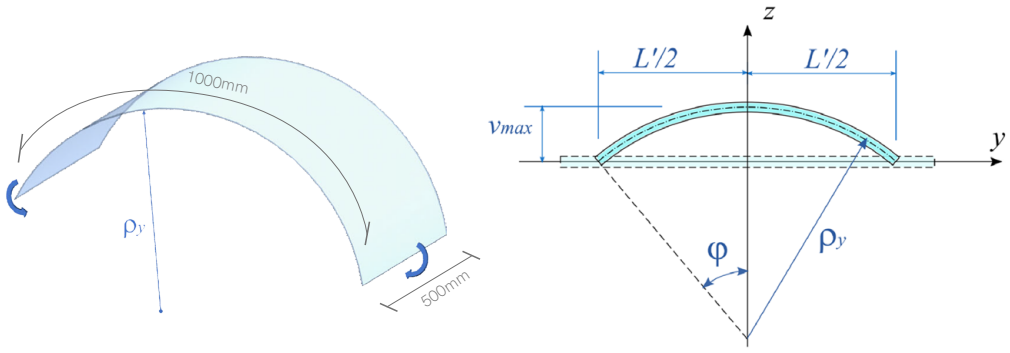

h [mm]	φ [°]	ρ_y [mm]	v_{max} [mm]	L' [mm]	$M_{b,max}$ [Nm]
1.1	106.21	269.72	345.03	517.99	15.125
2.1	55.64	514.92	224.27	850.1	55.125

Correspondent to maximum stress 150 MPa (prEN 12337-1)

Fig. 2.6 | Single curvature bending test (Galuppi & Riva, 2024)

2.3.7 Double Curvature Deformation

Cold-bending glass to achieve synclastic (double-curvature) geometries presents significant challenges due to the high stresses involved and the limitations of Poisson's effect, which impacts deformation (Galuppi et al., 2014). Therefore to achieve double-curved shapes require high-strength thin glass, as noted by Galuppi & Riva (2022). Studies by Hassen et al. (2024) and Ullmer (2023), successfully implemented inflatable insulated glass units (IGUs) to create synclastic geometries using thin glass, though their focus was more on human perception than structural deformation, and high stress was observed at the edges (Figure 2.7). In contrast, saddle-shaped geometries (anticlastic) are hard to achieve, therefore, no studies has been done to achieve such shapes. However hyperbolic paraboloids (hypar), are easier to achieve using twisting edges or corners. Research by Van Herwijnen et al. (2004) identified instability during hypar deformation, with compression in the middle zone and tension along the edges causing buckling. Bensend & Zaccaria (2024) noted that excessive deformation can reduce stiffness, while Datsiou & Overend (2016) highlighted that thin, large glass panels with appropriate aspect ratios are more efficient for deformation. Additionally, van Driel et al. (2022) found that asymmetric hypar shapes emerge when a critical load is exceeded in IGU systems. A common issue in anticlastic geometries is unintended surface buckling deformation under high loads, which, while not causing glass failure, prevents ideal deformation and limits performance compared to monoclastic structures.

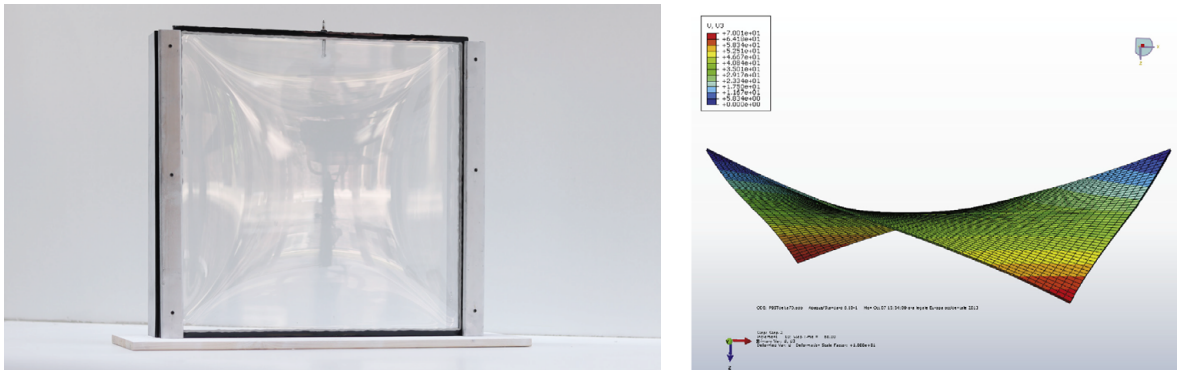

Fig. 2.7 | Examples of double curved cold-bent glass research
Note. Left: Inflatable glass (Ullmer, 2023) Right: Hypar deformation (Galuppi et al., 2014)

2.3.8 Support Condition

The method of supporting glass can be categorized into roller-support (RS), pin-support (PS), and clamp-support (CS), and these supports can be applied into point support types or edge support types. Compared to point support, line support offers better stress diffusion across the frame due to its stiffening effect, allowing for greater displacement limits when deforming a glass pane into a hypar (Galuppi et al., 2014). Silveira et al. (2018) emphasized that during deformation, considerations should include protecting panel edges, preventing stress concentration, and allowing movement at the supports. They noted that the type of support is deeply tied to the glass's movement, and insufficient degrees of freedom in

the support system can lead to stress concentration but also increase design complexity and unpredictability. Additionally, they suggested that a middle actuator could facilitate smoother deformation when needed. Datsiou & Overend (2016) observed that the degree of freedom and maximum displacement allowed by supports follow the order of RS, PS, and CS, with RS allowing the greatest freedom and displacement. However, in double-curved geometries, unwanted flaws coming from elastic deformation occur in the opposite order—CS is most prone to flaws, followed by PS, and then RS (Figure 2.8).

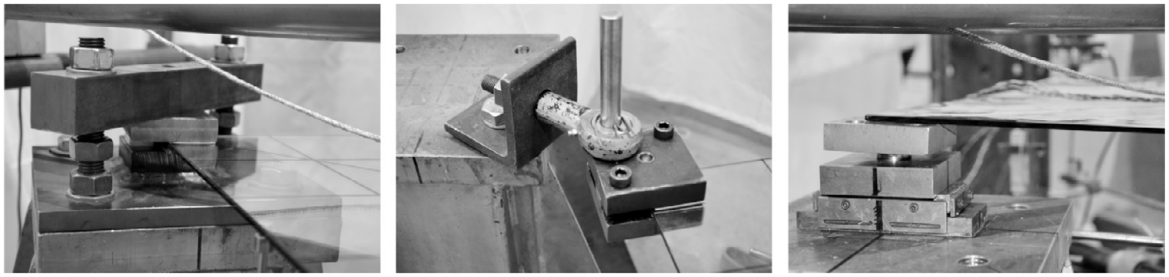

Fig. 2.8 | Different types of support conditions (Datsiou & Overend, (2016)
Note. From left to right: clamped, pin, and roller support.

2.4 Lamination

2.4.1 Post-Breakage Behaviour

When glass fails, the fracture pattern varies depending on the type of glass and the residual stresses released during breakage. Annealed glass breaks into large, dangerous, sharp pieces due to its low strength. Heat-strengthened glass, being stronger, breaks into smaller pieces while retaining some load-bearing capacity. Fully tempered glass is the strongest among the three but shatters into very small fragments, losing almost all load-bearing capacity after failure (Figure 2.8). Lamination significantly improves the post-breakage behaviour, with heat-strengthened glass being the most widely used in the building industry for its balance of strength and safety. Chemically tempered float glass, with high strength, breaks into large fragments similar to annealed or heat-strengthened glass. When laminated, it shows promise as a post-failure element, though safety concerns arise due to limited central tension levels caused by ion exchange. Galuppi & Riva (2024) noted that when extreme

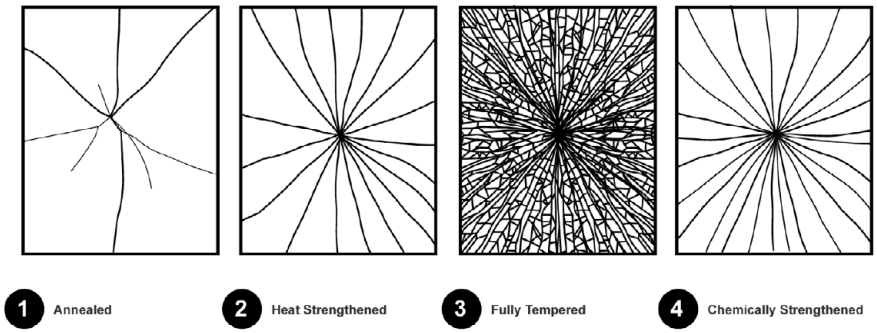

Fig. 2.8 | Glass failure patterns with different degrees of strengthening (Rammig, 2022)

strain energy is stored through bending, the glass can shatter into extremely thin shards, less than 1 cm in size (Figure 2.9). Therefore, the failure pattern varies depending on the type and extent of stress, emphasizing the need to adopt strategies to minimize post-failure risks tailored to the intended application (Overend et al., 2007).



Fig. 2.9 | Chemical strengthened Falcon 2.1 mm glass breakage during bending (Galuppi & Riva, 2024)

2.4.2 Lamination Process

Laminated glass is composed of two or more glass layers bonded by an interlayer, designed to enhance both safety and structural performance. The lamination process involves heating the glass to approximately 140 °C and applying pressure of up to 14 bar, typically within an autoclave. Figure 2.10 illustrates the lamination process of a typical 2-stage lamination production. Although lamination does not change the brittle nature of glass, it ensures that shattered fragments remain securely attached to the interlayer, preventing the panel from falling apart and enhancing its residual load-bearing capacity. When glass breaks, the interlayer holds the pieces together, reducing hazards. Common interlayer materials include polyvinyl butyral (PVB), SentryGlas Plus (SGP), ethylene vinyl acetate (EVA), and cast-in-place resin (CIP), each offering distinct properties for use in various structural and safety applications. Table 2.2 describes the key features of different interlayer types.

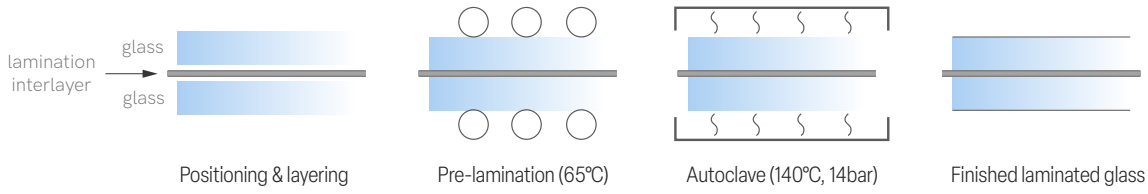

Fig. 2.10 | Typical 2-stage lamination process

	Original state	Process	Structural character	Cold-bending compatibility
❶ Polyvinylbutyral (PVB)	Film (roll)	Pre-lamination (65°C) -> Autoclave (140 °C, 12-14 bar)	Low shear elastic creep	Higher degree of spring-back
❷ SentryGlas Plus (SGP)	Film (sheets)		High shear rigid	Low curvature poss.
❸ Cast-in-place resin (CIP)	Two-component resin	Edge seal & liquid pouring -> curing (e.g. UV light)	Lower shear than SGP diverse property	Compatible to any shape

Table 2.2 | Characteristic of different lamination types

2.4.3 Behaviour of Different Lamination Types

Lamination significantly increases residual load-bearing capacity and enhances post-breakage behaviour. However, the mechanical performance of a laminated glass unit is highly dependent on the properties of the interlayer. When a stiff interlayer polymer is used, the glass unit behaves almost like a monolithic structure, with a uniform compression and tension profile. In contrast, a more flexible interlayer allows the individual glass panes to perform independently, resulting in distinct compression and tension zones, as illustrated in Figure 2.11. The behaviour of interlayer polymers is highly sensitive to both time and temperature, making it critical to model the bending phase accurately and account for the transient relaxation that follows (Galuppi & Royer-Carfagni, 2014). Soft interlayers are prone to viscous deformation, which can significantly reduce the initial distortion over time, whereas stiff interlayers provide stronger bonding and are more reliable for the entire lifespan of a building.

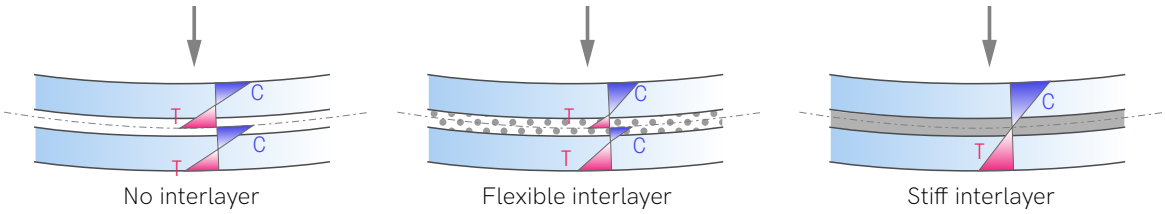

Fig. 2.11 | Structural behaviour depending on different types of lamination interlayers

2.4.4 Cold-Lamination-Bending (CLB)

For flat glass products, lamination typically does not pose significant challenges. However, when the final product is curved laminated glass, different manufacturing methods must be employed. One common approach is to produce hot-bent laminated glass by heating glass sheets to their softening point, shaping them against a negative form, and then performing the lamination process in an autoclave. A critical aspect of this method is ensuring that the glass plies align perfectly, with only slight differences in curvature. An alternative method for creating curved laminated glass involves starting with a flat glass product that is laminated using the standard autoclave process. The laminated flat glass is then cold-bent by elastically straining it to achieve the desired curvature. This process has gained popularity due to its cost-effectiveness, as it eliminates the need for expensive negative forms, making it ideal for constructing free-form glazed surfaces (Belis, 2007). However, it requires a strong structural frame to maintain the forces needed to keep the glass in its curved configuration; without these forces, the glass would revert to its original flat shape.
A more recent innovation is the Cold-Lamination-Bending (CLB) technique. In this method, the unbonded glass-interlayer package is first deformed into the desired shape using provisional constraints. The lamination process is then performed in an autoclave while the glass is held in this curved configuration. Once the constraints are removed, the curved laminate experiences an initial spring-back, followed by gradual relaxation due to the decay of shear coupling between the glass plies, which is influenced by the viscosity of the polymeric inter-

layer. Despite these effects, much of the curvature is retained, resulting in a product similar to hot-bent glass (Figure 2.12).

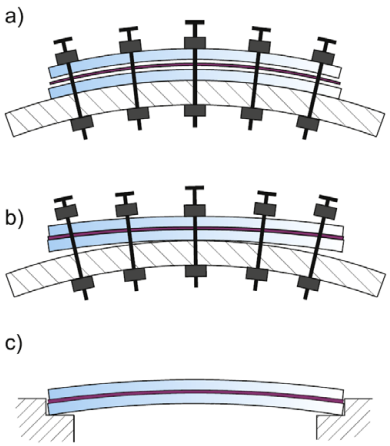

a) Cold bending of uncoupled package
b) Gradual release after lamination
c) Final placement

Fig. 2.12 | Cold-lamination-bending process (Galuppi & Royer-Carfagni, 2015)

Galuppi and Royer-Carfagni (2015) propose several strategies for effectively implementing CLB for glass. For instance, using a stiff interlayer like SGP ensures that the deformation remains stable over the entire lifespan of the glass. In contrast, soft interlayers such as PVB tend to modify the curvature immediately after the process due to their lower rigidity (Figure 2.13). While SGP provides higher shear stress, which helps maintain the desired shape, this also results in elevated stress at the plate edges, could potentially lead to delamination of the glass product. Additionally, the sudden release of constraints causes shear-stress concentration in the adhesive layer, increasing the risk of delamination or creep. To address this, a gradual release program can be designed, which has been shown to reduce shear stress by up to 50 %. Another highly effective method for minimizing peak stress involves reshaping the mould to feature a sinusoidal profile. This design reduces stress intensification, particularly near the plate edges, and is especially beneficial for stiff interlayers like SGP. By optimizing these parameters, the durability and structural integrity of cold-laminated curved glass can be significantly improved (Figure 2.13).

Time dependence for the secant shear modulus of a PVB and a IP at 20° C [8].

t	PVB	IP
	$G(t)$ [MPa]	$G(t)$ [MPa]
3 s	8.06	157.78
1 h	0.840	66.38
1 day	0.508	34.99
1 year	0.266	8.20
$t \to \infty$	0.052	3.78

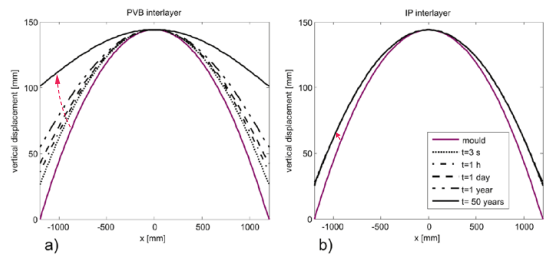

Fig. 4. Constant-curvature CLB. Vertical displacement at various times t for a) PVB interlayer and b) IP interlayer (elastic moduli of the interlayers from Table 1).

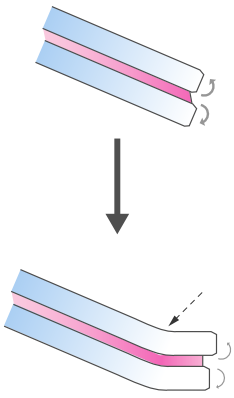

Fig. 2.13 | Time dependent shear modulus change on interlayer (Galuppi & Royer-Carfagni, 2015) & Sinusoidal edge shaping preventing delamination (Author)

2.4.5 Cast-in-Place (CIP)

Cast-in-Place (CIP) method for lamination, which differs significantly from film or sheet-based methods like PVB or SGP, as it uses a liquid resin. Despite involving a less automated production process, CIP offers the advantage of being more suitable for laminating complex formed shapes. While CIP does not achieve the same stiffness as SGP, it provides relatively high stiffness, good adhesion quality with glass, and performs well under long-term loads. CIP materials range from epoxy to polyurethane (PU) to acrylics, each offering a wide range of viscosities tailored to specific needs. These resins are available either as single-part formulations, which are primarily UV-cured, or as two-part systems that cure through a catalytic process. Additionally, a secondary heat cure can be used to ensure the complete curing (Gross, 2002).

Generally, CIP bonds effectively to glass and other substrates, including metal. Volakos et al. (2021) conducted an experimental study using H.B. Fuller | Kömmerling's LOCA (Liquid Optically Clear Adhesive), PU based 2-component resin to laminate heat-strengthened flat glass with aluminium fillings. Their process included edge sealing, resin pouring, curing, and structural performance testing. The study focused on designing the LOCA manufacturing process and observing resin relaxation and delamination, offering valuable insights into the durability and structural integrity of LOCA-laminated glass (Figure 2.14).

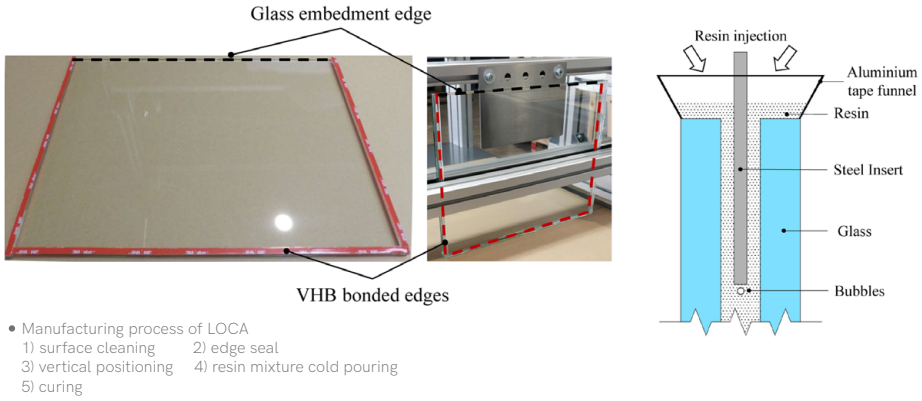

Fig. 2.14 | CIP lamination process with aluminium filling (Volakos et al., 2021)

2.5 Solar Control

2.5.1 Transparency

Transparency is the most distinctive and significant property of glass, setting it apart from any other building material. Transparency can be defined as the physical property of allowing light to pass through the material without significant scattering. However, glass is not perfectly transparent; a portion of light is reflected when it interacts with the surface, while another portion is absorbed by the colour of the glass. This diverse and intricate optical interaction lies at the core of the unique allure of glass as a building material (Wurm, 2007).

A particularly detrimental effect on transparency, often considered highly distracting, is the reflection of incident light off the surface of the glass façade. Such optical distortion arises from the surface quality of the pane and significantly affects visual perception to a degree that is easily noticeable to the naked eye (Figure 2.15). This phenomenon occurs even more frequently when the glass pane is curved, as the geometric complexity intensifies the reflective distortions. Managing the surface quality of glass requires the use of both qualitative and quantitative methodologies, making it a particularly challenging field. In the case of curved glass, the geometrical complexity further exacerbates the issue, and there remains a lack of established standards for quality assessment in such applications (Schlösser, 2019).



Fig. 2.15 | Glass distortions in a building façade (© Jonas Ferlin, 2019)

2.5.2 Solar Transmittance

Transmittance designates the radiation permeability of a material, irrespective of the quality of the image of an object behind the component. It describes the proportion of incident light that passes through a glass pane. In contrast, absorption refers to the property of a material to convert penetrating light into other forms of energy, such as heat. The extent of absorption depends on the thickness of the pane, with thicker panes absorbing a greater proportion of solar energy. The relationship between transmittance, reflectance, and absorptance is illustrated in Figure 2.16. These interdependent properties are fundamental to understanding how light interacts with glass. Additionally, the concept of the g-value is important in architectural glass applications. The g-value represents the total solar energy transmittance, which includes both the directly transmitted light and the secondary thermal energy emitted into the room through radiation, conduction, and convection. This metric is vital for evaluating the energy performance of glazing systems, as it indicates the extent to which solar energy contributes to heating interior spaces (Schittich et al., 2007). As illustrated in Figure 2.16, when the solar incident angle (θ) is low, reflection decreases, resulting in higher transmittance (τ). Therefore, when glass is utilised as a roofing element, the solar radiation will often strike the glass surface at angles close to perpendicular, lead-

ing to significant transmittance. Consequently, controlling transmittance becomes a critical issue in such applications. For curved glass, the incident angle varies continuously across the surface due to its geometry, making it more challenging to predict transmittance. This complexity increases with the intricacy of the curved form.

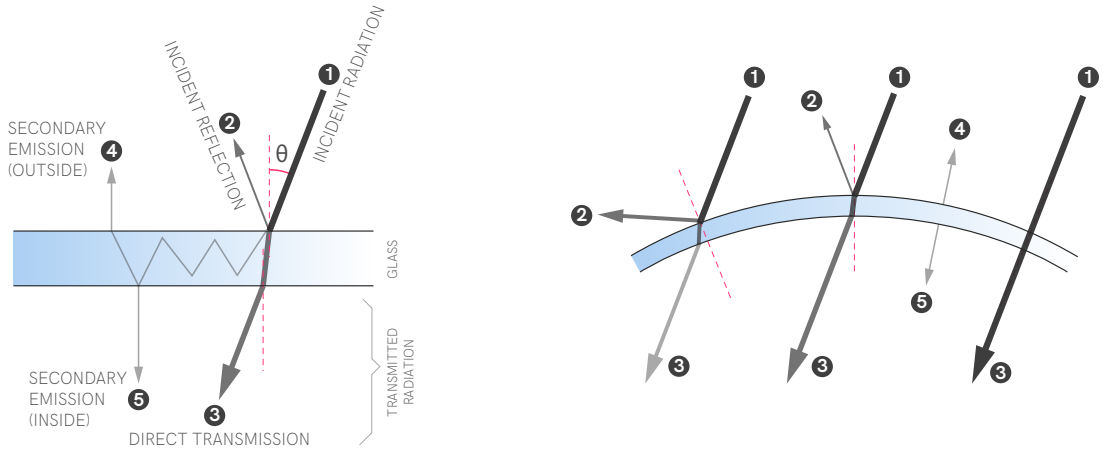

Fig. 2.16 | Solar transmission on a glass pane
Note. θ is solar incident angle, (1) incident radiation (2) incident reflection (3) direct transmission (4) secondary emission-outside (5) secondary emission-inside.

To understand how we perceive colour and what solar transmittance entails, it is essential to first comprehend electromagnetic radiation, as shown in Figure 2.17. Electromagnetic radiation exists in various forms and wavelengths, and humans are only able to detect light within a specific range of wavelengths with human eyes, typically between 380 and 780 nanometres (nm), which constitutes the visible light spectrum. However, just because wavelengths outside of this range are not visible to the human eye does not mean they do not exist. In fact, transmittance can vary across different wavelengths, even those beyond

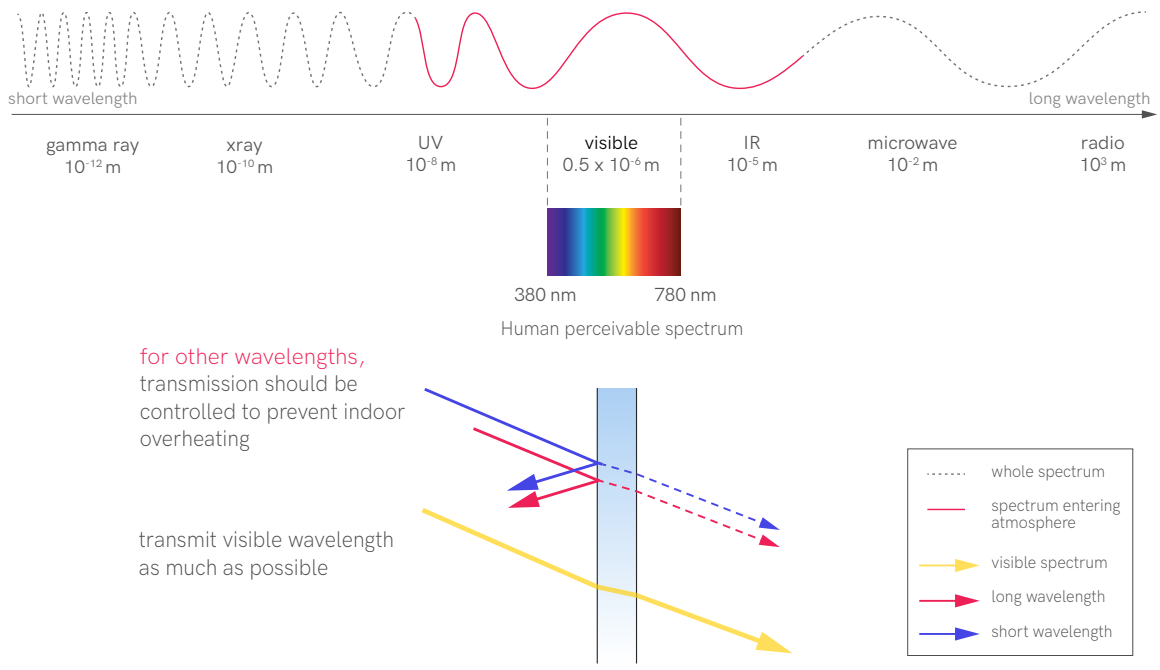

Fig. 2.17 | Spectrum of electromagnetic radiation and transmittance

the visible spectrum (Shelby, 2005). For example, Figure 2.17 presents an idealised scenario—while it may be practically difficult, imagine a material that appears fully transparent to the eye. Such a material would transmit light within the visible spectrum exactly as it strikes the surface. However, wavelengths outside the visible spectrum, though undetectable to the human eye, would likely undergo reflection and absorption. As a result, it would be inaccurate to describe the material as truly fully transparent, since transparency would not be uniform across all wavelengths. Therefore, the combination of moderate daylight transmittance (harvesting) and low total energy transmittance (e.g. comfortable indoor illuminance and little heat) would be the ideal transmittance performance for the glass in buildings.

2.5.3 Solar Control Methods

According to Wilson&Elstner (2018), several methodologies are proposed for controlling solar transmittance. The first method involves using tinted glass or selective coatings to reflect radiation within a desired spectrum. However, tinted glass can affect the overall colour and appearance of the building, and while it blocks transmission, the absorbed energy may still impact the building or indoor spaces. The second method is the use of cavity elements and switchable glazing. Cavity elements, such as blinds inserted between the layers of an IGU (Insulated Glazing Unit), low-E coatings applied to cavity surfaces, textiles, or micro-louvres that have less effect on transparency, can help regulate solar transmittance. Switchable glazing, such as electrochromic glazing, allows dynamic adjustment of transparency. However, these methods are typically limited to IGU units or primarily flat glass surfaces. The third method involves adjusting the position of coatings to control transmittance or changing the thickness of the glass itself. The fourth method is the treatment of the glass pane, where physical or chemical changes, such as screen printing or etching, are applied to the surface to modify its transmittance. Finally, the use of shading devices—either external or internal—can help control solar transmittance independently from the glass pane itself. While external solar control systems using shading devices are generally advantageous because they keep absorbed solar energy separate from the internal space or glass panel, they do have the downside of impacting the overall building aesthetics and adding additional load to the structure due to the installation of extra solar blocking devices (Figure 2.18).

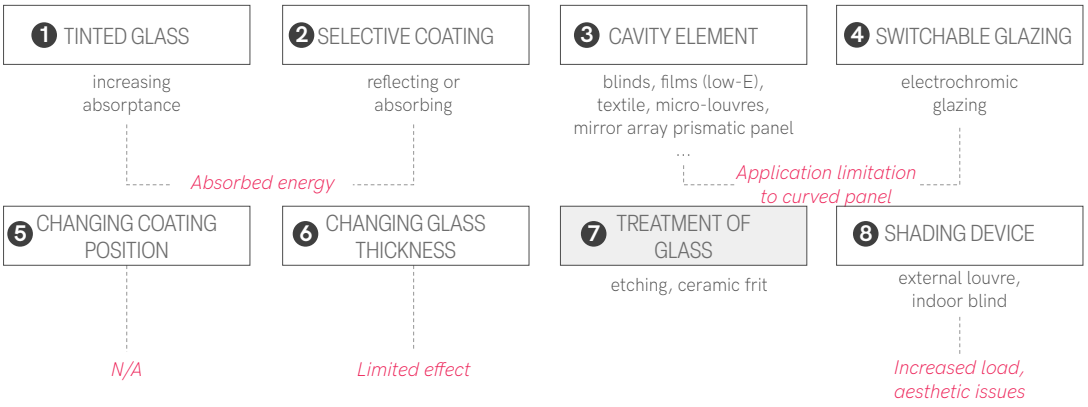

Fig. 2.18 | Solar control mechanisms and conformity with research design goal

2.5.4 Surface Treatments

Surface treatment methods for glass include enamelling, acid etching, and sand-blasting. Enamelling involves applying a coloured ceramic layer to the glass, which is then baked during the manufacture of toughened or heat-strengthened glass. This process allows for easy customisation of patterns through spraying or silk-screen printing. Acid etching creates a matt finish by chemically reacting with the glass. The degree of the finish depends on how long the acid is in contact with the surface. Etched glass can be patterned by masking areas. The more intense the etching, the rougher the surface, reducing transparency and scattering light. Objects behind the glass appear clearer when close to the surface but become more diffused as they move away. Sand-blasting also creates a matt finish by roughening the glass surface, with optical effects similar to acid etching. Patterns can be applied by masking specific areas. Table 2.3 (EN 19100-1, 2024) shows that when surface treatments like enamelling, acid etching, or sand-blasting are applied, the design bending stress of the glass decreases compared to standard float glass, with the most significant reduction for sandblasted glass.

Glass material[a] (whichever glass composition)	Factor for the glass surface profile k_{sp}	
	As produced[c]	Sandblasted[c]
Float glass	1,0	0,6
Drawn sheet glass	1,0	0,6
Enamelled float or drawn sheet glass[b]	(1,0)	(0,6)
Patterned glass	0,75	0,45
Enamelled patterned glass[b]	(0,75)	(0,45)
Polished wired glass	0,75	0,45
Patterned wired glass	0,6	0,36

[a] All coated glass, painted glass (not enamelled glass), mirror glass etc., where the applied material does not affect the glass structure, can be treated the same as the substrate glass without the applied material.

[b] These glass types are not generally available as annealed glass, but the values of k_{sp} are also required in the formulae for pre-stressed glass.

[c] For acid etched glass, the 'as produced' value of k_{sp} should be used.

NOTE 4 The values of k_{mod} are given in Table A.3.

Glass material per product (whichever composition)	Values for characteristic bending strength $f_{b,k}$ for pre-stressed glass processed from:		
	thermally toughened safety glass to EN 12150-1, and heat soaked thermally toughened safety glass to EN 14179-1	heat strengthened glass to EN 1863-1	chemically strengthened glass to EN 12337-1
float glass or drawn sheet glass	120 N/mm²	70 N/mm²	150 N/mm²
patterned glass	90 N/mm²	55 N/mm²	100 N/mm²
enamelled float or drawn sheet glass	75 N/mm²	45 N/mm²	
enamelled patterned glass	75 N/mm²	45 N/mm²	

NOTE 1 The values for thermally toughened safety glass and heat soaked thermally toughened safety glass can also be used for glass conforming to EN 13024-1, EN 14321-1 and EN 15682-1.

NOTE 2 The characteristic bending strength values in the table are the same as in the product standards at the time of publication of this document. In the case of revision of the values in the product standards, then the values in the product standards take precedence.

Table 2.3 | Surface treatment factor k_{sp} for design bending strength for glass
Characteristic bending strength difference between additional treatments (EN 19100-1, 2024)

According to Wilson & Elstner (2018), there are several methods for applying ceramic fritting to glass, including digital printing, screen printing, roller coating, and curtain coating. Ceramic frit is a type of enamelling, as it involves the application of a ceramic coating that is fused to the glass surface through firing. The most commonly used method is screen printing, which involves different mediums and varying viscosities for each process. During the thermal toughening process, firing occurs, causing the glass and ceramic coating to fuse together. In addition to the surface treatment factor defined earlier, the characteristic bending strength value of the glass decreases too when an enamel pattern is applied (Table 2.3), depending on the type of tempering used (Figure 2.19).



Fig. 2.19 | Fracture origin from ceramic frit pattern (Bergers et al., 2016)

When considering methods to control transmittance, one might think that choosing a single method from the previously mentioned options is sufficient. However, as shown in Figure 2.20, each control method blocks different wavelengths, so it is necessary to combine them appropriately.

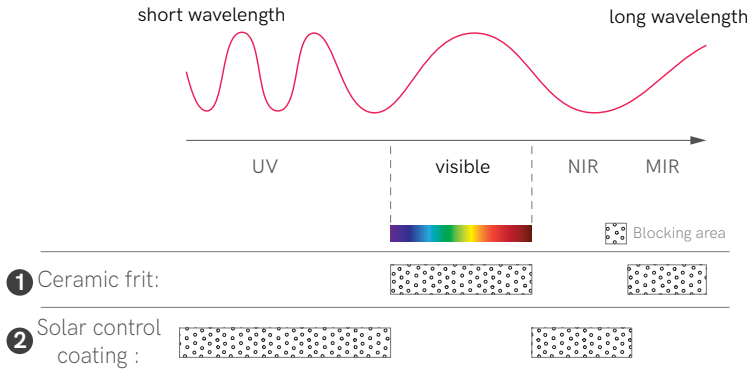

Fig. 2.20 | Changes in wavelength response according to different solar control methods

2.5.5 Frit Pattern

Some notable examples of enamel frit patterns successfully applied to glass include the orange coloured linear frit pattern on The Diana Center at Barnard College (Weiss/Manfredi, New York, 2010), shown in Figure 2.21, and the distinctive black fonts applied to the Museum of the History of Polish Jews (Kuryłowicz & Associates, Lahdelma & Mahlamäki,

Warsaw, 2013). While the physical properties of glass and ETFE (Ethylene Tetrafluoroethylene) differ (Table 2.4), there has been limited research on applying frit patterns to complex curvature in glass. However, Monticelli et al. (2013) were focusing on optimizing frit pattern (geometry) and percentage of opaqueness that is applied on a hemispherical synclastic shape with ETFE foil. Lau et al. (2024) conducted a study on the application of various frit patterns (Table 2.5) on the parabolic shape of ETFE to measure their performance. Additionally, Roudsari & Waelkens (2015) explored the application of frit patterns on complex geometries, focusing on daylight simulation methods.

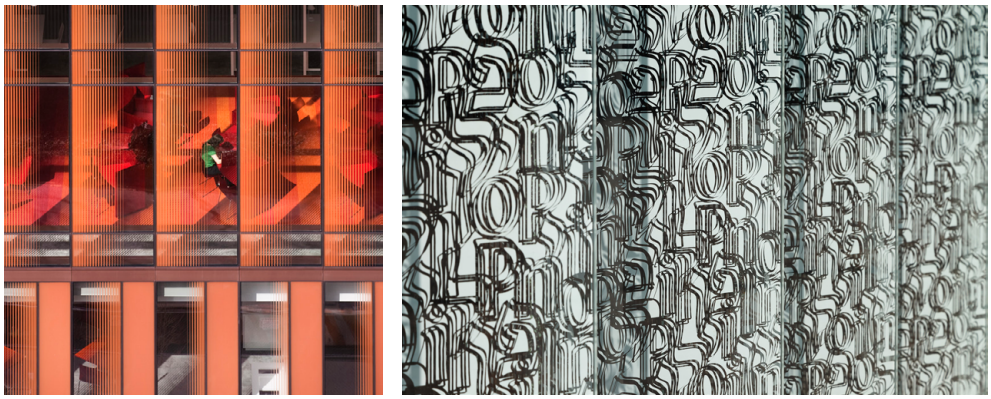

Fig. 2.21 | Examples of unique frit patterns applied on buildings
Note. Left: The Diana Center at Barnard College, Weiss/Manfredi, New York, 2010 (© Albert Vecerka/Esto)
Right: Museum of the History of Polish Jews, Kuryłowicz & Associates, Lahdelma & Mahlamäki, Warsaw, 2013 (© Pawel Paniczko)

	Uncoated float glass	low E outside	low E inside
Thickness [mm]	4	4	4
Radiation transmittance	0.83	0.79	0.79
g-value	0.85	0.811	0.808
Light transmittance	0.89	0.84	0.88
Light reflectance outside	0.081	0.1	0.081
Energy reflectance outside	0.075	0.13	0.075
Shading coefficient	1.0	0.95	0.94
U-value [W/m²K]	5.63	5.34	3.8

	U-value (W/m^2K)	g-value
6mm monolithic glass	5.9	0.95
6-12-6 Double Glazing Unit (DGU)	2.8	0.83
6-12-6 High Performance Double Glazing Unit (DGU)	2.0	0.35
2 Layer ETFE Cushion	2.9	0.71-0.22 (with frit)
3 Layer ETFE Cushion	1.9	0.71-0.22 (with frit)
4 Layer ETFE Cushion	1.4	0.71-0.22 (with frit)

Table 2.4 | Comparison of glass/ ETFE U&G values (Schittich et al., 2007, Monticelli et al.,2013)

Image	Types of Fritting Patterns	Size of Fritting Patterns	Percentage of Light Transmittance
	Clear	Not Applicable	100%
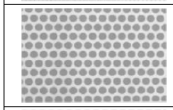	Dots	16mm	73%
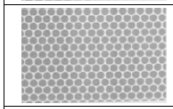	Dots	16mm	65%
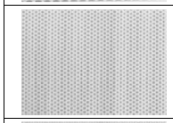	Dots	4.3mm	85%
	Inverted	2.8mm	64%
	Honeycomb	2.8mm	65%

Table 2.5 | Customised fritted pattern on ETFE foils differing in light transmittance (Lau et al., 2024)

2.5.6 Radiation and Geometry

Jiang et al. (2020) highlighted that in real-world environments, not only does the intensity of radiation play a role, but as the complexity of a shape increases, it becomes significantly more challenging to measure and predict radiation due to the effects of reflection and scattering from surrounding objects and the shape itself. Their research explored how different roof shapes influence the distribution of received radiation. Generally, paraboloid geometries exhibit a smooth transition of radiation across their surfaces, while the northern sections of protruding geometries tend to experience lower radiation intensity (Figure 2.22).

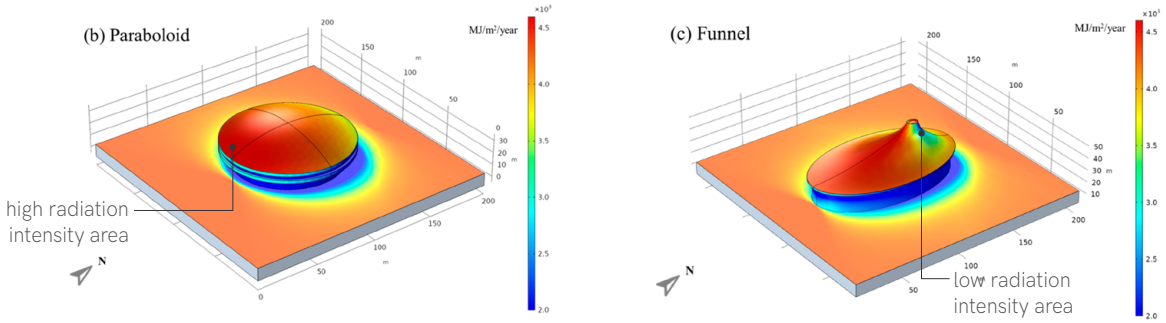

Fig. 2.22 | Incident radiance change depending on roof geometry (Jiang et al., 2020)

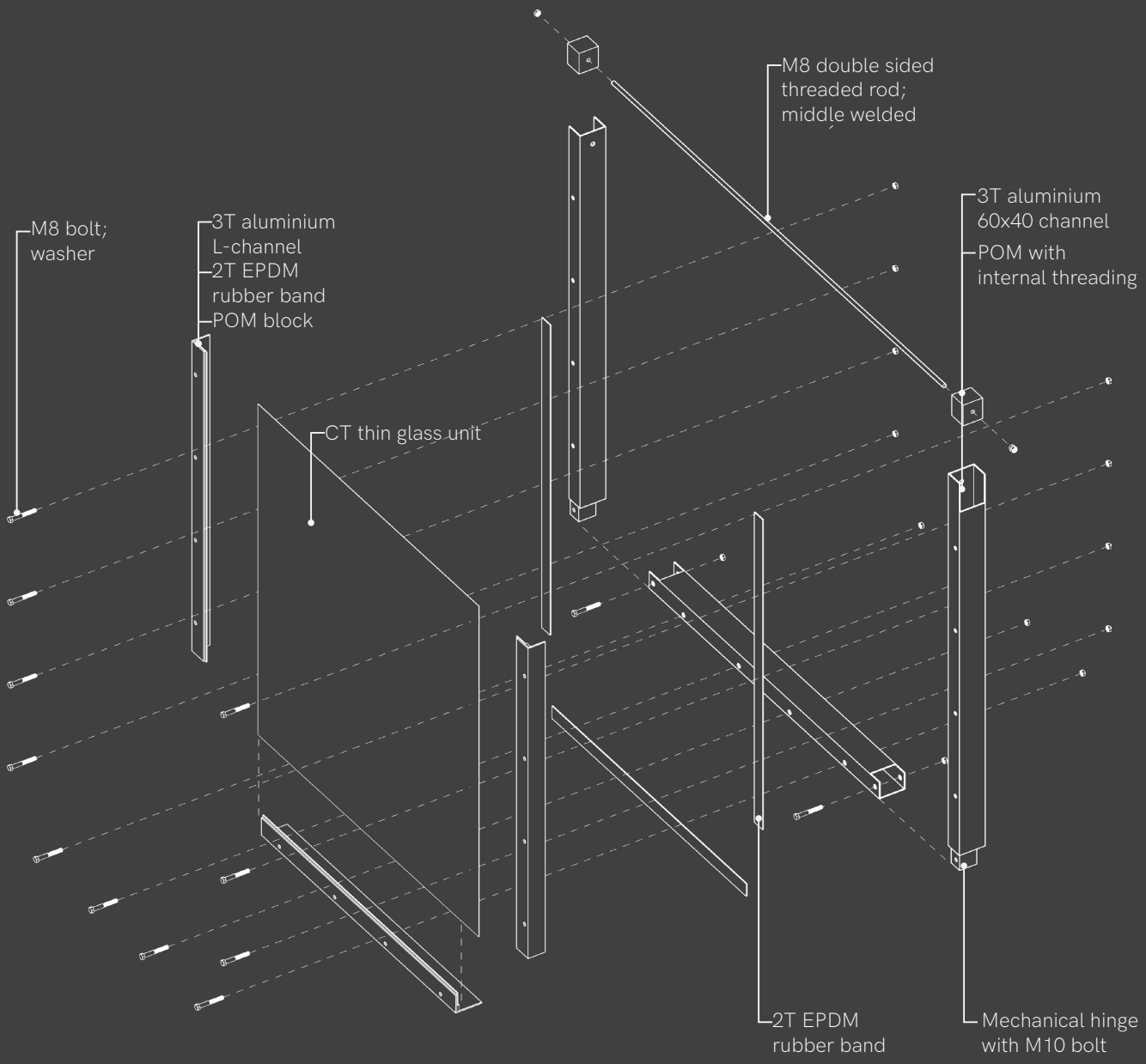

· Buckle Bending Machine: 3-edge fixture

III. CONCEPTUAL DESIGN

3.1 The OWO Pavilion

The OWO Pavilion, completed in 2023 in London, UK, is a sculptural structure located in the courtyard of the former Old War Office in Whitehall. Its roof features an organic, fluid form inspired by the rippling patterns of ocean waves (Figure 3.1). To achieve a natural interplay of reflections, each roof panel is geometrically designed to mimic the movement of water. The panels are crafted from mirror-polished stainless steel, utilising the material's elongation properties and shaped through hydraulic pressure in moulds. The final design incorporates around 20 distinct double-curvature panels, each measuring under 1 square metre. This study explores a hypothetical design scenario in which the originally stainless steel components are replaced with cold-bent glass.



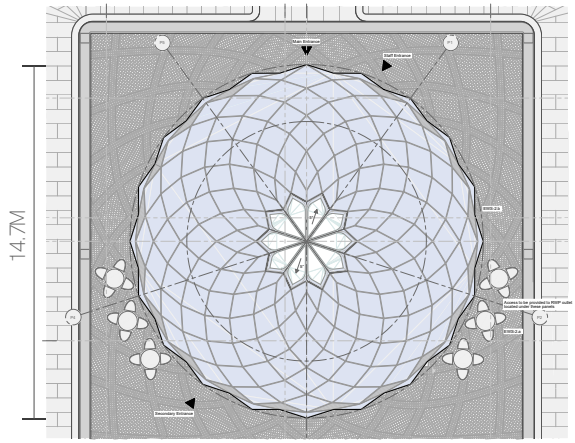

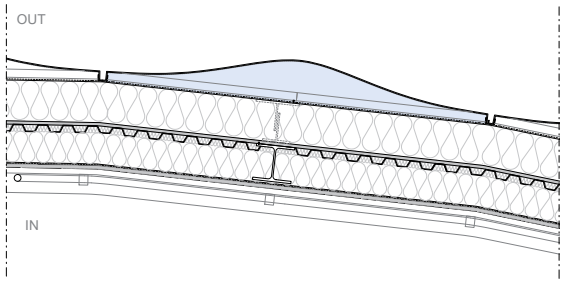

Elements where stainless steel panels are going to be replaced with glass within this research

Fig. 3.1 | The OWO Pavilion, plan, and sinusoidal roof shape section (Daewha Kang Design, 2023)
Note. Top picture © Kyungsub Shin.

3.2 Design Objectives

· Replicate the original design using glass, preserving its organic double-curved fluid form and reflective qualities through cold bending methods.

· Optimise internal stress distribution caused by the cold-bending process.

· Ensure structural performance, so that the glass panels satisfy fundamental load requirements for roofing applications.

· Apply a solar protection strategy to the roofing system to maintain indoor comfort quality.

3.3 Buckle Bending

In the context of cold bending glass, typical methods involve out-of-plane corner displacement, such as twisting, or in-plane edge displacement techniques. However, the geometry targeted in this research deviates from these established forms. Specifically, the cross-sectional profile of the panel used in the OWO Pavilion closely resembles the first buckling mode of an end-restricted Euler column (Figure 4.9). This insight inspires the development of a novel method that uses in-plane forces to induce *controlled buckling deformation*, thereby achieving the desired double curvature.

As this approach does not align with existing cold bending techniques and appears to be unprecedented in glass manufacturing field, a new term is proposed to describe the method: *buckle bending*. This term will be used consistently throughout the dissertation to refer to the cold bending strategy introduced and tested in this study.

As illustrated in Figure 3.2, the diagram outlines the geometry obtained through buckle

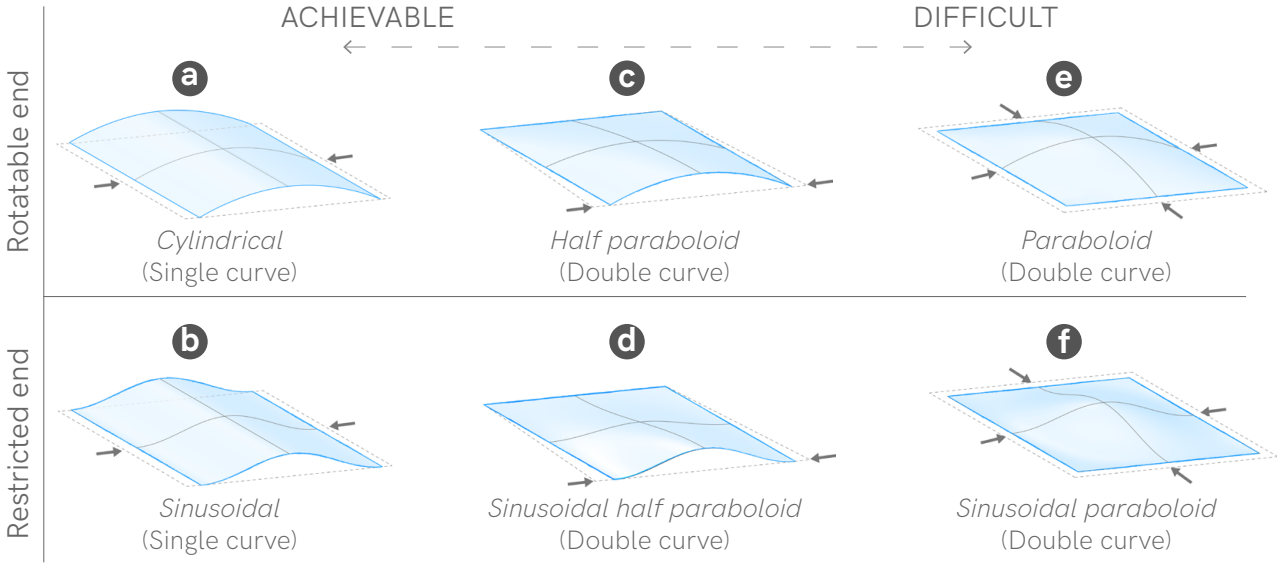

Fig. 3.2 | Thin plate buckle bent geometries according to different boundary conditions

bending, highlighting both the deformation mechanics and associated implementation constraints. To realise the intended water droplet-like geometry *f*, several key boundary conditions must be fulfilled: in-plane loads must be applied at all four edges, and rotational movement at the edges must be constrained to preserve the desired curvature.

3.4 Buckle Bending Test - Sinusoidal Paraboloid

To prototype the buckle bending process using a thin plate material with similar brittle properties to glass, easily accessible PVC sheet is selected. A 1:5 scale deformation experiment is conducted using this material to simulate the approximate behaviour of the full-scale panels. To facilitate the sinusoidal buckle-bent shape, a custom frame capable of clamping the sheet edges to restrict rotation is 3D-printed using PLA filament. After assembly, manual force has been applied to induce the intended shape. However, achieving the expected form requires significant force, and unintended wrinkles and folds are observed near the corners (Figure 3.3). This experiment reveals that the proposed deformation method and boundary conditions involves excessive constraints and complexities, making it impractical for real-world application. As a result, this approach is deemed unsuitable for fabricating the desired glass panels.

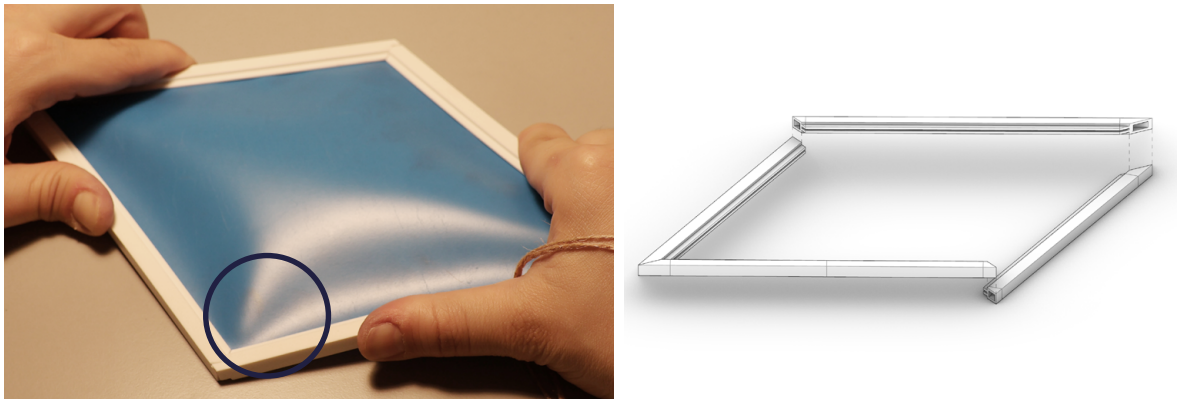

Fig. 3.3 | Sinusoidal paraboloid surface buckling test & fixture frame assembly

3.5 Buckle Bending Test - Half Sinusoidal Paraboloid

Through the literature review, it was identified that excessive boundary conditions—specifically, the number and type of supports—lead to higher internal stress, making deformation more difficult. The clamping support type is necessary to achieve the specific sinusoidal geometry, so the approach has been refined by reducing the number of edge supports. By completely removing support along one edge, it becomes possible to achieve a *half-sinusoidal paraboloid shape*, as illustrated in Figure 3.2d. Building on this concept, a schematic sketch (Figure 3.4) is developed to design a full-scale buckle bending device. The proposed system consists of a rigid frame supporting three edges while using a threaded rod along the

free edge to induce buckling. To mitigate geometric defects such as local stress concentrations and wrinkles, which are likely caused by continuous rigid supports along segmented edges, the design intentionally omitted support at the two rotating corners. Additionally, to prevent unwanted out-of-plane torsion due to the compressive forces from the threaded rod, two key strategies are considered: installing a robust mechanical hinge mechanism at the corners that prevents out-of-plane rotation and tension-induced displacement enabling the most efficient implementation of minimal path of deformation.

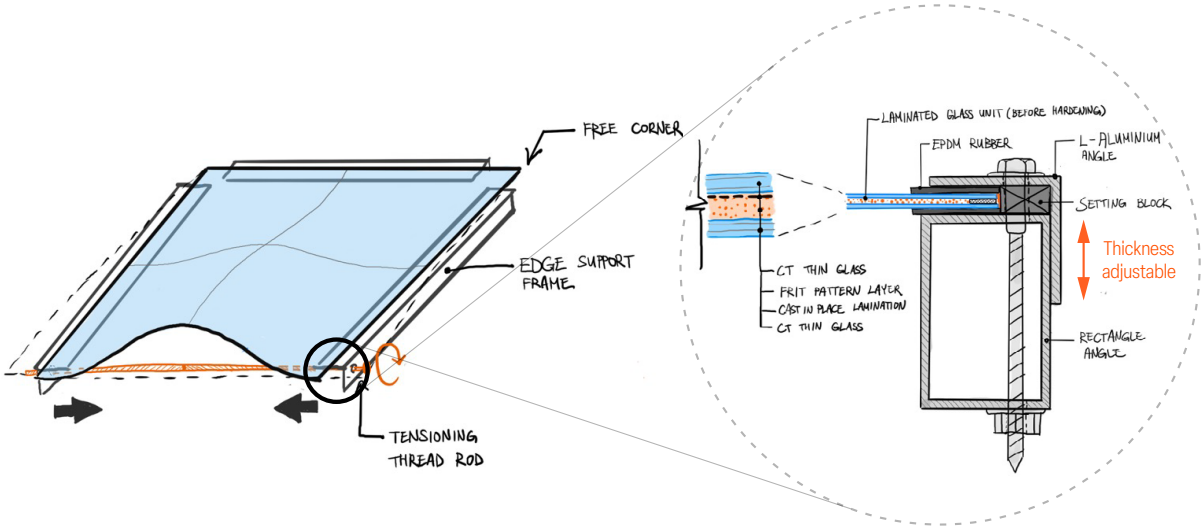

Fig. 3.4 | Schematic design of half sinusoidal paraboloid buckle bending machine

3.5.1 Considerations for Manufacturing

Modular Assembly

The device should be designed for easy assembly and disassembly to facilitate transportation.

Reusability

Rather than being a single-use apparatus, it should allow for multiple uses.

Adjustable Panel Thickness

The design should accommodate variations in glass thickness by incorporating a mechanism that allows for thickness adjustments for different types of glass units.

Fine-Tuned Displacement Control

A mechanism should be integrated to precisely control and fine-tune the displacement, ensuring accuracy in the deformation process.

Structural Stability

To prevent unwanted out-of-plane torsion, the frames holding each edge must be connected with robust mechanical hinges, ensuring stability during the buckling process.

3.5.2 Materials

The main frame is constructed using 3T 60×40 mm rectangular aluminium profiles. To clamp glass panels of various thickness, detachable 3T 40×40 aluminium L-angles are attached to the frame using adjustable bolt connections. M6 bolts are installed at equal intervals along each frame, with four per edge, to ensure an even distribution of clamping force along the edges. For deformation control, an M8 right- and left-threaded rods are welded at the centre, allowing simultaneous inward movement when adjusted from a single side. This ensures precise and consistent buckle bending of the panel. In the section profile in Figure 3.5, EPDM (Ethylene propylene diene monomer) rubber has been placed between the aluminium and the glass to prevent direct contact and to act as a damping layer. Additionally, POM (Polyoxymethylene) setting blocks are used at the points where the glass edges could touch the frame, providing structural support while minimising the risk of local edge stress concentrations.

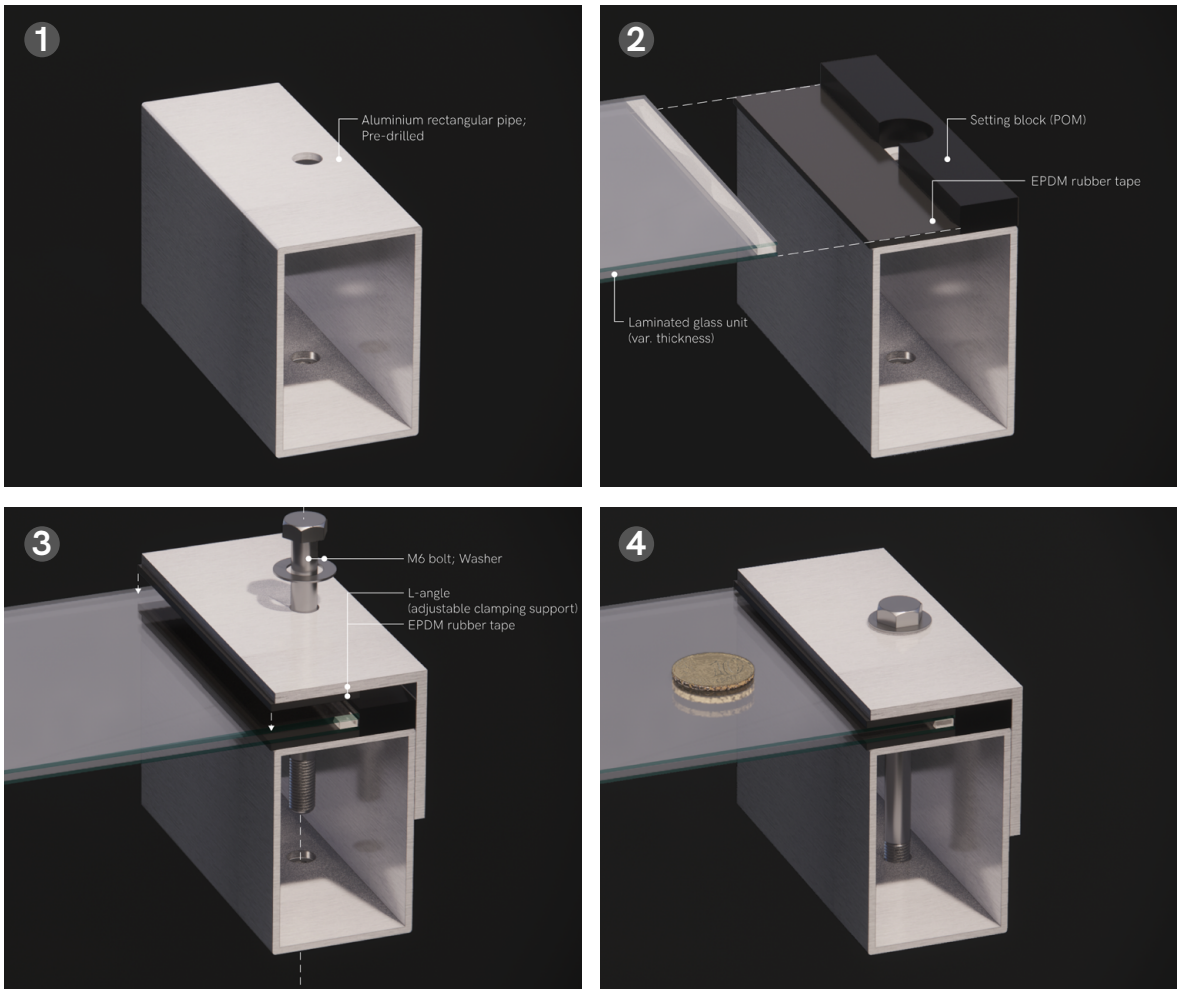

Fig. 3.5 | Edge support assembly sequence and material specification of buckle bending machine

3.5.3 Testing & Result

Considering this as a conceptual testing phase, thin glass is not used. Instead, a 1 mm Vivak® single sheet, made of thermoplastic copolyester (PETG), It is select-

ed for the buckle bending experiment. The material properties of Vivak® include an elastic modulus (E) of 2,020 MPa and Poisson's ratio (υ) of 0.35. Compared to glass (E = 70 GPa, υ = 0.22), this material is approximately 1/35th as stiff and more flexible. Due to the flexible nature of the material, initial geometrical imperfections required for buckle bending, is naturally formed under gravity. As shown in Figure 3.6, when a displacement along the planar direction is applied, a very similar geometry can be achieved to that of the intended sinusoidal half paraboloid. However, unintended folding and bulging are observed symmetrically to either side of a convex deflection point (Figure 3.7).

No additional experimental testing has been conducted to resolve these defects. However, the results indicate that the 3-edge rigid support condition still contributes to geometrical imperfections. Keeping this in mind, the study proceeded to the next phase: numerical experiments to further refine the boundary conditions to achieve an effective geometry and buckle bending method.

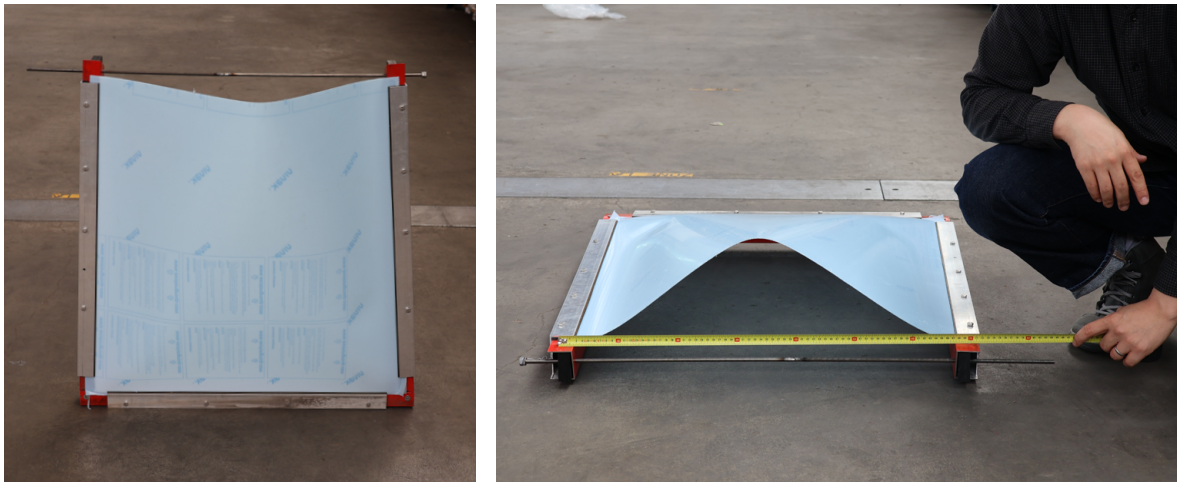

Fig. 3.6 | 1 : 1 prototyping of sinusoidal half paraboloid geometry
Note. 10 cm displacement along in-plane direction.

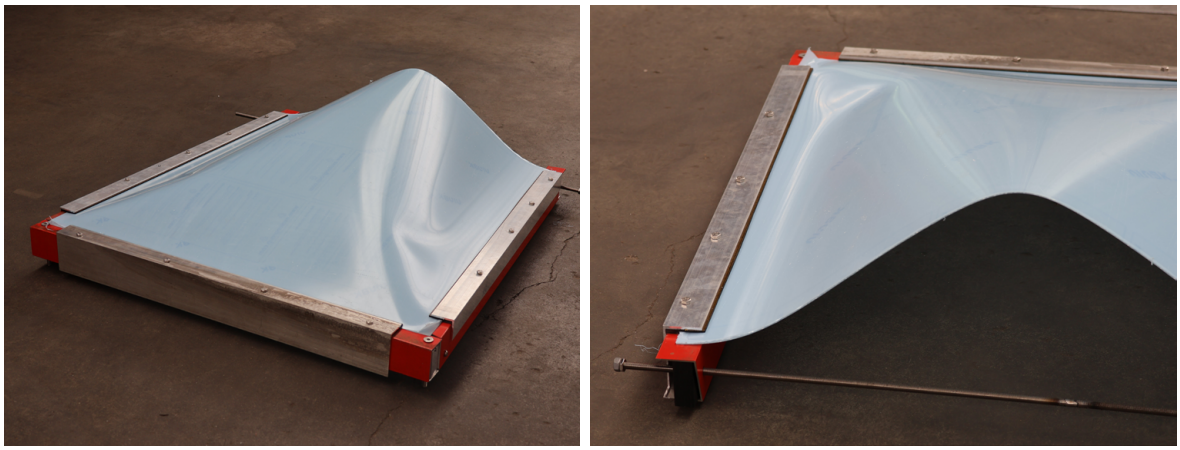

Fig. 3.7 | Reflection distortion caused by folding of the sheet

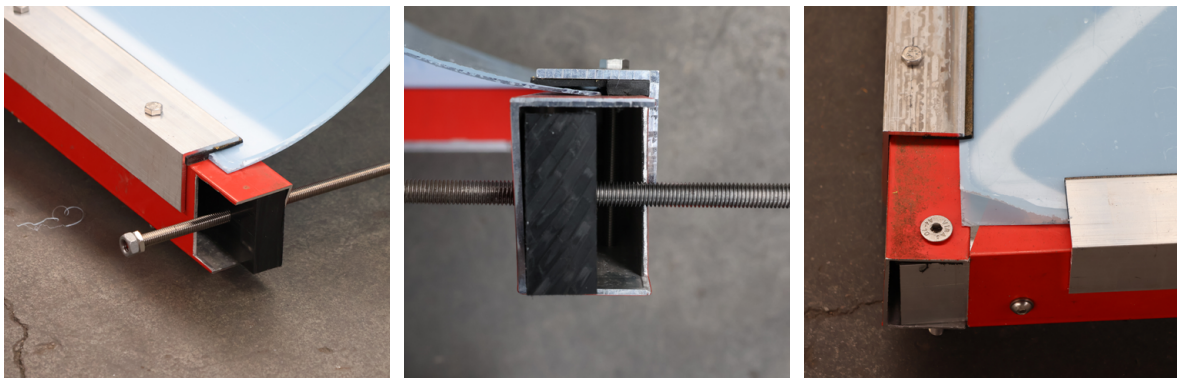

Fig. 3.8 | Buckle bending machine detail
Note. Left: Operation mechanism Middle: Frame section Right: Mechanical hinge detail

3.6 Lamination & Solar Control

To integrate cold buckle bending, solar control application, and lamination manufacturing, the process can be broken down into three sequential steps:

1. Solar Control Application

A pre-designed ceramic frit pattern—an optimised solar control design based on the double-curvature geometry—is applied to one of the flat glass pane and then thermally fused onto its surface. This process enhances solar control performance while also ensuring strong adhesion to the glass prior to lamination and during cold bending (Figure 3.9).

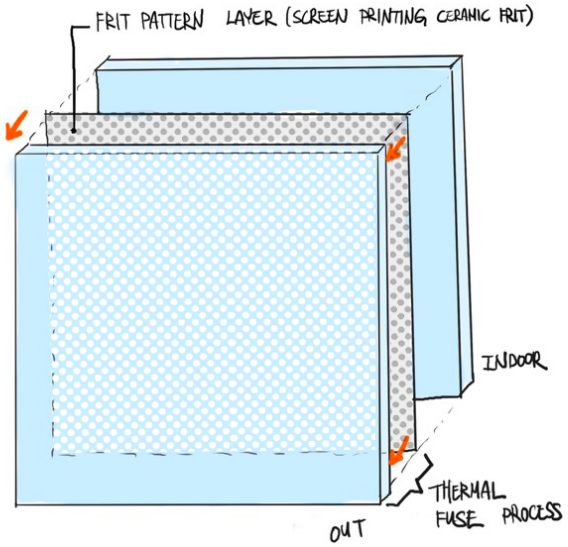

Fig. 3.9 | Proposed solar protection method on glass unit

2. Liquid Lamination Injection

A cold liquid lamination process is selected for its high flexibility in laminating complicated double-curved panels. This method does not require an autoclave or any additional thermal processing. To accommodate the viscous interlayer material, an edge-sealed cavity is formed between the glass sheets, providing space for the lamination liquid to be injected.

The panel edges are sealed to prevent leakage (Figure 3.10).

3. Cold Buckle Bending and Curing

While the interlayer material remains in a liquid state, the panel is positioned within the buckle bending device, where it is clamped and deformed into the desired shape. The frame fixture holds the panel in its cold-bent geometry throughout the curing period, allowing the material to harden while maintaining its shape. Once fully cured, the hardened interlayer material helps retain the deformed shape by holding the glass layers in place. When the frame is removed, a spring-back effect may occur due to the internal stress state, leading to a partial return toward the original flat shape.

A key benefit of this liquid interlayer-phase deformation is that each thin glass layer remains flexible—less stiff—by avoiding full bonding with the core during shaping. This allows deformation under lower applied force and reduces internal stress. In contrast, if the glass were shaped after full curing, it would behave more like a thick, monolithic plate, making deformation significantly more difficult. By leveraging both the flexibility of thin glass and the viscosity of the uncured interlayer, this method enables cold bending with larger deformation, reduced applied force, and minimized internal stress (Figure 3.10).

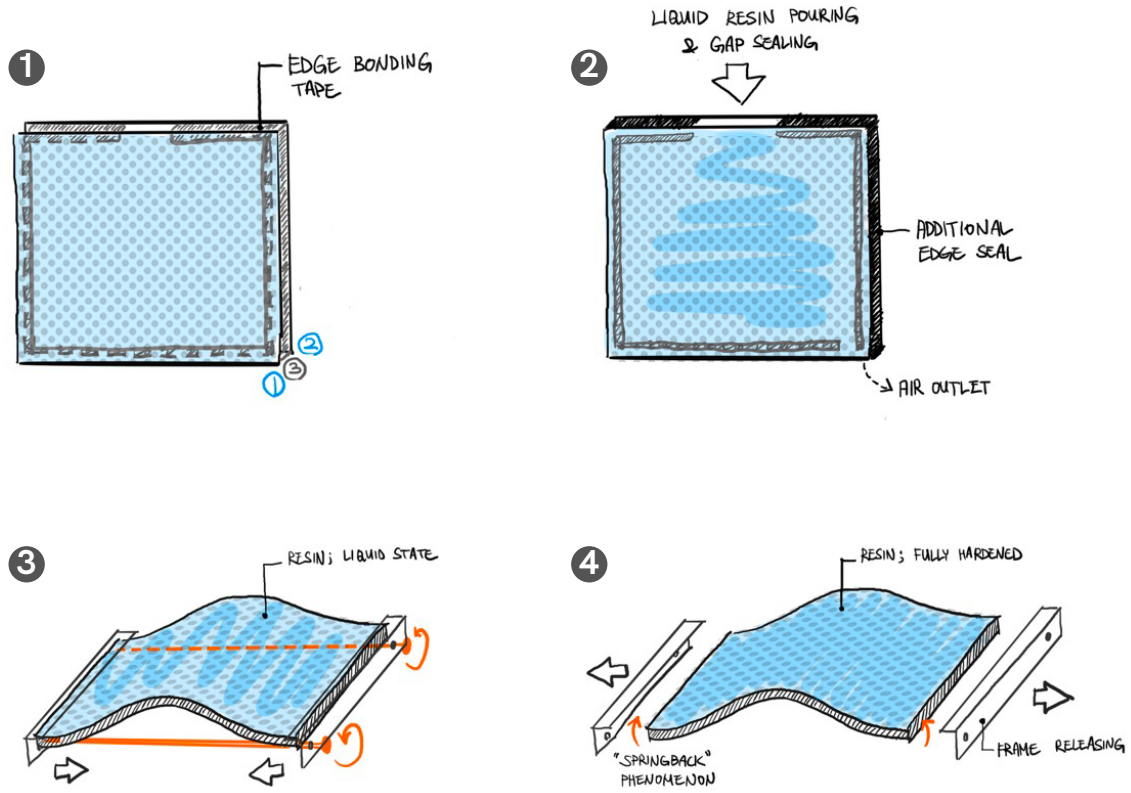

Fig. 3.10 | Cold lamination & cold buckle bending manufacturing process

3.7 Discussion

To rapidly and conveniently investigate the behaviour of thin plates, a preliminary experiment was conducted using an easily accessible plastic sheet as a substitute for glass. The aim was to assess whether the theoretical cold bending geometry could be replicated in practice. From a purely material property perspective, however, it is evident that Vivak® behaves significantly differently from real glass. Glass exhibits far greater stiffness and a lower Poisson's ratio, making it substantially less flexible. Therefore, the wrinkling and folding observed during the 3-edge restricted buckle bending using Vivak® are attributable to the ductile characteristics of thermoplastic materials. In contrast, glass is likely to exhibit signs of folding and localised deformation at smaller bending angles. It is expected that fracture would initiate near the edges, particularly at the termination points of support or in locally stressed areas, occurring well before the wrinkle geometry observed in the Vivak® test is reached.

In designing a glass unit that integrates lamination, cold bending, and a solar control mechanism, the process begins with a thorough examination of potential incompatibilities between fabrication steps and a careful planning of the manufacturing sequence. This research introduces a novel cold bending approach, along with a dedicated fixture developed to implement the method effectively.
Rather than relying on the conventional sheet-based interlayer lamination—typically using PVB and an autoclave—this study employs a liquid-phase core material. This approach maximises the flexibility of thin glass while eliminating the need for thermal processing and high-pressure conditions associated with autoclave use. As a result, it prevents unintended glass movement that may arise from thermal expansion mismatch or pressure differences between glass and the bending fixture.

For the solar control mechanism, a ceramic fritting is applied, allowing bending and lamination to proceed with the coating already integrated. However, during the fritting process, micro-notches can form at the fused interface between the ceramic frit and the glass, potentially serving as initiation points for crack propagation due to altered mechanical behaviour at the surface.

The polymer-based interlayer selected in this study promotes stress relaxation, supports molecular flow, and provides adhesion that compensates for the brittleness of the fritted surface. Nevertheless, its effectiveness in mitigating this inherent weakness requires further investigation. Additionally, depending on the specific interlayer formulation, chemical compatibility and adhesion with the frit-fused glass surface is not fully guaranteed.

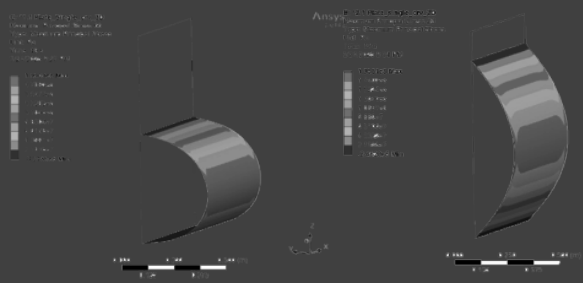

· Single curved surface

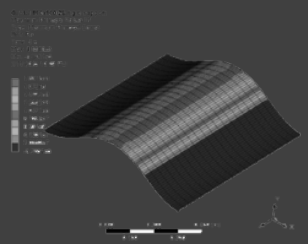

· Sinusoidal single curved surface

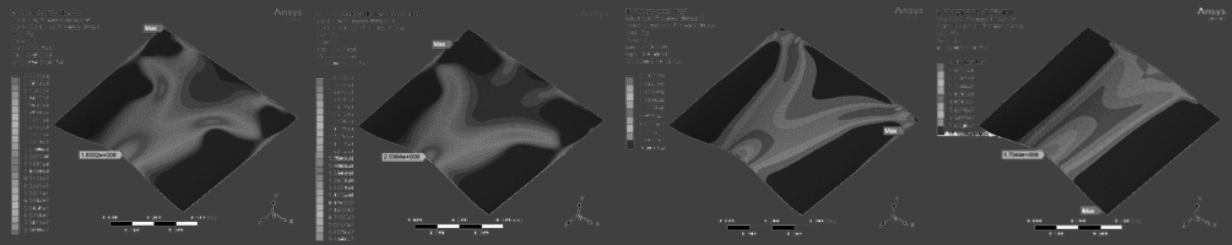

· Boundary condition optimisation

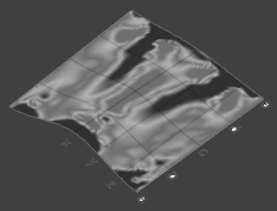

· Surface curvature validation

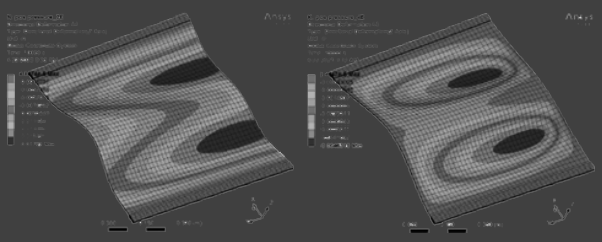

· Deflection on different load cases

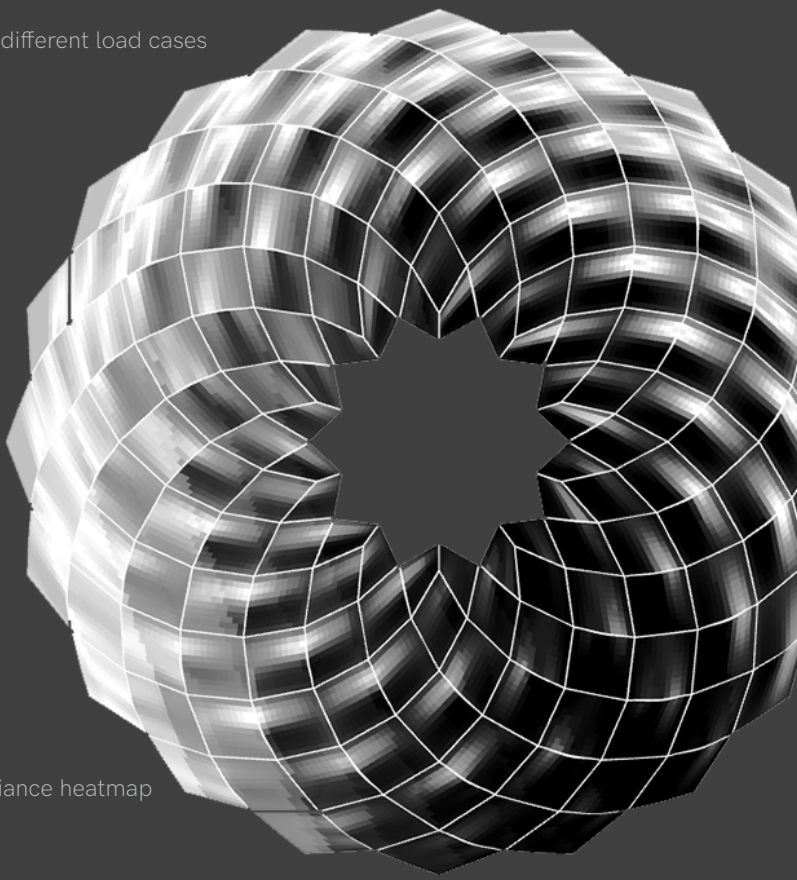

· Instant irradiance heatmap

IV. DESIGN DEVELOPMENT

4.1 Structural Design - Single Plate

This part of the study explores new double curvature geometries with cold-buckle bending methods beyond conventional forms such as twisted geometry or hypar, which are commonly used in the building industry. There are limitations in achieving accurate geometry and stress optimisation solely through physical testing (Chapter 3); therefore, numerical analysis is conducted as a necessary precursor to guide and refine the design process. The goal is to optimise in-plane stress and achieve an efficient stress distribution within the newly proposed geometry, while ensuring that the structural design remains within the material's stress capacity.

4.1.1 Methodology

The numerical analysis in this chapter is validated through numerical experimentation using non-laminated, chemically strengthened single thin glass. As the maximum available sample size for this type of glass under sponsorship is 800 × 800 mm, the same dimensions are adopted for the numerical simulations presented in this chapter. Before conducting the Finite Element Analysis (FEA), the relationship between stress, plate thickness, and geometry will be examined. First analysis focuses on feasible boundary conditions and geometries for a monolithic glass pane, as introduced in Section 3.5. This configuration resembles the original OWO roof geometry and is used to determine the extent of deformation achievable within the defined design stress limits. An iterative simulation approach is used to identify optimised parameters, ensuring the resulting design remains within safe mechanical thresholds while maximising deformation potential.

4.1.2 Finite Element Analysis (FEA)

Finite Element Analysis (FEA) is conducted using Ansys Workbench 2024 R2 software. FEA method breaks the original geometry into smaller finite elements, which are connected at nodes to form a mesh representing the structure's geometry and properties (Fish & Belytschko, 2007). The analysis process includes developing a detailed geometric model, defining material properties and boundary conditions, and discretizing the structure into meshes. Once prepared, numerical equations governing the system's physical behaviour are solved to generate results that guide design decisions and validate theoretical predictions. Proper material definition and accurate support conditions are critical for FEA.

Unless mentioned, in this research all FEA are being done in geometrical non-linear simulations (referred to as *Large Deformation* in Ansys software). This approach is essential because brittle materials such as thin glass can experience significant changes in geometry

even under relatively small loads. Therefore, the initial configuration can no longer be used to calculate stress and strain in large-deformed glass structures. To accurately predict material behaviour, geometrical non-linearity must be considered. Large deformation analysis is an iterative calculation process that continuously updates the stiffness matrix as the structure changes shape during loading (ANSYS, Inc., 2022).

To ensure the reliability of the study, the initial setup and accuracy of the analysis are verified by replicating the research conducted by Galuppi & Riva (2024) in Chapter 2.3.6 using Ansys software, establishing a solid foundation for further investigations. For the numerical analysis in Sections 4.1.3–4.1.5, an isotropic material with an elastic modulus of 70 GPa and a Poisson's ratio of 0.22 has been used for the mechanical property of the thin chemically strengthened glass, ensuring comparability with the study by Galuppi & Riva (2024).

As a structural material, thin glass is a relatively new development, and its tensile bending strength is not yet covered by regulations. While suppliers typically recommend a design strength at about one-third of the ultimate bending strength, no established standards exist for chemically toughened aluminosilicate glass. Since studying its fragility limit is beyond the scope of this research, tensile strength values are taken from Schlösser (2018), based on an internal design guide for chemically toughened thin glass by Eckersley and O'Callaghan (2018). Based on this data, the design tensile strength for chemically strengthened glass in this study is set to 200 MPa (Table 4.1). The experimental study of Zaccaria et al. (2022) also supports this claim suggesting characteristic bending strength of 230MPa for chemically strengthened hybrid aluminosilicate Falcon glass.

Glass product	Ultimate bending strength [MPa]	Design bending strength [MPa]
Xensation glass	800	± 260
Gorilla glass	-	200
Dragontrail glass	600	± 200
Leoflex glass	-	260
Falcon glass	-	200
glanova	-	200

Table 4.1 | Tensile bending strength of thin chemically strengthened glass
Note. Based on Eckersley and O'Callaghan (2018).

4.1.3 Single Curvature Cold Bending

The relationship between bending stress, geometry, and glass thickness for a single-curved thin plate is best described by the following equation (Ashwell, 1957):

$$\sigma_b = \frac{M(x)}{W} = \frac{IE}{Wr(1-v^2)} = \frac{Etp}{2r(1-v^2)} \tag{4.1}$$

Where σ_b is bending stress, $M(x)$ is bending moment, W is section modulus, I for second

moment of area, E is Young's modulus, r for radius of curvature, υ is Poisson's ratio, t_p is plate thickness. This equation clearly shows that bending stress is proportional to curvature (inverse of radius) and glass thickness. However, it is only valid for single-curved surfaces with zero Gaussian curvature.

Table 4.2 presents a comparison between the theoretical arc radius, calculated using Equation 4.1 at a bending stress of 200 MPa, and the results obtained from numerical simulations based on the computational model developed in this study, under identical conditions. This comparison illustrates the relationship between plate thickness and bending stress, as well as radius and bending stress. The results confirm that at the same stress limit, thinner plates can be bent into smaller radii in proportion to their thickness (Figure 4.1).

E [Gpa]	υ	t [mm]	r_{theory} [mm]	r_{FEA} [mm]	Error rate [%]
70	0.22	1.1	202.29	204 (at 199MPa)	0.36
		2.1	386.19	403 (at 196MPa)	2.51

*Radius correspondent to design bending strength of 200 MPa

Table 4.2 | Single curvature radius at design bending strength limit

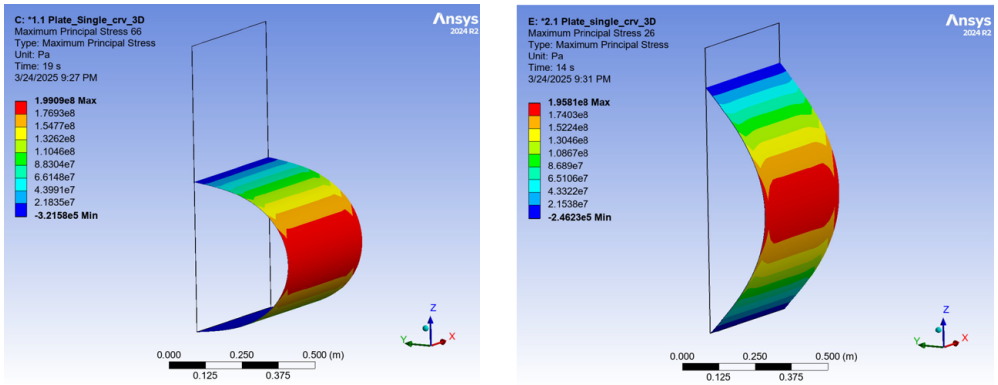

Fig. 4.1 | Single curvature bending shape and maximum principal stress at 200 MPa
Note. Left: 1.1mm thick plate Right: 2.1mm thick plate

4.1.4 Sinusoidal Single-Curved Cold Buckle Bending

This analysis step focuses on simulating varying single curvature bending in one direction, where the curvature continuously transitions into a sinusoidal shape resembling the Euler 1st buckling mode with fixed end supports. To induce buckle bending, an initial pressure is applied normal to the 800 x 800 mm plate, creating initial imperfections that are fully released before completing the cold bending. The plate edges are displaced inward, inducing a buckling deformation shape. To achieve the sinusoidal shape, rigid support constraints are applied at the edges, preventing the edge supports from rotation. As shown in Figure 4.2, the intended deformation is successfully achieved, with maximal principal stress occurring at the smallest radius point near the middle peak of the plate. For the 1.1 mm and 2.1 mm plates, simulation results at 200 MPa are plotted using a mesh comprising 80 divisions along the curved edge, 20 divisions along the orthogonal direction, and 3 elements through the thickness. The displacement pattern closely matches the expected sinusoidal curve, in-

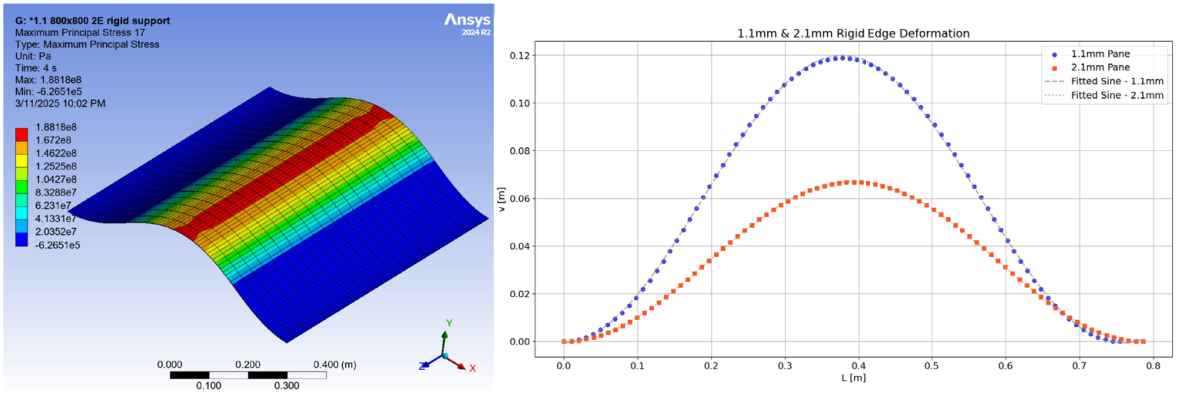

Fig. 4.2 | Left: Sinusoidal curvature single plate bending stress (1.1 mm plate)
Right: Deformed geometry comparison with theoretical curvature

dicating the continuous changing single-curved deformation follows the theoretical sine/cosine form.

Table 4.3 presents the radius at the largest curvature for the buckling deformation geometry under the rigid support condition. Comparing this with the single-curved bending radius from Section 4.2.3 shows how much the radius deviates from the theoretical single curvature value. This verifies that when the geometry is deformed from single curvature to a more complex form, the radius deviates from the value predicted by equation 4.1. Additionally, according to the FEA simulation, to deform the 1.1 mm and 2.1 mm plates to the desired shape, 384 N and 2604 N of buckling loads are applied, respectively. This result follows a cubic relationship, where the critical buckling load increases eight times when the plate thickness doubles. The relationship is expressed by the following equation, where P_{cr} is critical buckling load, K is effective length factor based on end support condition, L is length, b is width of the plate, and t the thickness of the plate:

$$P_{cr} = \frac{\pi^2 EI}{KL^2} \qquad I = \frac{bt^3}{12} \tag{4.2}$$

Considering the manufacturing scenario of the end product and the complexity of the geometry to be implemented, it is concluded that using a thinner plate (1.1 mm) would be more advantageous than using a thicker one (2.1 mm). Therefore, the plate thickness is decided as 1.1 mm for the subsequent analyses. If it becomes thinner than 1.1 mm, it is expected that it will be too thin and flexible considering the size of the plate (800 x 800 mm), causing great difficulties in handling and manufacturing.

Edge support type	t [mm]	r [mm]	Deviation from theory [%]	Buckling load [N]
Free to rotate	1.1	202.29	-	-
	2.1	386.19	-	-
Fixed	1.1	231 at 188 MPa (FEA)	7.46	384
	2.1	459 at 194 MPa (FEA)	15.28	2,604

Table 4.3 | Achievable minimum radii depending on geometry type and thickness of the plate

4.1.5 Boundary Condition Optimisation - 3 Edge Fixture

While maintaining the previously defined stiffness and strain properties of the glass, numerical adjustments to the boundary conditions are carried out to achieve structural optimisation while preserving the intended half-sinusoidal paraboloid form. The specific conditions applied in the simulation, as detailed in Sections 4.1.5 to 4.1.7, are summarised in Table 4.4. To implement a semi-rigid edge condition, materials assigned to the edge supports in the model include Aluminium Alloy and EPDM Rubber (Shore A70), which are predefined in Ansys software.

Following this setup, Figure 4.3 shows the result of a comparative simulation in which a 800 x 800mm, 1.1 mm thin glass panel undergoes buckling deformation by rotating two opposite edges inward by 1° each under 3 edge support fixture condition. The simulation proceeds in four iterative steps, with each stage refining the residual stress based on observations from the previous step.

Experiment	E_{glass} [Gpa]	υ_{glass}	t_{glass} [mm]	Meshing Count [L x W x T]	Deformation	Edge Condition
4.1-1	70	0.22	1.1	80 x 80 x 3 (glass)	Both corners rotated inward by 1°	Fully rigid
4.1-2						Fully rigid
4.1-3						Semi-rigid
4.1-4						Semi-rigid
4.1-5	70	0.22	1.1	80 x 80 x 3 (glass)	1) Small inward edge displacement 2) Both corner inward contraction	Semi-rigid
4.1-6						
4.1-7						
4.1-8	70	0.22	1.1	80 x 80 x 3 (glass)	1) Large inward edge displacement 2) Both corner relaxation	Semi-rigid
4.1-9						

Table 4.4 | Baseline parameters and boundary conditions for sinusoidal half paraboloid bending in FEA

Experiment 4.1-1

One free edge is maintained, while the remaining edges are fully constrained using rigid edge supports, preventing out-of-plane rotation. This setup leads to unintended folding and bulging defects, geometrically similar to the prototype testing results in Chapter 3.5. Stress peaked significantly at these bulging locations.

Experiment 4.1-2

To reduce edge corner restrictions, a 100 mm long support free-corner zone is introduced on both sides. While this modification reduces in-plane stress and mitigates plane folding, it resulted in stress concentrations and higher peak stress around the newly introduced support ends around the fixture-free corners.

Experiment 4.1-3

Since fully rigid edge supports are identified as a major cause of excessive stress, a semi-rigid support—modelled after the fixture edge support detail (Aluminium Alloy and Rubber, TPV EPDM, Shore A70) in Chapter 3.5—is introduced. This lowers the maximum stress values, and stress distribution becomes more continuous and predictable compared to the previous tests.

Experiment 4.1-4

To examine the effects of increased corner freedom, the edge support length is further reduced. While maximum stress dropped below 200 MPa, folding-back phenomenon becomes more pronounced due to Poisson's effect near the free corners. This occurs because the deformed shape induces in-plane strain compensation, causing the two free corners to deform in the opposite direction of the paraboloid curve shape.

The key observations from each experiment, along with the maximum principal stress val-

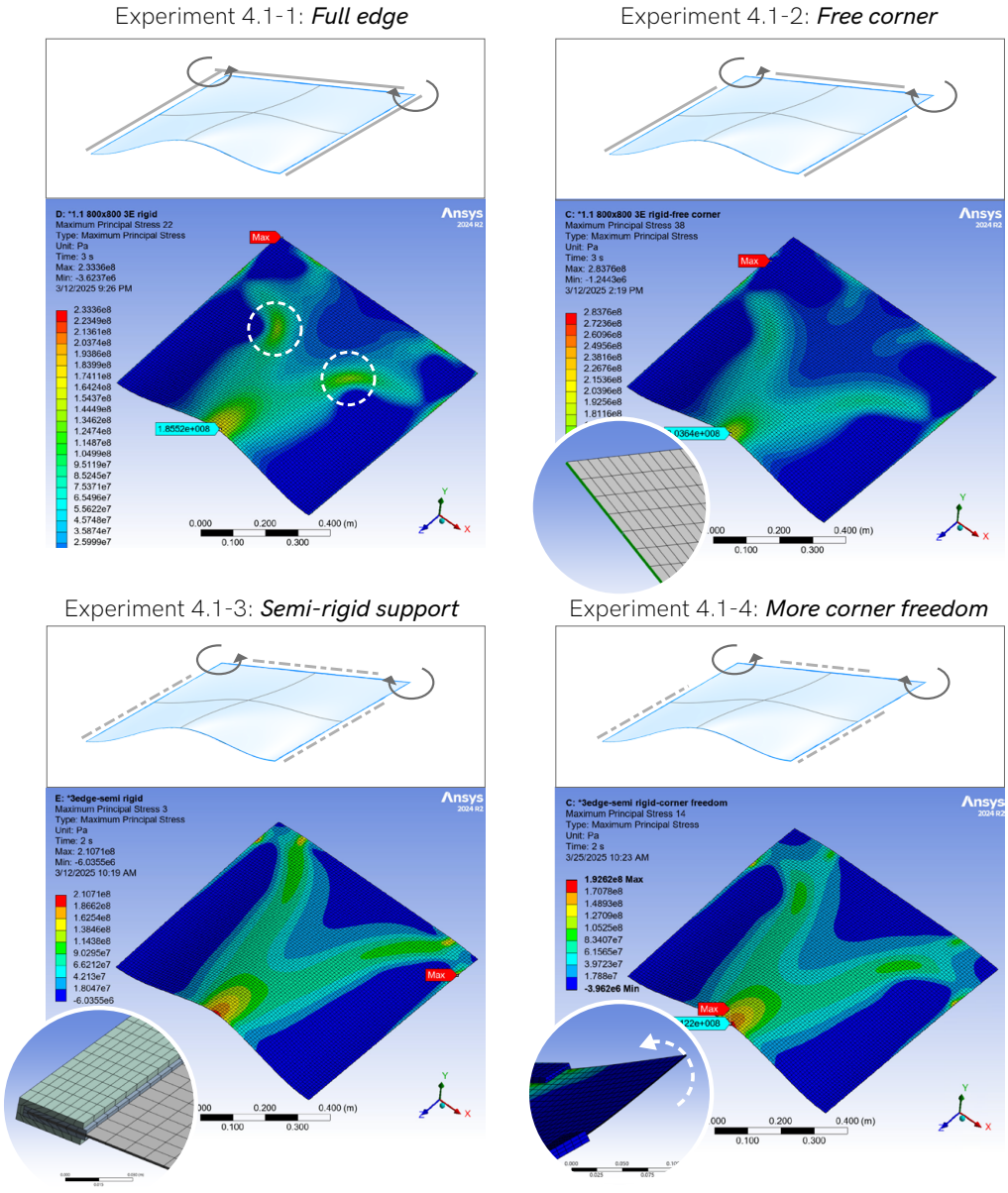

Fig. 4.3 | Numerical experiment results of sinusoidal half paraboloid geometry with 3-edge fixtures
Note. Plotted heatmap represents the distribution of flexural stress in Pa. In the schematic diagram, solid lines indicate fully rigid edge supports, while dashed lines represent semi-rigid supports.

ues at the 1° buckling point, are summarized in Table 4.5.

Experiment	Max. stress [MPa]	Findings
4.1-1	234	Folding, bulging defects in middle of the pane
4.1-2	284	Peak stress near the end of edge supports
4.1-3	211	Continuous stress distribution
4.1-4	193	Significant corner folding-back phenomenon

Table 4.5 | Summary of 3-edge fixture cold bending experiments

4.1.6 Boundary Condition Optimisation - 2 Edge Fixture

Previous boundary condition modifications are based on the schematic design concept from Chapter 3.5, focusing on refining boundary conditions under a three-edge support configuration. While experiment 3 and 4 successfully keep the maximum stress close to the design stress range (200 MPa), the stress distribution remains unpredictable, with wide area of high residual stress due to in-plane strain and the non-developable nature of the surface. To address this, a new boundary optimisation strategy introduces an alternative buckle bending method aiming to achieve a sinusoidal half paraboloid while bringing it closer to a developable surface to mitigate residual stress (Figure 4.4).

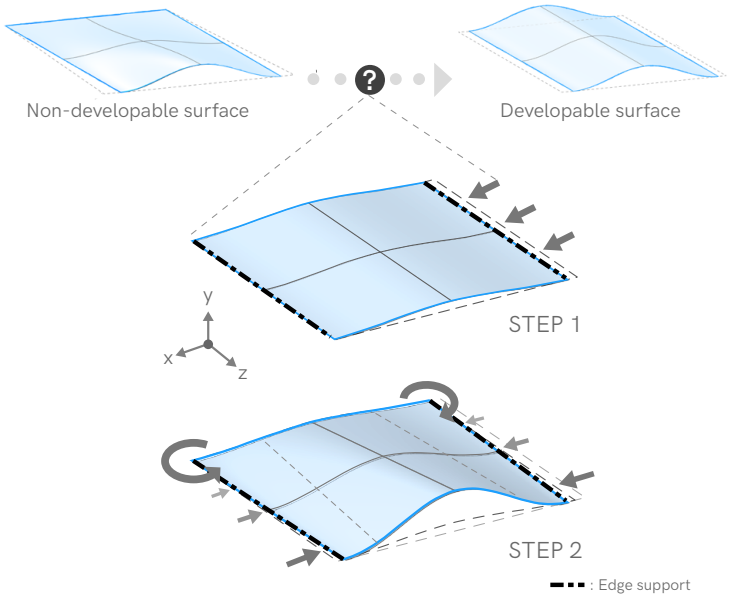

Fig. 4.4 | Concept of 2-edge support and 2-step cold buckle bending strategy

This approach involves setting two opposite edges as support free while restricting out-of-plane rotation along the remaining two edges. The deformation process consists of two steps: first, one of the restricted edge supports slightly moves inward equally, inducing a buckling deformation forming a slight sinusoidal curvature along the two free edges, creating a developable surface. In the second step, one free edge remaining fixed at both end points while the opposite edge contracts further, generating a sinusoidal curvature with a

larger amplitude only on one side. Figure 4.4 shows the result, a surface that partially resembling a cone, making it more akin to a developable surface. While still a non-Gaussian surface, this geometry is closer to a developable form compared to the first optimisation result, suggesting lower maximum bending stress and total residual stress.

In Step 2, when one free edge is contracted by 1 degree, the stress values at the lowest radius point remains below the design stress limit of 200 MPa. Step 1 involves incrementally displacing one fixed edge support by 10 mm, 5 mm, and 3 mm in experiment 4.1-5 to 4.1-7 (Table 4.6). All three experiments exhibited an almost linear stress distribution along the peak curvature. Among them, experiment 4.1-5 shows the most pronounced out-of-plane displacement, but the final deformation shape resembles a conical geometry rather than the intended half-paraboloid form. Experiment 4.1-7, on the other hand, produces a deformation pattern that is nearly identical to the targeted shape, with a significantly reduced peak stress area at the minimum radius edge and lower stress along the opposite free edge compared to the other experiments. Therefore, the deformation approach in experiment 7 represents the most optimised solution, effectively balancing both structural integrity and

FEA [principal stress] / Step-1 disp.	Max. stress [MPa]	X displacement [mm]	Z displacement [mm]
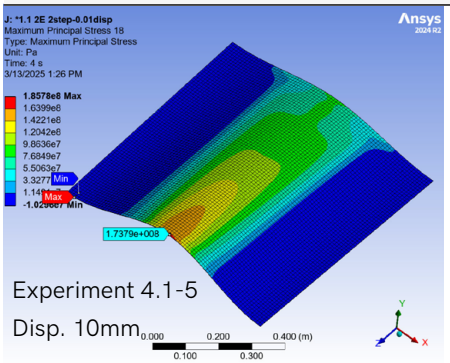	186	38	110
	· Not fit the desired half sinusoidal paraboloid shape criteria · Peak stress area largest		
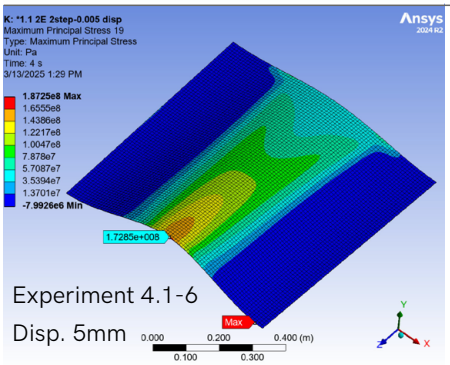	187	33	103
	· All characteristics are average		
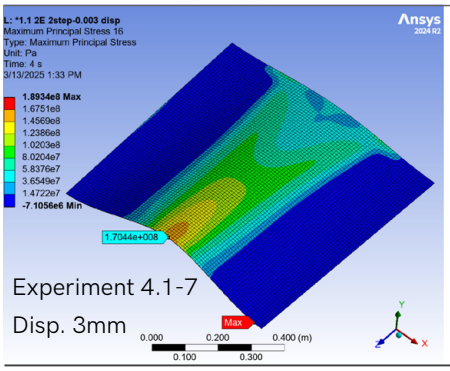	189	31	101
	· Best fits the desired shape · Least peak stress area and less stress along edges		

Table 4.6 | 2 edge support - half sinusoidal paraboloid cold buckle bending experiment result

geometric accuracy.

Figure 4.5 presents a graph plotting the maximum bending stress against the maximum X displacement (where the smallest radius occurs) for experiments 4.1-5 to 4.1-7. The grey coloured line represents the control group, where Step 1 is omitted, and only edge supports have contracted inward up to 1 degree. This control group demonstrates a distinctly non-linear relationship between displacement and stress in thin plate bending. Due to the varying Step 1 deformation values across the experiments, establishing a precise quantitative correlation between displacement and maximum stress on the peak curvature point is challenging. However, in all experiments, after a certain level of displacement, the maximum stress increases at a relatively consistent slope. In the control group experiment, the radius at the point of maximum curvature within the design stress limit is 250 mm. In contrast, experiments 5–7 produce smaller radii, confirming that the Step 1 deformation effectively contributes to stress relief. Although there are differences in the minimum radius values, they all remain within a range comparable to the 250 mm of the control group. Notably, the minimum radius in experiment 7, the most optimised case, is 246 mm, closely aligning with the control group's radius.

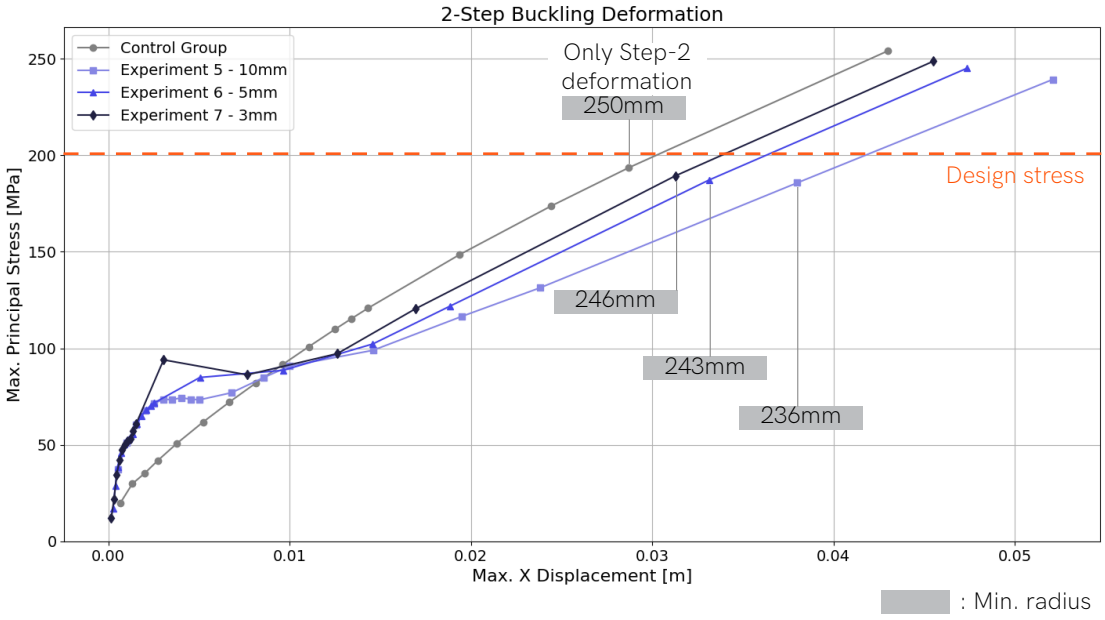

Fig. 4.5 | X displacement-bending stress relation from experiment 4.1-5 to 4.1-7

4.1.7 Displacement Step Adjustment

In Section 4.1.6, the deformation process initially involves an equal edge displacement along one axis, following by contracting one support free edge to form a half-sinusoidal paraboloid shape. However, this part explores an alternative deformation method based on the idea that first achieving a highly deformed single curvature geometry through equal edge displacement (Step 1B) and by relaxing one edge curvature (Step 2B) might allow for a better residual stress management during cold deformation process (Figure 4.6). Acknowledging the possibility that releasing curvature on one edge could increase the maximum stress on

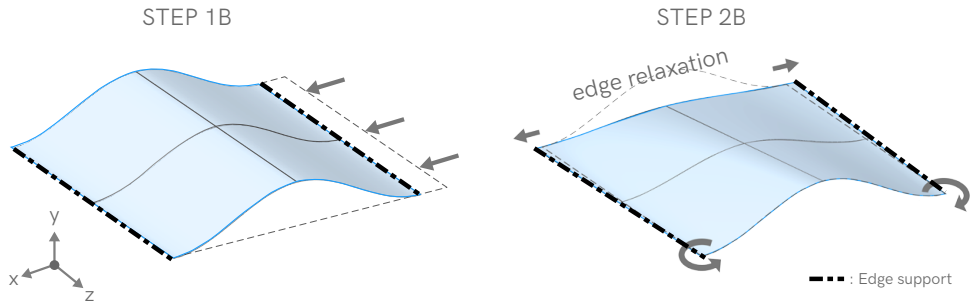

Fig. 4.6 | Alternative buckle bending 2-step sequence

the opposite edge, the experiment is conducted to compare the final geometry and residual stress results of Section 4.1.6 and 4.1.7 to determine which cold buckle bending method is more effective and whether the residual stress at the final deformed stage changes depending on the buckle bending sequence.

In experiment 4.1-8, the equal displacement along the edge in Step 1 is applied up to 30 mm before edge relaxation, while in experiment 4.1-9, the displacement is increased to 40 mm before relaxation. In experiment 8, the design stress limit is reached at a 1-degree relaxation point, whereas experiment 9 could reach the limit up to a 1.1-degree relaxation point. The final deformation of experiment 8 closely resembles that of the optimised experiment 7, with a maximum principal stress of 190 MPa and a minimum curvature radius of 248 mm, making it nearly identical. Although experiment 9 results in lower bending stress and a larger curvature, which would generally be considered more effective, its final shape is closer to a conical surface (similar to experiment 5) rather than the targeted sinusoidal half paraboloid (Table 4.7).

FEA [principal stress] / Step disp.	Max. stress [MPa]	Z displacement [mm]
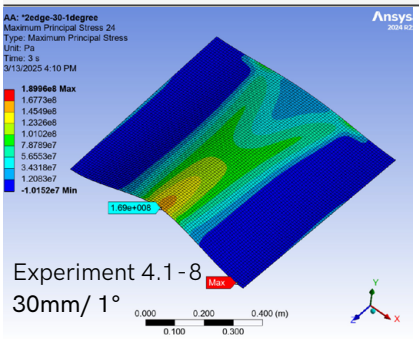	190	100
	· Result similar to experiment 4.1-7	
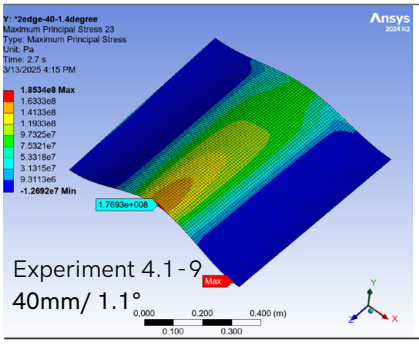	185	112
	· Result similar to experiment 4.1-5	

Table 4.7 | 2 edge support - alternative 2-step stress relaxation buckle bending experiment result

Figure 4.7 plots how the maximum principal stress changes with out-of-plane displacement (Z) in experiments 8 and 9. The sharp change in slope in each graph marks the moment Step 2B (edge relaxation) occurs, where the Z displacement of the relaxed edge decreases while the Z displacement and curvature of the opposite edge increase slightly due to Poisson's effect, causing a sharp rise in stress compared to Step 1B.

Ultimately, the results indicate that if the target geometry (total displacement) remains the same, the difference in residual stress is negligible regardless of the bending step order. While the bending methodology in this chapter aims to control residual stress more effectively by relaxation instead of contraction, the displacement relaxation influences the opposite edge, increasing its Z displacement, curvature, and consequently, maximum bending stress. Thus, in actual cold bending processes, either the method from Section 4.1.6 or 4.1.7 can be applied without significant stress differences. The key takeaway is that precisely controlling the buckling deformation in accordance with pre-engineered parameters is crucial to ensuring residual stress does not exceed expected limits.

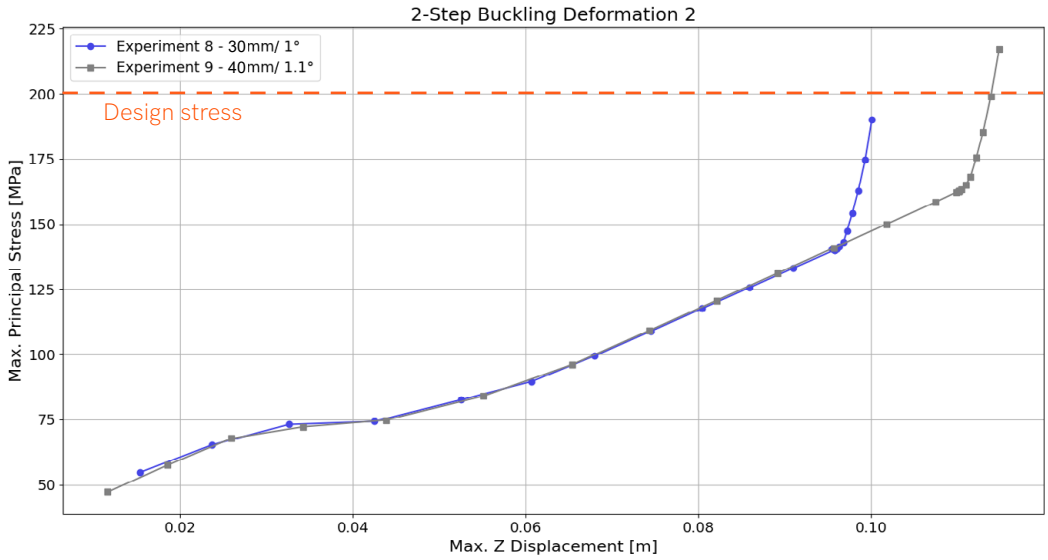

Fig. 4.7 | Z-displacement and stress relation graph from experiment 4.1-8 & 9

4.2 Geometry Design

From a user perspective, the most striking characteristic of the OWO Pavilion roof design is its free-form shape, which can be geometrically classified as a sinusoidal paraboloid. During the engineering process of the OWO Pavilion stainless steel panel, surface optimisation was carried out with a strong focus on reflection quality using line test simulation (Figure 4.8). This methodology is commonly used in aerospace and automotive design, because the appearance is primarily influenced by the reflection mapping artefacts introduced by surface curvature.

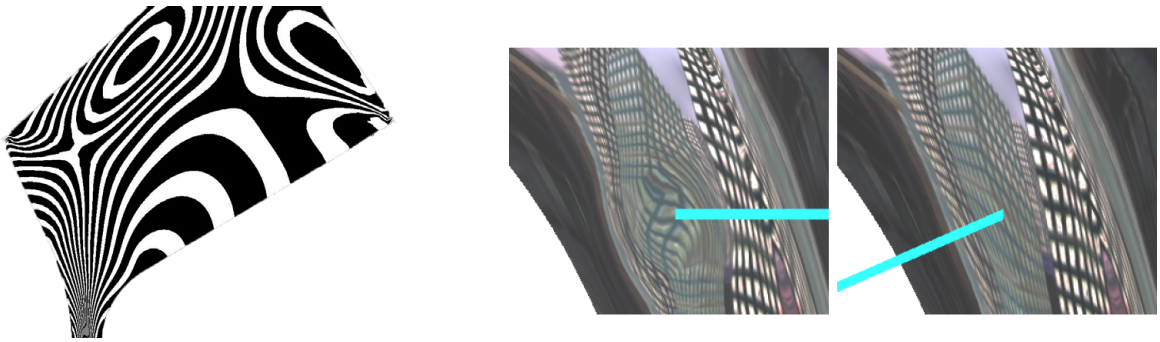

Fig. 4.8 | Shape optimisation using reflection line test (Left: Octatube, 2021, Right: Tosun et al., 2007)

4.2.1 Methodology

The existing OWO Pavilion design provides known coordinates for each panel's four vertices. The edges along the primary curvature direction are assumed to follow a sinusoidal paraboloid profile, while the edges along the other direction are considered straight lines connecting the vertices based on the adjusted panel geometry in Chapter 4.1. In conventional curved surface design, the typical approach involves manipulating the primary splines defining the surface using subdivision control points and evaluating the results using interrogation tools (Tosun et al., 2007). To ensure that the buckling-induced deformation results in intended shape and surface quality, the study will analyse the curvature and spline characteristics of the deformed geometry. Additionally, it will assess whether further surface optimisation strategies are necessary to obtain the goal.

4.2.2 Continuity

A continuous surface without visible segmentation does not necessarily imply a consistent level of surface continuity. In computer-aided design (CAD) and manufacturing (CAM), surface continuity is classified into different levels, commonly referred to as G0, G1, G2, and beyond, each defining a higher degree of smoothness (Figure 4.9):

G0 (Positional Continuity)

Two surfaces meet without gaps or overlaps, but there is no guarantee of a smooth transition.

G1 (Tangential Continuity)

The surfaces meet with a continuous tangent direction at the junction, ensuring a smooth directional flow.

G2 (Curvature Continuity)

Not only are the tangents continuous, but the rate of change of curvature is also smoothly matched, eliminating abrupt shifts in reflections.

While a surface satisfying only G0 or G1 continuity may appear visually continuous, disruptions in tangential or curvature continuity can introduce reflection distortions or unwanted



Fig. 4.9 | Continuity classification on a sinusoidal shaped surface

surface defects. This is particularly problematic in highly reflective surfaces and double curvature geometry, where even minor imperfections in continuity can lead to noticeable optical inconsistencies (Figure 4.9). As part of this study, a theoretical evaluation will be conducted to determine whether the buckle bent geometry produces a G2 continuity surface meaning uninterrupted reflection quality.

4.2.3 Curvature Continuity in Buckling Deformation

The buckling-induced geometry aimed for in this study closely resembles the Euler 1st mode buckling shape with both ends fixed. According to the general equation of Euler buckling, the lateral deflection $v(x)$ of a 2D geometry with boundary conditions at both ends C1 and C2 can be can be expressed as:

$$v(x) = C_1 \sin\left(\frac{n\pi x}{L}\right) + C_2 \cos\left(\frac{n\pi x}{L}\right) \tag{4.3}$$

Where L is the length of the panel, and n represents the mode number. For the given displacement conditions $v(0)=0$, $v(L)=0$, $v'(0)=0$, and $v'(L)=0$ the equation can be simplified to:

$$v(x) = C_1 \sin\left(\frac{n\pi x}{L}\right) \tag{4.4}$$

To analyse the curvature properties of this deformation, the second derivative of $v(x)$ is computed, yielding equation:

$$v''(x) = -C_1 \left(\frac{2\pi}{L}\right)^2 \sin\left(\frac{2\pi x}{L}\right) \tag{4.5}$$

Since this function is sinusoidal, it inherently exhibits smooth and continuous changes in curvature, satisfying G2 continuity. The theoretical analysis confirms numerically that the buckling deformation results in curvature transitions smoothly without abrupt changes and reflecting light following a consistent and undistorted path, meaning high reflection surface quality on a sinusoidal half paraboloid geometry (Figure 4.10).

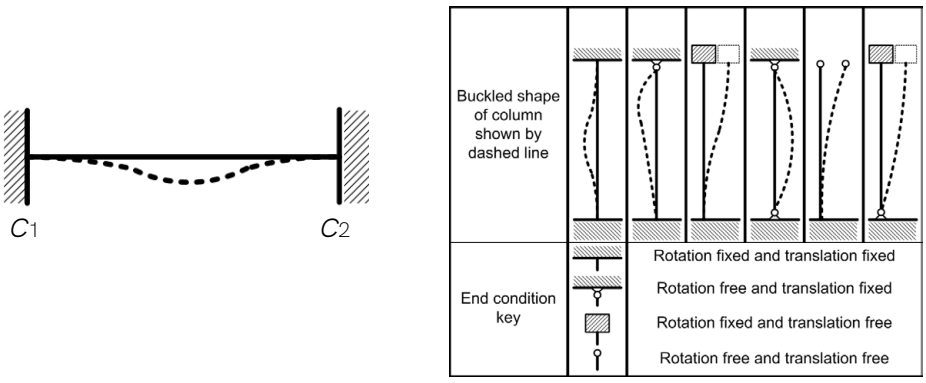

Fig. 4.10 | Euler 1st mode buckling geometry & different buckling shapes (Wikipedia contributors, n.d)

4.2.4 Cold Bending Distortion

According to Mansfield's inextensional theory for thin flat plates (2.3.4), cold-bending a plate into a developable geometry does not cause material elongation or contraction. Such deformation is defined as having zero Gaussian curvature, where bending occurs primarily through rotation, with minimal in-plane strain (stretching or compression). Since glass is brittle and cannot withstand excessive in-plane strain, it naturally deforms in ways that avoid it. In contrast, transforming a plate into a double-curved shape (non-zero Gaussian curvature) requires parts of the surface to stretch or compress, which glass resists. This results in high internal stresses, distortion, or breakage. Cold-bending thin glass into double curvature is therefore impossible without in-plane strain, and excessive forced deformation leads to wrinkling (folding) or fracture. A simple analogy is attempting to form a convex dome with a sheet of paper—it inevitably wrinkles unless cut or stretched.

Datsiou & Overend (2016) (2.3.8) studied the cold-bending distortion of glass when formed into a hypar (double curvature) shape. They found that in-plane stress causes minor surface deflections, varying with support conditions, which can affect optical quality. Since the target geometry of this study is inherently non-developable, in-plane stress is unavoidable. However, minimising this stress through cold bending optimisation (buckle bending support condition iteration) is crucial for maintaining surface continuity and quality.

4.2.5 Cold Bent Geometry Analysis

In Chapter 4.1, the most optimized cold deformed geometry obtained numerically is from experiment 4.1-7. This section aims to compare this geometry with the theoretically defined shape to determine any discrepancies and their potential causes. The intended half-sinusoidal paraboloid, based on geometrical logic, the two edges along the U direction are straight, while in the V direction, one edge forms a high-amplitude sinusoidal curve and the other appears visually almost straight, with minimal-amplitude curvature. This results in a surface where the endpoints and peaks along the V-directional curvature exhibit zero Gaussian curvature, while the rest of the surface exhibits anticlastic curvature (Figure 4.11, top-left).

The top-right side of Figure 4.11 illustrates the computed numerical model deformed through buckle bending 4.1-7. Notable differences in curvature between this model and the theoretical geometry necessitate a comparison of the cross-sectional curvature along the indicated section lines. In the U-direction, sections a to e show a macroscopic similarity to the theoretical sinusoidal curvature. Sections b and e align closely with the expected curvature, while sections a and d generally follow an Euler first-mode buckling shape but exhibit multiple cycles of wave patterns resembling Euler n-th mode buckling. Section d, in particular, displays a widely spread peak area at the highest Z displacement point. In the V-direction, the theoretical expectation is a perfectly straight x-section, but the actual curvature forms a convex shape. Sections y and z show a relatively stable and straight form near the high-amplitude curvature edge, but as they approach the opposite edge, synclastic and anticlastic curvature alternate, creating a complex surface curvature. This complexity is consistent with the unexpected shape observed in section d. The intricate surface deformation is likely caused by double-curvature cold bending distortion due to in-plane strain-induced structural instability. Interestingly, the area near the high-amplitude curved edge maintains geometrical stability, while significant cold bending distortion occurs near the opposite edge (Figure 4.11, bot).

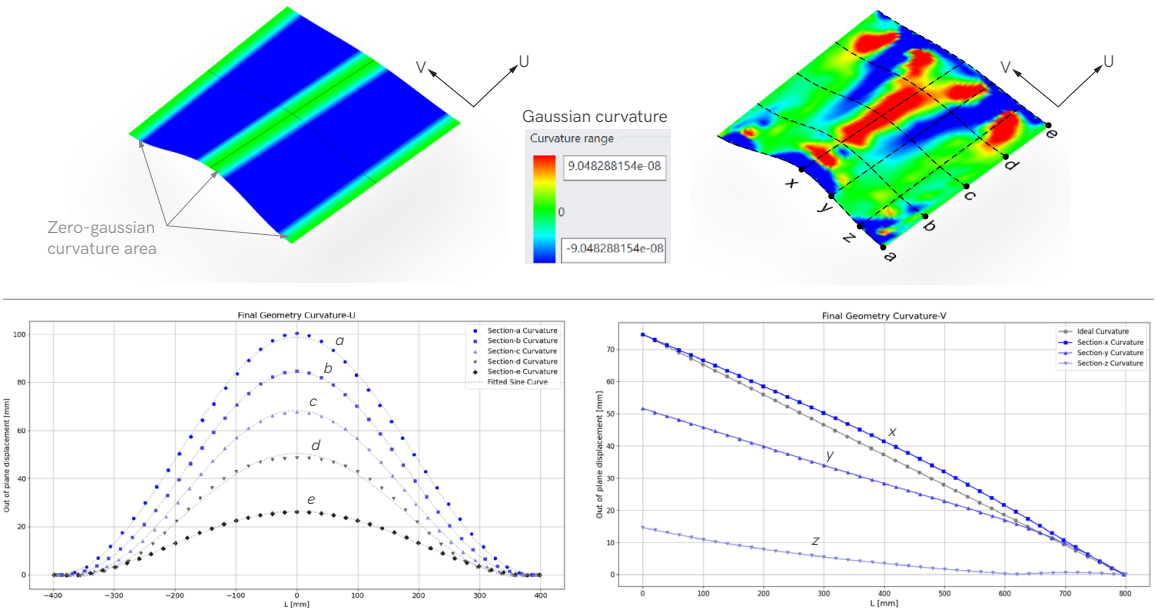

Fig. 4.11 | Curvature comparison between ideal geometry and cold-deformed geometry from FEA
Note. Top-left: Theoretical Gaussian curvature analysis of sinusoidal half paraboloid surface
Top-right: Gaussian curvature analysis of experiment 4.1-7 geometry (FEA output)
Bottom: Sectional curvature analysis of experiment 4.1-7

4.3 Structural Design - Sandwich Panel

In conventional glass lamination, PVB and SGP are commonly used; however, these sheet based methods could require thermal bending of glass before the lamination process and an additional autoclave process, which presents a limitation for double curvature cold

bending. Therefore, to achieve the OWO Pavilion roof design, CIP (Cast-in-Place) method is adopted in this research, as it allows for greater geometrical complexity and maintaining the aluminium cold bending fixture device in room temperature during curing. To withstand the high in-plane residual stress associated with double curvature, a cold-poured core material with a high shear modulus (G) is required. For this purpose, H.B. Fuller | Kömmerling's LOCA (Liquid Optically Clear Adhesive), Ködistruct LG is selected due to its superior resistance to shear deformation (Hänig et al, 2025).

4.3.1 Methodology

A lamination application strategy is first established to ensure an even thickness across the sandwich panel. Following this, the interlayer thickness is calculated to determine the overall stiffness of the panel. Basic characteristics of the viscoelastic interlayer are then analysed to understand its mechanical behaviour. Finally, a numerical study on the time-dependent behaviour of the 800 × 800 mm sandwich panel, which would be used for actual prototyping, will be conducted to evaluate its long-term performance under applied load conditions.

4.3.2 Interlayer Application Strategy

To ensure a uniform sandwich panel thickness throughout the cold bending process and to minimise induced deformation forces, the lamination strategy is carefully designed to avoid excessive shear stress between the individual layers. Double curvature cold bending inherently induces significant in-plane stress, making the deformation process highly challenging. If the interlayer is to behave as a fully bonded composite from the beginning, achieving the desired curvature would require immense force due to the panel's increased stiffness. Therefore, as illustrated in Figure 4.12, the cold-bending process is designed so that the individual glass layers could slide relative to one another during bending, minimizing shear force transfer between glass and the core material.

The stiff core material initially behaves with low Young's and shear moduli in its liquid state before curing, allowing the layers to move more freely during bending. The lamination pro-

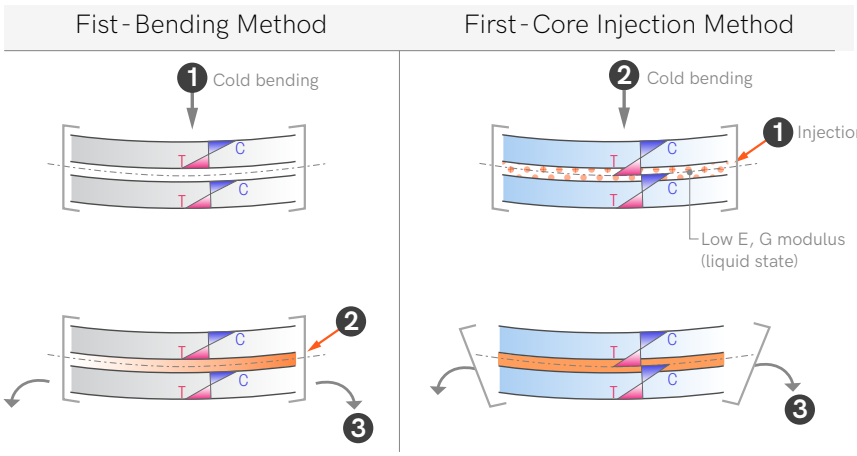

Fig. 4.12 | Different interlayer application strategy

cess starts with the sandwich panel in a flat configuration, where the two-component interlayer is applied in its uncured state. The panel is then bent into the target geometry, and the interlayer is allowed to fully cure while maintaining the deformed shape (Figure 4.12 right). The LOCA material locks the shape in place during the curing process while maintaining the desired thickness of the composite panel. Once the interlayer is fully set, the external supporting frame used to hold the deformation can be removed, leaving a structurally stable cold-bent laminated panel with the required curvature.

4.3.3 Interlayer Thickness Calculation

Using a simple hand calculation, the maximum deflection of the composite panel under given conditions can be determined by utilizing the concept of effective thickness. Considering that the interlayer material is a PU-based two-component resin, the manufacturer allows for varying thickness between 0.9 mm and 8.0 mm (H.B. Fuller | Kömmerling, 2018). Since the glass panel itself is relatively thin, an initial comparison is made between interlayer thickness of 1 mm and 2 mm to evaluate their performance differences. According to the effective thickness formula (Bennison et al., 2009):

$$t_{\text{eff}} = \sqrt[3]{\sum_k t^3 + 12\omega\left(\sum_i t_p t^2{}_{m,p}\right)} \tag{4.6}$$

Where t_{eff} is effective thickness, t_{p} is thickness of glass ply, ω is shear transfer coefficient varying with time and temperature (approximately estimated as 0.5, based under the assumption of an initial E modulus of 65 MPa and that the coefficient generally falls between that of PVB and SGP), and $t_{\text{m,p}}$ is distance between glass mid-plane & interlayer mid-plane. When using a 1 mm core, the actual panel thickness is 3.2 mm, with an effective thickness of 2.58 mm. With a 2 mm core, the actual sandwich panel thickness becomes 4.2 mm, and the effective thickness is 3.25 mm (Table 4.8).

E_{glass} [Gpa]	υ_{glass}	t_{p} [mm]	t_{int} [mm]	t_{tot} [mm]	t_{eff} [mm]
75.4	0.24	1.1	1	3.2	2.58
			2	4.2	3.25

Table 4.8 | Effective thickness result depending on interlayer thickness

The maximum deflection for a simply supported flat plate on four edges is given by the following equation:

$$\delta = \frac{qL^4}{Dk} \qquad D = \frac{Et^3}{12(1-\nu^2)} \tag{4.7}$$

For a simply supported span of 800 mm, the deflection (δ) limit is set to L/100, which corresponds to 8 mm. Under these conditions, the uniformly distributed load (q) that the panel can withstand is calculated as 0.173 kN/m2 for a 1 mm interlayer thickness and 0.345 kN/m2 for a 2 mm interlayer thickness. In both cases, although the serviceability performance conditions does not satisfy to be safely used as a structural element, this calculation con-

firms that the load-bearing capacity increases proportionally with the effective thickness. Considering that additional geometrical stiffness is gained through cold bending and taking into account manufacturing constraints, particularly the difficulty of processing a liquefied interlayer at excessive thickness, the interlayer thickness is not increased beyond 2 mm in this project (Table 4.9).

L [mm]	Support type	δ [mm]	t_{eff} [mm]	q [kN/m2]
800	Simply supported on 4 edges	8 (L/100)	2.58	0.173
			3.25	0.345

Table 4.9 | Flat laminated panel deflection capacity depending on interlayer thickness
Note. ω assumed as 0.5 for lamination interlayer material.

4.3.4 Viscoelastic Material

Viscoelastic materials exhibit both elastic (spring-like) and viscous (fluid-like) behaviour, meaning their deformation depends on both time and temperature. This property is crucial for glass lamination interlayers, which enhance structural integrity and safety. Under short-term impact loads, the elastic component dominates, providing instantaneous stiffness. In contrast, under long-term loading, the viscous component prevails, leading to gradual deformation (creep). Regarding temperature dependency, at low temperatures, the material behaves more like a stiff solid, with elasticity being the dominant factor. As the temperature increases, the material transitions towards a more fluid-like state, allowing the material to flow more easily (Ferry, 1980). According to the material law published by H.B. Fuller | Kömmerling for Ködistruct LG (2016), this time-temperature dependency operates as illustrated in Figure 4.13.

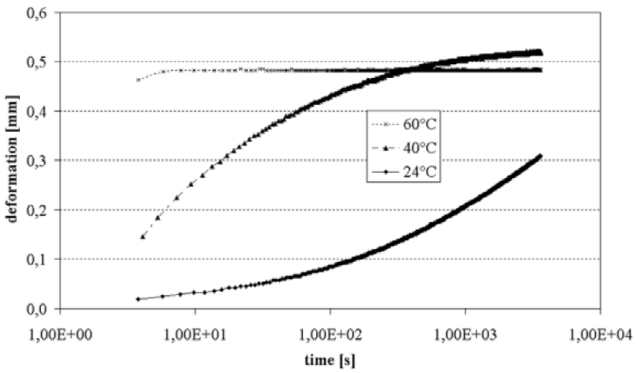

Fig. 4.13 | Time-temperature dependency of Ködistruct LG (H.B. Fuller | Kömmerling, 2016)

In this chapter, temperature dependency will not be considered, so all numerical analyses will be conducted at a fixed room temperature of 22°C. In addition to creep behaviour, the study will also address the effects of spring-back effect, where the composite panel attempts to revert to its original flat state upon the removal of the supporting frame due to stored elastic energy, and stress relaxation, where molecular structure rearrangement leads to an internal stress reduction over time (Figure 4.14).

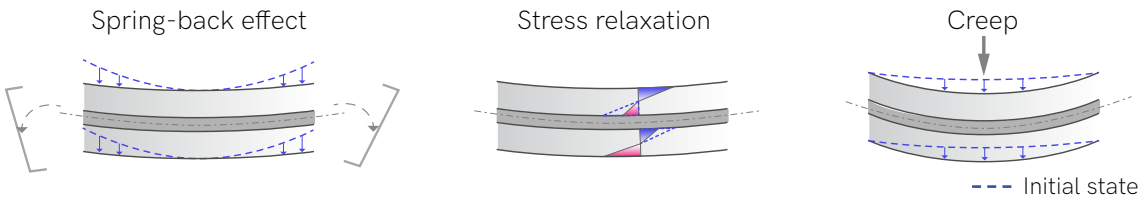

Fig. 4.14 | Characteristics of viscoelastic interlayer laminated glass panel

4.3.5 Numerical Analysis Setup

As in Chapter 4.1, Ansys Workbench 24 R2 software is used for numerical analysis. The composite panel is modelled at a size of 800 × 800 mm, which corresponds to the actual dimensions for real fabrication size in Chapter 5. Pilkington glanova® 1.1 mm, chemically strengthened (E = 75.4 GPa, υ = 0.24) is used for the glass (Appendix 1), while the interlayer is modelled as 2 mm thick Ködistruct LG as shown in Figure 4.15. The viscoelastic behaviour of the interlayer is represented using the Prony series, following the material law (Appendix 2). The edge support conditions are modelled identically to those in Chapter 4.1. For practicality of the modelling, VHB adhesive edge seal is excluded for the finite element method. The overall mesh division size is being done in 2 cm and specifically along the thickness direction, each layer of the sandwich panel is discretised into 2 meshes (3,200 meshes for each layer, 9,600 meshes in total, for the whole composite panel). The mechanical properties of the glass and interlayer materials used in the FEA are listed in Table 4.10. To replicate the semi-rigid edge support conditions, the same materials applied in Chapter 4.1 are utilised in the edge support modelling.

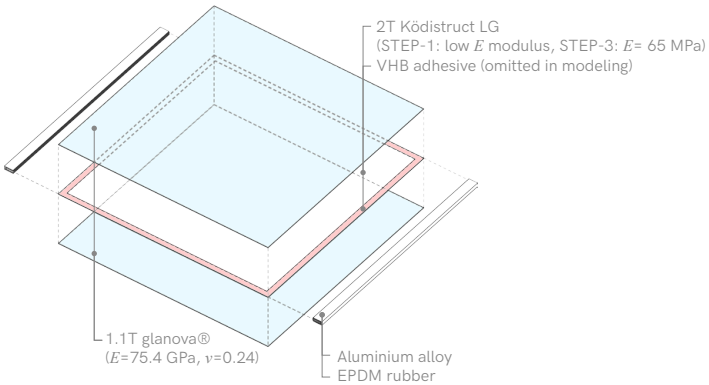

Index [*i*]	G_i / G_0	τ_i [s]
1	2.00E-03	2.77E+05
2	3.10E-03	6.86E+04
3	1.02E-02	2.17E+04
4	3.79E-02	4.13E+03
5	1.26E-01	3.69E+02
6	7.87E-01	1.51E+00

*At temperature 22 °C, $G(0)$ = 21.8 MPa
($G(0)$ automatically constructed based on Ansys)

Fig. 4.15 | Sandwich panel numerical analysis set-up
Left: Panel components
Right: Ködistruct LG Prony series coefficients (Based on DIBt, 2016)

E_{glass} [Gpa]	υ_{glass}	t_{glass} [mm]	Meshing Count [L x W x T]	Edge Condition	
75.4	0.24	1.1	40 x 40 x 2 (single glass)	Semi-rigid	
E_{int} [Mpa]	υ_{int}	t_{int} [mm]	Meshing Count [L x W x T]	Viscoelasity	Temperature [°C]
$E(0)$ = 65	0.49	2	40 x 40 x 2	Prony Series (Fig. 4.15)	22

Table 4.10 | Baseline properties and boundary conditions for sandwich panel materials applied in FEA

The manufacturing and load testing process can be divided into three stages:

Step 1. Cold lamination pouring & cold buckle bending (static structural)
The resin remains in a low E modulus state, allowing cold deformation to occur with less deformation force.

Step 2. Curing phase
During this phase, a chemical reaction gradually increases the stiffness of the interlayer. Once fully cured, the core material exhibits the mechanical properties defined in its material law.

Step 3. Load testing phase (transient structural)
Once curing is complete, the final mechanical properties are evaluated under applied load scenarios.

Instead of explicitly modelling the time-dependent modulus changes in Step 2, a simplified approach is adopted. As illustrated in Figure 4.16, the final cold buckle bent geometry from Step 1 (static structural analysis), along with normal stress and shear stress data from each node after cold bending, is applied as initial stress input data for Step 3 (transient structural analysis), where the load testing is conducted.

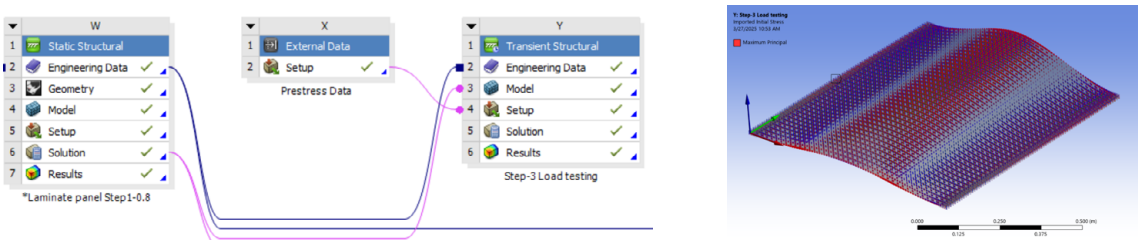

Fig. 4.16 | Numerical FEA workflow for composite glass panel
Note. Left: Ansys Workbench workflow Right: Pre-stress data input for Step 3 taken from Step 1

Accurately modelling Step 2 is highly challenging on FEA. By omitting Step 2 and proceeding directly to Step 3, two key limitations arise in the simulation.
First, molecular rearrangement during the liquid phase induces stress relaxation, meaning that the residual stress state from Step 1 and Step 3 (initial state) is not equal.
Second, under the assumption that the evolution of residual stress during Step 2 remains unknown, it is likely that the cold deformation has already introduced internal stress into the system. This residual stress acts as a time-dependent internal load on the viscoelastic interlayer, meaning that by the time Step 3 begins and any external load is applied, the shear modulus has already been influenced by time-dependent viscoelastic effects. As a result, the material response at Step 3 is more dominated by its viscous behaviour than by its initial elastic properties.
However, in transient numerical simulations, Step 3 is modelled as beginning at $t = 0$, where

the interlayer still exhibits its initial elastic shear modulus $G(0)$. This discrepancy leads to a mismatch between the actual material behaviour and the numerical prediction, since the simulation does not account for the time-dependent softening that has already occurred prior to loading in Step 3.

Therefore, during load testing, it is essential not to rely too heavily on the results obtained at the beginning of the simulation timeline, as they may not accurately reflect the real behaviour of the cold-bent interlayer. Instead, greater attention should be given to the gradually converged values over tiame and the creep recovery behaviour observed after load removal, as both are important in representing the material's viscoelastic response and are theoretically considered to yield results that more closely reflect real-world behaviour.

In Chapter 4.1.6, the previously applied two-step buckle bending, consisting of a 3 mm displacement followed by a 1° inward rotation, is developed for a single glass panel without consideration of additional load scenarios. Therefore, this deformation magnitude cannot be directly applied to the laminated sandwich panel, where both structural performance under load and the sandwich panel configuration must be taken into account. Instead, an iterative simulation process has been used to determine a revised deformation output. The adjusted deformation—(1) 3 mm displacement and (2) 0.8 ° inward rotation on both edges—is used for FEA workflow Step 1. The simulation results show a maximum bending stress of 168 MPa, a maximum in-plane displacement of 25 mm, and an out-of-plane displacement of 92 mm.

4.3.6 Load Scenario

Under the given conditions, the structural integrity of the designed glass panel must be ensured by verifying its capacity to withstand critical load scenarios. Since the panel is designed for use as a roof, it will be installed in a nearly horizontal orientation. Due to this configuration, wind-induced uplift pressure is expected to be the dominant loading factor rather than direct lateral pressure from wind loads. Additionally, as the building is a single-storey structure, maintenance loads are not considered in the analysis, given that any necessary maintenance will be carried out using machinery rather than direct human access to the roof structure.

To establish the critical load scenarios based on Eurocode EN 1990, multiple cases are examined. When wind and snow loads act simultaneously, their opposite directionality leads to partial cancellation of the total load effect, making this scenario less critical. Therefore, only two primary load cases are considered: the case where only snow load is applied (1.35G + 1.5S) and the case where wind uplift is applied (1.35G + 1.5W). The design snow load is calculated following EN 1991-1-3 using the formula $S = \mu_s \cdot C_e \cdot C_t \cdot S_k$, where the characteristic snow load (S_k) for London is 0.32 kN/m2, the shape coefficient (μ_s) is 1, the exposure coefficient (C_e) for an urban setting is 0.8, and the thermal coefficient (C_t) is 1. Substituting these values, the design snow load is determined to be S = 0.256 kN/m2.

For wind load calculations, as per EN 1991-1-4, the uplift force is considered significant due to the convex and irregular shape of the roof. The wind pressure is determined using the equation $q = 1/2 \cdot \rho \cdot v^2$, where the air density (ρ) is 1.25 kg/m2 and the wind speed (v) is conservatively assumed as 30 m/s, exceeding the fundamental wind velocity of 22.1 m/s in London. This results in a wind velocity pressure (q) of q = 0.563 kN/m2. For the wind load, $W = q \cdot C_p$, roof wind coefficient (C_p) of -2 is applied as the most critical scenario, yielding a wind uplift load of -1.13 kN/m2. Multiplying by the load combination factor of 1.5, the final uplift pressure is calculated to be approximately 1700 Pa (Table 4.11).

Load combination	Temperature range	Load duration	Load amount [kN/m²]
1.35G + 1.5S	-20°C < θ < 0°C	5 days (432,000s)	0.4
1.35G + 1.5W	0°C < θ < 20°C	3 seconds	1.7
1.35G + 1.5W + 1.5S	-20°C < θ < 0°C	3 seconds	Load offset by negative load from uplift

*Based on EN 16612, self-weight omitted for load amount, maintenance load not applicable

Table 4.11 | Load cases for the OWO Pavilion roof design
Note. G for gravity load, S for snow load, and W for wind load.

4.3.7 Creep Behaviour

Based on the typical load scenarios established earlier, a distributed load of approximately 2 kN/m2 can be assumed conservatively as the design target under a two-edge supported condition with two unsupported edges. Considering the convex shape of the panel facing outward and its geometrical asymmetry along the exterior and interior, a numerical simulation is conducted to evaluate how the deflection behaviour differs under distributed loads of ±3 kN/m2, where the load acting in the direction of gravity (positive load) and in the opposite direction (negative load) excluding gravitational effects. To check the difference in deflection depending on support conditions, 2 supported edge and 4 supported edge condition has been analysed for each load direction. The analysis aims to identify the location and magnitude of the maximum deflection under each scenario, examine the creep deformation induced by the viscoelastic property of the interlayer under sustained loading, and quantify the degree of recovery once the load has been removed.

In this simulation, the load application and time-history behaviour are divided into four stages. The distributed pressure of 3 kN/m2 is being applied in both directions for each experiment cases. In the first stage, from 1 to 100 seconds, the distributed pressure is gradually applied up to 3 kN/m2. In the second stage, from 100 seconds to 10,000 seconds (2.75 hours duration), the pressure is maintained as a constant sustained load. In the third stage, from 10,000 seconds to 10,100 seconds, a gradual unloading phase is introduced, where the pressure is linearly removed over 100 seconds. Finally, in the fourth stage, the panel is left without external pressure for a further 9,900 seconds to observe the creep recovery behaviour. This analysis procedure is summarised in Table 4.12.

Load Step	Step 1. (0 - 100 s)	Step 2. (100 - 10,000 s)	Step 3. (10,000 - 10,100 s)	Step 4. (10,100 - 20,000 s)
Load [kN/m2]	0 to ±3	±3	±3 to 0	0

Table. 4.12 | Load steps for creep simulation experiment

Figure 4.17 presents a graph illustrating the values at the points of maximum deflection over time. Under the 2-edge support condition, positive pressure produced a significantly larger deflection amount (17 mm) than negative pressure (7 mm). However, under the 4-edge support condition, there is little difference between the deflections for positive and negative pressures, both showing values around 5 mm. Given that the experiment does not account for gravitational effects, it can be inferred that depending on the bulging direction (concave or convex geometry), the increased vulnerability to positive pressure under 2-edge support condition is likely due to the sinusoidal convex shape of the roof.

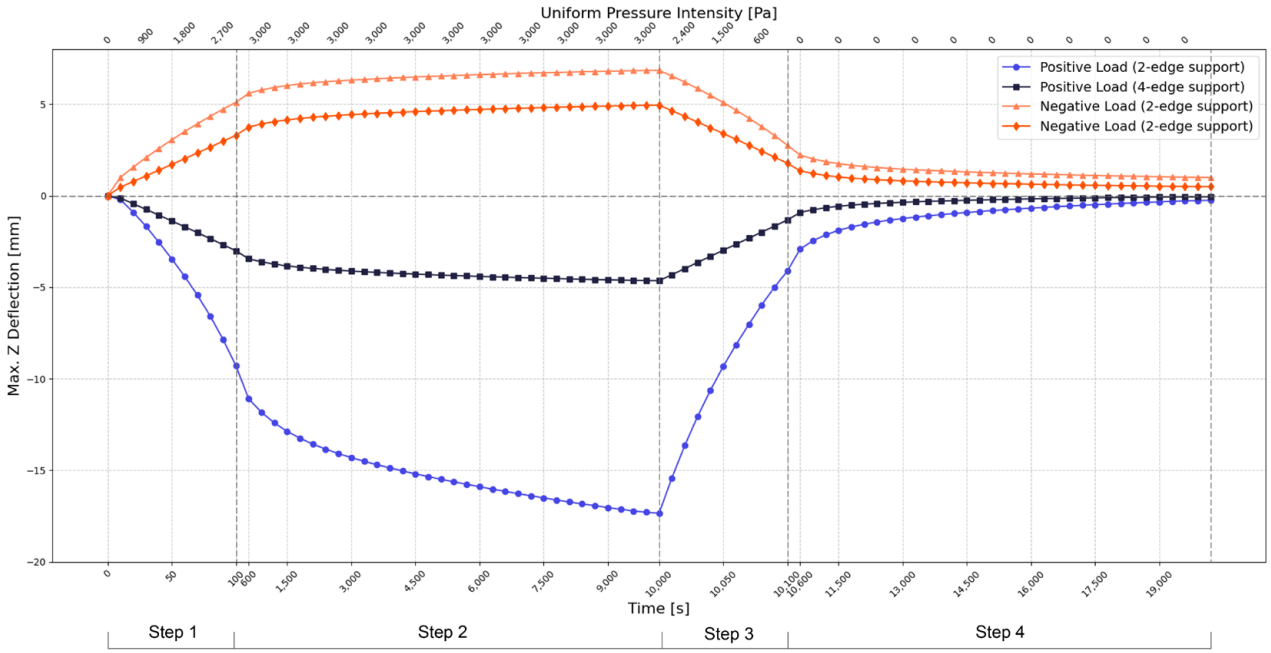

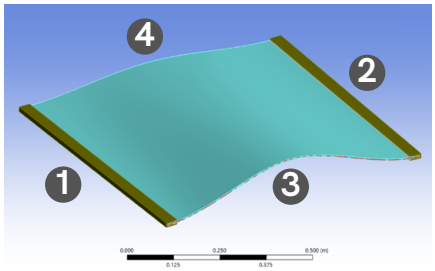

Experiment	Edge 1 & 2 condition	Edge 3 & 4 condition
Pos. - 2E	X, Y, Z disp. fixed X, Y, Z rotation fixed	free
Pos. - 4E		only Z disp. fixed
Neg. - 2E		free
Pos. - 2E		only Z disp. fixed

*Self load (gravity) omitted in this experiment

Fig. 4.17 | Creep behaviour experiment result & support condition

Creep effects are most apparent during Step 2, where sustained loading leads to continued deflection over time. A comparison of Step 4 results under both positive and negative load conditions further reveals that recovery to the original form occurs more rapidly under positive loading. Therefore, under the given experimental conditions, the positive load is identi-

fied not only as a more critical condition for deflecting the sinusoidal convex shape, but also as one that enables quicker recovery once the pressure is fully removed.

In Chapter 4.3.3, the deflection of a flat composite panel under a 4-edge simply supported condition was calculated. Although a direct quantitative comparison is not appropriate due to differing boundary conditions (simply supported versus fixed support), Figure 4.18 illustrates how cold buckle-bent geometrical stiffness influences the stiffness of the glass unit. Unlike the flat panel where the maximum deflection occurs at the centre, the cold-bent sinusoidal geometry shifts this point to approximately one-quarter of the span from the edges, symmetrically on both sides. This indicates that the added geometrical stiffness significantly improves the serviceability of the roof. The behaviour resembles that of column buckling, where introducing a central support highly reduces overall deflection. Under the two-edge support condition (Figure 4.18, left), the greatest deflection occurs at the free edge with the smaller curvature, while the edge with the larger sinusoidal curvature exhibits only about one-quarter of that displacement.

While the four-edge support condition provides an excellent boundary for controlling deflection (Figure 4.18, right), it results in a higher level of internal stress compared to the two-edge support case, under the same load conditions. In this numerical experiment, the internal stress slightly exceeds the design stress limit of 200 MPa.

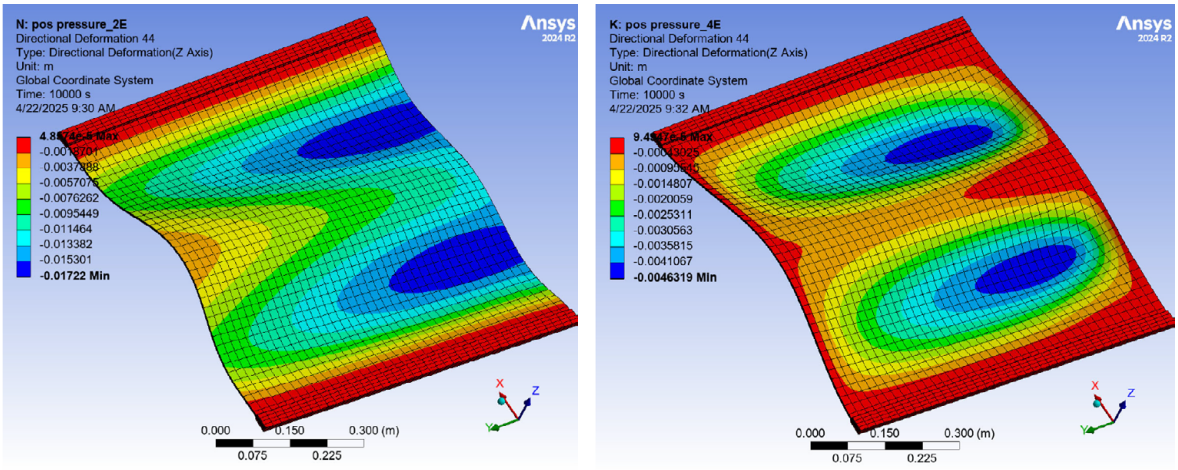

Fig. 4.18 | Z directional deformation results under positive pressure on 2-edge, 4-edge supports
Note. Left: 2-edge support with x 3.3 deflection scale factor at 10,000 s
Right: 4-edge support with x 12 deflection scale factor at 10,000 s

4.3.8 Spring-back Effect

The phenomenon of spring-back refers to a material's tendency to return towards its original, undeformed shape due to the release of residual stresses during cold deformation. In the context of Chapter 4.3.7, this effect is not initially considered, as the cold-bent shape was held in place by a supporting fixture frame even after the curing process had been completed. However, this chapter explores the potential influence of spring-back once the frame is entirely removed post-curing. The degree and rate of the spring-back deformation are largely determined by the interlayer's shear strength, which itself is governed by

the material's viscoelastic properties (Fildhuth & Knippers, 2012). These properties are described by the Prony series coefficients introduced earlier in Figure 4.15. The shear modulus G rapidly decreases in the early stage and then gradually stabilises over time, exhibiting an exponential time-dependent behaviour.

Figure 4.19 presents two graphs illustrating the differences in spring-back responses once the supporting frame is fully released without any gradual release program steps (Galuppi & Royer-Carfagni, 2015), depending on the cold bending geometry. The three geometries compared are the sinusoidal half-paraboloid (black), sinusoidal single-curved geometry (grey), and the cylindrical single-curved geometry (silver). For objective comparison, the initial maximum stress is set to similar levels across all cases, and the plates are placed horizontally with the most prominent bulging curve facing against the direction of gravity.

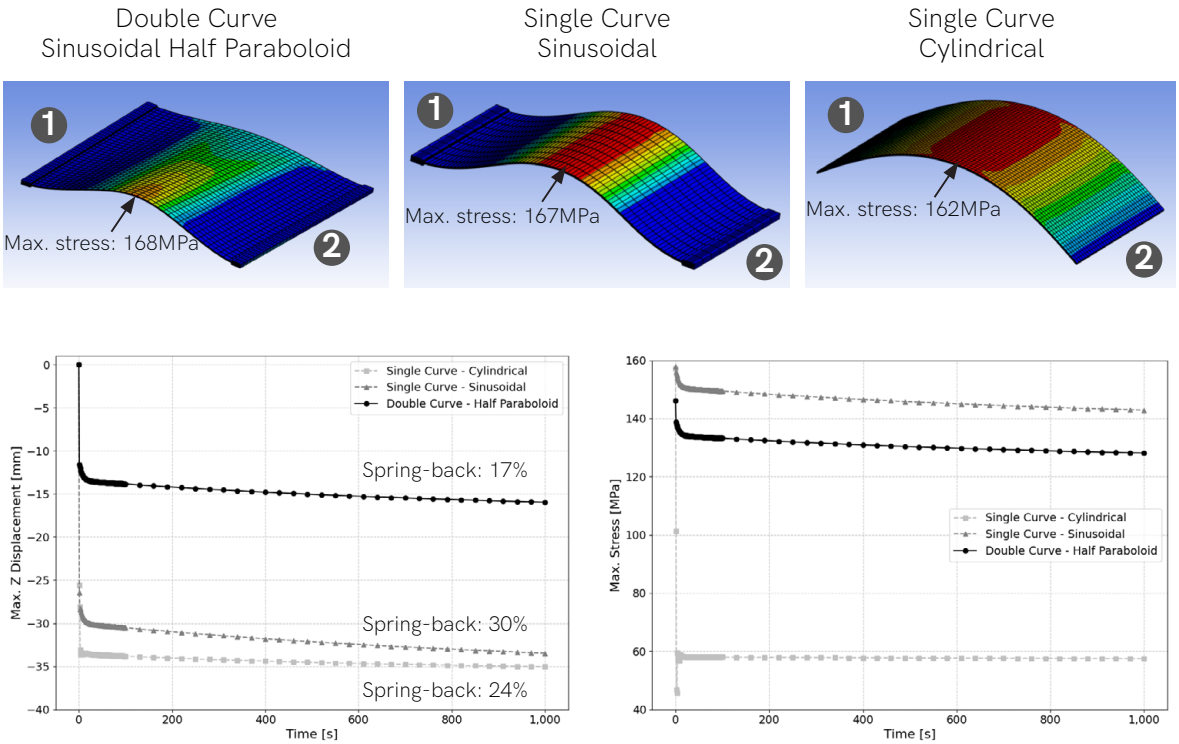

Experiment	Self weight	Edge 1 & 2 condition
Sinusoidal half paraboloid Sinusoidal single curved Cylindrical single curved	1.0 G (1.0 gravity)	Only Z disp. fixed

Fig. 4.19 | Spring-back effects on displacement and stress in varying cold-bent glass geometries

The first graph plots the displacement changes at the point of maximum curvature over time, while the second graph shows the corresponding reduction in residual stress. Both graphs demonstrate time-dependent behaviours that closely follow the exponential pattern predicted by the Prony coefficients. In terms of geometry, spring-back is most significant during the initial second, with an abrupt displacement of nearly −12 mm observed for the half-paraboloid geometry. Over the subsequent 20 seconds, this displacement increases to

approximately –13.5 mm, after which it progressed more gradually, reaching around –16 mm at 1000 seconds. Analysis of residual stress reveals a proportional decrease relative to the displacement changes throughout the entire time frame.

A significant difference in spring-back between the double-curved surface and the single-curved surfaces is observed. Although the initial maximum residual stress values are set similarly for all three cases, sinusoidal single-curved and single cylindrical surfaces (developable geometries) exhibit much wider regions with high stress along curvature peak. Consequently, it can be inferred that the developable surfaces initially contain greater amounts of residual stress compared to the double-curvature surface, and therefore likely experience larger displacement due to spring-back after release.
An additional observation emerges from the comparison of the maximum stress graphs. For the cylindrical geometry, a rapid release of stress is recorded, with values dropping from 160 MPa to 60 MPa almost immediately after release of the support. In contrast, the sinusoidal geometries maintain considerable residual stress even after the spring-back, attributed to its undulating profile. Additionally, due to its geometric characteristics, the sinusoidal profile exhibits slower convergence of both displacement and stress towards steady-state values compared to the cylindrical curvature.

Due to the asymmetry inherent in the initial half sinusoidal paraboloid cold-bent geometry, it is also insightful to observe the differences in displacement along edges A and B, as shown in Figure 4.20. The half-paraboloid form appears to redistribute in-plane stresses effectively. After support release, edge A, which initially bore greater in-plane stress, experienced approximately 15 mm of displacement, whereas edge B, which had lower curvature and stress, showed only about 6 mm of displacement after 1000 seconds. Assuming that no significant geometrical changes occur beyond 1000 seconds, the spring-back effect observed at Edge A shows an approximate 17 % recovery towards its original shape. This numerical expriment aligns reasonably well with the rule of thumb provided by TTEC engineers, who suggested a typical recovery rate of approximately 30 % for a single-curved bending geometry due to springback, indicating that the numerical model produces a meaningful and credible outcome (Figure 4.20).

In Chapter 2.4.4, Galuppi and Royer-Carfagni (2015) suggested that sinusoidal edge shaping profiles offer advantages in cold-lamination bending, particularly by mitigating delamination issues. This assertion is further supported by the geometric transformations observed along the two free edges A and B after spring-back phenomenon. The sinusoidal shape at the panel edges remains intact even after spring-back, which indicates an enhanced geometrical resistance to interlayer shear forces. Compared to the cylindrical constant curvature, the sinusoidal profile not only helps better preserve the original deformed shape but also retained a greater amount of internal stress, as stress relief is less pronounced than in the cylindrical case.

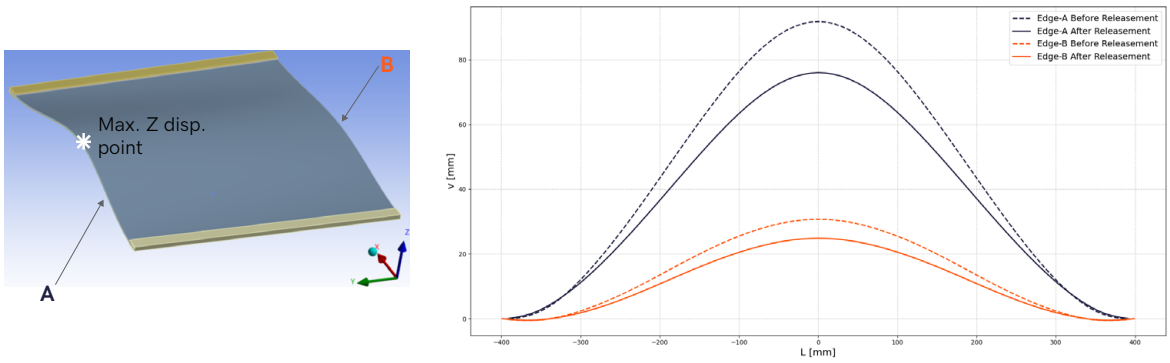

Fig. 4.20 | Post spring-back deformation observed along Edges A & B

4.4 Solar Design

The OWO Pavilion, with a glass roof, would essentially function as a green house, making solar control a critical design consideration. The options for modulating light transmittance in double-curvature glass are extremely limited. One viable solution is ceramic fritting, which, when fused onto the glass surface in its flat state, remains firmly bonded even after the cold-bending process. This ensures that the fritting provides a consistent level of solar protection without compromising adhesion during deformation. However, the potential reduction in glass strength due to fritting is not explicitly accounted for in the structural design in this research.

Even before conducting a detailed analysis, it is anticipated that the highly transparent nature of the pavilion would allow an excessive amount of light to penetrate the interior. Which means that a significant portion of the glass surface might need to be covered with solar control mechanisms to regulate solar gain effectively. Given the flexibility of customisable fritting patterns, the density of the frit will be designed to vary depending on solar exposure: regions with lower solar impact receives a lower frit density, while areas exposed to higher solar radiation are going to be covered with denser frit patterns. This approach aims to optimise both transparency and solar performance, ensuring an appropriate balance between natural daylighting, glare control, and energy efficiency.

4.4.1 Methodology

Jiang et al. (2020) demonstrated that the incident radiation distribution on a roof surface varies depending on its geometric form. Building upon this finding, the design strategy in this study focuses on the adjustment of frit pattern based on radiation mapping on the roof, with the ultimate goal of achieving an evenly distributed indoor irradiation under specific threshold. The methodology follows a sequential approach to ensure a well-structured performance-driven frit pattern optimisation.

The first step involves defining the simulation conditions and establishing the material properties required for the analysis. To understand the impact of geometry on solar exposure,

a comparative study is conducted between a flat roof configuration and the structurally optimised free-form roof, assessing the differences in incident radiation values. Following this, the methodology proceeds with the mesh division of the double-curved roof geometry, the transmission calculation of glass panel, and the initial analysis of indoor irradiance distribution without any appliance of ceramic fritting. These preliminary results are used to refine the design objectives. The next stage involves implementing a simplified computational method to determine the optimised frit density for each area of the roof. Finally, these panel-specific frit densities are incorporated into a gradient dotted frit pattern design, achieving a seamless performance-based solar shading across the entire roof (Figure 4.21).

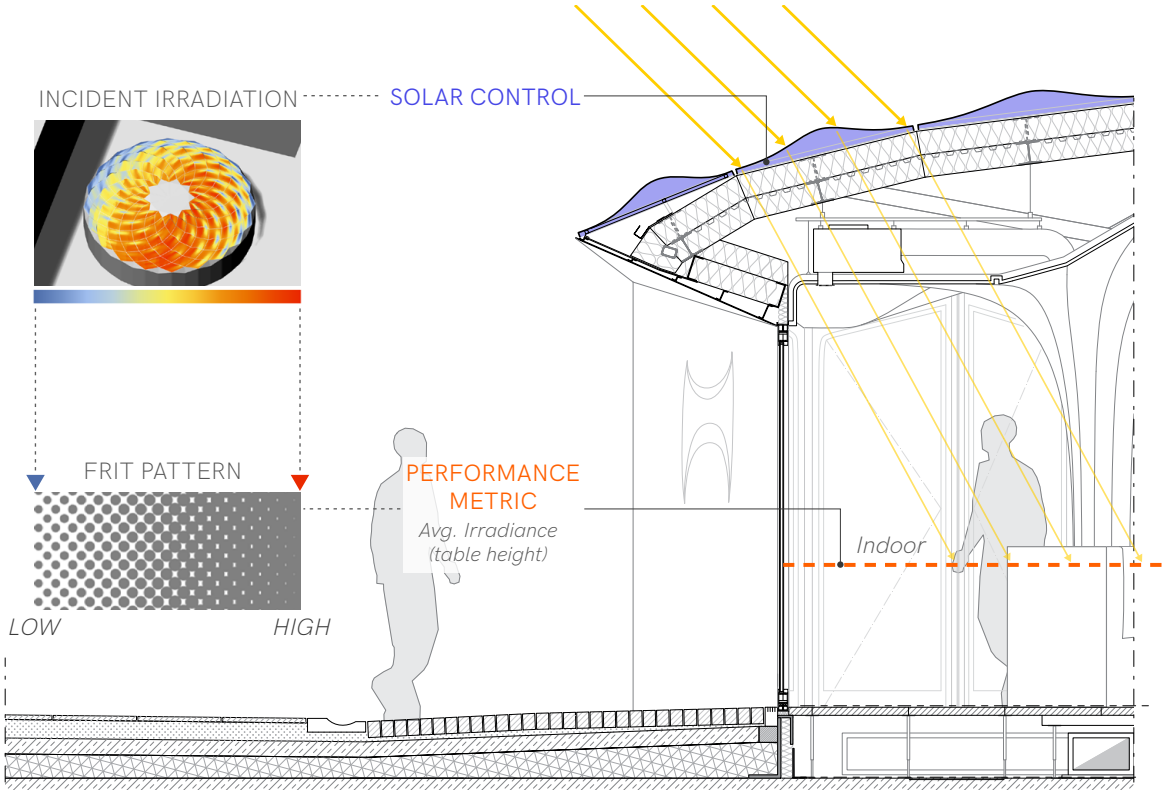

Fig. 4.21 | Roof ceramic frit design concept

4.4.2 Simulation Setup

The simulation period is defined from March to October, between 09:00 and 18:00, as these months and hours are expected to experience the most significant impact from solar radiation. Given the pavilion is positioned inside the courtyard of Whitehall, where the surrounding buildings are approximately four to five times taller than the pavilion itself, considerable effects from shading and secondary reflection from the surrounded office building are anticipated. To ensure accuracy, these boundary conditions are incorporated into the simulation.

For the simulation process, Rhino Grasshopper 8.0 with the Ladybug plug-in (version 1.8.0) is utilised to perform radiation mapping and Honeybee is used for daylight analysis where Radiance is used for simulation engine. The complex Neoclassic-style buildings surrounding the site are simplified in the digital model to streamline the analysis, while the sun path

variations are illustrated in Figure 4.22. The Old War Office (OWO) building, which encloses the courtyard, is clad in bright Portland stone. To account for its reflective properties, a reflection index of 0.5 is assigned to it in the simulation.



Fig. 4.22 | Base simulation condition
Note. Left: Boundary building model & sun path
Right: OWO office building. (Daewha Kang Design, 2021)

4.4.3 Incident Radiation on Roof Surface

The first step is to examine how much the incident radiation changes depending on the roof shape. To do this, a comparison is made between a flat glass pane roof and the previously structurally optimised curved glass unit roof (based on Chapter 4.1), in which the four corner points of each panel are fixed based on the original roof design. The simulation is conducted for the predefined period (Figure 4.23).

For the flat glass panel, the maximum incident radiation is found in the south-southeast area of the roof due to the influence of surrounding buildings, whereas the minimum values are located in the north-west-west region. The heat map for the flat roof panels, composed of 160 panels in total, shows a smooth gradient distribution, as if the entire surface functions as a single continuous plane.

In contrast, the double-curved structurally optimised roof exhibits a similar macro-level distribution of high- and low-radiation regions compared to the flat roof. However, within the individual roof panels, more significant variations in radiation values are observed depending on the degree of curvature and orientation of the concave-convex bulging of the panel compared to the flat roof panel. While the heat map indicates notable differences in incident irradiation distribution between the two roof designs, the total incident irradiation values show that the flat roof receives 105,529 kWh of radiation, whereas the curved roof receives 110,281 kWh. The average incident irradiation is 706.3 kWh/m2 for the flat glass and 688 kWh/m2 for the curved design. Although the curved roof exhibits a lower average radiation per unit area, the total incident radiation is approximately 4.50 % higher due to the increased surface area.

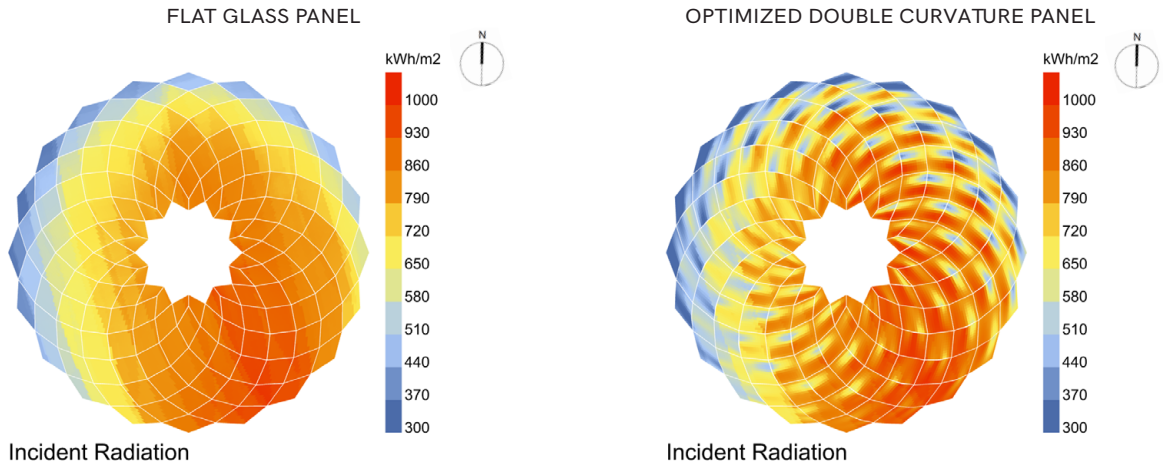

Fig. 4.23 | Incident irradiation comparison on different roof geometries
Note. Left: Flat glass roof geometry Right: Double-curved roof geometry (optimised based on Chapter 4.1)

4.4.4 Roof Meshing

Indoor irradiance simulation is conducted using Ladybug Honeybee-Radiance, which requires geometry input as an .obj format. Therefore, the double-curved surface modelled in Rhino with NURBS-based (Non-uniform rational B-spline) geometry needs to be subdivided into mesh units. For flat surfaces, it is efficient to minimise the number of meshes to expedite the simulation. However, for a roof geometry with varying curvature and complex forms, excessive simplification of the geometry could result in significant difference in result between the real output and the digital twin (inaccurate solar incident angle at each mesh unit). This, in turn, would lead to incorrect incident reflection and transmission values, ultimately compromising the accuracy of the simulation results.

While a customised adjustment of the mesh count is explored, it is found that first simplifying the surface with *FitSrf* command in Rhino and using the *HB Planarize Brep* component in Honeybee Grasshopper provided an optimal balance between computational efficiency and geometric fidelity. This method ensured that the original geometry is not overly simplified while still allowing for effective data processing. As illustrated in Figure 4.24, the final mesh model maintains a suitable distribution of mesh units per panel, ranging from 32 to 102 meshes, depending on panel size and curvature complexity. This segmentation has been used for the subsequent simulation steps.

4.4.5 Glass Transmission Calculation

Given the extensive use of transparent surfaces in the building design, it is anticipated that the simulation would yield an excessive amount of indoor irradiation. The way in which the glass properties are defined would have a significant impact on the simulation results. Therefore, the total transmission value of the laminated glass panel used for the roof is calculated to ensure the correct input data. The glass panel consisted of glanova® and Ködistruct LG interlayer, which possess the light transmittance and refractive index values

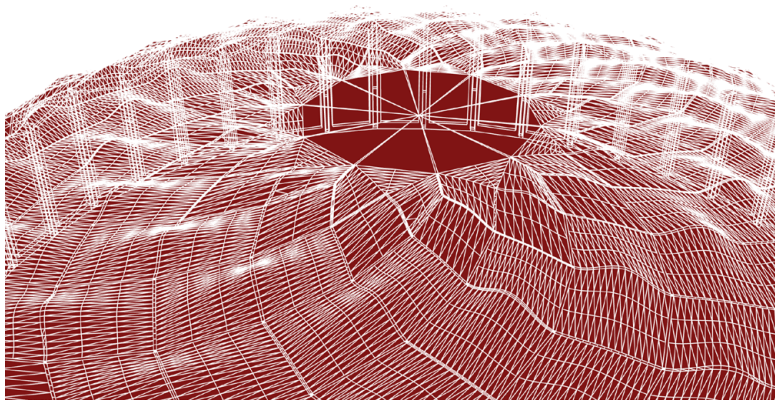

Figure. 4.24 | Curved surface meshing using HB Planarize Brep component

specified in Table 4.13. According to EN-410:2011, the total transmission of a glass unit can be determined using the following equation:

$$T_{\text{total}} = T_{\text{glass,direct}} \times T_{\text{lamination}} \times T_{\text{glass,direct}} \tag{4.8}$$

For the direct transmission of glass ($T_{\text{glass,direct}} = (1-\text{R})^2$), Fresnel's Equation is applied ($R = ((n-1)/(n+1))^2$), where R stands for reflectance and n for refractive index . The calculated $T_{\text{glass,direct}}$ value is 0.9587, leading to a total transmission T_{total} of 0.819. Since no explicit refractive index value for Ködistruct LG is available, the refractive index 1.51 for glanova® is adopted as a representative value for the final panel.

To contextualise this transmittance value, a reference calculation is performed using AGC's light property simulation software. The transmittance of a 4-0.76-4 mm (total thickness, 8.76 mm) laminated glass panel, composed of *Planibel Clearlite* 4 mm glass and a *PVB clear* 0.76 mm interlayer, is determined to be 0.89 (Appendix 3). Comparing this with the T_{total} value of 0.82 (total thickness 4.2 mm) for the designed panel, it can be inferred that the glazing for this design allows a lower amount of light transmission than the thicker glass unit with coating free lamination panel from AGC.

For the glass used in the transparent pavilion walls, generic_exterior_window_sol_0.37 material from Honeybee's material database is applied. The remaining opaque materials follow the default setting values.

Product	Light transmission [%]	Refractive index
glanova®	91	1.51
Ködistruct LG	89	N/A
Laminated panel	82	1.51

Table 4.13 | Solar transmittance and refraction properties used for simulation
Note. Based on technical data sheet of each product.

4.4.6 Optimisation Objective

Using the input values, an indoor irradiance simulation is conducted. The results are pro-

cessed based on the average irradiance [W/m2] over the designated simulation period. Irradiation sensors are positioned at 0.8 m above the floor level, corresponding to the typical table height, and arranged in a 0.25 m grid interval. The simulated indoor average irradiance values can be observed in Figure 4.25.

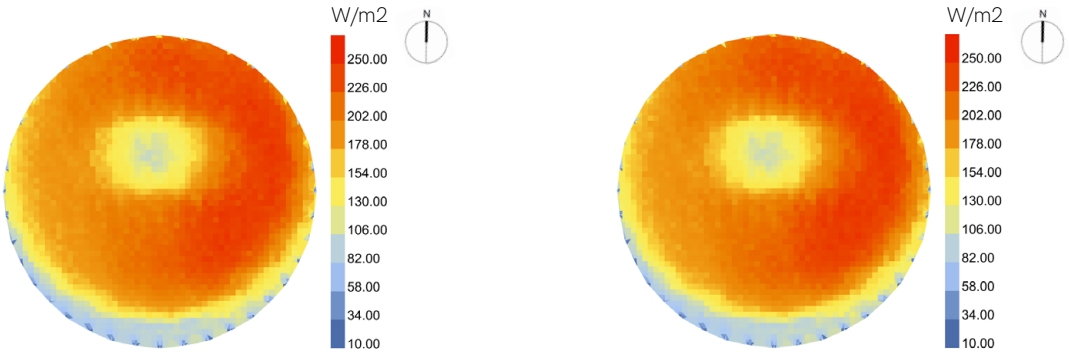

Figure. 4.25 | Indoor irradiance simulation using clear glass composition without fritting
Note. Left: Curved glass geometry Right: Flat glass geometry

To verify the accuracy of the simulation, a comparative simulation is performed using a flat glass roof geometry. While some areas of the curved roof recorded slightly lower irradiation intensity than the flat roof, the overall difference is negligible. Approximately 31.2 % of the total floor area recorded an average irradiance over 200 W/m2. This result provides the basis for establishing the design optimisation objectives.

The irradiance values obtained from the simulation directly and indirectly impact indoor thermal comfort, glare, and indoor illuminance, all of which are crucial considerations for the purpose of solar controlling this building. Consequently, the design optimisation process will be based on irradiance values. However, there is no established code or recommendations defining an appropriate threshold for indoor irradiance. This is because various factors, such as internal surface reflectance and glazing properties, interact in complex ways, making it difficult to establish a universal standard. Since the building functions primarily as a café or bar and can also serve as a semi-outdoor space during favourable weather conditions, the threshold has not been set too strictly. Pan et al. (2022) categorised indoor solar radiation into low-intensity and high-intensity levels, setting 100 W/m2 as the dividing threshold. Hodder & Parsons (2007) found that for every 200 W/m2 increase in solar radiation, skin temperature and thermal comfort rise by approximately 2°C. Currently, 30-40 % of the indoor area records irradiance values exceeding 200 W/m2. To mitigate this, the optimisation objective is set such that 90 % of the area remains below 150 W/m2, while simultaneously minimising the frit coverage on the roof glazing to secure enough transparency (Table 4.14). The choice of 150 W/m2 as the threshold is based on existing research suggesting a reasonable range of 100 - 200 W/m2 and further validated by results from subsequent frit pattern simulations.

	Performance metric	Condition
Objective 1	Avg. indoor irradiance [W/m2]	90 % of sensors ≤ 150 W/m2
Objective 2	Frit coverage [m2]	Minimize

Table 4.14 | Optimisation objectives for solar design

4.4.7 Optimisation Strategy

Ceramic fritting commonly employs dot patterns, which can be highly customizable in terms of dot size, frit shape, spacing, and transparency of the applied material. To avoid excessive variability in the design process, the physical properties of the frit pattern (transparency and reflection) are kept constant. Smaller dot sizes generally provide better light diffusion and minimize visual obstruction, making the pattern less noticeable. When dot diameters exceed 10 mm, they create a strong visual effect, which can be undesirable in maintaining the transparency of the glass (Oldcastle Building Envelope, 2011). For example, a 10 mm diameter dot arranged in a 15 mm grid spacing results in approximately 4,000 dots per square meter. Given that the OWO Pavilion consists of 160 glass panels, accurately simulating the frit pattern at this scale would require processing approximately 640,000 individual frit elements. Using circular dots instead of square ones would further increase computational complexity by 90 times (Essary, 2022), making this approach inefficient for simulation purposes. To address this issue, Essary (2022) proposed a simplified method for modelling frit patterns. His study found that even if larger frit patterns are used instead of smaller dots, and rectangular geometries replace circular patterns, the overall illuminance based metric result (Spatial Daylight Autonomy & Annual Sunlight Exposure) remains largely consistent (Figure 4.26). While Essary's approach is a validated simplified method based on visual experience and uses illuminance as the primary metric, this study relies on irradiance for simulation and optimisation. Therefore, it cannot be assumed that the same simplified method applies with equal validity. However, due to the geometric complexity and significant simulation time associated with actual frit pattern geometry, this simplification strategy is adopted here for irradiance-based simulations, acknowledging its practical advantages despite the lack of full methodological validation. According to the previous theoretical calculation, it is possible to shorten the calculation time up to 6000 times faster compared with a conventional method using a real frit geometry for simulation in case of the OWO roof frit design optimisation.

Figure 4.27 illustrates the step-by-step methodology used in this study to generate an optimised, panel-specific ceramic dot frit pattern mapping across the double-curved roof geometry.

In the first step, instead of using the real double-curved geometry, flat glass panels has been used to reduce the optimisation step calculation time. Each individual roof panel is divided along the U and V directions into smaller sub-surfaces that function as shading units con-

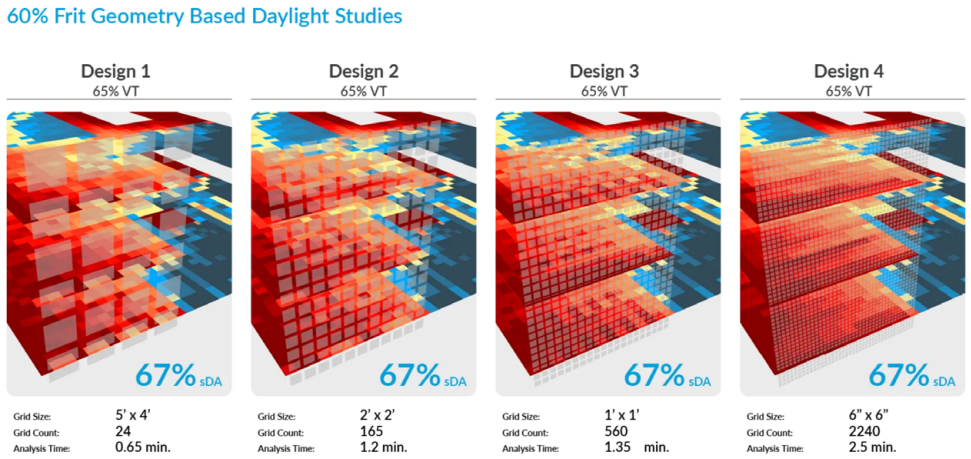

Fig. 4.26 | Simplified approach to model frit patterns for daylight analysis (Essary, 2022)

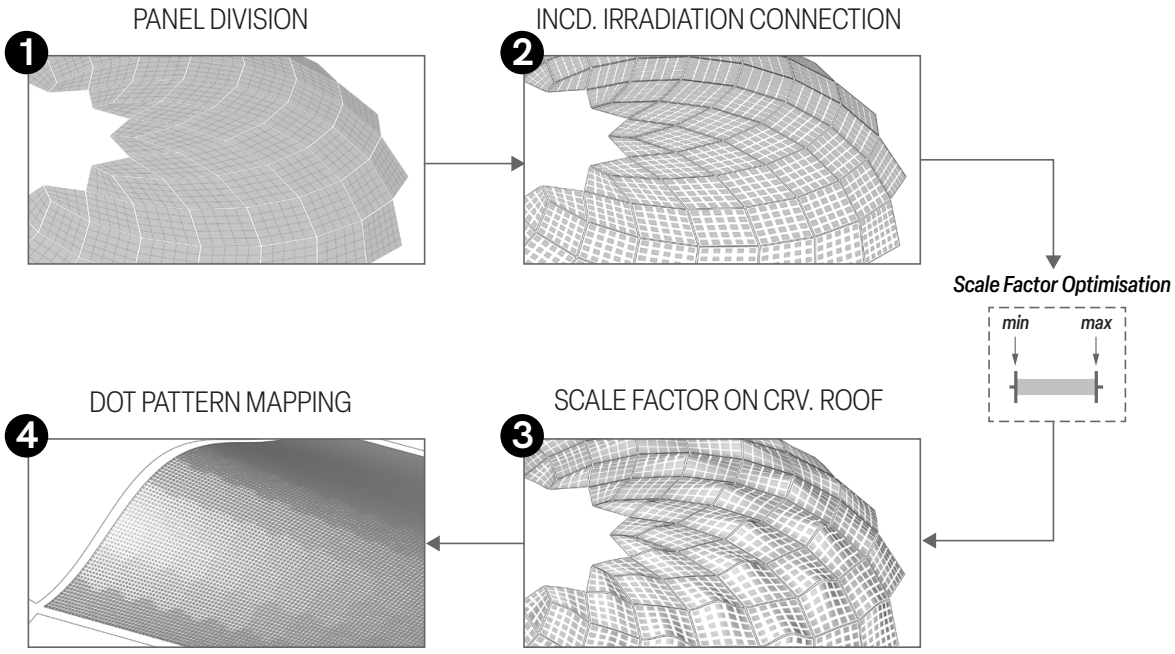

Fig. 4.27 | Frit design optimisation methodology

trolling light transmittance. To ensure adequate resolution in representing a continuous gradient and to avoid geometric distortion upon application to the curved surface, the number of divisions is determined by dividing the average edge length within each panel by 200 mm. In the second step, the incident radiation values obtained from incident roof radiation simulation is used to assign a unique scale factor to each sub-surface element. These scale factors determine the effective coverage of the frit pattern. A key part of this step is the optimisation of the minimum and maximum values of the scale factor range, which is carried out to meet the previously established design objective: achieving average indoor irradiance values below 150 W/m2 for 90 % of the interior area, while simultaneously minimising total frit coverage. This optimisation is done with the result of the indoor irradiation simulation using HB-Radiance simulator.

The third step applies the optimised range of scale factors to the actual double-curved

geometry of each roof panel, generating a mapped gradient pattern. The resulting indoor irradiance result is then evaluated to assess whether the simulation outcomes of the real geometry aligned with the design goals.

Finally, in the fourth step, the actual dotted ceramic frit pattern is generated. Using the panel-specific gradient values computed in the previous step, the dotted frit pattern will be generated and applied to the roof geometry.

4.4.8 Multi-Objective Optimisation

To achieve a balance between functional performance and material efficiency, a multi-objective optimisation is conducted with the goals of (1) ensuring that over 90 % of the indoor area maintains irradiance levels below 150 W/m2, and (2) minimising the total fritted surface area. The *Opossum* component in Grasshopper is used to facilitate this process, utilising the RBFOpt (Radial Basis Function algorithm for black-box optimisation) algorithm. A total of 226 iterations has been performed, with an overall simulation time of approximately 9 hours. The input parameters for the optimisation are the minimum and maximum scale factors of the frit pattern (Figure 4.28). The ceramic frit used to control the transmittance of the glass functions as shading element. A *translucent modifier* is applied, with each input parameter calibrated to appropriately represent the physical characteristics of a semi-transparent frit pattern (Figure 4.28, bottom – HB input).

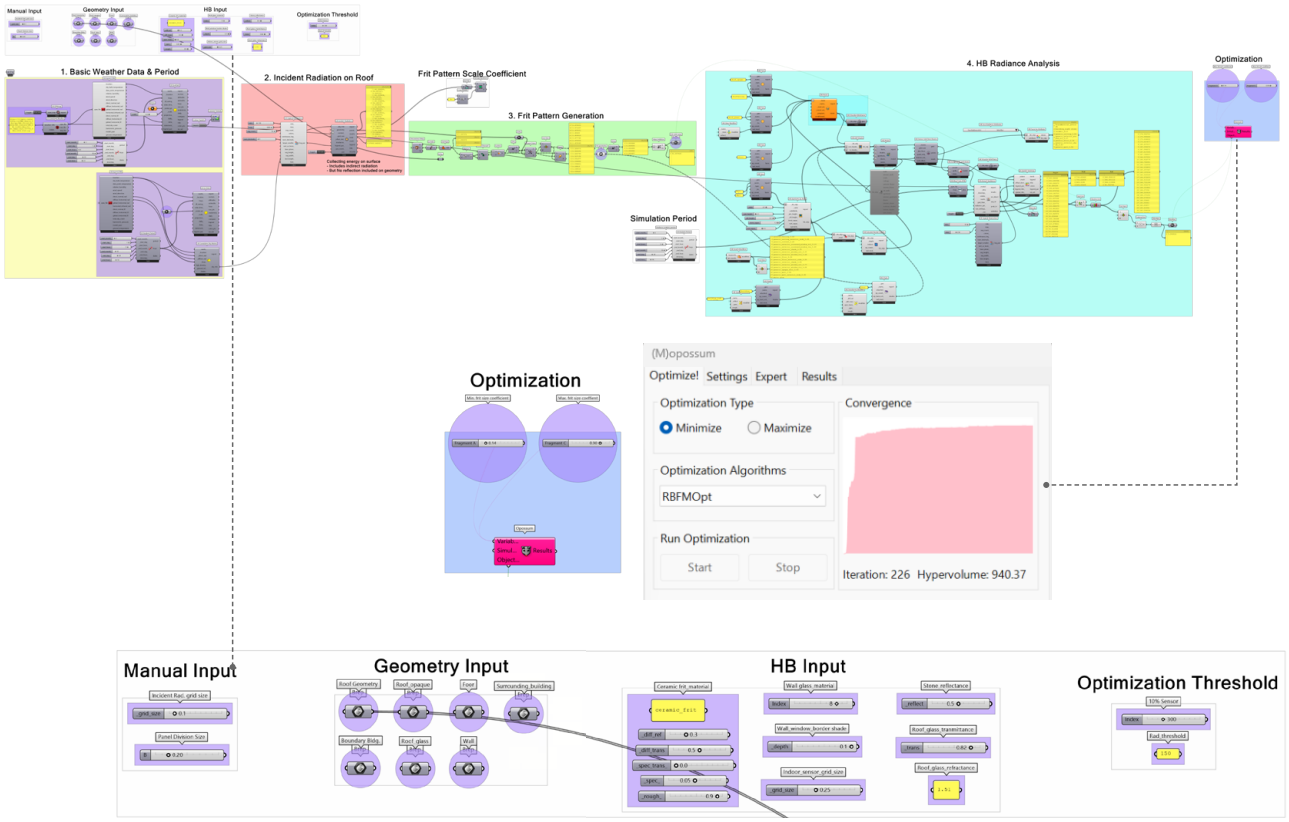

Fig. 4.28 | Grasshopper optimisation workflow script for solar design
Note. In detailed image: Optimisation convergence & input parameters.

In multi-objective optimisation processes, the optimiser typically generates a set of classified, high-performing outcomes, from which the designer selects a preferred solution based on trade-offs. Table 4.15 presents a selection of top-performing optimisation results. Among them, the configuration with a minimum scale factor of 0.14 and a maximum of 0.9 is chosen. Although this option exhibited a slight exceeding in the top 10 % of indoor irradiance values (reaching 153.7 W/m2, 3.7 W/m2 over the 150 W/m2 threshold), it reduces the fritted surface area to 52.858 m2, slightly outperforming alternative configurations in terms of material efficiency and visual transparency. For comparison, if a uniform (non-gradient) frit pattern is applied across all panels to meet the same irradiance threshold, the required frit area would amount to 70.64 m2. This demonstrates that the optimised gradient-based pattern achieves an approximate 25.2 % reduction in coverage, enabling a more transparent yet equally effective solar control solution (Table 4.16). A comparison of the mean irradiance values presented in the Table 4.15 confirms that when the two optimisation objectives set in this study are satisfied, the resulting indoor average irradiance aligns well with the intended performance targets. The optimised parameters within the Rank 1 results consistently achieve desirable outcomes, indicating their effectiveness in meeting the design objectives.

All optimisation procedures are carried out on the flat roof geometry to improve computational efficiency. Once the optimal scale factors (0.14 and 0.9) are derived, they are subsequently applied to the actual double-curved roof geometry. The frit area increases slightly due to surface curvature, resulting in a total fritting area of 58.77 m2. However, the irradiance performance improves further, with the top 10 % indoor irradiance value decreasing to 147.87 W/m2 — thereby satisfying the initial design objective (Table 4.16).

Parameter [min / max factor]	Rank	Frit Area [m²]	Top 10% th irradiance [W/m²]	Mean irradiance [W/m²]
0.44 / 0.81	1	60.941	150.15	121.81
0.1 / 0.95	1	56.217	150.18	122.45
0.18 / 0.9	1	56.193	150.29	123.98
0.17 / 0.9	1	54.513	151.39	124.42
0.14 / 0.91	1	53.954	152.18	124.62
0.17 / 0.89	1	53.414	152.73	125.31
0.14 / 0.9	1	52.858	153.71	125.46

Table 4.15 | Optimisation result on flat glass geometry

Condition (Parameter)	Frit Area [m²]	Top 10% th irradiance-value [W/m²]	Simulation result [W/m²]
Flat gradient frit (0.14, 0.9) 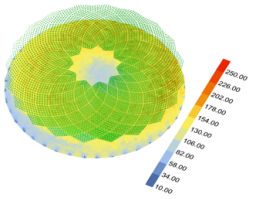	52.858	153.71	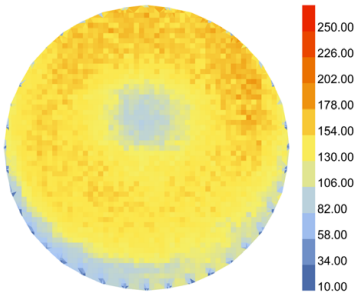
Flat equal frit (0.72) 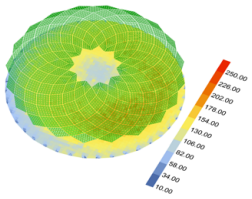	70.64	152.53	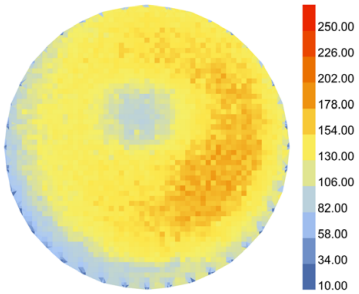
Curved gradient frit (0.14, 0.9) 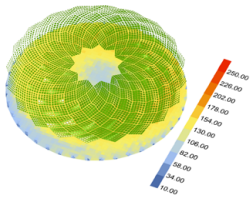	58.77	147.87	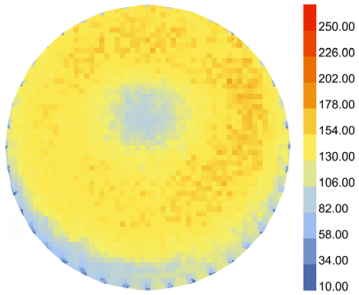

Table 4.16 | Indoor irradiance simulation results between different frit pattern and roof geometry

4.5 Discussion

Necessity of Structural FEA

Due to the non-standardised and irregular form of the cold bent geometry studied in this study, relying solely on experimental testing presents clear limitations (Chapter 3). While conventional hand calculating analytical approaches may suffice for typical single curved cold-bent geometries, they fall short in addressing the added complexity of asymmetric double-curvature geometries. To address these challenges, particularly those arising from the time- and temperature-dependent viscoelastic behaviour of interlayer materials and the geometric non-linearity caused by large deflections, a numerical approach using finite element analysis (FEA) is essential.

Stress-Curvature Relationship

A proportional relationship between radius of curvature and bending stress is proved in single-curved geometries. While this relationship becomes invalid for complex double-curvature surfaces, a correlation between minimum radius and stress still emerges during shape

optimisation. In the case of near-developable surfaces such as the sinusoidal half-paraboloid explored in this study, radius may serve as a useful secondary indicator of structural performance, though not for direct calculation.

Role of Stepwise Buckle Bending

The necessity of dividing the buckle bending strategy into two separate steps using two-edge support may be questioned in terms of its relevance to stress optimisation. However, numerical simulations conducted in this study demonstrate that initiating deformation with the first step, which forms an initial developable surface, followed by a second step that introduces double curvature deformation, enables the formation of more complex geometries within the defined stress limits.

Compared to the direct application of double-curvature deformation without a preceding developable phase, this two-step approach results in a greater range of curvature without exceeding the stress threshold. The initial buckling phase therefore serves as an effective intermediate stage for constructing intricate cold-bent geometries in case of forming the sinusoidal half paraboloid. Moreover, it plays a meaningful role in relieving residual stress, validating the two-step buckle bending method as a practical and efficient strategy in this research.

Irregular Buckle Bent Geometry

The cold-buckled geometry introduces significant asymmetry and residual stress, particularly during Step 2 of the cold buckle bending process, in which edge supports are rotated inward. This results in asymmetric loading conditions and complex local stress accumulations that lead to unexpected deformation patterns. Micro-scale discrepancies in surface curvature are observed between the theoretical geometry and the cold-formed geometry during the numerical analysis. In particular, the cold buckle-bent geometry exhibits more complex and unpredictable variations in local curvature, ranging from synclastic to anticlastic forms, which manifest differently across various regions of the panel. These deviations reflect the geometric sensitivity and non-uniform stress distribution inherent to this complex double curvature form.

Interlayer Performance

In the current FEA setup, assigning the interlayer material properties based on Young's modulus and Poisson's ratio results in an automatically calculated initial shear modulus $G(0)$ of 21.8 MPa. This is notably lower than the material-law-defined value of 36.39 MPa for Ködistruct LG, suggesting that the model provides conservative estimates of interlayer performance. Furthermore, since the curing phase of the interlayer—during which residual stresses develop due to molecular rearrangement—has not been modelled (step 2), the simulation does not yet fully capture the actual post-curing stress state. Accurate simulation of the curing phase remains an important area for future research.

Geometry-Specific Load Directional Behaviour

One of the key insights from this chapter is that the direction of loading interacts non-trivially with the cold-bent geometry. The panel's surface includes both convex and concave regions, and depending on the load direction, some areas amplify deformation while others resist it more effectively. No single region is universally stronger or weaker across all scenarios; instead, local vulnerability is highly dependent on the interaction between geometry, boundary conditions, and load orientation. As such, structural performance cannot be generalised using simplified design rules, and each case requires individual evaluation.

Advantage of Sinusoidal Geometry

Despite its complexity, the sinusoidal half-paraboloid geometry demonstrates structural benefits compared to conventional cold-bending forms. The edge profile helps minimise spring-back and may reduce the risk of delamination. Compared to single-curved geometries, the sinusoidal shape distributes curvature more effectively, with a smaller proportion of the surface area experiencing high curvature. This contributes to a reduced overall residual stress state, allowing the geometry to retain its intended shape more effectively after the removal of supporting fixtures. Further validation of this behaviour could highlight an additional advantage of double-curved geometries in cold-bending applications.

Necessity of Gradient Frit Optimisation

When comparing indoor irradiance performance using numerical simulations, the optimised frit pattern proposed in this study shows a clear advantage over an equally spaced frit pattern. Despite offering similar indoor irradiance levels, the optimised pattern reduces roof coverage by approximately 17%, effectively increasing glass transparency without sacrificing performance.

An equal frit pattern tends to concentrate stronger sunlight transmission onto localised southern interior zones, potentially causing visual discomfort or overheating. In contrast, the optimised frit design distributes high irradiance more evenly across the entire interior surface, promoting a balanced and comfortable light environment. This demonstrates that the gradient frit optimisation method used in this research is an effective design strategy, particularly in buildings like the OWO Pavilion where maintaining roof transparency while minimising negative solar impacts is a key goal.

Solar Transmission of Complex Geometry

Complex geometries, such as the sinusoidal roof surface explored in this study, introduce several challenges in evaluating and optimising solar transmittance. Accurately tracking how double-curved geometry affects solar transmittance and determining how to control it requires a computational approach. The degree of geometric segmentation directly influences both the accuracy of the simulation and the required computation time. Therefore, it becomes essential to determine an appropriate level of discretisation for reliable yet efficient performance analysis.

The study proposes a structured optimisation workflow tailored for long-running simulation tasks. By segmenting the workflow into smaller sub-processes, not only is the computation time reduced, but meaningful optimisation parameters can also be extracted at intermediate steps. These parameters can then be reused or adapted in subsequent design stages, even if the geometry evolves—supporting a more flexible and design-integrated approach to solar control.

The sinusoidal convex-concave roof form raises a potential issue: transmitted light may converge and create interior heat spots. While this study does not explicitly address the problem due to the expected scattering effects of the complex geometry, further investigation into this phenomenon could be valuable.

Limitations of Irradiance as a Design Threshold

Although the solar simulation process itself is fairly straightforward and technically manageable, a major challenge arises when defining the threshold for irradiance as a design criteria. The results are highly sensitive to a wide range of interrelated factors, and there is no universally accepted standard for what constitutes an "ideal" irradiance level. The threshold of 150 W/m2 in this study originates from a simplified model and does not fully reflect the complexity of real-world conditions. Therefore, rather than treating this threshold as an absolute design target, it should be understood as a reference point that enables relative optimisation within the design process. The value of this research lies not in confirming a fixed performance figure, but in demonstrating a methodological framework for improving indoor solar control. Assessing whether this type of solar control design truly delivers measurable comfort benefits to users remains a compelling question for future studies.

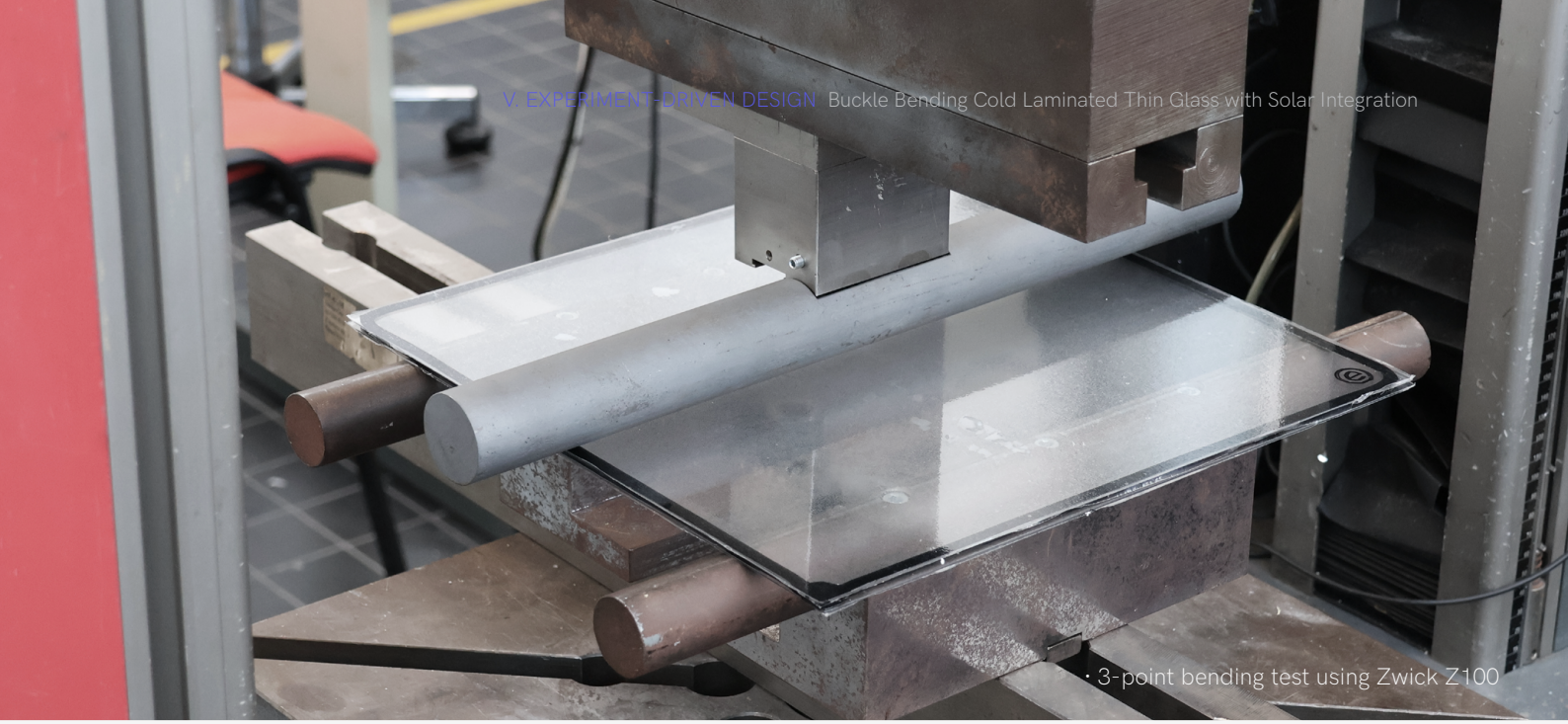

· 3-point bending test using Zwick Z100

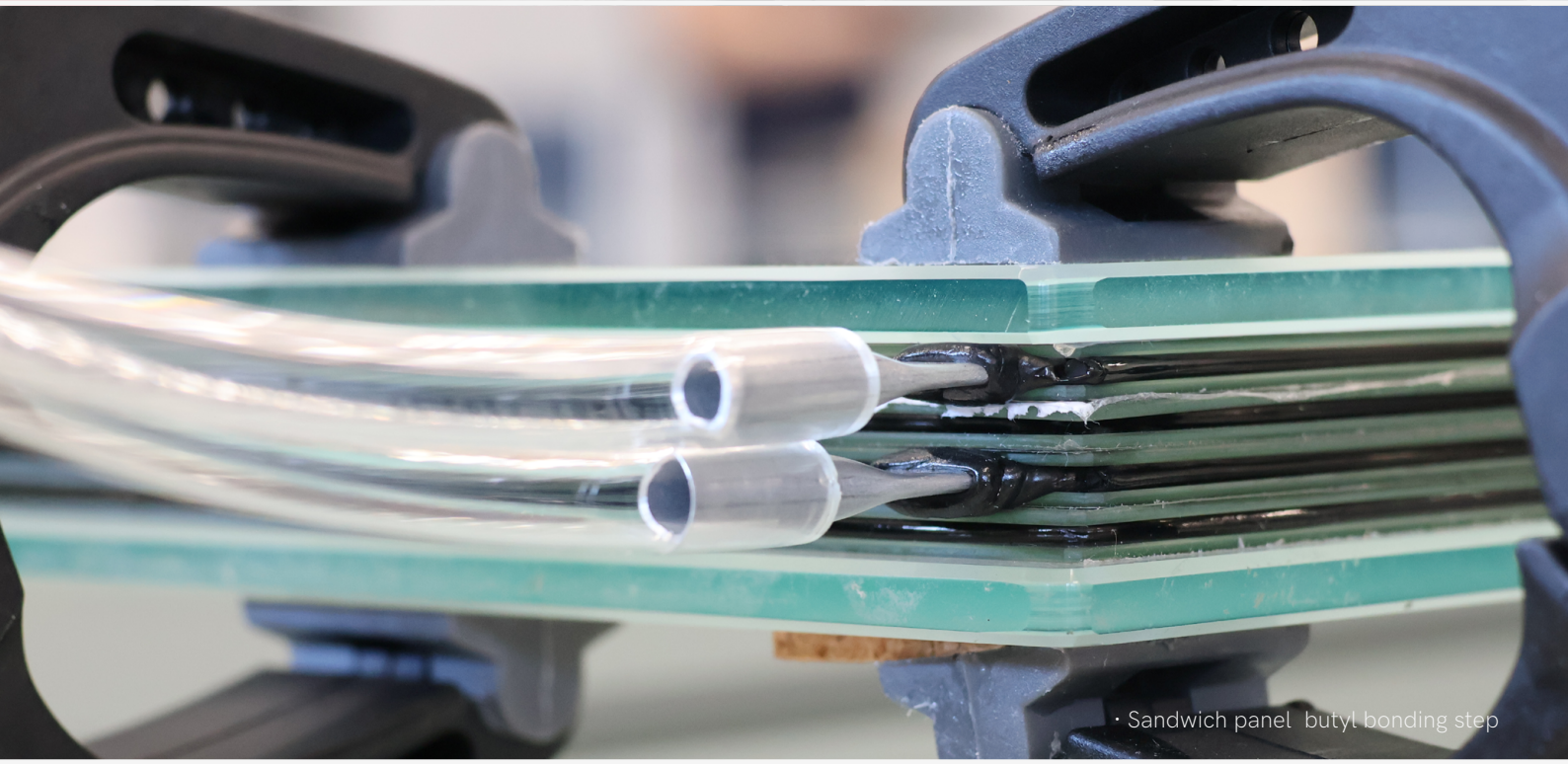

· Sandwich panel butyl bonding step



· Frit pattern transmitted light projection

V. EXPERIMENT-DRIVEN DESIGN

5.1 Structural Validation Experiment

This chapter presents validation experiments for the numerical simulations discussed in the previous chapter. The aim is to verify the reliability and limitations of the previously obtained numerical results by comparing them with physical test data. To this end, a three-point bending test is conducted on a 300 mm × 300 mm laminated composite panel. The experimental results are then compared with those obtained from the finite element analysis (FEA) performed using Ansys software, allowing validation of the interlayer's viscoelastic properties and the strength–stiffness characteristics of the chemically toughened (CT) thin glass.

5.1.1 Experiment Preparation

For the preparation of the test specimens for a three-point bending experiment, CT Falcon thin glass sheets (edge manually ground) measuring 300 mm × 300 mm and 0.7 mm in thickness are provided by AGC. In typical three-point bending experiments, glass specimens with a narrow width are preferred, as using glass samples with a 1 : 1 aspect ratio can lead to an imbalanced stress field (CEN, 2016; EN 1288-1; EN 1288-3). However, in this study, the provided glass samples had already undergone tempering, making further cutting or resizing difficult. Consequently, the specimens are tested using their original dimensions as received.

The lamination process is carried out at a LOCA manufacturing facility, TTEC in Bexbach, Germany. Although the initially intended interlayer material, Ködistruct LG, which is the stiffest and highest shear-capacity product within H.B. Fuller | Kömmerling's range and the one used in the numerical simulations in this research, is not available, an alternative material is used. Since this substitute is a not fully commercialised product, it will be referred to in this study as a two-component polyurethane-based LOCA (2K PU LOCA) for clarity and consistency. 2K PU LOCA is a cold-poured, PU-based two-component lamination designed for safety glass manufacturing applications used for construction and automobile (Kömmerling Chemische Fabrik GmbH, n.d.).

Using the provided glass samples, five laminated sandwich panels (0.7–2–0.7 mm composition) are fabricated in help by TTEC and H.B. Fuller | Kömmerling. To secure the liquid polymer in place during the lamination process, the edges of each glass assembly are sealed with 2 mm butyl tape with a stiff core, replacing the VHB tape originally planned in Chapter 4.3.5, prior to injecting the interlayer material. It has been found that residual moisture in VHB, if not properly removed, can react with the PU and form CO_2 bubbles during curing when the LOCA is injected, potentially affecting visual quality. To maintain

consistent thickness and avoid optical issues, butyl tape with a stiff core is used instead. To prevent excessive lateral spreading of the butyl, it is applied around the perimeter of the panel, approximately 2 mm offset from the glass edge (Figure 5.1). Two opposite corners are fitted with inlet and outlet nozzles with plastic tube to allow the cold lamination material to be injected and trapped air to escape. To ensure a uniform spread and bond between butyl tape and glasses, additional glass plates are placed on both the top and bottom surfaces and clamped together for approximately 30 minutes. Once the butyl sealing is sufficiently stabilised, a pre-calculated volume of 2K PU LOCA (considering the 4-5 % volume shrinkage after fully curing) is injected through the inlet nozzle. During this process, the lamination material spreads laterally through the cavity, gradually filling the space while the outlet nozzle, positioned at a slightly elevated level, helps to prevent air bubbles from forming (Figure 5.1). Depending on the size, thickness, and geometry of the panel, the filling and initial stabilisation time could vary. For a 300 mm × 300 mm × 2 mm interlayer volume, the panel is left to cure at room temperature for 24 hours, after which the interlayer exhibits near-final stiffness suitable for handling. To ensure complete curing and stabilisation of mechanical properties, the bending and fracture tests are carried out one week after fabrication. To prevent glass fragments from scattering during fracture tests, a protective film is applied to both sides of each composite panel.

The thickness of the fabricated sandwich panel is measured using a calliper. Minor deviations of up to ±0.1 mm per layer are observed in both the glass and interlayer components, which are considered to result from typical manufacturing tolerances. No visually perceptible thickness differences are detected during measurement, and the panel appears to have been manufactured with a generally uniform thickness across its surface.

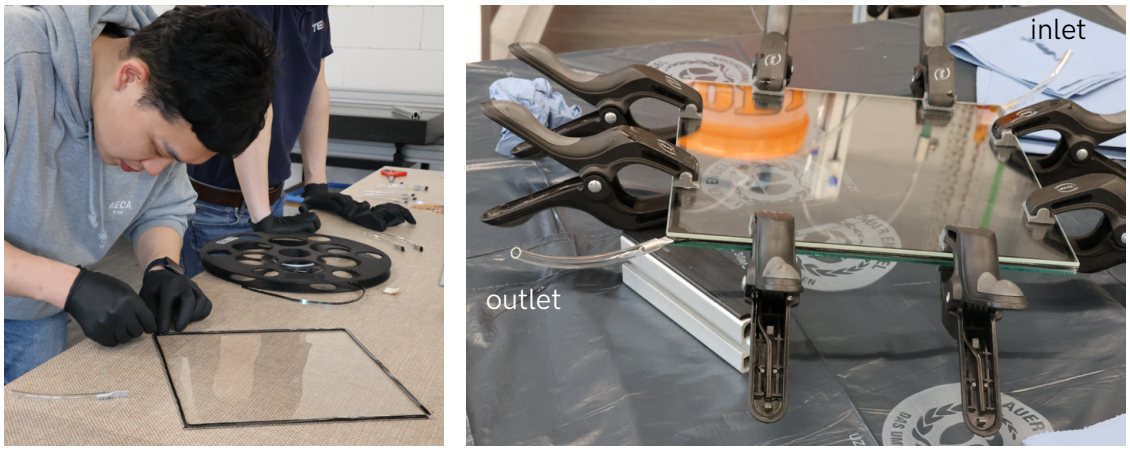

Fig. 5.1 | Flat 300 x 300 mm laminated glass unit manufacturing process
Note. Left: Edge butyl sealing and nozzle placement Right: Setup for LOCA injection

5.1.2 Apparatus Setup

The rig used for the three-point bending experiments is Zwick Z100 machine. Throughout the experiments, applied force, displacement, and time data are continuously recorded. For each laminated glass specimen, two types of tests are conducted: experiment 1 is holding tests and experiment 2 is bending tests until the fracture of the plate. Experiment 1-A

is a stress relaxation test, where the glass panels are loaded until a displacement of 4 mm is reached, the displacement is held in place for 10 minutes before unloading. After completing the holding tests, fracture test experiment 2 (bending test) is performed on the fully recovered panels until fracture. One intact panel is set aside for experiment 1-B to observe its creep behaviour under sustained loading. A load of 1000 N—determined empirically in experiment 2 as inducing significant deformation without causing failure—is applied during which time the creep response is monitored (Table 5.1). After the load is released, the recovery behaviour is visually assessed, focusing on both the speed and extent to which the panel returns to its original state.

Experiment	Number of specimen	Loading rate [mm/min]	Duration [s]	Obtained data
1-A (Stress relaxation)	5 (specimen a-e)	240	600	Reaction force at 4mm displacement
1-B (Creep)	1 (specimen e)	120	300	Creep (strain) at 1000N force
2 (Bending)	4 (specimen a-d)	10	N/A	Bending strength

Table 5.1 | 3-point bending experiment description

Viscoelastic materials are sensitive to both time and temperature, no temperature variation is considered in this study; the laboratory environment is maintained at a constant room temperature of approximately 26 °C and humidity of 49 %. Figure 5.2 illustrates the exper-

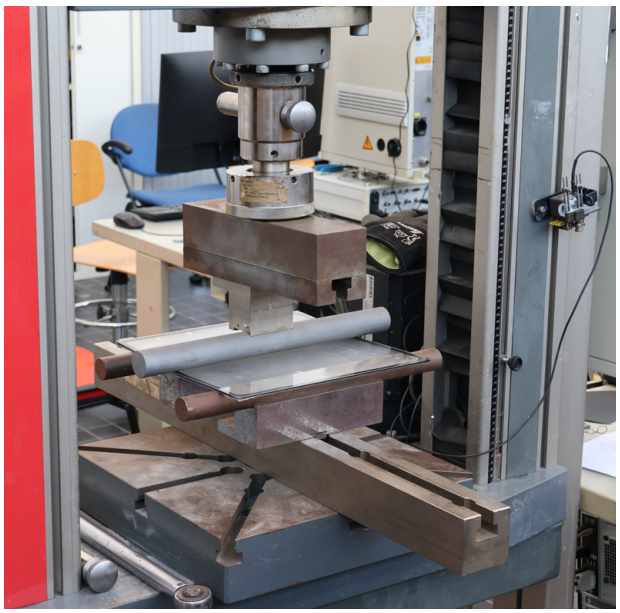

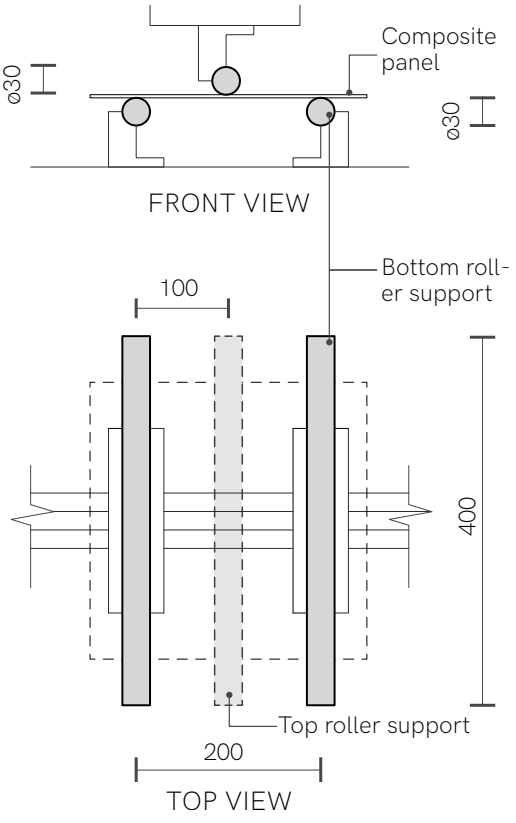

Fig. 5.2 | 3-point bending test rig setup and dimensions

iment setup and dimensions of the rig, including the spacing between the support rollers and the central bending roller. According to EN 1288-3, rubber strips are sometimes used between the specimen and the support rollers to prevent slipping, depending on the specimen size and stiffness. However, in this experiment, they are omitted.

5.1.3 Numerical Model Setting

The experimental results are compared with numerical simulations conducted in Ansys software, where the same experimental conditions are replicated. In particular, the force data obtained over time from the experiments are directly compared with the corresponding numerical results to validate the accuracy of the simulation model. The composite panel is discretised into a solid model consisting of 2,700 elements, with a mesh size of 1 cm and each composite layer is modelled with a single layer of mesh, 3 meshes in total along the thickness. The panel is modelled using Ansys Composite PrepPost (ACP), and as in the previous numerical models, the butyl edge sealing is omitted. The simulation is performed under general gravity conditions and the regions where the rig's supports and the panel are in contact are modelled using frictionless contact conditions. Only the central displacement support is configured to apply displacement over time to induce bending in panel, while the other two supports are fixed (Figure 5.3). Because of the low deformation rate, the analysis uses an iterative stiffness updating non-large deformation simulator. The material properties for each constituent layer of the composite panel are set to their original values, as the fabricated specimens did not exhibit deviations significant enough to warrant theoretical thickness adjustments. These properties are summarised in Table 5.2.

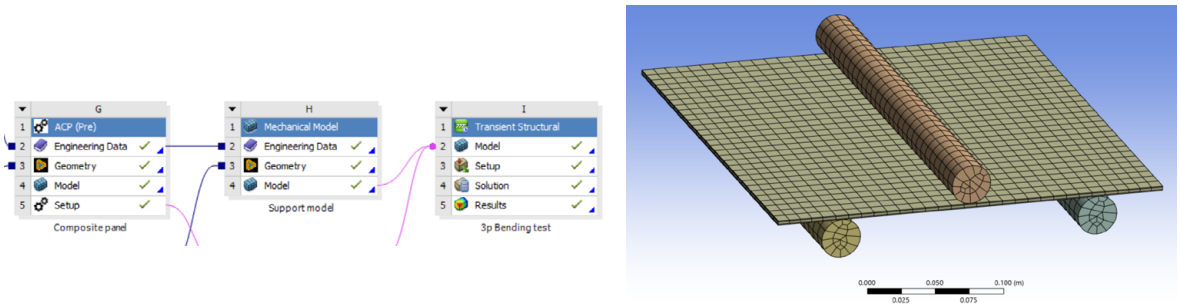

Fig. 5.3 | Numerical setup for 3-point bending test for digital validation model

Part	Material	E [Mpa]	υ	t [mm]	Viscoelasity
Glass layer	Falcon glass	70,000	0.21	0.7	N/A
Lamination layer	2K PU LOCA	E_0=31	0.49	2	Fig. 5.4
Support roller	Structural steel	200,000	0.3	-	N/A

Table 5.2 | Material properties for 3-point bending test input for FEA
Note. Glass sandwich panel meshed with 30x30x3 element configuration, edge seal modelling omitted, contact interface between support rollers and the glass defined as frictionless with stiffness update enabled, and linear analysis (non-large deflection) setting. The E_0 value for the lamination material is not provided by the manufacturer, so the value used here is an estimated approximation based on the supplied material law.

Due to the lack of available material data on the viscoelastic behaviour of 2K PU LOCA, particularly the absence of Prony series parameters, the shear modulus data under varying time and temperature conditions (Appendix 4) is used to manually fit a Prony series at 22 °C (Appendix 5). This fitted data informs the numerical input data that can be used for the simulation (Figure 5.4). The numerical simulation runs at 22 °C, whereas the physical experiment takes place at 26 °C—a difference that would affect the performance output. Therefore, in the subsequent comparison of stress relaxation results, the numerical outputs are compared considering a time-temperature shift approach to enable valid comparison.

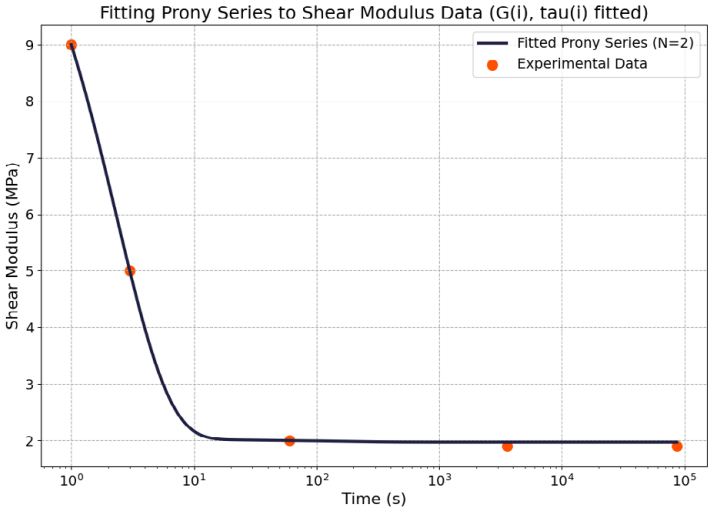

Index [i]	G_i/G_0	τ_i [s]
1	8.4E-01	2.35E+01
2	3.6E-03	1.42E+02

*At temperature 22 °C, G0 = 10.4 MPa

Fig. 5.4 | Fitted Prony series of 2K PU LOCA based on experimental shear modulus data (Experimental data taken from Appendix 4)

5.1.4 Stress Relaxation

Viscoelastic materials exhibit both elastic, spring-like behaviour and viscous flow characteristics. When stress is applied, they respond instantly with an initial resistance while simultaneously undergoing increasing deformation over time. In this experiment, a displacement of 4 mm is applied to the specimen via the upper loading roller within 1 second, followed by a 10-minute holding phase. During this period, an initial reaction force occurs in response to the displacement, which gradually decreases due to the material's viscous nature. Given that the stiffness of the interlayer decreases exponentially with time, a relatively fast loading rate (240 mm/min) is applied to capture the initial stress relaxation behaviour without causing impact force on the plate.

Stress relaxation is measured across five specimens (a–e), and the results are plotted in Figure 5.5 (top), including a graph representing the mean. Overall, the five specimens show consistent trends: the initial reaction force reaches approximately 190 N within the first few seconds, then gradually decreases and stabilises around after roughly 100 seconds at the reaction force of 160 N. From 200 seconds onwards, minor periodic fluctuations are observed. These may result from the limitations of the Zwick Z100 machine in accurately logging small forces generated by low displacement. The Zwick Z100 is primarily designed for

testing larger specimens and materials such as concrete or metal, which normally require stiffer specimens and higher loads that can be up to 100 kN. Its internal components are comparatively heavy, requiring significant baseline force to maintain equilibrium. This may limit its ability to capture low-magnitude reaction forces with high precision.

Figure 5.5 (bottom) compares the experimental mean curve with the numerically simulated model. Both exhibit an overall exponential decay pattern, and beyond the 100-second

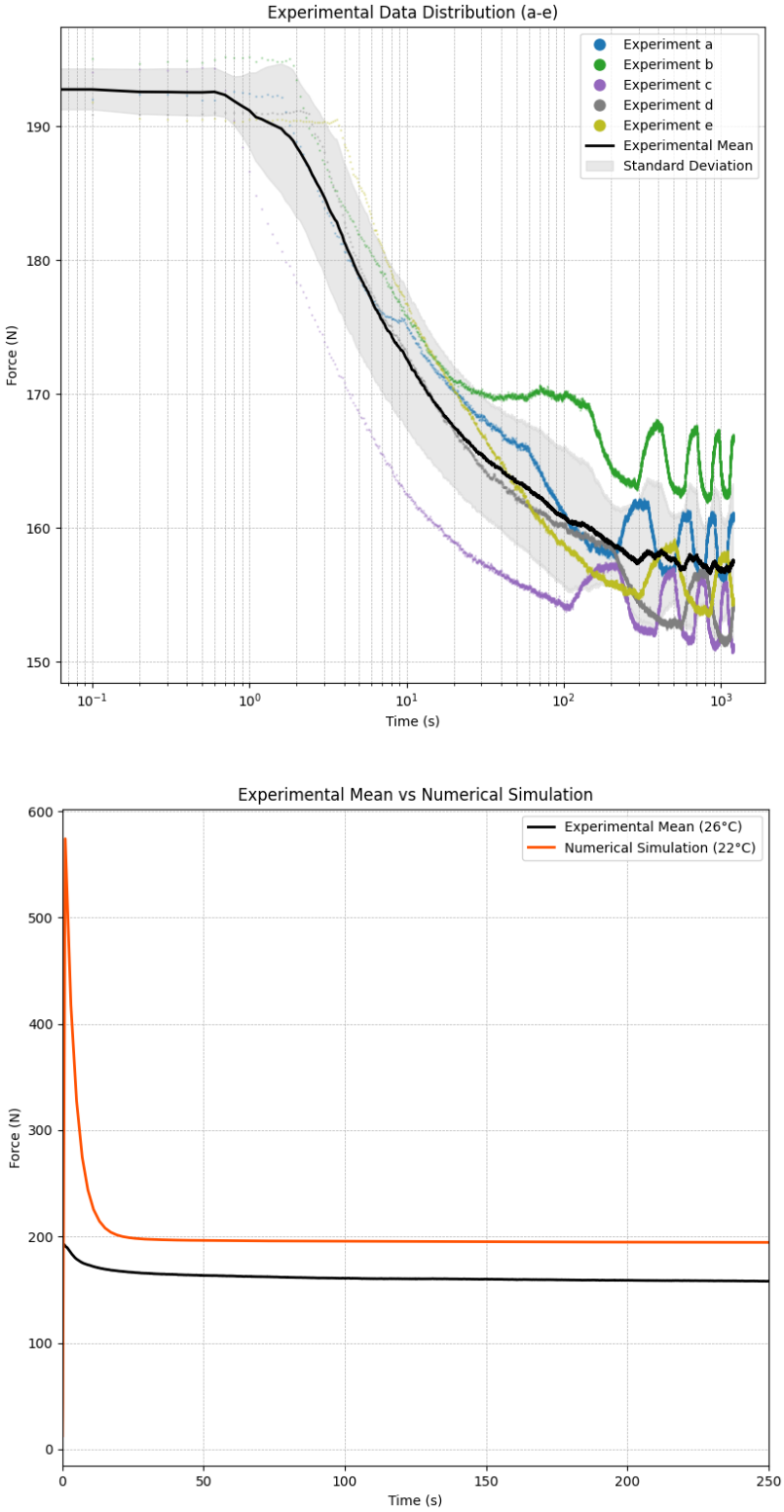

Fig. 5.5 | Stress relaxation test result
Note. Top : Experimental data Bottom : Numerical result vs. experiment mean

mark, the simulated and experimental curves show a difference of approximately 30 N. Although insufficient data is available to derive a reliable time-temperature shift function for converting the 22 °C numerical simulation to match the 26 °C experimental condition, the expected effect—molecular acceleration leading to faster relaxation—is likely to shift the numerical curve leftward along the time axis. This supports the qualitative agreement between the two curves.

A significant deviation in the initial reaction force primarily results from the temperature discrepancy between the experimental and numerical conditions. If the simulation is run at 26 °C, which corresponds to the laboratory environment, the curve is likely to shift leftward along the time axis, thereby reducing the observed gap. The remaining discrepancy appears to arise from limitations in the measurement equipment in the test. After the interlayer stiffness stabilises, the numerical model shows a deviation of approximately 19 % from the experimental results. This difference is attributed to a combination of factors: the mismatch in ambient temperature between simulation and experiment, measurement equipment limitation, minor variations in the actual thickness of the glass and interlayer materials compared to the numerical inputs, and uncertainty in the mechanical properties of the 2K PU LOCA product. Because the Young's modulus and Poisson's ratio are estimated, and the Prony series is fitted from a few experimental data, the model exhibits slightly stiffer behaviour than the actual laminated panel. However, the viscoelastic behaviour of the interlayer is captured which supports the feasibility of the numerical analysis method used in this study, particularly in modelling time-dependent interlayer responses.

5.1.5 Bending Strength

In three-point bending, glass, as a homogeneous and isotropic material, is the most stress-sensitive component of the composite panel. The maximum flexural stress occurs at the bottom surface of the bottom glass layer, which corresponds to the location where shear stress is zero and normal stress reaches its maximum. At this point, the maximum principal stress is equal to the flexural stress, particularly along the upper bending roller support.

For specimens *a* to *d*, Z-direction displacement is applied at a constant rate of 10 mm/min until failure. The corresponding force is recorded by the testing software. The recorded reaction force values are plotted against displacement (Z) in Figure 5.6. In all four specimens, failure occurs when the maximum force reaction exceeds 1100 N and 28 mm displacement. The bending simulation in the numerical model is shown in Figure 5.7. When compared with the experimental results, the numerical model exhibits a slightly steeper force-displacement curve, indicating that it assumes a stiffer response than the actual physical specimen. This observation remains consistent with the findings from the stress relaxation test in Section 5.1.4, reinforcing the overall reliability of the experimental outcomes. This discrepancy in real experiment and the numerical model partially arises from the difference in temperature conditions: the numerical simulation is conducted at 22 °C, whereas the experiment is carried out at 26 °C. Due to the viscoelastic nature of the interlayer, higher temperatures

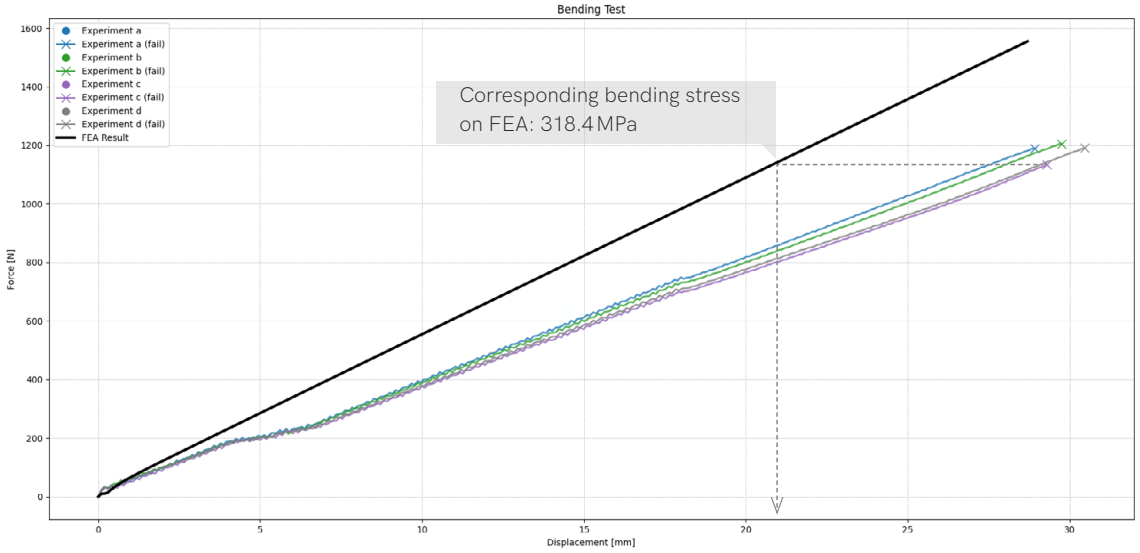

Fig. 5.6 | Bending strength results

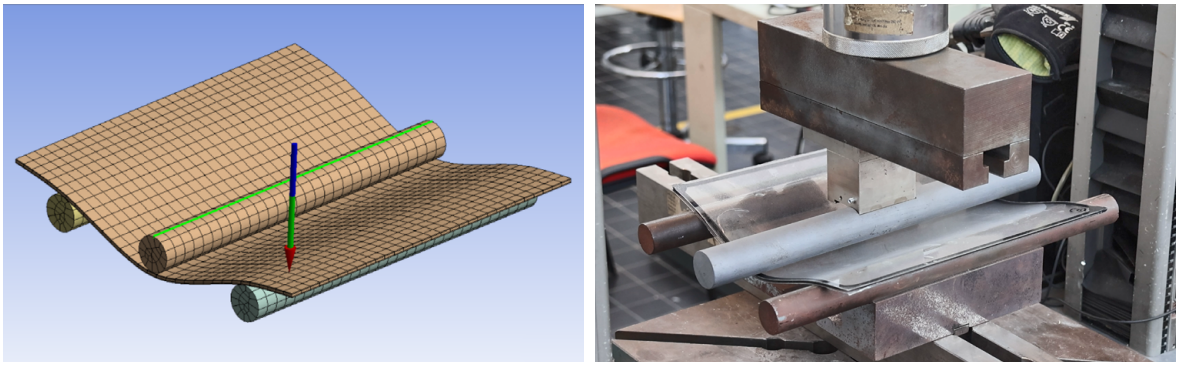

Fig. 5.7 | Bending geometry comparison between numerical model and real testing

reduce stiffness, which accounts for the softer response observed in the physical test. Although the interlayer stiffness gradually stabilises over time—leading to a convergence in mechanical behaviour between the simulation and experiment—the force-displacement slopes do not ultimately align. As a result, it remains difficult to conclude that the numerical model achieves a high level of accuracy in replicating the physical behaviour under these conditions. In the experimental data, several anomalies are observed. Slight slipping of the glass plate on the 3-point bending machine support causes small variations in slope (at 5 mm displacement), and large deflections appear to slightly reduce the apparent stiffness as the test progresses. By contrast, the numerical model used to validate the experiment is based on a linear analysis, resulting in a more uniform slope. Initially, the model matches the experimental stiffness quite well, but over time, deviations become more apparent due to the model's inability to capture geometrical non-linearity and time-dependent viscoelastic effects.

To conservatively estimate the bending stress at failure, Figure 5.6 shows a comparative analysis where the experimentally observed failure force from specimen *c* is mapped onto the numerical displacement axis. Assuming failure occurs at a displacement of 21 mm, the

corresponding bending stress computed from the numerical model is 318.4 MPa. Although this value is slightly lower than the 330–350MPa bending strength range reported by Zaccaria et al. (2022) for Falcon Glass, it is still in reasonable agreement, further validating the overall fidelity of the model within the limitations of the current setup.

Figure 5.8 illustrates the fracture patterns resulting from bending-induced failure. Fractures initiate at the bottom surface of the lower glass layer, where maximum flexural stress occurs. Specifically, they originate at both ends where the central support line intersects the glass, indicating stress concentrations near the contact points with the outer bending rollers. This observation supports the notion that micro-cracks tend to appear more frequently near the panel edges, where stress-relief mechanisms are less effective than within the central area, making crack nucleation more likely. Additionally, the regions where crack propagation initiates are located in close proximity to the edge seal, suggesting that the presence of the butyl and the core material may have some influence on fracture behaviour. However, this aspect is not investigated in detail within the scope of this study..
Although many literature (Rammig, 2022) describes chemically strengthened (CS) glass as typically breaking into large shards, the experimental results here reveal a different behaviour. When the total residual stress due to bending becomes significantly high, the release of energy upon failure produces a fine fracture pattern with small shards, as also observed by Galuppi & Riva (2024).

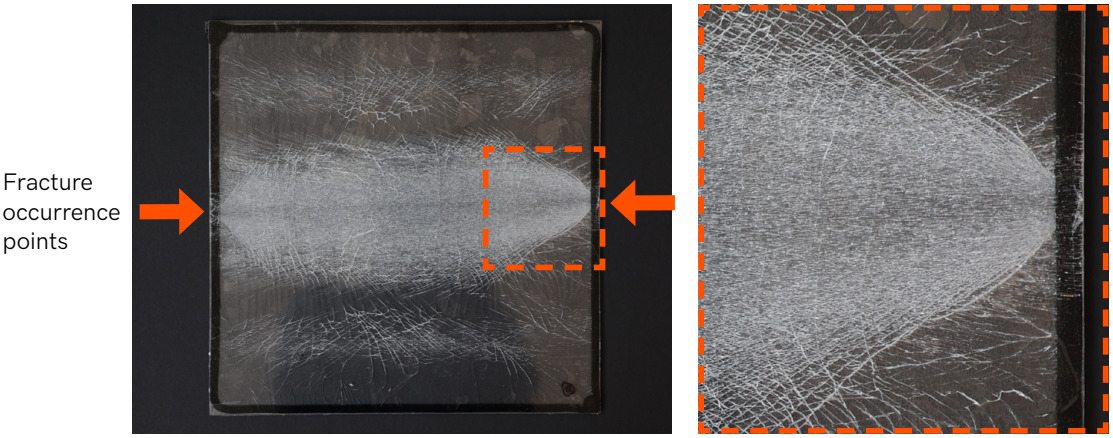

Fig. 5.8 | Fracture pattern of specimen a panel

5.1.6 Creep Behaviour

Experiment 1-B functions as a creep test, where a large displacement force—previously identified empirically in experiment 2—is applied (1000 N at a rate of 120 mm/min at 26 °C) to observe how the panel behaves under sustained load. This test closely resembles the creep behaviour of the panel under consistent snow load conditions. Figure 5.9 shows the time-dependent displacement curve of specimen e over a 5-minute period. Due to the viscoelasity of the interlayer, the curve follows a logarithmic trend, with rapid displacement occurring in the early phase, followed by a gradual reduction in creep rate. Around 100 seconds, the displacement begins to stabilise, approaching an approximate plateau of 26 mm.



Fig. 5.9 | Creep test result

After unloading the central support, the panel's response is observed. Immediately upon load removal, the panel springs back almost entirely to its original flat state, visibly resembling the recoil of a mechanical spring. A small residual deflection remains, which is likely due to the viscous component of the interlayer, preventing full recovery to the initial geometry (Figure 5.10).

This experiment also serves to validate the numerical model presented in Chapter 4.3.8, which predicts a pronounced spring-back effect occurring within the first few seconds after load removal.

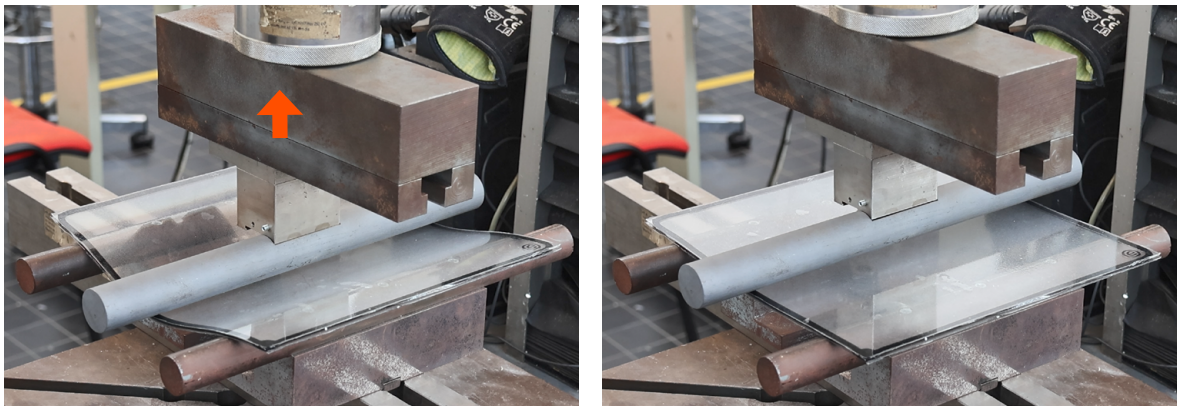

Fig. 5.10 | Spring-back effect observation
Note. Time interval between two images is 4 seconds.

5.2 Panel Prototyping

5.2.1 LOCA Manufacturing for Curved Geometry

In contrast to the 300×300mm laminated flat panels with LOCA, several challenges arise when attempting to create an 800×800 mm double-curved panel. While a method involving the use of front and rear supporting glass is employed to prevent bulging of the panels, the

irregular geometry and increased panel size in the double-curved case cause the interlayer cavity spacing to become unequal. As a result, the self-weight of the materials and the injected viscous LOCA can cause change in the thickness of the interlayer. This issue is particularly problematic as it directly affects surface reflection quality.

Additionally, when the interlayer is in a liquid state during cold deformation, gravity causes the liquid to migrate from the highest point towards the lower regions (hydrostatic pressure) which is caused by the curved geometry, hindering LOCA to stay in place (Figure 5.11 - left). To address this, in collaboration with engineers from TTEC and Kömmerling, a method is devised where the interlayer is allowed to cure to until a gel-like state, similar to jelly, where the viscosity and self-fluidity due to gravity has largely disappeared, without any cold deformation in a flat state. This approach ensures that the interlayer material's movement is minimised, while still maintaining a liquid core capable of minimising shear stress within the system. To determine the curing time for the appropriate viscosity for this gel-like state, a sample specimen with the same section build-up as the target panel has been prepared, with a 2 mm cavity filled with 2K PU LOCA. The viscosity of the material has been observed over time (Figure 5.11 - right). After three hours, the LOCA exhibits a gel-like consistency, and it has been decided to proceed with the cold deformation process after this 3-hour curing period at a flat state.

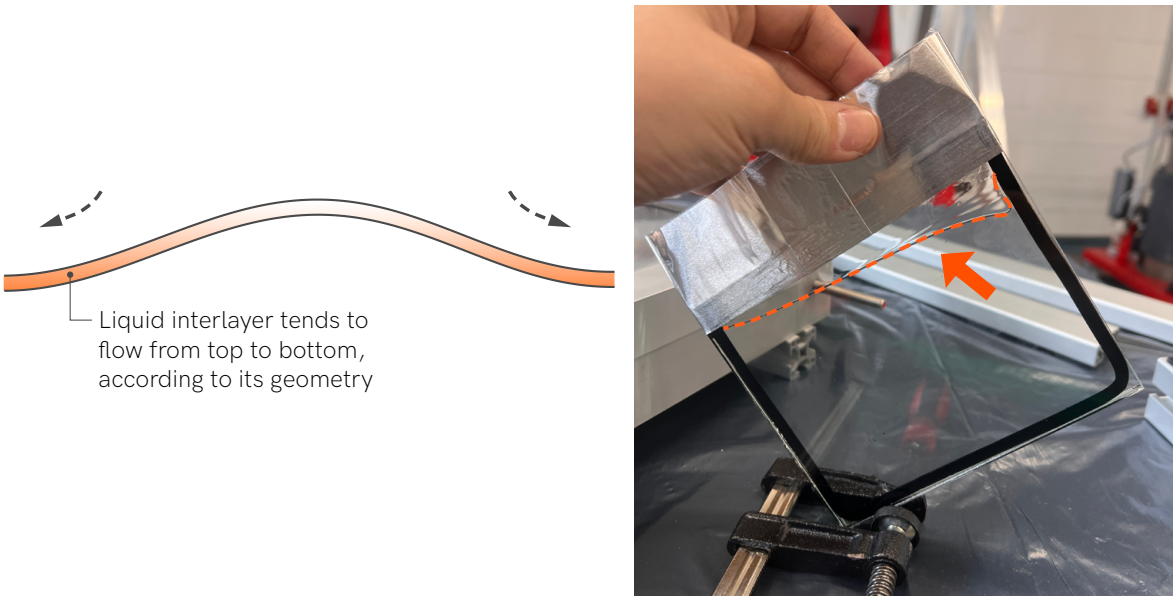

Fig. 5.11 | Finding appropriate intermediate viscosity state to solve hydrostatic pressure problem

5.2.2 Development of Buckle Bending Device

To realise the intended sinusoidal shape, it is crucial to prevent out-of-plane rotation at the edge fixings. However, due to the high residual stresses induced by the large curvature deformation, it is observed that rotation occurs at the support edges, leading to a tendency for the geometry to deform more into a single continuous curve with less curvature. Although the manufacturing of support profiles using rectangular aluminium pipes embedded with POM inserts proves to be effective because the perpendicular relationship between

frame and threaded rod is well maintained, out-of-plane deformation is still observed, on the threaded rod itself, causing the overall geometry to flatten into a reduced curvature (Figure 5.12). To overcome this issue, a method involving the attachment of a U-profile cap guides to the ends of the support fixtures is proposed, to assist prevention of out-of-plane rotation during the buckling process. Given the constraints on available materials, an alternative approach is adopted by installing additional aluminium profile guides at the rear side of the edge supports in perpendicular direction.

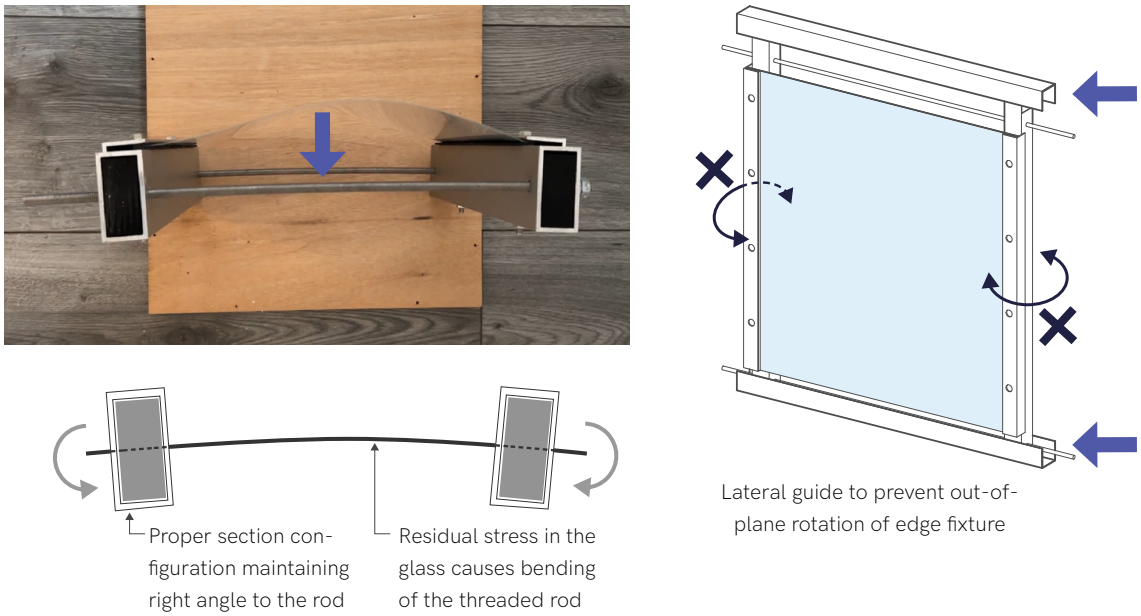

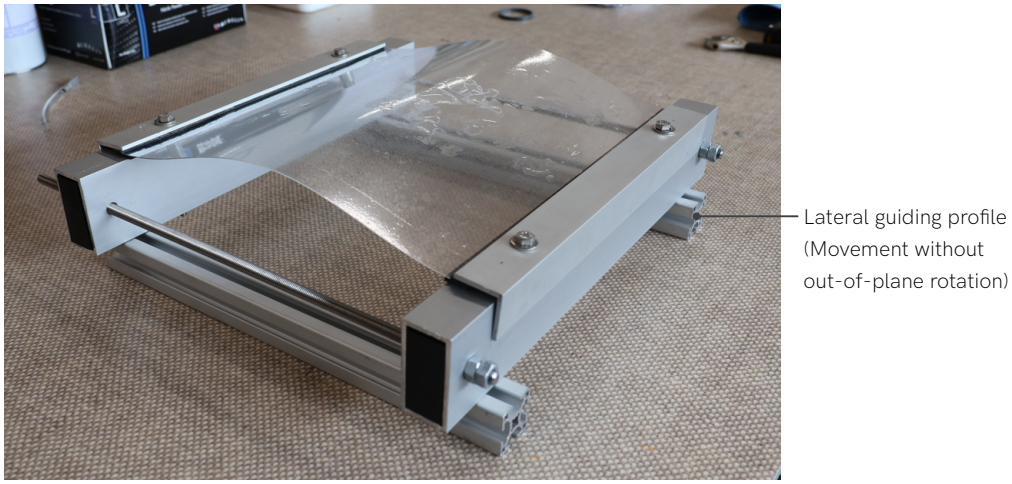

Fig. 5.12 | Out-of-plane rotation problem and lateral guide as solution

It is noted that if the L-shaped edge fixture profiles are not rigidly bolted to the main frame, rotational deformation could occur. Since the entire buckling device is constructed from aluminium, a small degree of flexural deformation within the apparatus is inevitable, making it challenging to replicate the idealised boundary conditions (fully restricted edge condition) modelled in the FEA simulations.

To guide the sagging of the glass panels and promote the correct upward buckling direction

during cold deformation, either auxiliary supports are placed beneath the glass or manual force is temporarily applied to introduce an initial imperfection into the composite panel. Once tension rods are slightly tightened, the manually applied force can be removed, as the induced imperfection is sufficient to direct the buckling in the desired direction.

Following the injection of the interlayer material and the completion of cold bending, slight separation of the butyl tape is observed near the edges around the highest curvature. This occurs while the core layer remains in a viscous, uncured state. To prevent delamination during the curing stage, adhesive tapes are pre-applied to critical edge regions prior to the injection of the interlayer material as part of the final manufacturing process (Figure 5.13).

While the buckling mechanism relies on adjusting two threaded rods to control edge displacement, it is observed that buckling one end first and then adjusting the other to compensate the displacement could induce unintended higher curvatures due to its antisymmetry. Therefore, to achieve equal displacement along the edges and to form a balanced buckling shape, it is essential to tighten both rods simultaneously at a consistent speed (Figure 5.14).

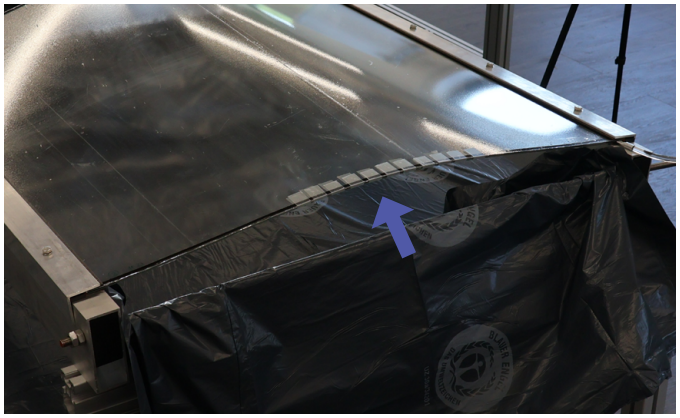

Fig. 5.13 | Adhesive tape application on critical delamination points

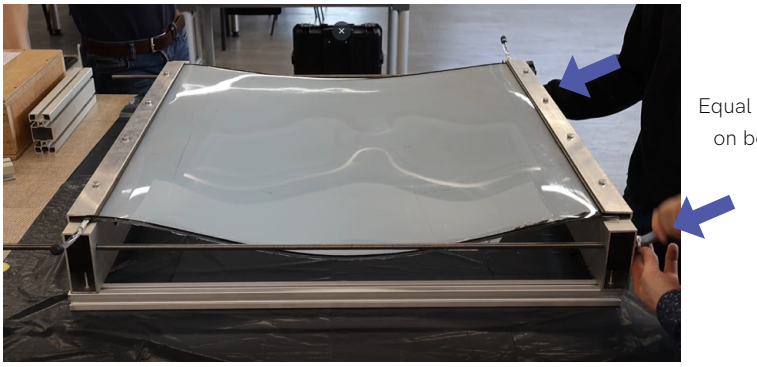

Fig. 5.14 | Simultaneous threaded rod tightening for equal displacement

During the cold buckle bending process, the composite panel failure occurs even before the expected deformation is achieved. Upon investigation, the origin of the fracture is traced to the contact point between the setting block (POM) and the glass, specifically at the point

where the penetrating bolt makes direct contact with the glass edge (Figure 5.15). As a preventive measure, a 2 mm thick thin strip of VHB tape is added on the setting block to ensure that the bolts never come into direct contact with the glass. This acts as a secondary safety buffer, providing additional protection to prevent edge-induced failure during cold buckling. The final buckle bending machines are illustrated in Figure 5.16.

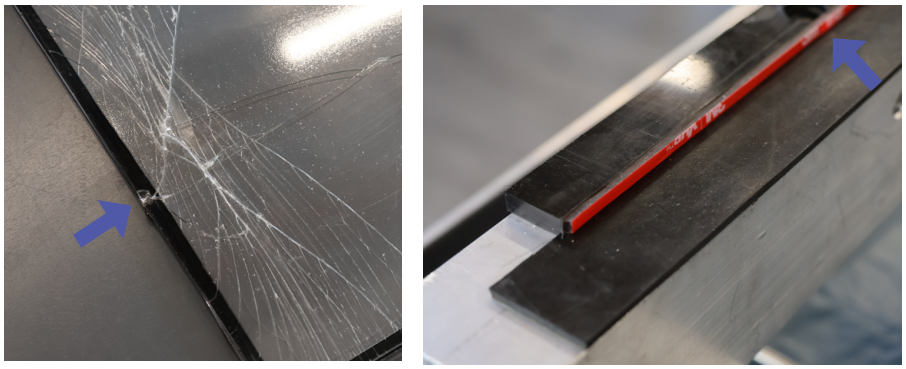

Fig. 5.15 | Propagation point and additional safety tape to prevent contact between glass & bolts



Fig. 5.16 | Final glass buckling devices without displacement guides

5.2.3 Sinusoidal Half Paraboloid Cold Buckle Bending

A total of three final prototypes are produced using the prepared buckling devices. Aware of the risk of glass fracture during cold buckling, each panel unit is fabricated with progressively increasing displacement to minimise the likelihood of failure. After establishing the buckling direction through initial tension, Step 1 deformation is applied with a uniform displacement of 3 mm, followed by asymmetric tightening of a single thread to induce greater displacement at one free edge. The resulting displacements for the three panels are 16 mm, 21 mm, and 23 mm, respectively, and are hereafter referred to as Panel A, B, and C, as summarised in Table 5.3.

Although the optimised sandwich panel extracted in Chapter 4.1 requires a 26 mm in-plane

displacement on one edge for full validation, Panel C concludes just short of this target (Figure 5.17). Nevertheless, the fabricated geometries closely resemble the numerical results in form. Based on fabrication experience and the material's observed behaviour, it is cautiously anticipated that the glass could have withstood the full 26 mm displacement if additional test specimens had been available.

Panel	In-plane disp.$_{max}$ [mm]	In-plane disp.$_{min}$ [mm]	Remark
Panel A	16	3	-
Panel B	21	3	Threaded rod is bent more than the other panels
Panel C	23	3	Close to the desired geometry

Table 5.3 | Sandwich panel prototypes with sinusoidal half paraboloid geometry

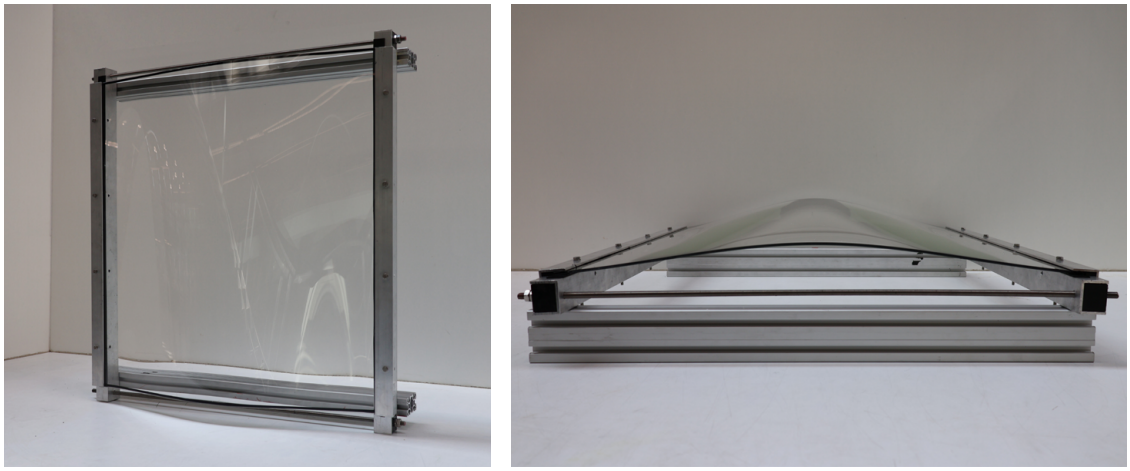

Fig. 5.17 | Panel C with 23 mm in-plane displacement

With the fixture still in place, Panel B exhibited greater bending at the threaded rod compared to the other two panels, resulting in a relaxed sinusoidal geometry that did not fully align with the theoretical form. The cause is identified as a loosened guide intended to prevent out-of-plane rotation of the edge support, which failed to function as intended.

5.2.4 LOCA Cold Buckle Bending Surface Quality

During the LOCA injection and cold buckle bending process, no visible bubbles or optical flaws that could cause visual distraction are observed within the interlayer. After a full two-week curing period, an optical qualitative assessment is conducted to evaluate surface quality. None of the three specimens shows any optical flaws attributable to the curing process, and no haze or other clarity-reducing effects are detected.

Reflected and refracted images on the glass surface are directly influenced by surface curvature. In Figure 5.18 left, the curvature observed in the horizontal line of the fixture jig through Panel C is caused by the double curvature of the geometry. As the central centreline

forms anticlastic curvature symmetrically to each side, the repeated rippling sinusoidal pattern appears as a natural outcome of the geometry. These phenomena do not indicate cold bending distortion, but rather represent inherent optical effects of viewing double-curved surfaces. The degree of image distortion varies depending on the viewer's position, with distortion typically increasing when viewed from oblique side angles (Figure 5.18 right).

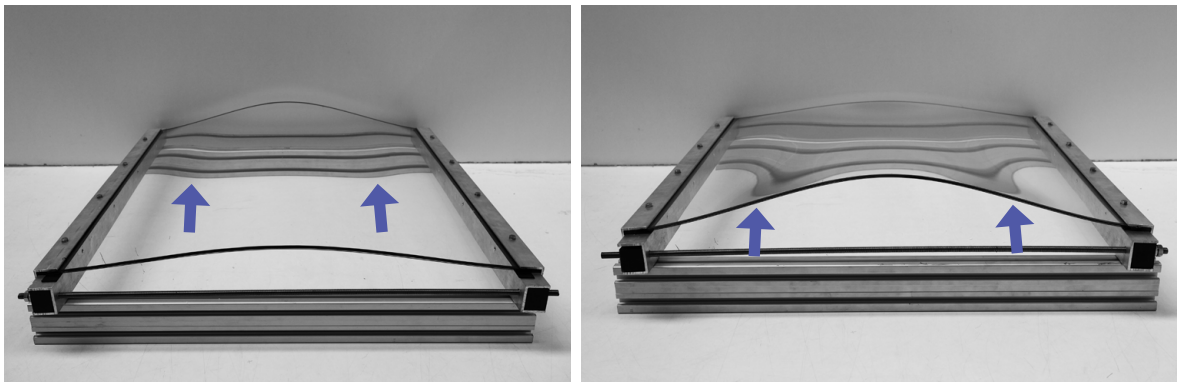

Fig. 5.18 | Refraction effects induced by double curved geometry in Panel C

The qualitative assessment focuses on two criteria: first, whether the G2 continuity (continuously varying curvature) discussed in Chapter 4.2 is achieved in the fabricated sandwich panel; second, whether cold bending distortion occurs during the cold buckle bending process.

G2 continuity is verified by observing that the reflected and refracted images remain continuous and connected (Figure 5.18). To evaluate cold bending distortion, a comparison is made between the ideal surface generated from the theoretical surface generation principle and the actual surface geometry obtained through cold buckle bending. Using the *Zebra* tool in Rhino, Figure 5.19 illustrates this comparison. The ideal surface shows smoothly changing curvature and stripe thickness, whereas the cold-bent geometry (result of cold buckle bending simulation in FEA model) reveals abrupt changes in curvature, irregular variations in stripe thickness, and with more frequent sinusoidal ripples. These indicators suggest the presence of cold bending distortion.

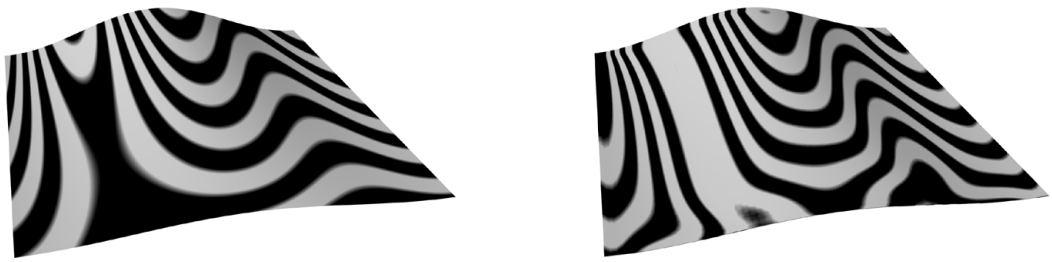

Fig. 5.19 | Computational comparative line test analysis of theoretically generated and FEA-simulated cold-bent geometries

Note. Left: Theoretically generated cold-bent geometry Right: FEA simulated cold-bent geometry

In Figure 5.20, a surface quality assessment is conducted on the fabricated Panel C by observing the refracted image through the transparent glass, positioned to closely match the

location used in the computational line test. Qualitative evaluation does not reveal any severe cold bending distortion. However, minor rippling (i) and subtle irregularities in curvature transitions (ii) are observed in a localised area (iii).

The fact that these cold bending distortions appear in regions where the numerical model predicts abrupt transitions between synclastic and anticlastic curvature suggests that some aspects of surface quality can indeed be predicted at the computational stage. Nevertheless, the degree of distortion observed in the physical panel appears less visually disruptive than what is indicated in the computational line test. This difference is likely attributable to two factors: first, the interlayer undergoes molecular rearrangement during the curing phase, relieving part of the internal stress; second, the physical cold buckle bending apparatus does not fully constrain the out-of-plane rotation of the edge supports as rigidly as

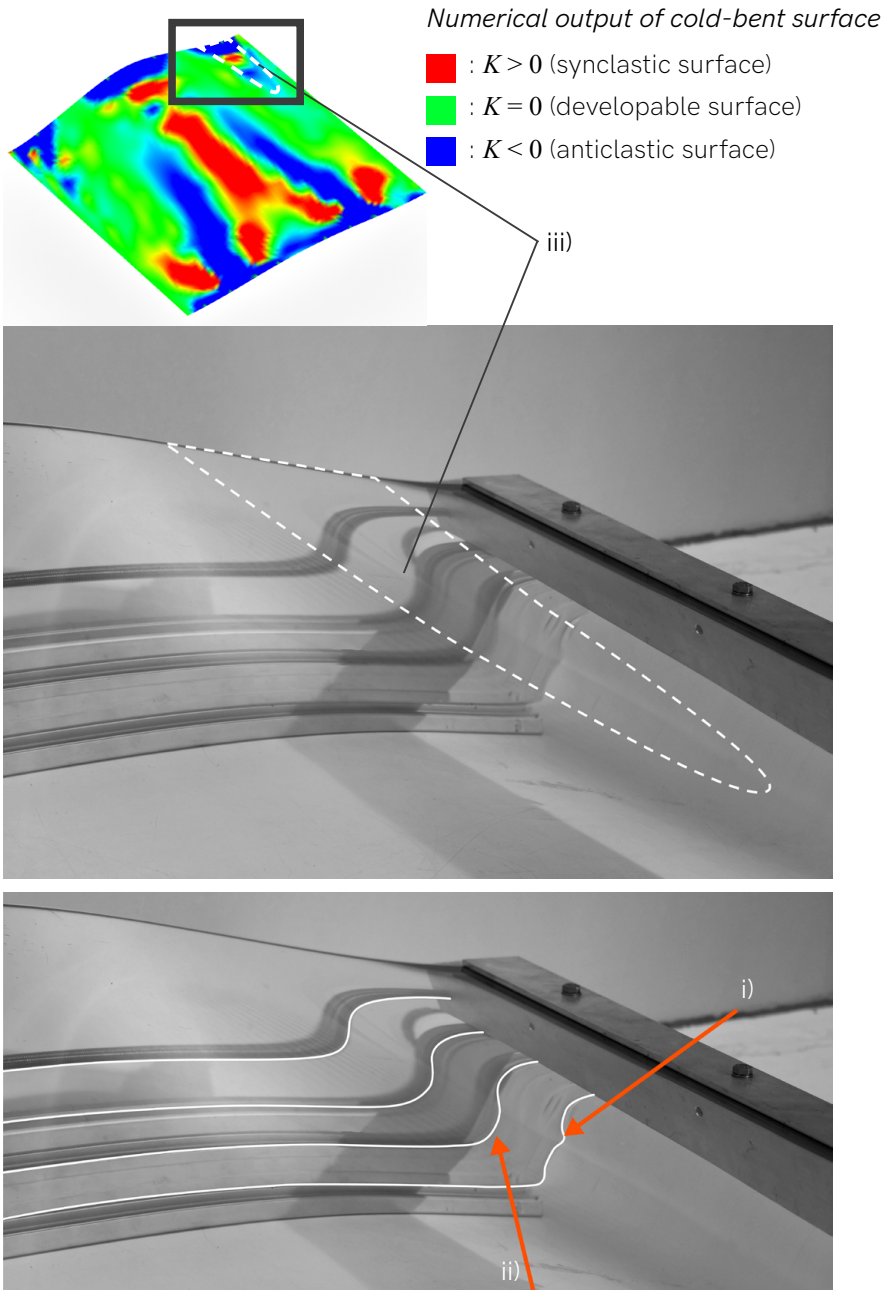

Fig. 5.20 | Cold bending distortion in Panel C
Note. i) Rippling distortion ii) Irregular curvature transition iii) Area of rapid change in curvature

the numerical model assumes. As a result, the actual in-plane stress imposed on the panel is likely lower than in the simulated scenario, contributing to the reduced level of observable distortion.

5.2.5 Sinusoidal Half Paraboloid Light Reflection

A qualitative analysis of light reflection on the double-curved surface is conducted using Panel C while it remains fixed in the buckle bending fixture. As shown in Figure 5.21, the convex surface of the panel is positioned facing upward, with the higher-curvature edge oriented farther from the light source. Electric lighting is used to illuminate the panel from a middle right-to-left trajectory, gradually shifting the angle of incidence across the surface. The analysis reveals that reflected light consistently forms two distinct, bright streaks near each lateral edges, where the edge fixtures grip the panel. When light is incident at approximately 45 degrees from the side, the reflection contour becomes particularly sharp, forming a clear sinusoidal shape. As the angle of incidence moves further toward the side of the panel, the reflected light spreads more broadly across the surface, indicating that the angle of incoming light significantly affects the spread and clarity of the reflection pattern.

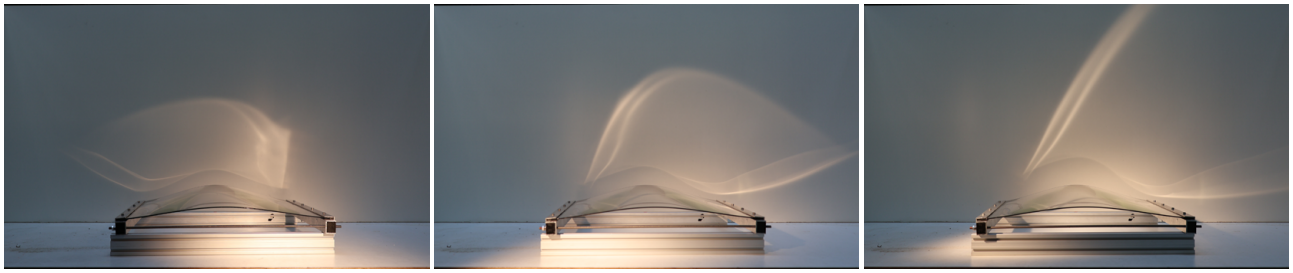

Fig. 5.21 | Reflected light trajectories on Panel C at varying angles of incidence

A qualitative observation under natural daylight is conducted to examine the appearance of both reflected and transmitted light with Panel C. When the convex side of the panel faces the light source and is positioned nearly perpendicular to the incoming light, the reflected light appears dominant, and no significant characteristics are observed in the transmitted light. However, in Figure 5.22, when the light source enters from a lateral angle, the inten-

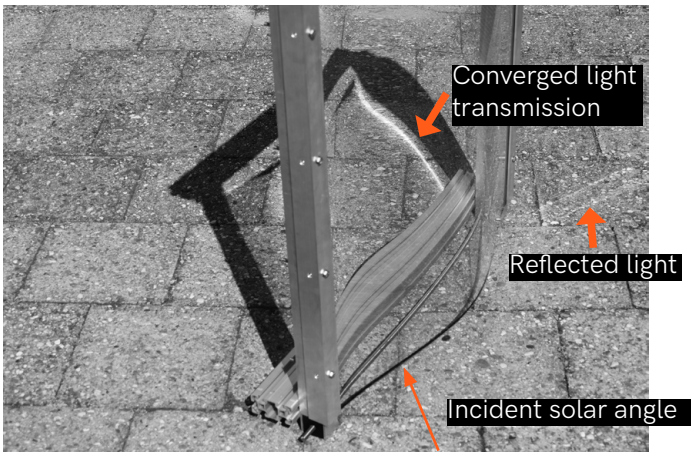

Fig. 5.22 | Reflection and converged light transmission under lateral daylight incidence

sity of the reflected light decreases notably. In contrast, the transmitted light shows a distinct phenomenon: near the edge supports, linear light convergence occurs, forming visibly bright zones where light concentrates through the panel.

5.2.6 LOCA Cold Buckle Bending Spring-back

In Chapter 4.3.8, a computational simulation is conducted to evaluate the spring-back behaviour of a sinusoidal half-paraboloid glass panel under a maximum bending stress of 168 MPa. Upon removal of the fixture, the simulation records a spring-back of approximately 17 %, measured as the degree to which the out-of-plane deformation at the most displaced point returns toward the original flat configuration once the constraints are released. To validate the real spring-back effect of the fabricated panel, Panel B is tested by removing its edge fixtures. The maximum Z displacement before and after fixture removal is measured manually using a ruler, and the percentage change is calculated to assess how much of the deformation recovers due to spring-back. Table 5.4 summarises the comparison between the experimental results and a digital twin model adjusted to match the cold bending geometry to Panel B, while maintaining other simulation condition as Chapter 4.3.8. This comparison provides insight into how accurately the simulation predicts post-fabrication deformation behaviour under real-world constraints.

Experiment Type	Measurement time after fixture removal [s]	Z disp.$_{max}$ before releasing fixture [mm]	Z disp.$_{max}$ after releasing fixture [mm]	Recovery ratio [%]
Panel B	≈ 300	78.8	71.8	8.9
Digital twin 2K PU LOCA	290	80.9	60.6	25.1
Digital twin Ködistruct LG	310	80.9	67.3	16.8

Table 5.4 | Comparison of geometry recovery due to spring-back: Real panel vs. digital twin

The edge support removal experiment is conducted under ambient indoor temperature conditions. Although Panel B uses 2K PU LOCA as the interlayer material, the mechanical behaviour defined in the FEA model is based on Ködistruct LG, due to the lack of reliable material property data for 2K PU LOCA. Therefore, the results from two separate FEA models, one using the properties of Ködistruct LG and the other approximating 2K PU LOCA, are compared with the experimental outcome.

The physical experiment records the lowest recovery ratio at 8.9 %, indicating that the panel maintains most of its cold-bent geometry after support removal. This is notably lower than the spring-back predicted by the 2K PU LOCA-based numerical model, which shows a 25.1 % recovery, and the LG-based model, which shows a recovery of 16.8 %. The experimental result supports the feasibility of the simulation approach, as it aligns closely with the recovery ratio of 17 % previously introduced in Chapter 4.3.8.

Compared to the numerical predictions, the physical panel exhibits a significantly smaller spring-back, maintaining more than twice the geometric displacement. This favourable result is likely due to two factors: first, the edge support condition in the physical setup is less constrained, allowing stress relief; second, viscoelastic stress relaxation occurs during the interlayer curing period, reducing residual stress and thus lowering the driving force for spring-back.

Figure 5.23 presents a qualitative comparison of Panel B before and after the removal of the edge fixture. The left image shows the panel in its fully constrained state, while the right image captures the panel approximately 5 minutes (300 seconds) after fixture removal. Although the recovery ratio remains below 10 %, indicating that a significant portion of the out-of-plane displacement is retained, it is visually evident that the sinusoidal curvature across the glass cross-section has noticeably relaxed. This suggests that while the global form is largely preserved, local concave-convex transition points relaxes upon spring-back.

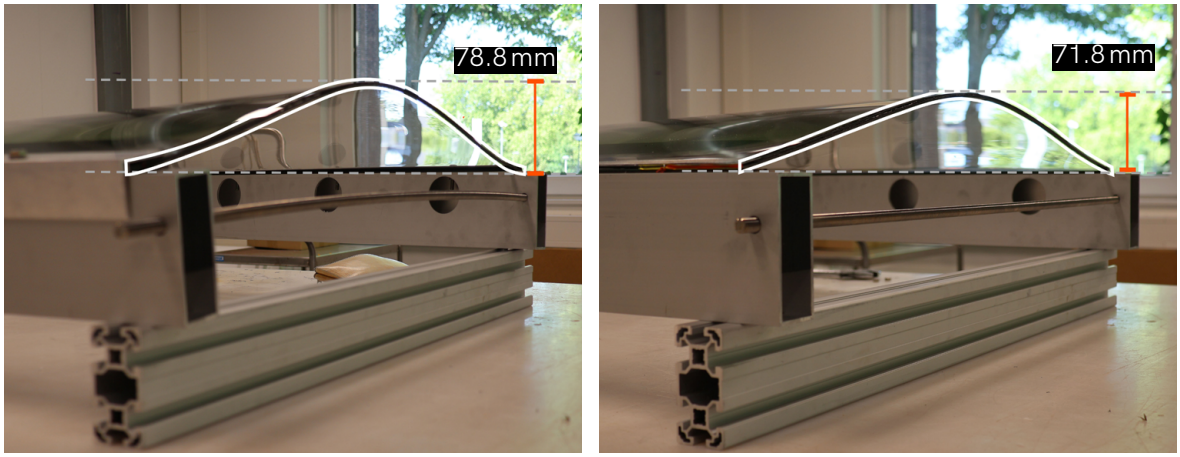

Fig. 5.23 | Panel B geometry before and after spring-back
Note. Left: Before fixture removal Right: After fixture removal (approx. 300 s)

5.3 Solar Design Validation Experiment

While ceramic-fritted glass is commercially manufacturable, the customised production process, particularly for unique frit patterns, involves high cost and multiple processing steps. For this reason, sample fabrication including the ceramic frit was not available within the scope of this research. As a result, it was not possible to directly assess the absolute solar performance of the designed roof unit using fully processed ceramic-fritted glass. Instead, an experimental test is conducted using a single cold-bent roof unit that resembles the sinusoidal half paraboloid geometry of the newly designed OWO roof made from plexiglass (PMMA), to which a clear printable adhesive vinyl with frit pattern is applied (Table 5.5). This setup allows for the observation of how transmittance varies according to the frit design, under controlled indoor lighting conditions. The main purpose of this experiment is to verify through actual experiments whether the optimised frit pattern in this study per-

forms better than the non-optimized design and to check the accuracy of the numerical model.

5.3.1 Experiment Preparation

The same buckle bending device is also employed as the fixture for the roof unit in this test. A plexiglass measuring 800 × 800 mm and 2 mm in thickness is used as the base panel. The difference in solar transmittance between the actual laminated glass panel and the test panel is summarised in (Table 5.5), which compares the transparent (non-fritted) regions. For the actual glass unit transmission value, calculation from Table 4.10 has been used. For PMMA and clear adhesive vinyl (PVC), for which exact data from the manufacturer is unavailable, data is estimated using a comparable product (Evonik Industries AG., 2013; Solar Screen International S.A., 2019). As the experiment is logging visible light transmittance data, comparison is based on visual transmittance (T_{vis}). For the experimental panel, the overall T_{vis} is approximated by multiplying the individual transmittance values of each layer. Although composed of different materials, the experimental panel is designed to achieve an equivalent total visible light transmittance to the actual laminated glass panel, thereby enabling valid comparison of optical behaviour under controlled lighting conditions.

Panel type	Build-up	T_{vis} [%]
Actual design panel	1.1 - 2 - 1.1 mm (G (frit) - L - G)	≈ 82
Experimental panel	2 mm (Plexi G - frit PVC)	≈ 82 (91 % x 90 %)

Table 5.5 | Transmittance comparison between actual glass panel and experimental panel
Note. G stands for glass, L stands for lamination, and transmittance value referring to the transparent part of the fritted panel unit.

The frit pattern applied to the panel follows a similar optimisation strategy developed in earlier chapters, using Grasshopper Honeybee for analysis-based design. The solar position used for the incident radiation analysis corresponds to June 1st at 10:00, 11:00, and 12:00 (Figure 5.24). While June 21st marks the actual summer solstice, June 1st is selected as a representative early-summer date to reflect peak solar conditions around midday, when the angle of incidence is nearly perpendicular to the roof surface. This setup is intended to simulate the most critical solar impact. The frit pattern forms an incident solar radiance intensity based gradient pattern, varying across the surface according to the distribution of incident radiation intensity. The frit pattern applied to the panel follows a similar optimisation strategy developed in Chapter 4.4. However, in this experiment, accurate numerical optimisation of the frit pattern is constrained by two key factors: (1) the physical experiment uses electric lighting, whereas the computational simulation uses natural sunlight; and (2) it is difficult to define material properties equivalent to the experimental frit pattern for input into the simulation. Due to these limitations, the optimisation process lacks the proper cor-

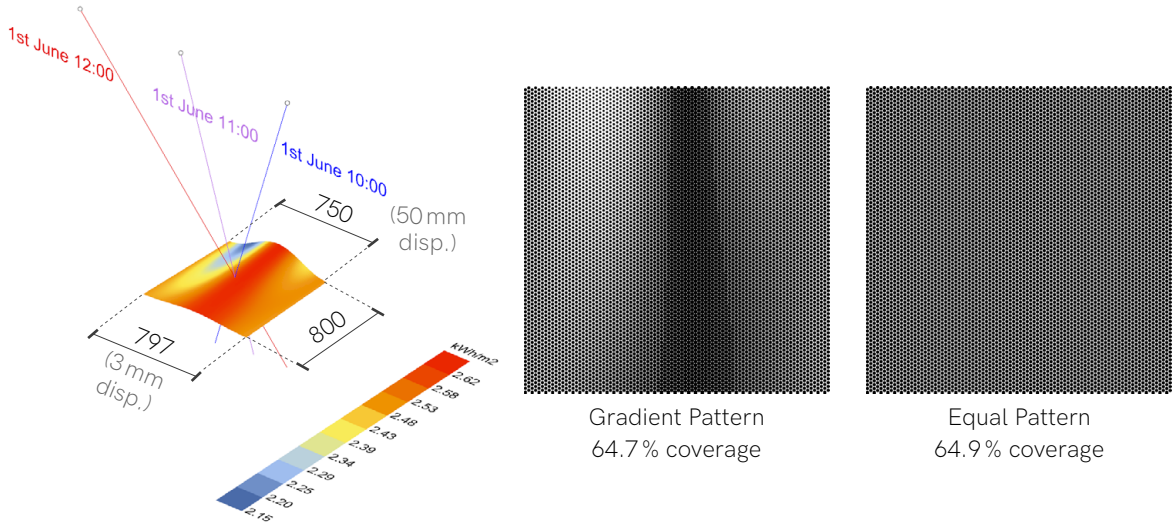

Fig. 5.24 | Gradient frit pattern generation from incident radiation simulation and derived frit pattern design

respondence between the simulated and physical conditions, making it challenging to derive a truly performance-driven gradient frit design. While the transmitted light amount (irradiance) can still be evaluated, the resulting pattern may not reflect a fully optimised solution for the actual experimental setup. When the same simulation settings from Chapter 4 are applied, the resulting gradient frit design is visually almost indistinguishable from an equal dot density pattern. This limitation occurs because, within a single 0.8 × 0.8 m panel, the variation in incident radiation is not significant enough to produce a pronounced gradient.
To generate a more noticeable difference between the experimental groups, an arbitrary scale factor is applied to the radiation-derived coefficients, resulting in a more dramatic gradient frit pattern (Figure 5.24, right).
To assess performance between a gradient and an equal frit pattern, a second panel with an equal fritting area but uniform dot density is produced as a comparison group. This allows for evaluation of transmittance performance between the gradient design and an equal-density design. While the actual ceramic frit applied in the final roof design is white, this experimental setup uses a black tone ink (K 100% on digital file) to represent the frit pattern. Even if the colour is set to 100% in CMYK mode, the actual printed output may differ due to printer settings such as ink-saving or economy modes from the manufacturer. These settings can override the specified ink values, resulting in less saturated or lighter colours. Upon reviewing the printed output, a personal qualitative assessment of the printed black frit areas suggests that 100% K (black) is not fully realized in the final print (Figure 5.25).

A quantitative comparison of transmittance between the actual design panel and the experimental panel with frit patterns could ideally be achieved using a spectrophotometer to directly measure visible light transmittance (T_{vis}). However, as no laminated specimens incorporating ceramic frit patterns on glass are available, only theoretical estimations or previously reported data can offer approximate insights. According to Wilson & Elstner (2018),

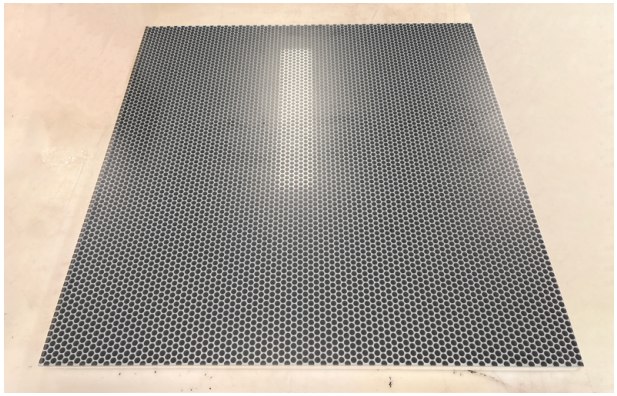

Fig. 5.25 | Experiment PMMA panel with ink printed equal frit pattern applied

using integrating spheres of 220 mm and 620 mm diameter, white screen-printed coatings on 6 mm low-iron glass panes exhibited T_{vis} values between 22–32 % as measured following the EN 410 standard. In contrast, the inkjet-printed frit pattern used in this experiment—assumed to be printed in ink-saving mode with black ink (K 60–80 %)—is likely to have a lower transmittance due to higher optical density. Based on X-Rite (n.d), black ink with K 60–80 % coverage can reach an optical density (OD) of 1.0, corresponding to approximately 10 % transmittance. Therefore, the experimental panel is estimated to exhibit greater light-blocking performance than the actual laminated glass-ceramic frit panel.

5.3.2 Experiment Setup

Because the purpose of the experiment is to evaluate how the double-curved panel modulates transmittance based on the angle of incident light, it is conducted under fully controlled indoor conditions rather than with natural sunlight. The setup takes place in the Photo Studio at TU Delft's Faculty of Architecture. An artificial light source—Godox SL-100 W—is used to simulate the sun. The value of 6500 Lux shown in Table 5.6 refers to the measured illuminance at a distance of 1 m from the source. To avoid multiple overlapping shadows and to replicate the clarity and diffusion of natural light, the reflective hemispherical lamp cover is removed during the experiment (Figure 5.26).

Colour Temperature [K]	Power [W]	Max. Brightness [Lux]
5600	100	6500

*Measurement taken from 1m

Table 5.6 | Electric lighting Godox SL-100W technical specification (Based on Godox Photo Equipment, n.d.)

The double-curved roof panel is elevated on a 0.58 m high support to prevent any direct transmission of light onto the ground surface, and positioned 0.8 m away from a white background where the transmitted light pattern is projected. The lamp is placed 4 m away from the background, simulating the sun's position at 10:00, 11:00, and 12:00 on June 1st (Figure 5.27). To capture and analyse the transmitted light patterns numerically, a Canon EOS R10 camera paired with a Canon RF-S 18-150 mm F3.5-6.3 IS STM lens (focal length fixed at



Fig. 5.26 | Light source for the experiment with lamp cover removed to avoid light diffusion

18 mm) is used. The camera is controlled using *Qdslr Dashboard* software, with the following settings: f-number 8.0, bracket images of shutter speed: 1/100 - 1/50 - 1/25 - 1/13 - 1/6 - 1/3 - 0.6 - 1.3 - 2.5 seconds, and ISO 100. A custom bracketing method capturing 9 images per lighting scenario, and manual focusing is adjusted and fixed individually for each of the three light source angles.

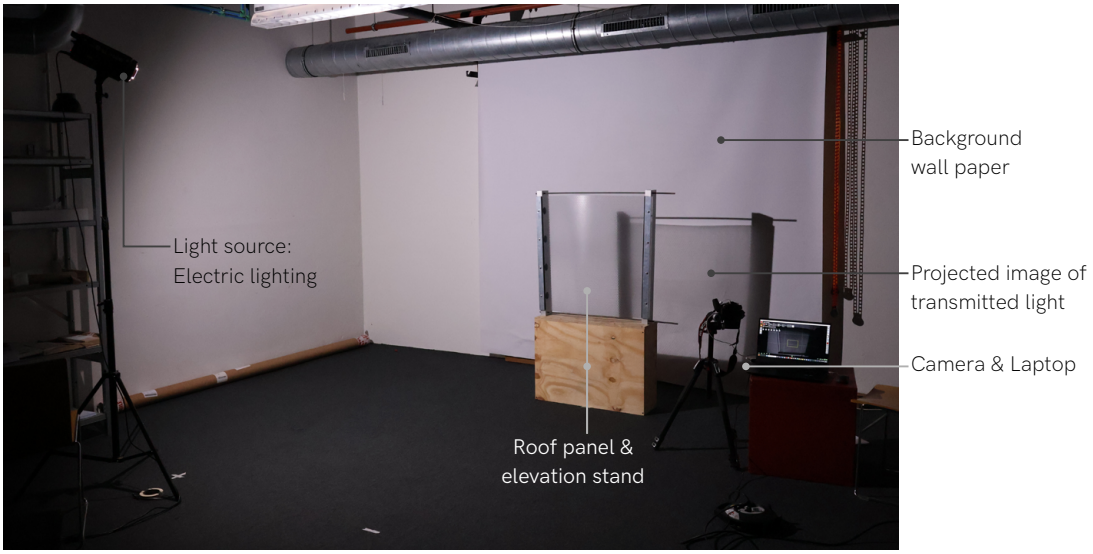

Fig. 5.27 | Solar transmittance performance experiment setup

5.3.3 Light Transmittance Measurement

Such instruments as a luminance meter, which measures luminance in cd/m2, and a pyranometer, which measures irradiance in W/m2, are available for use. However, since both measure only a single point, they are not suitable for evaluating the overall transmitted area or analysing the spatial distribution of transmitted light. Therefore, this study uses a false-colour luminance map (from high dynamic range (HDR) image) where pixel values represent the relative luminance (cd/m2) received by the camera sensor.

HDR images are generated by combining multiple photographs taken at different exposure times. Each exposure produces distinct pixel values based on the scene brightness,

and since the camera sensor converts luminance into digital values through a non-linear response, the original luminance value must be recovered through inverse estimation. This is done using the camera response function (CRF), which maps pixel values back to scene luminance (Debevec & Malik, 1997). As a result, each pixel in the HDR image holds a number value that closely estimates the actual luminance of the scene.

While HDR imaging can provide relative luminance values, it does not directly yield absolute luminance. This calibration requires real-world reference measurements to accurately scale the image data to physical units (cd/m2). However, in this study, the experimental panels differ from the actual architectural materials, making precise absolute luminance values unnecessary. Therefore, scale calibration is omitted, as relative luminance is sufficient for comparative analysis within the experimental context.

Since all other variables between the two test groups—the gradient frit pattern and the equal density control pattern—are held constant, the effect of the frit design on light transmittance can be inferred using relative luminance values derived from the false-colour luminance images. To further quantify transmittance, a base HDR image is also captured for each light source condition without any panel in place (i.e., without a light-transmitting medium). This base image represents the unobstructed projection of light onto the background and serves as a reference for calculating transmittance percentages.

To generate HDR images and false-colour luminance heatmap from bracketed RAW photographs, this study employs a standard computational imaging pipeline using Python. Multiple RAW files (4000 × 6000 pixels) captured at varying exposure levels are first demosaiced and linearised using the *rawpy* library. These linear RGB images are then merged into a single radiance map via OpenCV's *MergeDebevec* function, which implements the classical Debevec and Malik algorithm. For visualisation, a global tonemapping operator (*cv3.createTonemap*) is applied to compress dynamic range, producing an 8-bit false-luminance image suitable for display. Additionally, pixel-wise HDR values (in floating-point RGB) are extracted and saved as a .csv file to facilitate quantitative analysis.

Luminance is derived from the HDR radiance map using the standard perceptual weighting of linear RGB channels ($Y = 0.2126\,R + 0.7152\,G + 0.0722\,B$) as defined in ITU-R Recommendation BT. 709 (ITU-R, 2015). For improved visual interpretability across a wide dynamic range, the luminance values are logarithmically mapped using $\log(1 + Y)$ prior to false-colour rendering. This transformation enhances visibility in darker regions while aligning the representation more closely with human visual perception (Fechner, 1860).

Figure 5.28 illustrates the false-colour luminance maps generated under electric lighting positioned at point A, comparing three scenarios: (1) equal frit transmitted output, (2) gradient frit transmitted output, and (3) baseline projection where light is transmitted directly to the background without any panel obstruction. The results show that, regardless of the applied frit pattern, certain localised areas exhibit reduced transmittance unrelated to the intended design. These anomalies are attributed to small bubbles formed during the application of the adhesive frit PVC sheet onto the PMMA substrate, representing fabrication flaws in the

panel production process. It is assumed that such imperfections occur independently in each panel, and no separate correction process has been applied to compensate for them (Figure 5.28).

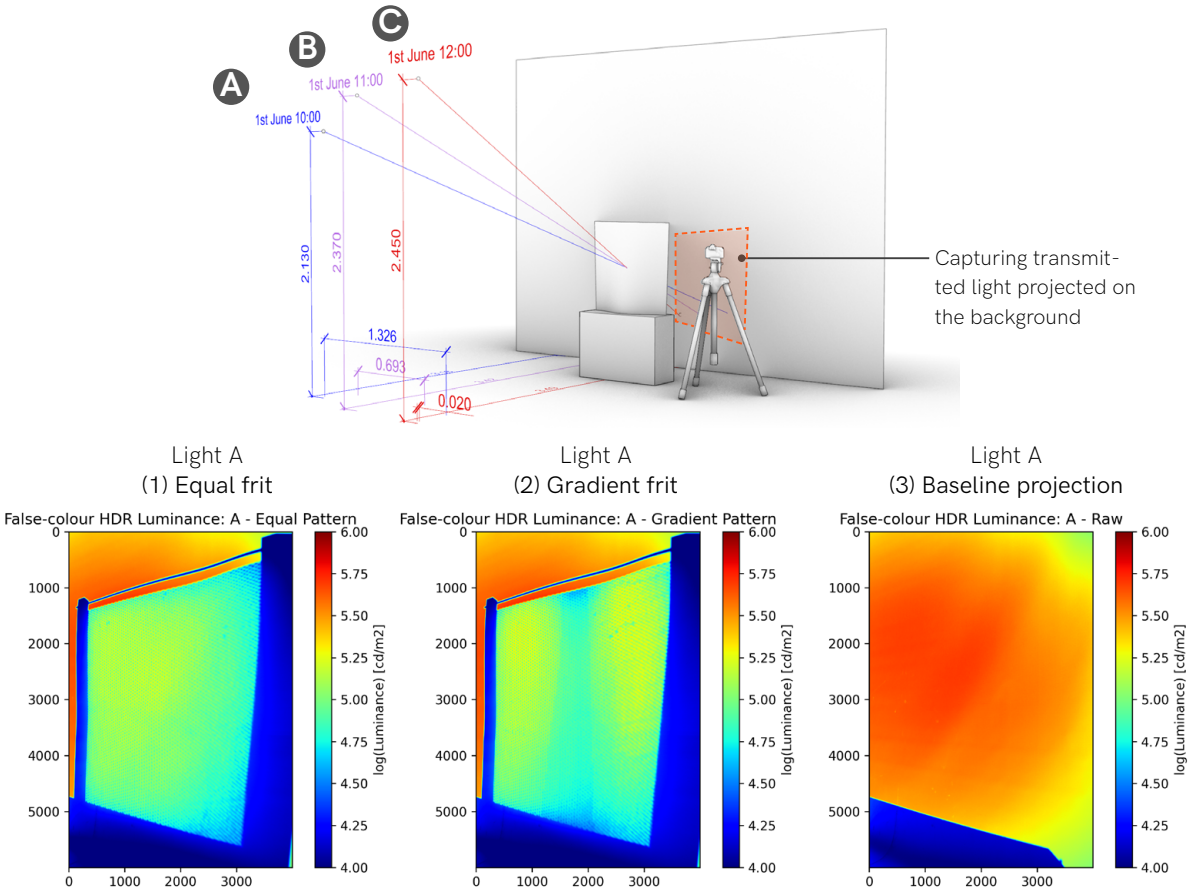

Fig. 5.28 | Experiment scheme & visualisation of HDR luminance output

Within each lighting condition (A, B, and C, representing side-angled to front lighting positions), the two test groups, one with an equal-density frit pattern and the other with a gradient frit pattern, are compared against a baseline result. For each group, the transmittance (%) is calculated across 4000 × 6000 pixels using the following equation:

$$T(x,y) = \frac{L_{\text{trans}}(x,y)}{L_{\text{base}}(x,y)} \times 100 \tag{5.1}$$

Region of interest (ROI) is selected to evaluate the panel's light control performance. Since luminance falloff near object edges results from natural shading effects when light interacts with a 3D surface, the ROI is positioned slightly offset from the panel boundaries rather than too close to the edges (Figure 5.29).

Since the physical experiment serves as a validation of the previously run numerical simulations, a digital twin model—rotated 90 degrees upward to match the experimental setup—is created. Using the same simulation script and material inputs developed in Chapter 4.4, computational simulations are conducted to replicate the average illumination values ob-

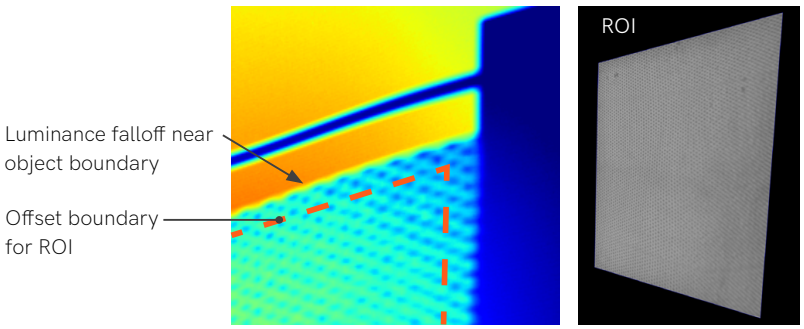

Fig. 5.29 | Luminance falloff effect and ROI boundary example

served under lighting positions A, B, and C for three conditions: equal frit setting, gradient frit setting, and a base illuminance reference (Figure 5.30). The simulations use Plexiglass panels to share the same optical properties as the glass unit in Chapter 4.4 and ink-printed frit patterns modelled with the same characteristics as ceramic frit in Chapter 4.4. To record irradiance values, sensors are placed 0.8 m below the panel at 0.1 m intervals across a sufficiently wide area to capture transmitted light effectively (Table 5.7).

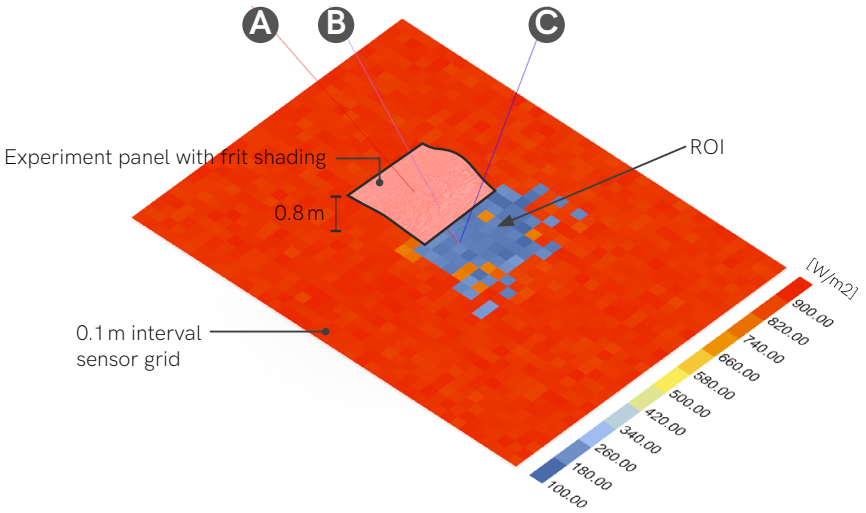

Fig. 5.30 | Digital twin setup replicating the physical experiment

Even under identical angles of light incidence, the distributed area of transmitted light varies depending on the frit pattern. Therefore, in order to calculate transmission accurately, it is necessary to establish a unified logic for defining the region of interest (ROI) across different lighting conditions.

First, only the sensor areas where clear transmission occurs in both the equal frit and gradient frit panels simultaneously are selected as the ROI. Areas with transmission in only one of the panels are excluded. Second, sensors that detect isolated light patches resembling "islands" are not considered part of the ROI, as such distributions are physically implausible; the selected ROI must show spatial continuity. Third, the number of sensors meeting the first and second criteria should remain roughly consistent across the A, B, and C lighting conditions. If major discrepancies arise, a revised logic for defining ROIs would be required. Following this method, Figure 5.31 visualises the process of defining the ROI under Lighting

Element	Specification
Panel	Laminated panel in Chapter 4.4
Frit	Ceramic frit in Chapter 4.4
Sensor grid	0.8 m below panel position
	0.1 m interval
Light A	Sun position at June 1 10:00 AM
Light B	Sun position at June 1 11:00 AM
Light C	Sun position at June 1 12:00 AM

*Sensor grid is defined as virtual surface that does not interfere with light transmission or sensor performance

Table 5.7 | Specifications for digital twin simulation elements

A conditions and presents the resulting ROI plots for each light case. The sensor sets selected under the first and second rules show consistent quantities across all three lighting conditions, confirming the robustness of the proposed logic. With the defined ROI, transmittance is calculated in a manner consistent with the physical experiment by assessing the relative irradiation values of sensors inside the ROI against those in a baseline irradiation (non-transmitting medium) result ROI regions.

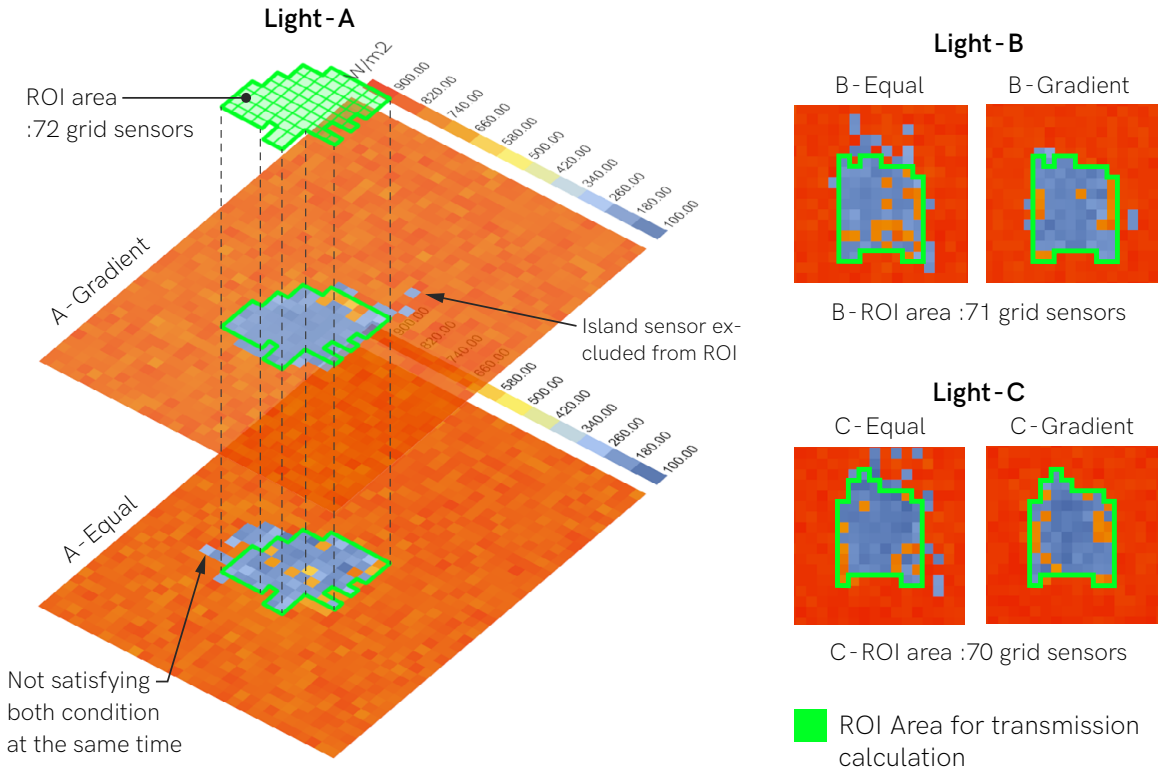

Fig. 5.31 | ROI selection for transmission analysis under varying lighting condition in digital twin model

5.3.4 Experiment Result

Table 5.8 summarises the average transmittance values for each test group of the frit panels, comparing the results from the physical experiments and the corresponding digital twin simulations. Assuming the physical experiment provides a

more accurate baseline, the results under each lighting condition show that, even with an intentionally amplified gradient frit pattern, the difference between T_{equal} and $T_{gradient}$ remains relatively small, ranging from about 1 % to 4 %. This suggests that, within a 1 m2 double-curved panel, varying the frit density does not yield a significant difference from equal pattern. While the physical tests consistently show superior light control performance for the equal frit pattern compared to the gradient pattern, the digital twin simulations indicate better performance of the gradient pattern under lighting conditions A and B. This discrepancy likely stems from several factors: the ±20 % characteristic error typical of solar measurements in real experiments (Jones and Reinhart, 2015); the ROI is manually defined in the digital twin, and the comparison relies on different performance metrics—luminance in the physical experiment and irradiance in the simulation. While both metrics reflect light transmission, their correlation depends on the spectral characteristics of the light source and the sensitivity of the measuring devices. Therefore, this study focuses not on the absolute transmittance values, but rather on the relative transmittance differences between the equal and gradient frit patterns within each method, which allows a more meaningful comparison despite the metric discrepancy. Additionally, the method used in the physical experiment—capturing the transmitted light projected onto a background surface using a camera—introduces limitations in accuracy. Due to constraints in the setup, the camera does not capture the transmitted light from a perpendicular angle to the projection surface (Figure 5.27), but rather from an oblique side angle. This viewing angle introduces potential errors in luminance readings, as reflections and diffusion effects may vary with the geometrical angle of observation. Despite this limitation, the absolute difference between $T_{Exp.diff}$ and $T_{Twin.diff}$ under lighting conditions A, B, and C exhibits a relatively consistent trend, without showing any anomalous deviation from the expected range. This consistency offers meaningful support for the validity of the numerical model, even under experimental uncertainty.

In the digital twin, the recorded transmittance values are generally lower (better light control) than those observed in the physical experiment. This discrepancy likely results from the fact that the optical properties of the glass unit and ceramic frit are not precisely calibrated to match those of the actual experimental materials. Additional contributing factors include differences in light source intensity between the electric lighting used in the experiment

Light location	A		B		C	
Frit type	T_{equal} [%]	$T_{gradient}$ [%]	T_{equal} [%]	$T_{gradient}$ [%]	T_{equal} [%]	$T_{gradient}$ [%]
Physical experiment	54.58	55.82	56.33	60.57	60.20	62.48
Digital twin	31.85	27.89	36.12	30.41	29.69	32.76
$T_{Exp.diff}$ [%]	-1.24		-4.24		-2.28	
$T_{Twin.diff}$ [%]	3.96		5.71		-3.07	

Table 5.8 | Average light transmittance comparison between real test and digital twin

and the solar radiation assumed in the simulation. However, this study does not consider calibrating the digital model's transmittance to the physical experiment as essential. The current results already provide a sufficient overall validation of the relationship between the experimental outcomes and numerical analysis, and further calibration or adjustment of transmittance values is therefore omitted.

5.4 Discussion

Structural Experiment

The structural experiment is conducted to validate the extensive numerical simulations presented in the preceding chapters. A flat LOCA-laminated sandwich panel is used to perform a three-point bending test. The same setup and conditions used in the previous numerical tests are replicated in a digital twin model, enabling a comprehensive validation of the FEA model employed throughout this research. By comparing the experimental results with the FEA outputs, the accuracy of the digital model is evaluated. The resulting error rate remains within 20 %, and the viscoelastic behaviour of the interlayer is captured in the numerical model, providing a reasonably reliable representation of the structural response of the composite panel. Notably, both experimental results consistently show that the real laminated panels are less stiff than the corresponding digital simulations, the simulation results represent an optimistic rather than conservative estimate of performance.

Applying a greater displacement in Experiment 1-A might have resulted in a stronger reaction force, enabling more accurate data logging by the testing machine. Alternatively, future validation experiments could benefit from selecting measurement equipment that is more appropriately matched to the sandwich panel's stiffness and scale, as well as using specimen dimensions better suited to smaller-scale test rigs, which may improve the accuracy of the results. Furthermore, if a reliable Prony series and time–temperature shift function for 2K PU LOCA becomes available, it would allow for a more robust validation of both the holding test experiment and the corresponding numerical simulations.
Given these considerations, there remains the possibility that the experimental outcomes could have been more closely aligned with the numerical model. Therefore, in the subsequent chapters, no additional safety factor is applied beyond those already embedded in the numerical methodology. The structural design proceeds using the same simulation-based workflow established in Chapters 4 and 5.

Despite the small panel size and limited number of specimens, all five composite samples exhibit consistent performance under loading. While this small sample set restricts broader generalisation, the results suggest that no critical surface flaws are present and that the handling, lamination, and overall fabrication process for the flat laminated panel does not introduce major defects on glass.

LOCA Manufacturing

Initial goal was to manufacture the LOCA lamination myself using the Kömmerling two-component material. However, this process requires a special dosing machine capable of mixing at 4000 RPM, which necessitates a visit to TTEC (Figure 5.32). The chemical reaction begins immediately after dosing, causing rapid curing. When the material is not dosed evenly, wavy pattern with small bubbles appear in the interlayer. While CIP (Cast-in-Place) lamination may seem straightforward in theory, in practice it demands specific equipment and substantial fabrication experience. The complexity of the CIP lamination method becomes evident during the manufacturing process. As the glass becomes thinner and the panel size increases, both handling and fabrication become more difficult. Challenges include evenly applying the uncured liquid interlayer, maintaining the cold-bent geometry with only edge fixtures (without a full mould), and achieving geometric consistency.

These challenges highlight the need for further research into cold bending methods that accommodate LOCA injection while reducing labour requirements and ensuring shape stability. Although the selection of glass thickness was not initially based on all the complexities of LOCA manufacturing, it becomes evident that an appropriate balance must be struck between pane size and thickness. Thicker glass simplifies interlayer application by providing structural stability, while thinner glass offers the flexibility necessary for cold deformation. The chosen glass thickness serves as an effective compromise: thinner glass would pose significant fabrication challenges, whereas thicker specimens would exceed the structural capacity of the buckling apparatus.

Cold Buckle Bending

To accurately implement semi-rigid edge support in real manufacturing, it is essential to control out-of-plane rotation at the edge fixtures. In the current buckle bending machine setup, lateral guiding profiles were constructed using available leftover materials, which limited the precision of rotational control. As a result, reproducing the exact curvature observed in the numerical simulations proved challenging. For future setups, the alternative



Fig. 5.32 | Left: Dosing machine for 2K PU LOCA with 4000 RPM auger
Right: Transmitted light of erroneously mixed laminated glass panel

lateral guide system proposed in Section 5.2.2 is recommended to enhance accuracy.
Despite these limitations, the fabricated panel achieves a geometry closely resembling the cold buckle bent form simulated in the numerical model. If sufficient materials for testing had been available, it would have been valuable to experimentally push the sinusoidal half-paraboloid formed by buckle bending to its ultimate limit and compare the outcome with the numerical predictions. Such an experiment could provide further insight into the accuracy and applicability of the proposed double curved cold bent glass unit.

Cold Buckle Bent Surface Quality, Spring-back, and Light Transmission

Cold buckle bending using the LOCA lamination method results in a high-quality laminated glass with excellent transparency and clarity, free from haze or visible micro-bubbles. While the double-curved surface inevitably causes optical distortion this is a natural consequence of the geometry itself and does not constitute a flaw. More localised surface imperfections, however, referred to as cold bending distortions, are observed and found to correlate with areas of abrupt curvature transition in the numerical model, particularly in regions where the curvature shifts between synclastic and anticlastic forms. This suggests that such distortions can be anticipated through FEA and curvature analysis and mitigated in the early design and pre-engineering stages.

Although quantitative validation is difficult, qualitative observations indicate that the cold bending distortion observed in the physical panel is less pronounced than in the computational model. This difference is likely due to unintentional stress relief during physical fabrication—possibly arising from incomplete restriction of edge rotation in the buckle bending machine—and viscoelastic stress relaxation occurring during the interlayer curing phase, which was not simulated in this study. These findings imply that the LOCA lamination method may contribute positively to surface quality by supporting stress dissipation during post-forming stages.
Additionally, the panel is observed after complete removal of the buckle bending support to assess its spring-back behaviour. The results show that the panel retains a greater portion of its deformed geometry than predicted in the numerical model, indicating reduced elastic recovery. This is consistent with the previously discussed explanation for the improved surface quality, namely the relaxation of residual stress during the curing process and fabrication stage.

The distinctive double-curved form of the panel results in reflected light patterns that appear both visually intriguing and unpredictable. When the incident angle approaches normal (perpendicular to the surface), light reflection becomes dominant, and due to the convex shape of the panel, no clear convergence of reflected light is observed on a single roof unit. As the incident angle increases relative to the panel surface, the intensity of reflected light gradually decreases, while the intensity of transmitted light increases. Under certain oblique lighting conditions, a linear light convergence area—not a single focal point—emerges,

which indicates that solar radiance is locally intensified. This concentrated transmission may potentially affect occupants inside the building, depending on the position of the panel and the path of incoming sunlight.

Solar Experiment

Although production limitations prevent a perfect replication of the digital simulation in the physical experiment, the experimental setup in this study is designed using alternative materials that closely mimic the intended material properties. By extracting luminance values from HDR images of the transmitted light and establishing a region-of-interest (ROI) logic within the proposed digital twin workflow, this study introduces a method for assessing transmittance through relative values without the need for separate calibration against absolute transmittance measurements. This approach enables a meaningful level of accuracy, with experimental results falling within the ±20% characteristic error commonly accepted in solar performance measurement studies.

Future implementations of this experiment methodology should be aware that this is an image-based experiment, it is essential to control all experimental conditions as precisely as possible. For each test condition—whether using the optimised frit pattern or the equal-density pattern—the roof panel must be removed from the stand, disassembled from the fixture, and replaced with a new glass (or alternative material) unit. Since buckling deformation occurs anew with each change of panel, maintaining consistent deformation dimensions and aligning the panel in exactly the same stand position is critical for meaningful pixel-by-pixel image comparison. While perfect consistency is difficult to achieve in practice, even small improvements in precision contribute to the reliability of the luminance value comparison between two images on the ROI.

Further limitation lies in the fact that Grasshopper Honeybee (version 1.8.0) does not currently support electric lighting simulation, which means the digital twin of the real solar experiment is based on actual sun solar radiation data rather than an electric lighting setup used in the real experiment. As a result, the earlier optimisation, which is based on roof incident radiation and indoor irradiance performance, does not fully correspond to the controlled artificial lighting conditions used in the physical experiment. Because of this discrepancy, the indoor irradiance performance is excluded from the gradient frit pattern design for optimisation, and it is made of solely on incident radiation on panel geometry. Therefore, the experimental frit pattern lacks a calibrated scale factor for each dot pattern, requiring the use of an arbitrary value for deciding the different size in physical prototyping. This choice introduces another layer of approximation between the simulation and the real testing result.

Chapter 5.3, where the designer uses alternative materials to test frit performance prior to real ceramic fritting on glass, could form the basis for future research on solar control

validation experiment using ceramic fritting. Developing a more standardised and numerically validated approach to correlate the mechanical relationship between glass-plastic and ceramic frit-ink printed pattern combinations proves valuable for facilitating easier performance-based design testing. This becomes particularly relevant when physical prototyping with actual ceramic-fritted glass is impractical due to cost, lead time, or manufacturing limitations. Establishing equivalency in solar and mechanical performance through calibrated substitutes not only streamlines early-stage testing but also enhances the reliability of simulation-driven design iterations.

Through this design experiment it becomes evident that achieving extremely steep curvature in cold-bent glass panels is practically limited, both by material constraints and panel size. Given these physical limitations, the effectiveness of an optimised gradient frit pattern, particularly when applied within a single panel with a relatively small size, does not demonstrate significantly superior performance compared to that of an equal-density frit pattern. This is particularly true when considering the heavy computational cost of gradient optimisation and the custom manufacturing required for each panel.

In this research, a gradient frit strategy is adopted to maintain design originality, with variation applied both between and within panels. However, for real-world architectural applications, it may be more practical to reduce fabrication complexity by applying a uniform frit density within each individual glass panel, while varying the density from panel to panel across the roof system. This approach enables effective solar control tailored to localised environmental conditions, without requiring complex gradient patterns within a single panel.

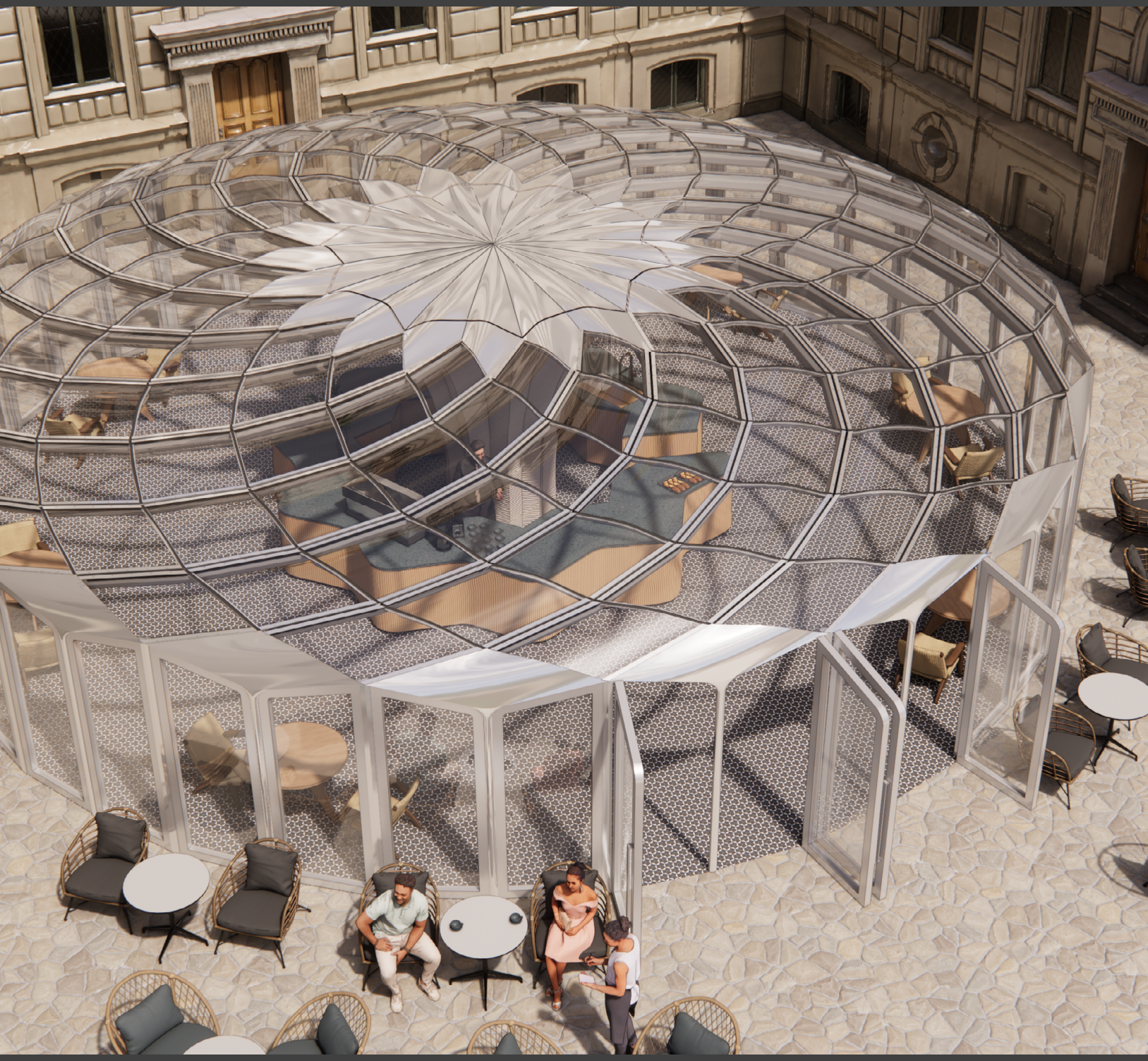

· New glass roof design of the OWO Pavilion (without ceramic frit)

VI. FINAL DESIGN

6.1 Methodology

Based on the research and findings from previous chapters, the final cold bent glass design is applied to the actual OWO Pavilion roofing. The design process follows the sequence of structural geometry design, load case simulation, and frit pattern design, using the actual rhomboid-shaped roof geometry instead of the 800 × 800 mm square panel used in earlier simulations. Although the structural experiment revealed that the numerical model tends to compute a slightly better structural performance than the actual specimen, this discrepancy is not deemed significant enough to warrant recalibration of the entire FEA model or the application of additional safety factors. Therefore, the analysis continues under the same settings and assumptions established in Chapter 4. As presenting the design for all roof panels is unnecessary in this research, a single representative panel with the most critical condition is selected to demonstrate the full workflow and outcomes.

6.2 Unfolding Cold-Bent Geometry

The revised OWO Pavilion roof design for this research, consists of 16 unique glass panel types, radially repeated to form 160 roof glass panels. Each rhomboid panel is defined by four fixed corner points according to the original design, with one corner intentionally displaced out-of-plane by 2 mm to 25 mm. For the structural design phase, however, this out-of-plane deviation is ignored, so that all four points are assumed to lie on the same plane for simplification. According to an internal numbering system of the roof elements, panel A2 in Figure 6.1 is selected as the representative panel for structural design.

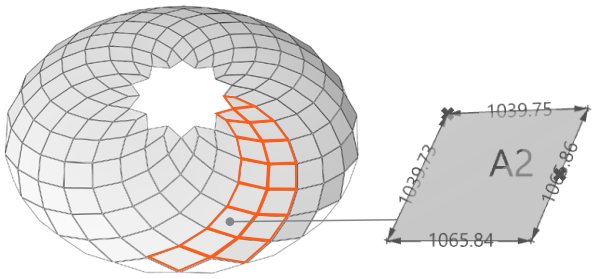

Fig. 6.1 | Representative panel for OWO Pavilion roof design

Unlike in Chapter 4, where the initial pre-cold-bent dimensions are defined as a rectangular panel measuring 800 × 800 mm, conducting structural optimisation when the predefined edge lengths and corner angles are unknown or uncertain is more challenging. Although an numerical relationship between deformed curvature radius and maximum stress could not be formally established, structural design is guided by empirical findings, serving as a

practical reference based on prior testing experience. Using the buckling-derived geometry equation from Euler's formula, where A stands for amplitude and L for length of the edge:

$$A \cdot \left(1 - \cos\left(\frac{2\pi x}{L}\right)\right) \tag{6.1}$$

A cold bending geometry generation script is developed using the *Galapagos* optimisation component in Rhino Grasshopper (8.0) based on the curvature of the geometry. This script adjusts the amplitude of the Euler buckling curve to achieve the double-curved geometry with the desired radius at the peak curvature point of maximum deformation (Figure 6.2). The computed shape is then flattened using the *Squish* command, yielding a 2D geometry that will be the cutting outline for float glass to realise the targeted geometry through cold bending. This flattened geometry is imported to Ansys Workbench, where cold deformation simulations are carried out. The resulting stress analyses are assessed, and iterative geometric fine-tuning can be performed to meet structural criteria.

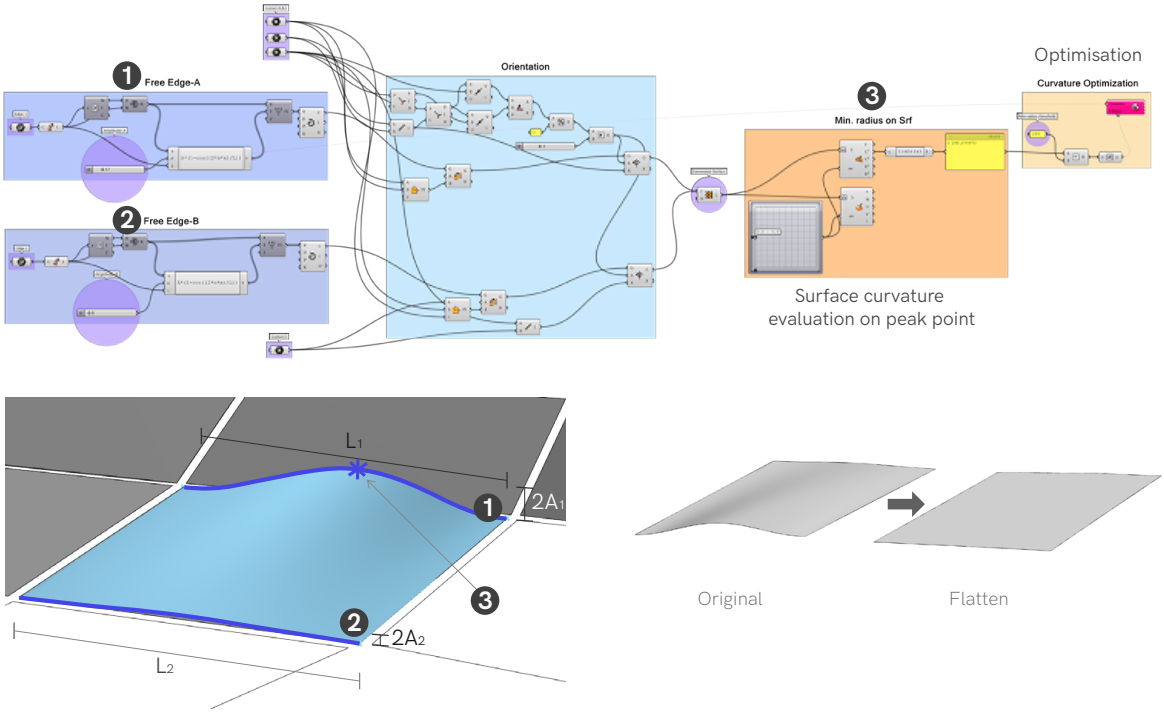

Fig. 6.2 | Flattened panel outline generation work-flow using maximum curvature as input

To account for residual stress induced by cold buckling and additional stress from external loads, a preliminary minimum curvature radius (e.g. 300 mm) is set to initiate the automatic unfolding geometry task. This script has two main limitations. First, as in Chapter 4, the most strained geometry and its corresponding maximum curvature radius must be identified through iterative FEA processes conducted outside of Rhino Grasshopper, in order to satisfy structural requirements. Second, since the deformed surface is non-developable, using Squish command to flatten it inevitably introduces distortion through stretching or compression. Rhino lacks mechanical material properties such as Poisson's ratio, and thus cannot simulate material behaviour accurately during flattening.

However, because the sinusoidal half-paraboloid geometry used in this study is optimised

to approximate a developable surface, it is assumed that the resulting distortion does not cause significant issues during actual fabrication.

6.3 Structural Design - Sinusoidal Half Paraboloid

To facilitate structural analysis, a simplified flattened surface is used instead of the actual derived shape. This surface takes the form of a rhombus with side lengths of 1040 mm (Figure 6.3). For the geometry meshing, basic mesh size is set to 3 cm, and each individual sandwich layer divided into two meshes according to thickness, 6 mesh layers in total when considering the entire composite panel. In the 2-step cold deformation process, an initial axial uniform displacement of 3 mm is applied, following by a 1-degree inward rotation for each two adjacent edges. The resulting cold-deformation shape, derived from this process, is computed.

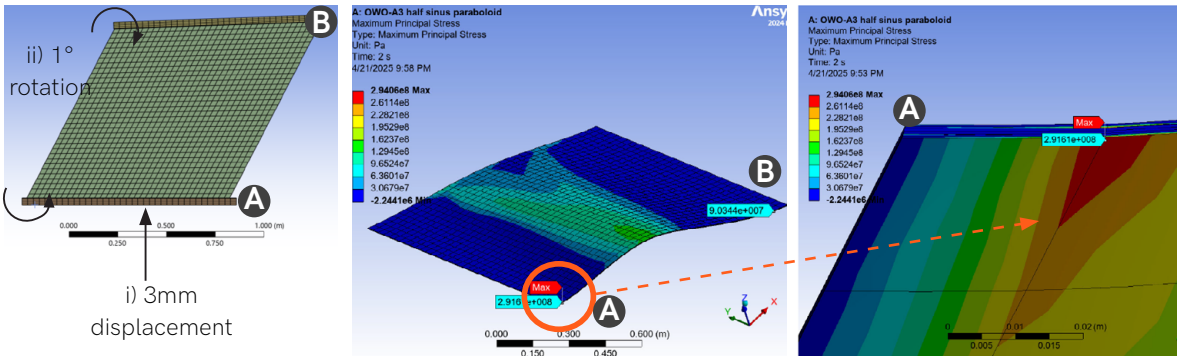

Fig. 6.3 | OWO Pavilion roof panel: sinusoidal half paraboloid cold bending FEA bending stress result

Although a rather conservative deformation angle has been applied to ensure stable cold deformation, significant stress concentration is observed after the completion of the Step 2 deformation process. Specifically, maximum stress of 291 MPa (corner A in Fig. 6.3) occurs at the obtuse corner of the edge that buckled inward. While the midpoints of the bulging edges exhibited stresses around 150 MPa (maximum curvature point), peak stresses are exclusively localised near the obtuse corner. This level of stress far exceeds the structural capacity tolerable of the material, which is caused by the asymmetrical rhombus-shaped geometry, where symmetric displacement is being applied on both corners A and B. In contrast, the opposite acute corner B exhibits significantly lower stress, around 90 MPa, indicating a highly uneven stress distribution with an approximate stress ratio of 3 : 1 (A : B) between the obtuse and acute corners.

To verify whether any errors existed within the simulation calculations, an additional analysis is performed, as shown in Figure 6.4. A square plate with the same edge length of 1040 mm is subjected to the identical cold bending procedure. In this case, the sum of the highest stress points at the corners is assessed to determine if it matches the sum of corner

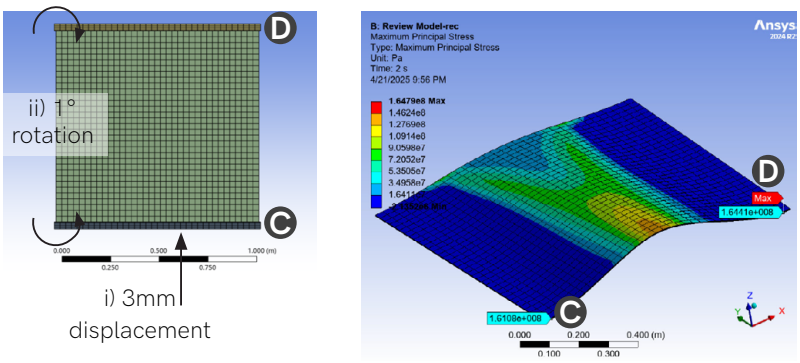

Fig. 6.4 | Rectangular geometry stress review for comparison

stresses observed in the rhombus case. In the symmetric square model, maximum stresses are found near the corners where inward buckling occurred. However, the stresses are evenly distributed, with values of 161 MPa at corner C and 164 MPa at corner D, respectively, across the symmetric corners. The combined stresses at for each case are found to be reasonably similar, confirming the simulation result of the rhombus plate deformation (Table 6.1). From these results, it can be concluded that the deformation boundary conditions and cold-bent sinusoidal half-paraboloid geometry is not suitable for a rhombus-shaped roof geometry for the OWO Pavilion.

Geometry	Corner	Angle [°]	Stress [MPa]	Combined stress [MPa]
Rhombus	A	117.42	291.6	381.9
	B	60.58	90.3	
Rectangle	C	90	161.1	325.5
	D	90	164.4	

Table 6.1 | Stress at critical corners comparison between symmetric and asymmetric plate geometries

6.4 Structural Design - Sinusoidal Single Curve

6.4.1 Cold Lamination Bending

From previous experiments, it is observed that the rhombus-shaped panel exhibited stress concentration at the obtuse corners due to its inherent geometrical asymmetry. Further investigation revealed that bending stress is highly amplified at corner A and B, when buckling becomes more pronounced through Step 2 deformation. To eliminate the asymmetric force effects introduced through Step 2 on corner A and B, a new test is conducted using equal edge displacement to form a single sinusoidal geometry. When an in-plane displacement of 2.3 cm is applied along the X-axis, a maximum principal stress of 165 MPa is recorded near the obtuse corners of the panel (Figure 6.5). The degree of deformation under this condition is documented in Table 6.2. Considering additional loads expected on the roof element in

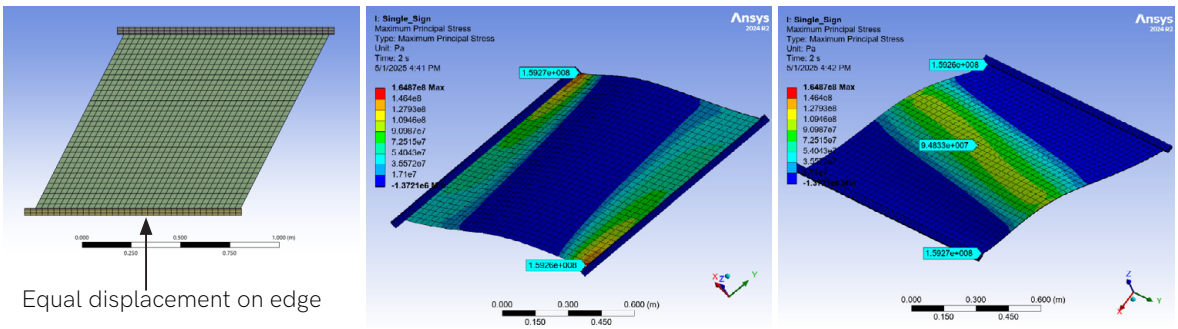

Fig. 6.5 | OWO Pavilion roof: sinusoidal single curvature cold bending FEA bending stress result
Note. Left: Boundary condition Middle: Bottom pane bending stress Right: Top pane bending stress

practical application, this stress level is identified as the cold deformation limit. The FEM (Finite Element Method) model is being set-up as the same method as Chapter 6.3.

Out-of-plane deflection typically reaches its maximum at the midpoint generally occurring along the central axis orthogonal to the loading direction. This behaviour is well-documented in structural mechanics and plate theory (Timoshenko & Woinowsky-Krieger, 1959) explaining that in thin plate bending, maximum deflection generally occurs along the central axis orthogonal to the loading direction under symmetric conditions.
In this study, however, the location of maximum deflection and the associated stress distribution deviate from the expected axis. Rather than aligning with the orthogonal central line, the peak forms along a skewed trajectory. This deviation is interpreted as a consequence of the initial geometrical asymmetry of the panel. The current research does not further investigate methods for idealising or re-centring the resulting convex form, and the behaviour is instead acknowledged as an inherent result of the initial form's asymmetry.

Step	X displacement [mm]	Z displacement [mm]	Max. stress [MPa]
Cold bending	23	90	165

Table 6.2 | Sinusoidal single curvature cold bending result for OWO roof panel A2

6.4.2 Load Test

Based on the load scenarios investigated in Chapter 4.3.6, structural performance assessments are conducted on two types of glass panel units intended for the OWO Pavilion roof: a stiffer interlayer composite panel using Ködistruct LG with an initial Young's modulus of 65 MPa, and a more flexible one, 2K PU LOCA with 31 MPa. Both panel types are subjected to wind and snow loads in order to evaluate whether they meet safety and serviceability criteria based on the sinusoidal single-curvature geometry (6.4.1). The A2 panel selected for testing is the largest among the roof elements and had the longest span between supports, making it the most structurally vulnerable. Therefore, if this unit meets the safety thresholds under the applied loading conditions, it can be roughly assumed that the remaining panels will also be structurally sufficient. The experiment conditions are summarised in Table 6.3.

Wind load simulations are conducted at 22 °C with a short 3-second loading duration, while snow load scenarios are applied over a 10-hour period at 0 °C. Temperature-dependent relaxation behaviour of the interlayer material is accounted for using a time–temperature shift model (DIBt, 2016). At 22 °C, the reduction in shear modulus (G) progresses more rapidly, whereas at lower temperatures (e.g. 0 °C), the viscoelastic response slows due to the time–temperature shift effect, which results in stiffer behaviour under sustained cold loading. To ensure a conservative evaluation, the applied load is rounded up to 2 kN/m2, which exceeds the originally calculated design load, and is combined with 1.35 times the panel's self-weight due to gravity as part of the load combination.

Considering the design of the secondary support structure that holds the glass panel in place, a series of experiments is conducted by varying the edge restraint conditions—from the highest degree of freedom to the more constrained. Support conditions under which the glass fails to withstand the given load are excluded from the results. The naming convention for each panel edge is defined in Figure 6.6.

Experiment	Panel composition	Load case	Temperature [°C]	Duration [s]	Load [kN/m²]
6.4-1	1.1 mm glanova® 2 mm Ködistruct LG 1.1 mm glanova®	1.35 G + 1.5 W	22	3	-2
6.4-2		1.35 G + 1.5 S	0	36,000	2
6.4-3	1.1 mm glanova® 2 mm 2K PU LOCA 1.1 mm glanova®	1.35 G + 1.5 W	22	3	-2
6.4-4		1.35 G + 1.5 S	0	36,000	2

Table 6.3 | Load testing for OWO Pavilion roof panel in different load conditions and compositions
Note. G stands for self weight load under gravity, W for wind load, and S for snow load

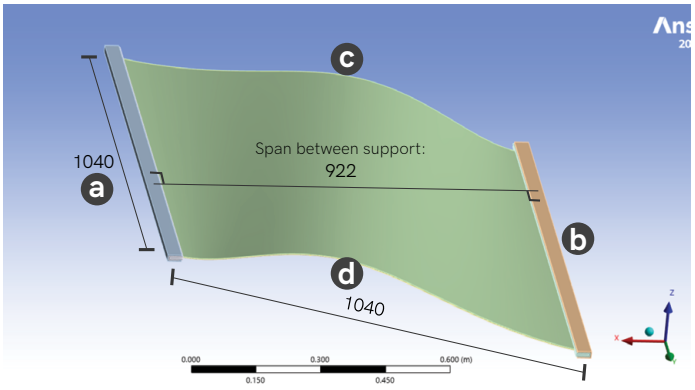

Fig. 6.6 | OWO Pavilion roof panel dimension and edge condition

For both interlayer materials, LG and 2K PU LOCA, in Experiments 1 and 3 concerning wind load simulation, the application of a 2 kN/m2 uplift load under support conditions where edges *a* and *b* restrict both displacement and rotation results in substantial deformation and bending stresses that significantly exceed the 200 MPa design threshold.

When the remaining two edges *c* and *d* are set to allow free rotation and translation in the X and Y directions, while restricting only movement in the Z direction, the simulation yields improved structural performance. In experiment 1, the maximum Z-direction displacement reaches 2.9 mm with a peak bending stress of 179 MPa, satisfying the L/300 deflection criterion. In experiment 3, the results show a maximum displacement of 3.7 mm and 181 MPa of stress, meeting the L/200 criterion (Table 6.4).

Under positive loading scenario(snow load), which are geometrically more advantageous when the convex side faces upward, the panel withstands the applied forces even when edges *c* and *d* remain fully unsupported. For the LG interlayer, a maximum stress of 166 MPa

FEA [total deformation] / max. step	Support condition	Max. stress [MPa]	Z deflection [mm]
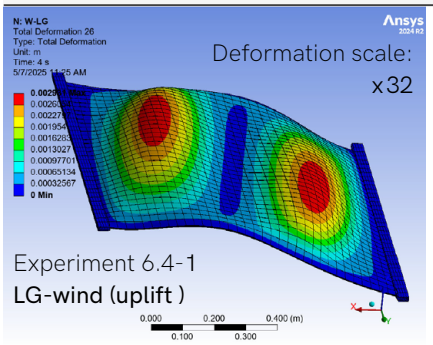	· a & b: Restricted movement and rotation to all directions · c & d: Only Z movement restricted	179	2.9
		Notes	
		· High initial shear modulus provides strong resistance to impact loads	
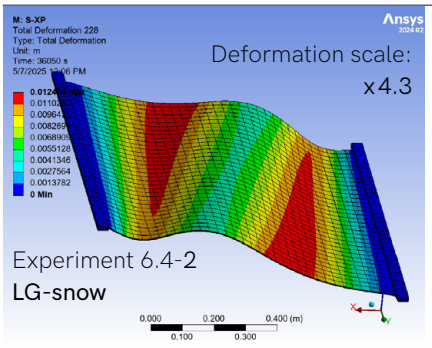	· a & b: Restricted movement and rotation to all directions · c & d: Free	166	-10.6
		Notes	
		· High initial shear modulus provides strong resistance to impact loads	
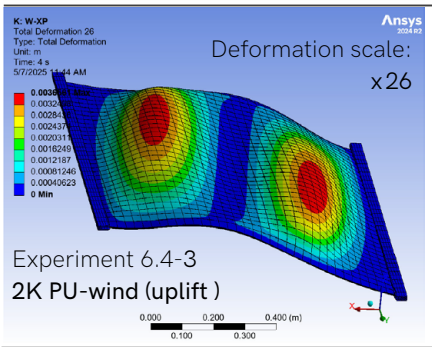	· a & b: Restricted movement and rotation to all directions · c & d: Only Z movement restricted	181	3.7
		Notes	
		· Maintains stable shear modulus under high temperatures and long-term conditions.	
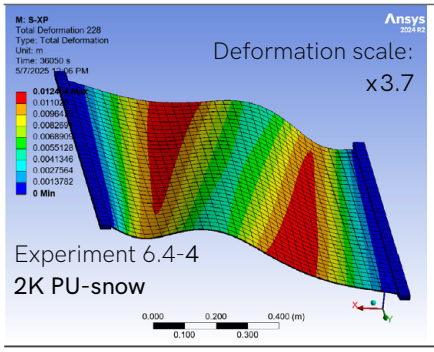	· a & b: Restricted movement and rotation to all directions · c & d: Free	171	-12.3
		Notes	
		· Maintains stable shear modulus under high temperatures and long-term conditions.	

Table 6.4 | OWO Pavilion glass panel load test results

and a Z-direction deflection of 10.6 mm are recorded. For the 2K PU interlayer, the values are 171 MPa and 12.3 mm, respectively, both satisfying the L/50 serviceability condition.
These findings inform the design of the future secondary beam structure. Edges *a* and *b* require restricted support conditions, while edges *c* and *d* can remain simply supported in the Z direction only. This support configuration provides freedom to avoid excessive stress while effectively controlling deflection.
Comparing the two interlayers, the initial modulus of elasticity at $t(0)$ under ambient temperature conditions is 65 MPa for the LG product and 31 MPa for the 2K PU product, confirming that LG is more than twice as stiff initially. However, over time, both materials exhibit an exponential reduction in shear modulus, eventually converging to long-term values of approximately 3 MPa for LG and 2 MPa for 2K PU LOCA at ambient temperature condition. This indicates that the stiffness difference diminishes over time, with both interlayers reaching relatively low moduli compared to their initial states.
Although not directly reflected in this experiment, material data from DIBt (2016) shows that LG's shear modulus drops significantly under high temperatures—down to around 1.25 MPa at 40–50 °C. In contrast, 2K PU LOCA maintains a more stable performance, retaining a shear modulus of around 2 MPa even under elevated temperatures. In conclusion, although this was not directly verified through targeted experiments, the available experimental data suggest that the LG interlayer may offer higher resistance to impact loads due to its initially high stiffness, while the 2K PU interlayer is likely to provide slightly better long-term performance under extreme high-temperature conditions.

6.5 Solar Design

The methodology developed in Chapter 4.4 is applied to the newly optimised roof panel design with sinusoidal single-curvature geometry. When the previously optimised frit pattern scale factors (Chapter 4.4)—0.14 and 0.9, derived from the flat glass optimisation—are applied to the new roof geometry, the first optimisation objective is successfully met: the highest 10th percentile of indoor sensor value reaches 150.14 W/m2, satisfying the approximate target of 90 % of sensors recording below 150 W/m2. The total frit area is calculated as 58.94 m2, which is consistent with the optimised result from Chapter 4.4 (Figure 6.7).
Therefore, the frit pattern design in this chapter does not involve additional high computational-loaded multi-objective optimisation tasks. Instead, it applies the scale factor derived from Chapter 4.4 to the new roof geometry and still achieves the intended design objectives. However, in light of the findings from the experimental study in Chapter 5.3, some reservations arise regarding the efficiency of the approach adopted here. The process of subdividing each panel into localised regions and assigning tailored gradient patterns requires considerable computational resources and custom fabrication efforts.
Given that the performance difference observed in small-scale, gradient pattern and equal density pattern within a panel is relatively minor—often within just a few percentage points—

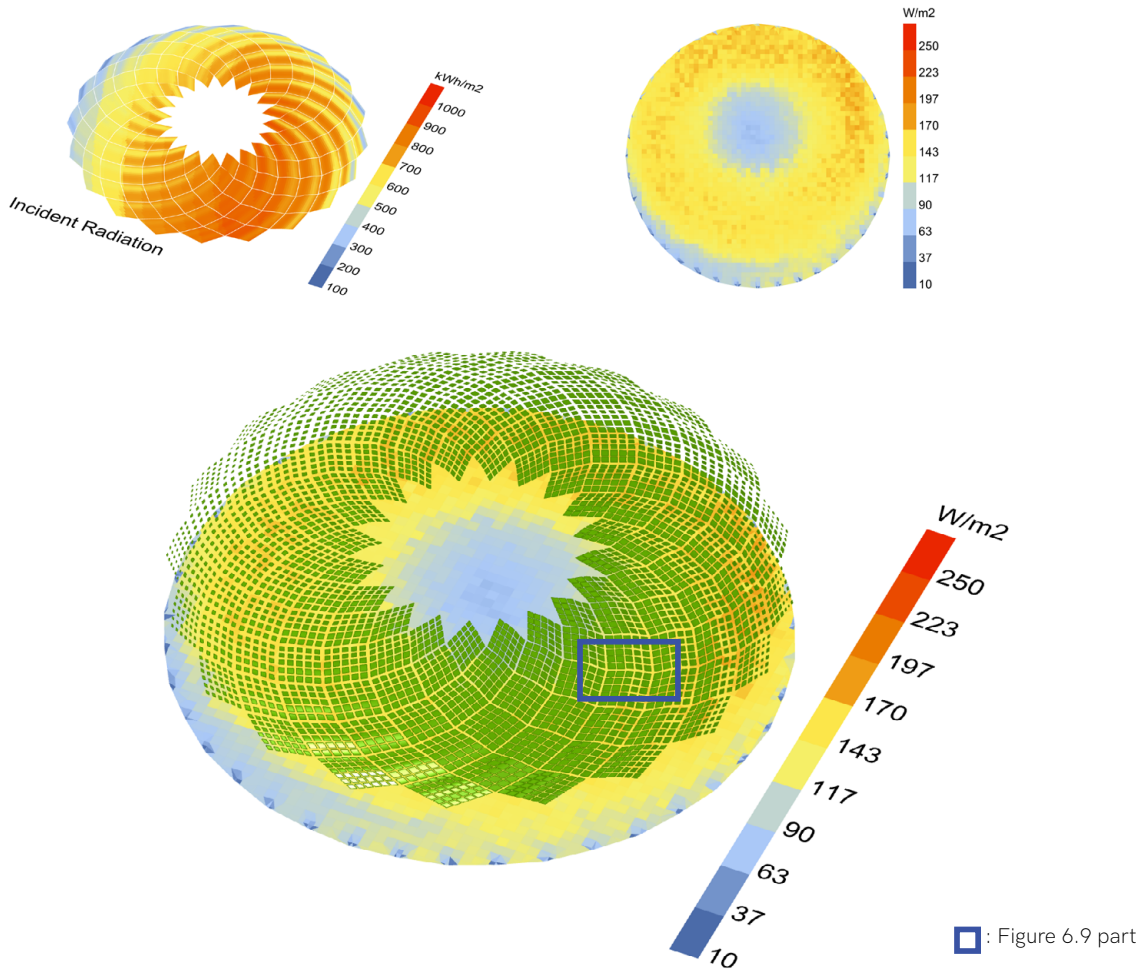

Fig. 6.7 | OWO Pavilion updated glass geometry frit pattern analysis
Note. Top-left: Incident radiation on roof geometry Top-right: Indoor avg. irradiance simulation result
Bot: Optimised density pattern with simplified frit geometry

it raises the question of whether such a computationally intensive method is truly justified, especially in the context of practical architectural implementation. As a result, this study also proposes a simplified alternative depending on the design task: maintaining a uniform frit density within each individual panel, while varying the density between panels based on their location and orientation. This approach reduces design complexity and manufacturing demands, while still offering meaningful control over solar transmittance at the system level. Figure 6.8 illustrates this alternative through a conceptual example, showing a case where the frit density remains constant within each panel and how this design performs in terms of solar irradiance. Although this study does not provide a direct performance comparison between the simplified and the original gradient-based methods, the alternative method can be considered as a practical design option derived from the findings of this research.

Based on the simulation results, the gradient dot pattern design is generated in the Grasshopper interface without the need for additional fine-tuning. The final design process includes adjusting the real dotted frit density to match the total frit area obtained from the simplified geometry, thereby completing the frit pattern design (Figure 6.9).

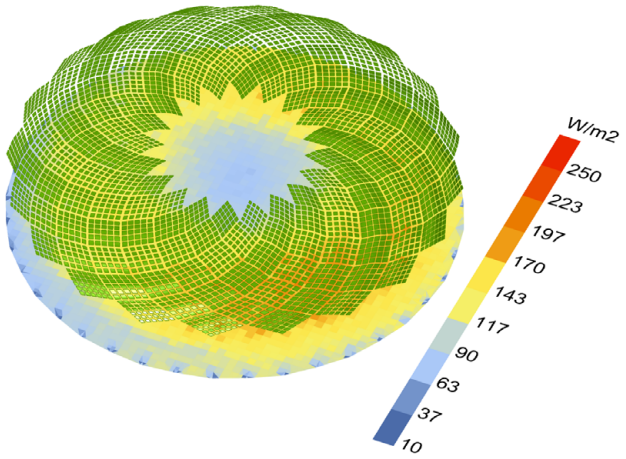

Fig. 6.8 | Simplified frit pattern generation proposal

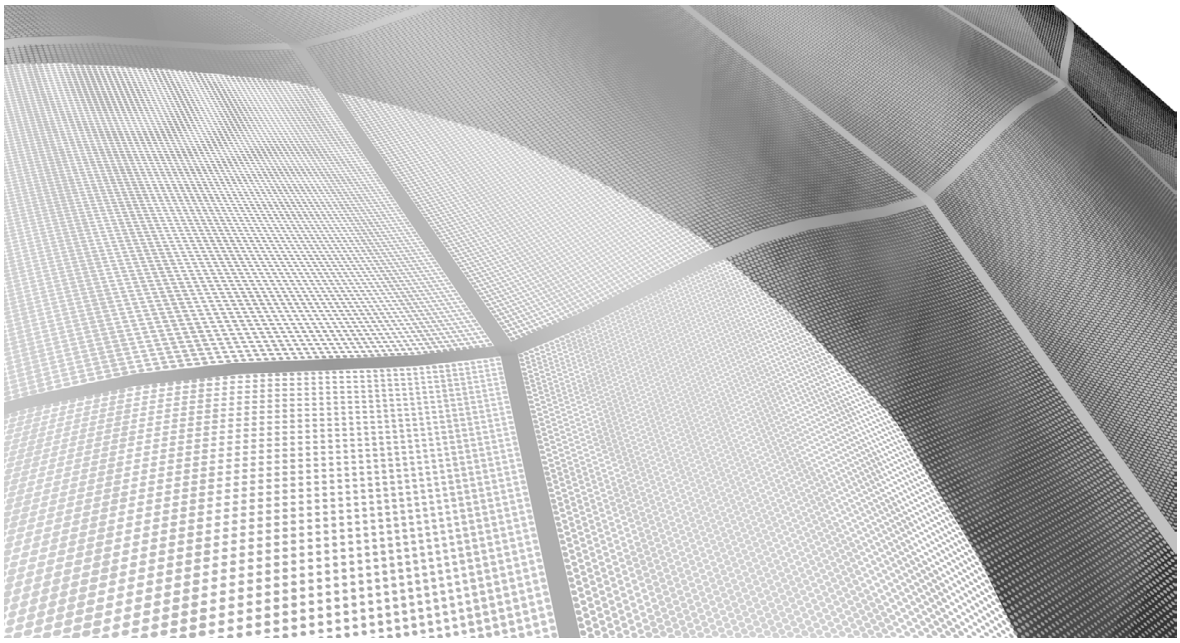

Fig. 6.9 | Final dot pattern based on optimisation methodology

6.6 OWO Pavilion Roof Assembly

The edge fixture used during the buckle bending process is directly integrated into the building element, serving as part of the permanent roof assembly. This approach eliminates material waste and maintains internal stress until the roof is fully assembled, thereby preventing geometry loss due to spring-back. Additionally, by combining the edge fixture and glass as a unit into a single system, the assembly allows for easier maintenance and potential glass replacement. The full roof assembly sequence, with step-by-step explanations, is illustrated in Figure 6.10.

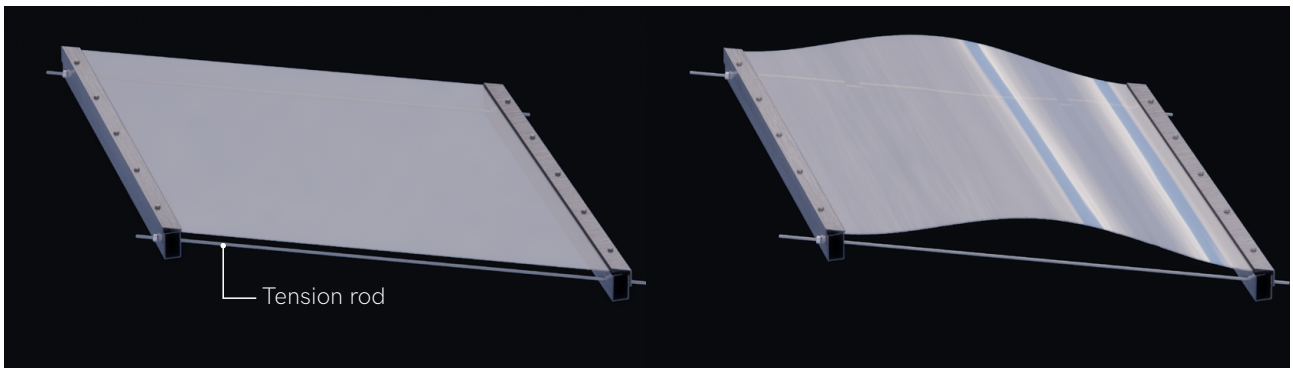

❶ Cold laminated sandwich panel subjected to cold buckle bending

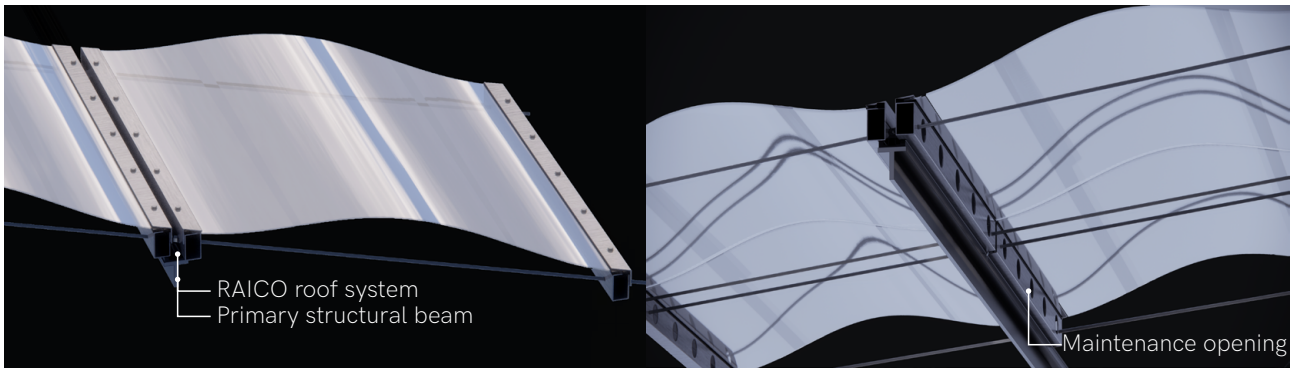

❷ Connection of the buckle bent panel to primary structural frame work

The threaded rod continuously holds the glass unit in tension while it remains connected to the roof's primary structure. Once the main structure stabilises the residual stress of the sandwich panel, the rod may no longer be required to resist panel deformation and can be removed. Maintenance openings are provided within the fixture frame to allow bolt tightening for securing the glass unit and to enable access for connection with adjacent units.

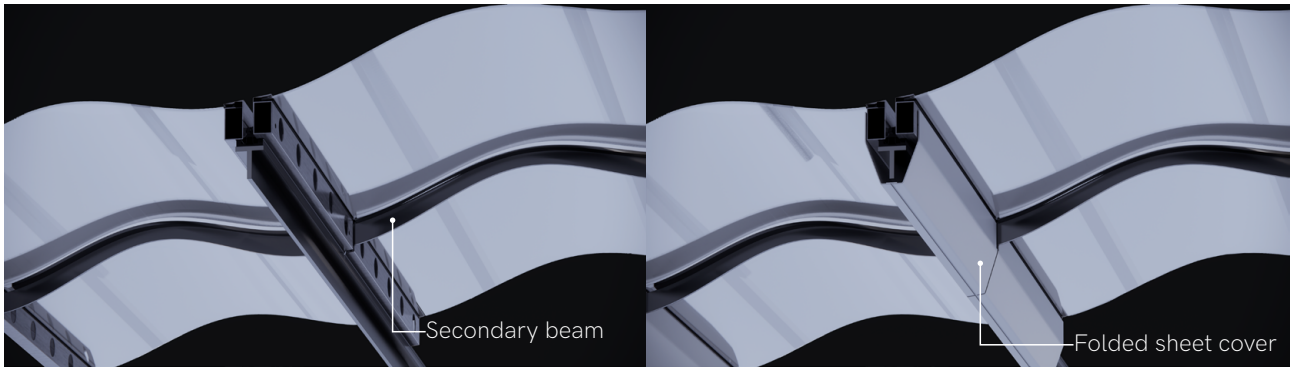

❸ Secondary beam

The secondary beam functions as a supplementary structural system to restrain out-of-plane deformation along the panel's free edge. The glass unit is secured to it using simple connections with gaskets and structural silicone joints.

❹ Primary beam covering

Folded aluminium sheets are applied as a cover along the primary fin to conceal the complex assembly formed around it.

❺ Open edge silicone joint finishing

Fig. 6.10 | OWO roof assembly sequence

6.7 Final OWO Pavilion Roof Design



Fig. 6.11 | Perspective from the front entrance of the OWO Pavilion
Note. Ceramic fritting is omitted in this perspective view for clarity.

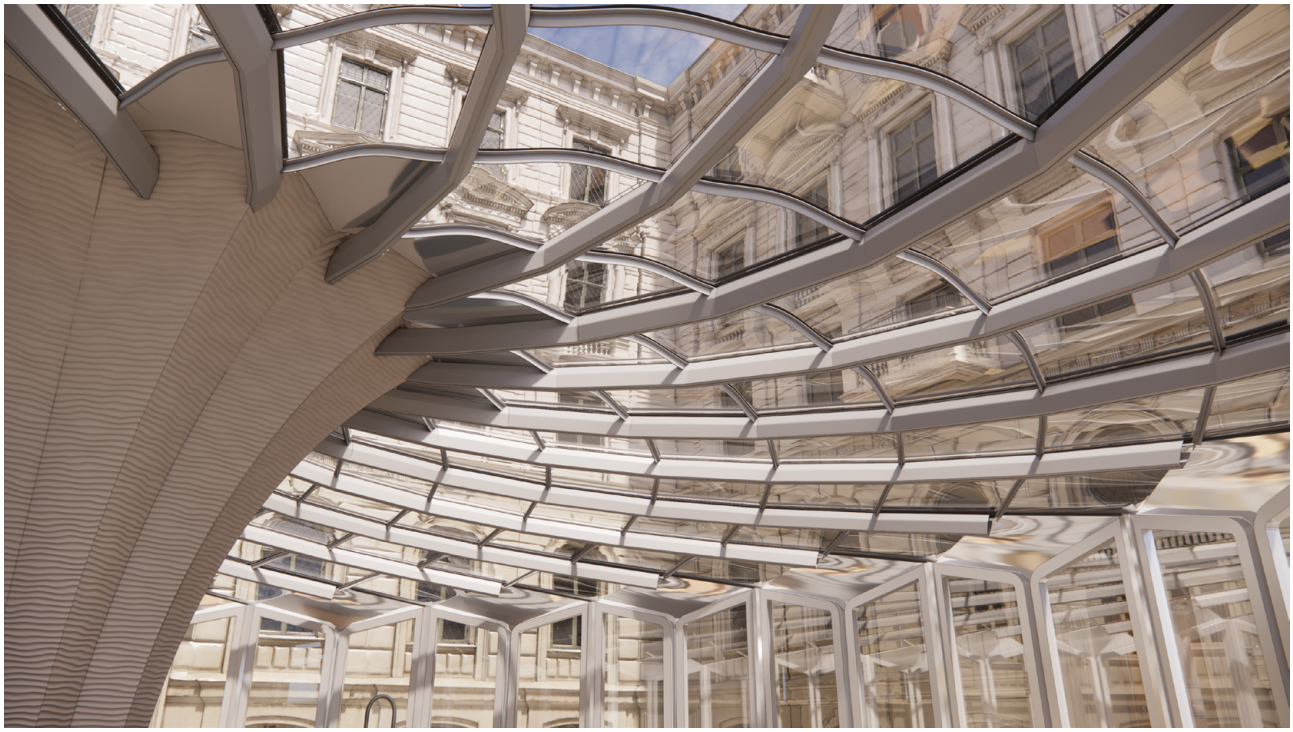

Fig. 6.12 | Interior view of the roof structure and reflections on the double curved surface
Note. Ceramic fritting is omitted in this perspective view for clarity.

6.8 Discussion

Final Structural Design

Square plates have been shown to be more effective in resisting stress than skewed or irregular geometries (Young et al., 2011), as increasing geometrical asymmetry tends to reduce structural efficiency. This principle is further reflected in the behaviour of cold buckle bent glass, where the degree of cold bending is significantly influenced by the shape of the panel itself. Square configurations are capable of accommodating greater deformation, whereas deviation from a square form introduces greater asymmetry, which in turn leads to imbalanced load and stress distribution. As a result, both the feasibility and extent of cold buckle bending become restricted.

In the case of double-curved geometries with continuously varying surfaces, complex residual stresses are introduced, making straightforward pre-calculation unfeasible. For instance, the rhombus-shaped geometry did not exhibit buckle bending perpendicular to the applied load, most likely due to its lack of symmetry with respect to the loading direction. To better realise the intended buckling deformation, fine-tuning of boundary conditions, including load application and restraint methods, may be necessary.

The final glass roof geometry for the OWO Pavilion, based on a sinusoidal single-curve with restricted edge conditions, does not deliver the same level of dramatic visual impact as the original sinusoidal paraboloid or sinusoidal half-paraboloid designs discussed in Chapter 4. A full FEA simulation is conducted for an alternative geometry featuring cold bending to form a single cylindrical curvature along the main beam. This configuration demonstrates both strong structural performance and enhanced architectural expression, owing to its pronounced out-of-plane displacement amplitude (Figure 6.13). However, as the primary objective of this research is to investigate the feasibility of applying previously untested cold-bent geometries within complex roof conditions, the decision has been made to retain the sinusoidal form and conclude the project with the sinusoidal profile configuration.

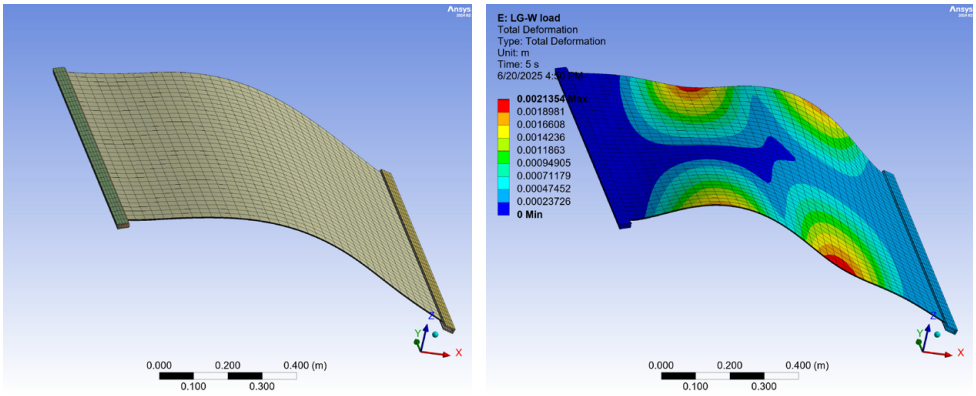

Fig. 6.13 | Single cylindrical cold bent roof geometry design for the OWO Pavilion
Note. Left: Cold-bent geometry Right: Total deformation with scale factor on a wind load scenario

Final Solar Design

The complexity of the geometry affects the simulation process beyond the optimisation tasks. Even obtaining basic solar analysis results without optimisation from a geometry linked to a Grasshopper script requires significant computation time, primarily for converting the original NURBS polysurface into discrete meshes. Approximately one hour of computational running time is required for the full presetting process prior to optimisation (with Intel® Core™ i7-12700H, and NVIDIA GeForce RTX 3070 Laptop GPU). While script optimisation through an efficient workflow that minimises redundant computations could help streamline the overall process, reduce simulation time, the relatively small scale of the OWO Pavilion means that these issues become far more relevant in larger and more complex design cases.

A meaningful finding of this study is that the frit generation method—developed through optimisation on flat panel geometry—continues to deliver design outcomes that meet the intended objectives, even when applied to cold-bent, double-curved geometries. One possible criticism of this methodology is that the final geometry to which the frit pattern is applied differs from the one used during the initial optimisation process. To address this, the approach taken in this study involves validating the numerical performance against the final geometry and, if necessary, making post-application adjustments to the frit scale factors. This approach is founded on the assumption that the optimisation results obtained from flat geometries remain sufficiently transferable to the final cold-bent configuration. This is based on the observation that, in this study, the glass panels can not be subjected to extreme or highly irregular deformation during cold bending. As a result, the overall surface orientation and curvature change only moderately, and the solar simulation results do not significantly deviate from those derived using flat panel geometries. This is particularly relevant in architectural practice, where design modifications often occur mid-process. The method proves efficient and robust, as it allows for the reuse of intermediate optimisation data without restarting from scratch. This saves time, labour, and computational resources while maintaining an acceptable level of design precision. Importantly, this assumption is supported by the findings in Chapters 4.4 and 6.5, where applying the same optimisation parameters across various cold-bent geometries consistently yields results that satisfy performance criteria. Additionally, as demonstrated in Chapter 5, inherent discrepancies between computational simulations and the actual performance of fabricated panels are inevitable. These discrepancies suggest that overly precise fine-tuning at the simulation stage may not translate into proportionally improved real-world performance.

Given these constraints, the study additionally proposes a simplified optimisation method—wherein frit density is kept uniform within individual panels, and only varied between panels based on overall geometry and solar exposure—offers a practical and effective alternative.

VII. CONCLUSION

7.1 Answers to the Research Questions

Sub-research questions:

1. What kind of deformation methods could be used to create a water-droplet like geometry for thin glass?

To achieve a water droplet-like geometry in thin glass, this study employs a buckling-based deformation strategy that uses semi-rigid edge constraints to induce controlled in-plane compression. The method limits constraint to only two diagonally opposing edge supports. This form of deformation results in a geometry that visually echoes the geometry of a half nature-driven droplet with a similar curvature, while remaining within the strength limits of the material.

2. What is the most effective form driven from the cold-bending process to implement the benchmark roof design?

Among the geometries explored in this study, the most effective cold-bent form for the benchmark architectural roof is the sinusoidal half-paraboloid developed through the refined two-stage deformation strategy. The adopted geometry—formed with two edge supports, facing each other—creates a smooth residual stress optimised surface that maintains curvature approaching close to the maximum achievable for a cylindrical single-curved surface. Based on numerical analysis, the case of a 800x800mm square, 1.1mm thick single glass pane results in in-plane displacements on edges of 31 mm and 3 mm at opposing edges, with a peak curvature radius of approximately 250 mm. Although double curvature is present, the method ensures that the resulting surface behaves similarly to a developable geometry, such as a cone, keeping the induced stress levels manageable. This approach proves effective for shaping thin double-curved CT glass without relying on moulds or high-temperature forming. Table 7.1 and Figure 7.1 summarise the effective cold defor-

Panel build-up	Geometry	Load case	Max. in-plane displ. [mm]	Max. out-of-plane displ.[mm]	Min. radius [mm]
800x800 square (*G*)	Sinusoidal half-paraboloid	N/A	31	101	246
800x800 square (*G - L - G*)	Sinusoidal half-paraboloid	3kN/m2 (+/ -)	25	92	293
OWO rhombus (*G - L - G*)	Sinusoidal single curvature	1.35G + 1.5W 1.35G + 1.5S	20	90	512

Table 7.1 | Comparative summary of cold-bent geometries results based on numerical experiments
Note. G refers to glass and *L* to lamination layer. G refers to gravity load, W to wind load, and S to snow load.

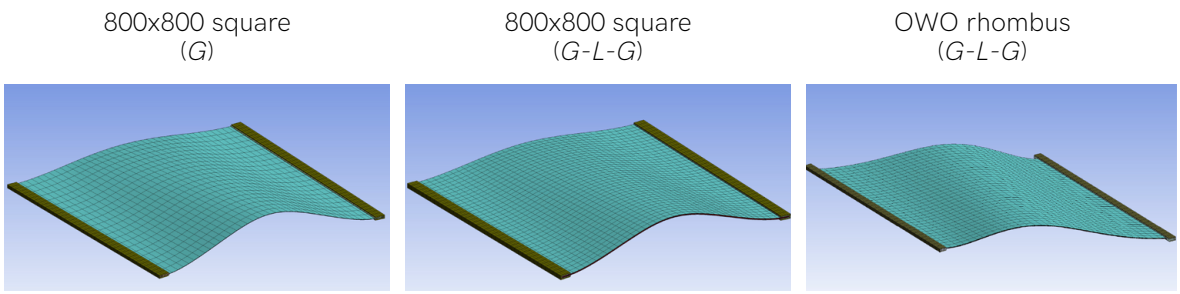

Fig. 7.1 | Comparative summary of cold-bent geometries results

mation shapes identified under various conditions throughout this study.
While this study does not include a direct structural performance comparison between the sinusoidal geometry and commonly used cold bending geometries (e.g. cylindrical surfaces or hyperbolic paraboloids) under identical curvature conditions, it is observed that the maximum achievable out-of-plane displacement is lower in the sinusoidal form due to its alternating concave–convex curvature. Nevertheless, the maximum curvature that can be achieved approaches similar levels to that of single-curved geometries.

3. How does the laminated glass panel behave under general load conditions, and what are its post-failure characteristics?

The laminated rectangular glass panel with a sinusoidal half-paraboloid geometry exhibits varying structural responses depending on the loading scenario. It is particularly vulnerable under positive pressure (e.g. gravity load direction when the convex surface faces upward). Within the geometry, the convex region functions as a stabilising spine, reducing mid-span deflection and providing superior serviceability compared to a planar glass panel. The concave area—especially along the edge with smaller displacement amplitude—experiences more significant deflection under the same load, making it the most structurally critical zone regarding deflection. Regions most susceptible to glass failure due to maximum stress are typically located near the edge supports and areas of maximum curvature. However, under applied loading conditions, the vicinity of the edge supports tends to be more critical.

Due to the viscoelastic nature of the interlayer, long-term loads induce creep behaviour. Over time, both deformation and internal stress begin to converge towards stable values. The interlayer also demonstrates its key role post-failure by effectively holding shattered glass fragments in place. When failure occurs under high in-plane bending stress, the resulting fracture propagates in the form of extremely fine cracks.
These findings highlight the importance of managing residual stress in cold-bent chemically toughened (CT) glass. If the geometry is overly prestressed (not only high peak stress but also overall elevated stress levels across a broad surface area), the risk of falling small fragments may happen. Therefore, ensuring that the final cold-bent form remains within a moderate residual stress range is essential when integrating such panels into real-world architectural applications.

4. How can solar simulations be utilised to design an effective solar transmittance control mechanism for double-curved thin glass?

Designing an effective solar transmittance control mechanism for double-curved thin glass presents several limitations, including the limited availability of applicable solar control methods and the extended computation time caused by complex geometries. The core design principle is to block more radiation in roof regions with higher incident solar exposure while allowing greater transparency in areas with less exposure, using ceramic fritting, chosen for its compatibility with a wide range of design freedom. Indoor average irradiance and frit coverage area serve as the performance metrics for the multi-objective optimisation task.

Simulating double-curved geometries requires discretisation of the surface, and computational time increases significantly with geometric complexity. To address this, the optimisation process is divided into smaller stages. A simplified flat glass geometry is used during the most computationally intensive stage (multi-objective optimisation) and the resulting parameters are then transferred to the actual double-curved roof geometry for validation and fine-tuning. This methodology allows for a significant reduction in computational load while maintaining meaningful intermediate result outcomes.

5. What are the main manufacturing challenges?

Due to the brittle nature of glass, which tends to fail without any prior warning, it is extremely difficult to empirically predict failure points through experimentation. This often leads to the unexpected breakage of numerous specimens, resulting in insufficient experimental data and limited sample availability. Therefore, precise pre-engineering of cold-deformed geometries becomes critically important.
Overall, the manufacturing process within this research proceeds largely in line with the initial concept and expectations. The aim is to develop an effective and material-efficient cold bending method using only edge supports, without relying on a full mould. While this approach proves successful in terms of sustainability and saving materials, it increases fabrication complexity.
A broader challenge in the lamination process lies in the requirement for specialised equipment and skilled labour at every stage of manufacturing. In particular, the use of LOCA as a lamination method for cold bending double-curved geometries introduces additional complexity, due to its relatively novel application and the current lack of established knowledge and standardised procedures. One of the key challenges is ensuring the uniform application of the uncured interlayer on a curved sandwich panel without introducing air bubbles, as any inconsistency or visual defect can directly compromise the surface quality. In addition, precise shape control during the cold deformation stage is essential to preserve the intended geometry.

7.2 Discussion and Further Research

7.2.1 Scientific and Societal Impact

The safe and aesthetically pleasing application of glass in architecture involves a highly intricate manufacturing process carried out in sequential stages. Due to the material's inherent complexity, most research focuses on one aspect of the glass. However, this segmented approach often overlooks the interdependencies between processes, which can lead to issues such as reduced performance of the final product, process incompatibility, or excessively high production costs. This study takes a holistic approach by considering the interconnected processes involved in working with thin glass, including cold bending, cold lamination, frit patterning, and the selection of materials for each step. By ensuring compatibility from start to finish, the research aims to avoid the unintended consequences that often arise when changes to one process negatively affect subsequent stages. Therefore, this study establishes a research framework that provides a more complete and integrated answer to the challenges of thin glass in architecture.
Existing cold-bent glass studies rely mostly on bending or twisting deformation, the introduction of buckle bending as a new methodology for achieving smooth and nature-driven sinusoidal double curved geometry is the main novelty of this research.

Due to the limited deformability of glass, architects have traditionally been forced to simplify glazing strategies when working with complex free-form buildings, typically by flattening the surface or subdividing curved geometries into discrete planar panels. As a result, glass has often remained the limiting factor in the realisation of truly continuous or expressive forms. However, if the high-curvature and geometrically complex cold-bent shapes explored in this study presents the potential to unlock a new domain of cold-bent three-dimensional glass architecture.
By reducing glass thickness, minimising material use and dead load, and compensating for strength through cold-bent geometrical stiffness, the proposed approach not only provides structural effectiveness but also transforms constraints into aesthetic opportunities. Furthermore, the fabrication process—designed to eliminate energy-intensive thermal treatment and custom moulds—offers benefits in terms of sustainability.

7.2.2 Interpretation of Results and Limitations

This research proposes an integrated methodology for exploiting the underutilised potential of double-curved, cold-bent, thin, chemically toughened glass—aiming to achieve geometrically expressive yet structurally viable forms without relying on energy-intensive thermal forming. By employing buckling-induced bending and sinusoidal geometries, the study introduces an alternative fabrication path that aligns performance, aesthetics, and sustainability. At the same time, it reveals the significant complexity involved in scaling such systems to architectural applications.

The potential change in mechanical properties caused by micro-notching during the ceramic frit fusing process is not investigated in depth within this study. However, this stage compromises the structural performance of the panel, particularly during cold bending or under long-term loading conditions. This highlights the need for further investigation into material behaviour of the ceramic fused glass and the interactions between the fused ceramic layer and the interlayer material, especially under thermal fluctuations and critical loading scenarios.

Structurally, the study highlights that even near-developable double-curved surfaces present significant difficulty in stress prediction due to asymmetric residual forces and localised deformation. Fundamental equations of statics become inapplicable for describing the cold bending behaviour of this complex geometry or its structural response under post-curing load scenarios through simple hand calculations.
Through iterative FEA development, optimised geometries are derived, and the simulation improves its predictive capacity by incorporating a viscoelastic modelling approach that approximates the entire process, including cold bending of the liquid-state interlayer, curing, and the transient load testing phase.
The sinusoidal edge profile shows a reduction in spring-back and a more even stress distribution, indicating that certain double-curved geometries may offer structural benefits often overlooked in conventional practice.

Solar performance also emerges as a critical factor. The tested geometry may cause light convergence and potential discomfort due to heat spots or glare (Nugraha, 2024). Although glare and illuminance are not quantified in this study, their importance suggests the need for comprehensive, multi-objective environmental analysis in future work. The reliance on a simplified irradiance threshold of 150 W/m2 serves as a relative optimisation parameter rather than an absolute target, and future studies should consider broader performance criteria that integrate comfort, usability, and visual quality.

At a systemic level, this research prompts questions regarding adaptability and methodological resilience in solar design. Despite deviations between the initial optimisation model and the final numerical geometry, applying earlier parameters still achieves effective outcomes. This supports a modular optimisation approach, where design evolution can proceed without fully restarting performance evaluations. However, broader validation across different geometries and boundary conditions is necessary to confirm the robustness of this workflow. Through experimental validation under the specific conditions tested in this study, it is confirmed that localised gradient patterns do not result in significant performance differences compared to equal frit density patterns. As a result, pursuing extremely high-precision optimisation may not be necessary. Instead, the research proposes a more simplified frit generation method that maintains both roof transparency and performance, while offering a more efficient and practical design approach.

Beyond solar irradiance, additional solar-related indicators play a significant role in indoor comfort—particularly glare and illuminance. Glare depends on the observer's relative position within the space. Given this, it could be valuable to investigate glare in parallel with light convergence, especially in complex geometries such as the one explored in this research. While this study already deals with a relatively complex two-objective optimisation, introducing illuminance as a third performance objective could offer deeper insights. Understanding how the results shift when balancing irradiance, glare, and illuminance simultaneously would be a meaningful direction for future work, especially in relation to occupant comfort and perception.

7.2.3 Future Research Directions

1. Investigating ceramic frit fused glass–interlayer chemical interactions in manufacturing phase and load capacity under elevated temperature and load conditions

2. Accurate simulation of residual stress development model during curing, as the cold-bent liquid-state interlayer undergoes time-dependent molecular rearrangement and stress relaxation upon solidification

3. Expanding cold laminated buckle bent glass unit to multi-layered insulated glass units

4. Exploring new cold bent geometries achievable through the cold buckle bending method, or investigate alternative bending methods to enable the development of novel cold bending geometries

5. Examining feasibility of applying the cold buckle bending method using sheet based interlayers such as PVB or SGP, instead of liquid-based CIP interlayer

6. Advancing solar control design performance simulations by incorporating glare, light convergence, and illuminance as simultaneous design criteria

7. Development and invention of new solar control strategies for double-curved laminated glass roofs

REFERENCE

AGC. (n.d.). Falcon Glass:for thin and lightweight applications. https://www.agc-yourglass.com/sites/default/files/agc_docs/Falcon_0420_EN.pdf

Alias Workbench. (n.d.). *Continuity 1*. Retrieved March 22, 2025, from https://www.aliasworkbench.com/theoryBuilders/TB3_continuity1.htm

ANSYS, Inc. (2022). *ANSYS Mechanical APDL Theory Reference*. Release 2022 R1. Canonsburg, PA: ANSYS, Inc.

Ashwell, D.G. (1957) The equilibrium equations of the inextensional theory for thin flat plates. *Q. J. Mech. Appl. Math. 10(2), 169–182* (1957)

Bartholomew, R. F. & Garfinkel H. M. (1980). Chemical strengthening of glass. *Uhlmann, D.R., Kreidl, N.J. (eds.) Glass Science and Technology, Vol. 5. New York*.

Belis, J., Inghelbrecht, B., Van Impe, R., & Callewaert, D. (2007). Cold bending of laminated glass panels. *Heron, 52(1/2), 123–146*. http://heronjournal.nl/52-12/6.pdf

Bennison, S. J., Davies, P. S., & Calderone, I. (2009). *Effective laminate thickness for the design of laminated glass*. In Proceedings of Glass Performance Days, Tampere, Finland, 12–15.

Bensend, A. & M. Zaccaria (2024). Reducing Deflection of Thin Glass by Prestress. *Challenging Glass Conference Proceedings 9.*

Bergers, M., Natividad, K., Morse, S. M., & Norville, H. S. (2016). Full scale tests of heat strengthened glass with ceramic frit. *Glass Structures & Engineering, 1(1), 261–276*. https://doi.org/10.1007/s40940-016-0032-3

Betanzos, A. (n.d). *Vakko HQ* [Photograph]. Istanbul. © Adrian Betanzos.

Bijster, J., et al. (2016) Glass Entrance Van Gogh Museum Amsterdam. *Glass Structures & Engineering 1: 205-231.* https://doi.org/10.1007/s40940-016-0022-5

Daewha Kang Design *(2021) Internal document.* London.

Datsiou, K. C. & M. Overend (2016). The mechanical response of cold bent monolithic glass plates during the bending process. *Engineering Structures 117: 575-590.*

Debevec, P. & Malik, J., 1997. *Recovering high dynamic range radiance maps from photographs.* Proceedings of the 24th annual conference on Computer graphics and interactive techniques (SIGGRAPH '97). New York: ACM Press/Addison-Wesley Publishing Co., pp. 369–378.

Deutsches Institut für Bautechnik. (2016, October 14). *Allgemeine bauaufsichtliche Zulassung Nr. Z-70.3-240: GEWE-composite Verbund-Sicherheitsglas mit Schubverbund.* Berlin: DIBt.

Eckersley, B & O'Callaghan, J. (2018) *Internal document*. London.

Eekhout, M. (2004) *Design, engineering, production & realisation of glass structures for ''free-form" architecture*. Paper presented at the CWCT Members Meeting. Bath, United Kingdom.

Essary, J. (2021). *A simplified approach to model frit patterns for daylight analysis.* Medium. https://jonathanessary.medium.com/a-simplified-approach-to-model-frit-patterns-for-daylight-analysis-e7fb19492ab3

European Committee for Standardization (CEN). (2016). *EN 1288-1: Glass in building — Determination of the bending strength of glass — Part 1: Fundamentals of testing glass*. Brussels: CEN.

European Committee for Standardization (CEN). (2016). *EN 1288-3: Glass in building — Determination of the bending strength of glass — Part 3: Test with specimen supported at two points (four-point bending)*. Brussels: CEN.

European Committee for Standardization. (2019). *EN 16612: Glass in building – Determination of the load resistance of glass panes by calculation and testing*. Brussels: CEN.

European Committee for Standardization. (2024). *EN 19100-1: Eurocode – Basis of structural and geotechnical design – Part 1: General rules.* Brussels: CEN.

European Committee for Standardization. (2002). *EN 1990: Eurocode – Basis of structural design*. Brussels: CEN.

European Committee for Standardization. (2002). *EN 1991: Eurocode 1 – Actions on structures* Brussels: CEN.

European Committee for Standardization. (2011). *EN 410: Glass in building – Determination of luminous and solar characteristics of glazing*. Brussels: CEN.

Evonik Industries AG. (2013). *PLEXIGLAS® GS/XT: Technical information – Properties and applications.* Evonik Industries AG. Retrieved from https://www.hydrosight.com/content/acrylic-vs-polycarbonate-a-quantitative-and-qualitative-comparison/acrylic/plexiglass-technical-data-sheet.pdf

Fan, B.-W., Zhu, K.-Q., Shi, Q., Sun, T., Yuan, N.-Y., & Ding, J.-N. (2016). Effect of glass thickness on temperature gradient and stress distribution during glass tempering. *Journal of Non-Crystalline Solids, 437, 72–79*.
https://doi.org/10.1016/j.jnoncrysol.2016.01.008

Fechner, G. T. (1860). *Elemente der Psychophysik*. Leipzig: Breitkopf & Härtel.

Ferlin, J. (2019). Glass distortions in a building [Photograph]. © Jonas Ferlin.

Ferry, J. D. (1980). *Viscoelastic properties of polymers* (3rd ed.). Wiley.

Fildhuth, T. & Knippers, J. (2012). Considerations Using Curved, Heat or Cold Bent Glass for Assembling Full Glass Shells. *engineered transparency. International Conference at glasstec, Düsseldorf, Germany 2012.*
https://doi.org/10.13140/2.1.1621.7604

Fildhuth, T., Schieber, R., & Oppe, M. (2018). Design and Construction with Curved Glass. *Engineered Transparency 2018 Glass in Architecture and Structural Engineering 2 (5-6): 369-381.*
https://doi.org/10.1002/cepa.937

Fish, J. & Belytschko, T. (2007). *A First Course in Finite Elements*. John Wiley & Sons. https://doi.org/10.1002/9780470510858

Galuppi, L., Massimiani, S., & Royer-Carfagni, G. (2014). Buckling phenomena in double curved cold-bent glass. *Journal of Non-Linear Mechanics, 67, 1-10* https://doi.org/10.1016/j.ijnonlinmec.2014.03.015

Galuppi, L. & G. Royer-Carfagni (2014). Rheology of cold-lamination-bending for curved glazing. *Engineering Structures 61: 140-152.*

Galuppi, L. and G. Royer-Carfagni (2015). Cold-lamination-bending of glass: Sinusoidal is better than circular. *Composites Part B: Engineering 79: 285-300.*

Galuppi, L. and E. Riva (2022). Experimental and numerical characterization of twisting response of thin glass. *Glass Structures & Engineering 7(1): 45-69.*

Galuppi, L. and E. Riva (2024). Constant-curvature bending response of thin glass: Analytical, numerical and experimental study of "clamp-bending tests. *Glass Structures & Engineering 9(2): 99-116.*

Glasbau Pritz. (n.d). *P&T Engelhornhaus Museum*, Mannheim [Photograph]. Engelskirchen: Glasbau Pritz.

Godox Photo Equipment Co., Ltd. (n.d.). *Godox SL-100W LED Video Light*. Retrieved June 4, 2025, from https://store.godox.pl/en/led-lamps/157-led-video-light-godox-sl-100w-day-light-6952344209394.html

Goss, B. (2002). Bonding glass and other substrates with UV curing adhesives. *International Journal of Adhesion and Adhesives 22.*

Guidi, M. (2019). *Thin Glass Cold Bent Sandwich Panel.* Master Thesis, TU Delft University.

Haldimann, M., et al. (2008). *Structural use of Glass.* International Association for Bridge and Structural Engineering (IABSE)

Hassen, M., de la Barra Luegmayer, P. P., Oke, S., Overend, M., Bilow, M., & Luna-Navarro, A. (2024). Glass serviceability limits: New evidence from human-centred studies. *Glass Structures & Engineering, 9(3), 657–669.* https://doi.org/10.1007/s40940-024-00280-1

Hänig, J., Gutjahr, A., Bukieda, P., Engelmann, M., Gantner, B., & Dillinger, S. (2024). Material characterization of three liquid interlayers for laminated glass solutions. *Challenging Glass Conference Proceedings, 9, 1–12.* https://doi.org/10.1007/s40940-024-00287-8

Hodder, S. G., & Parsons, K. (2007). The effects of solar radiation on thermal comfort. *International Journal of Biometeorology 51, 233-250.* https://doi.org/10.1007/s00484-006-0050-y

Hundevad, J. (2014). Super lightweight glass structures – a study, *In Proceedings of the GlassCon Global Conference. pages 314-327, Philadelphia*.

Jiang, L., et al. (2020). Investigation of the Geometric Shape Effect on the Solar Energy Potential of

Gymnasium Buildings. *Energies 13(23).*

ITU-R. (2015). *Recommendation ITU-R BT.709-6: Parameter values for the HDTV standards for production and international programme exchange*. International Telecommunication Union, Radiocommunication Sector.

Jones, N. L., & Reinhart, C. F. (2015). Validation of GPU lighting simulation in naturally and artificially lit spaces. In J. Mathur & V. Garg (Eds.), *Proceedings of Building Simulation 2015: 14th Conference of IBPSA* (pp. 1229–1236). IBPSA. https://doi.org/10.26868/25222708.2015.2461

Kang, D. (n.d). The OWO Pavilion Roof Detial [Photograph]. London. © Daewha Kang

Kömmerling Chemische Fabrik GmbH. (n.d.). *Technical data sheet: XP 44429-001 (Version V01.001).* https://www.koe-chemie.de

Lau, W. J. Y., Fachrudin, H. T., & Nelson, K. (2024). Assessment of daylighting performance on different frit patterns of ETFE foils of building facades. *Civil Engineering and Architecture, 12(5), 1–10*.
https://doi.org/10.13189/cea.2024.120501

Louter, C., Akilo, M., Miri, B., Neeskens, T., Ribeiro Silveira, R., Topcu, Ö., van der Weijde, I., Zha, C., Bilow, M., Turrin, M., Klein, T., & O'Callaghan, J. (2018). Adaptive and composite thin glass concepts for architectural applications. *Heron, 63(1/2), 199–218. Article 9.*
http://heronjournal.nl/63-12/9.html

Mansfield, E. H. (1955). The inextensional theory for thin flat plates. *Q.J. Mech. Appl. Math. 8(3), 338–352*.

Marburg, J. (n.d.). *Prada Aoyama* [Photograph]. Tokyo. © Johannes Marburg.

Monticelli, C., Lombardi, S., Würfl, C., & Mohamed Ibrahim, H. (2013). Ellipsoidal shape and daylighting control for the ETFE pneumatic envelope of a winter garden. *Proceedings of the VI International Conference on Textile Composites and Inflatable Structures (pp. 340–351)*. Barcelona, Spain: CIMNE.

Nategh, S. et al. (2022). Experimental strength characterisation of thin chemically pre-stressed glass based on laser-induced flaws. *Glass Structures & Engineering 2022, 7(3), 471-486.*
https://doi.org/10.1007/s40940-022-00205-w

Nategh, S., Zaccaria, M., Missinne, J., & Belis, J. (2022). Experimental strength characterisation of thin chemically pre-stressed glass based on laser-induced flaws. *Glass Structures & Engineering, 7(3), 471–486.*
https://doi.org/10.1007/s40940-022-00205-w

Nehring, G. & Siebert, S. (2018). Design concept for cold bent shell structures made of thin glass. *ce/papers 2(5-6), 43-56*.
https://10.1002/cepa.909

Nugraha, S. G. (2024). *Developing Scripts and a Guideline to Mitigate Adverse Effects of Converged Solar Reflection from Curved Façades* (Master's thesis). Delft University of Technology.

Octatube. (2021). *OWO roof panel optimisation using line testing*. Internal document

Oldcastle BuildingEnvelope. (2019). *Silk-screened spandrel glass technical manual (Version 11.0)*. https://cdn.obe.com/wp-content/uploads/2019/06/silk_screen_tech_11_0.pdf

Overend, M., De Gaetano, S., & Haldimann, M. (2007). Diagnostic interpretation of glass failure. Structural Engineering International, 17(2), 151–158. https://doi.org/10.2749/101686607780680790

Pan, J., Li, N., Zhang, W., He, Y., & Hu, X. (2022). Investigation based on physiological parameters of human thermal sensation and comfort zone on indoor solar radiation conditions in summer. *Building and Environment, 226, 109780.* https://doi.org/10.1016/j.buildenv.2022.109780

Paniczko, P. (n.d). Museum of the History of Polish Jews [Photograph]. Warsaw. © Pawel Paniczko.

Rammig, L. (2022). *Advancing Transparency: Connecting glass with heat – An experimental approach to the implementation of heat bonding into glass connection design for structural applications.* A+BE | Architecture and the Built Environment. TU Delft

Roudsari, M. S., & Waelkens, A. (2015). A new approach to modeling frit patterns for daylight simulation. In *Proceedings of the Symposium on Simulation for Architecture & Urban Design (pp. 22–27). Society for Computer Simulation International.*

Shin, K. (n.d). The OWO Pavilion [Photograph]. London. © Kyungsub Shin

Schittich, C., Staib, G., Balkow, D., Schuler, M., & Sobek, W. (2007). *Glass construction manual (2nd rev. and expanded ed.)*. Birkhäuser. https://doi.org/10.11129/detail.9783034615549

SCHOTT. (2014). Technical glasses: Physical and technical properties. SCHOTT AG. Retrieved May 22, 2019, from https://www.schott.com/-/media/project/onex/shared/downloads/melting-and-hot-forming/390768-row-schott-technical-glasses-view-2020-04-14.pdf

SCHOTT. (n.d.). Ultra-Thin Glass. Retrieved 22 May 2019. https://www.us.schott.com/advanced_optics/english/products/wafers-and-thin-glass/glass-wafer-and-substrates/ultra-thin-glass/index.html

Schlösser, N. (2019). Quality control and specification for distortions of curved glass. In *Proceedings of Glass Performance Days (GPD) 2019*, Tampere, Finland. Retrieved from https://www.glassonweb.com/article/quality-control-and-specification-distortions-curved-glass

Shelby, J.E., (2005). *Introduction to Glass Science and Technology (2nd ed.).* Royal Society of Chemistry..

Solar Screen International S.A. (2019). *Clear Print PET Easystick – Technical Data Sheet.* Solar Screen International. Retrieved from https://solarscreen.eu/en/products/clear-print-pet-easystick

Tosun, E., Gingold, Y., Reisman, J., & Zorin, D. (2007). Shape optimization using reflection lines. In *Eurographics/SIGGRAPH Symposium on Geometry Processing* (pp. 193–202).

Timoshenko, S. P., & Woinowsky-Krieger, S. (1959). *Theory of plates and shells* (2nd ed.). McGraw-Hill.

Ullmer, P. (2023). I*nflatable Glazing: Prototyping of a dynamic thin glass unit with switchable thermal insulation*. Master Thesis, TU Delft University.

Van Driel, T., et al. (2022). Investigations on the Cold Bending Behaviour of a Double Glazing Unit with a Rigid Edge-Spacer Frame. *Challenging Glass 8*. https://doi.org/10.47982/cgc.8.422

Van Herwijnen, F., Staaks, D., & Eekhout, M. (2004). Cold bent glass sheets in façade structures. *Structural Engineering International, 14(2), 98–101.* https://doi.org/10.2749/101686604777964134

Vecerka/Esto, A. (n.d). *The Diana Center at Barnard College* [Photograph]. New York. © Albert Vecerka/Esto

Veer, F. (2007). The strength of glass, a nontransparent value. *Heron.* 52(1/2), 87–104.

Volakos, E., Davis, C., Teich, M., Lenk, P., & Overend, M. (2021). Structural performance of a novel liquid-laminated embedded connection for glass. *Glass Structures & Engineering, 6(4), 487–510.* https://doi.org/10.1007/s40940-021-00162-w

Von Kármán, T. (1910). *Festigkeitsproblem im Maschinenbau*. In *Encyklopädie der Mathematischen Wissenschaften* (Vol. IV, pp. 311–385).

Wang, X. (2017). *Cellular cavity structure and its building technology for shell structure with thin sheet materials: Geometrical analysis and structural consideration in the design and building processes* [Doctoral dissertation, Technische Universität Darmstadt]. TUprints. https://tuprints.ulb.tu-darmstadt.de/6924/

Weber, F. (2009). Curved glass structures. *GPD - Glass Performance Days, 375–380.*

Wikipedia contributors. (n.d.). *Euler's critical load*. Wikipedia. from https://en.wikipedia.org/wiki/Euler%27s_critical_load

Wilson, H. R., & Elstner, M., (2018). Spot Landing: Determining the Light and Solar Properties of Fritted and Coated Glass. *Challenging Glass 6 6.*

Wurm, J. (2007). *Glass Structures*. Birkhäuser.

X-Rite. (n.d.). *Understanding graphic arts densitometry*. Retrieved from https://xritephoto.com/documents/literature/en/L7-093_Understand_Dens_en.pdf

Young, W. C., Budynas, R. G., & Sadegh, A. M. (2011). *Roark's formulas for stress and strain* (9th ed.). McGraw-Hill Education.

Zaccaria, M., Andreozzi, L., Foraboschi, P., & Louter, C. (2022). The clamp bender: A new testing equipment for thin glass. *Glass Structures & Engineering, 7(2), 173–186.* https://doi.org/10.1007/s40940-022-00188-8

APPENDIX

Appendix 1.



Unprecedented performance balance

glanova's most outstanding characteristic is its balance between performance and cost that breaks the conventional thinking on glass for chemical strengthening. Thanks to its newly-developed composition, glanova can keep costs down while maintaining highest-level strength, transparency and thermal processability.

Physical properties

Properties

Parameters	Unit	glanova
Density	g/cm^3	2.48
Young's Modulus	GPa	75.4
Poisson's Ratio	-	0.24
Vickers Hardness (before CS)	kgf/mm^2	528
Vickers Hardness (after CS)	kgf/mm^2	583
Reflactive index (λ=587.6nm)	-	1.51
Photoelastic constant	(nm/cm)/MPa	27.1
Softening point	℃	742
Strain point	℃	508
Annealing point	℃	552
Tg	℃	554
Coefficient of Thermal Expansion (50-350℃)	x10^{-7}/℃	91.8
Dielectric constant @1GHz	-	6.9
Loss tangent @1GHz	-	0.010
CS	MPa	600-800
DOL	μm	15-25

Appendix 2.

Tabelle 1: Kennwerte für Einfachverglasungen

Lastfall		Schubmodul G [N/mm²]	k_{VSG}[11]	k_{mod}
Fassadenbereich / Innenbereich	Lastfall Wind[12]	1,23	1	0,7
Überkopf-bereich	Lastfall Schnee (beheizte Fläche)[13]	1,23	1	0,4
	Lastfall Schnee (unbeheizte Fläche)[14]	4,81	1	0,4
	Lastfall Eigengewicht	0	1,1	0,25

Die in Tabelle 1 angegebenen Werte wurden mit einem visko-elastischen Modell für die Zwischenschicht ermittelt und durch Grenzfallbetrachtungen der Einwirkungen für die praktische Anwendung mit Berechnungsverfahren unter linear-elastischem Ansatz für die Zwischenschicht vereinfacht.

Wird im Rahmen der statischen Berechnung die Zwischenschichttemperatur mit genaueren bauphysikalischen Methoden ermittelt, kann der Schubmodul für den Lastfall Wind der Tabelle 2 entnommen werden. Hierbei wird zwischen dem Nachweis des 10-Minuten-Mittelwertes und der 3-Sekunden Böenspitze unterschieden.

Tabelle 2: Schubmodul Wind bei unterschiedlichen Zwischenschichttemperaturen

Zwischenschicht -temperatur [°C]	25	30	40	50
Schubmodul G [MPa] für 3 Sekunden	23,74	8,00	2,76	1,44
Schubmodul G [MPa] für 10 Minuten	2,71	1,75	1,26	1,23

Sofern Temperatur und Dauer der Einwirkungen im Einzelfall festgelegt werden können, kann alternativ der jeweilige Schubmodul direkt aus der Prony- Reihe und mithilfe der Aktivierungsenergie aus dem Arrhenius-Ansatz ermittelt werden. Die Vorgehensweise für eine genaue visko-elastische Berechnung ist in Anlage 1 angegeben.

Generell gilt, dass nur Zwischenschichttemperaturen von 0°C bis 60°C und Belastungsdauern bis 30 Tage durch diese Zulassung geregelt werden.

elektronische kopie der abz des dibt: z-70.3-240

11 Kvsg Faktor für Verbund-und Verbund-Sicherheitsglas siehe DIN 18008-1, Abschnitt 8.3.9
12 Für genauere Untersuchungen bei unterschiedlichen Zwischenschichttemperaturen siehe Tabelle 2
13 Gültig für eine Belastungsdauer von 30 Tagen und bei einer Temperatur von 23°C
14 Gültig für eine Belastungsdauer von 30 Tagen und bei einer Temperatur von 0°C

Für eine genaue visko-elastische Berechnung kann alternativ der jeweilige Schubmodul direkt aus der Prony-Reihe und mithilfe der Aktivierungsenergie aus dem Arrhenius-Ansatz ermittelt werden.
Temperatur und Dauer der Einwirkung müssen hierfür im Einzelfall festgelegt werden.

Temperaturabhängige Relaxationszeiten (Anwendung der Zeit-Temperatur-Verschiebung):

$$\tau_{i(T)} = \tau_i^{ref} \cdot e^{\frac{E_A(T_{ref}-T)}{R \cdot T_{ref} \cdot T}} \quad [s] \quad , \quad i = 1..6 \qquad \text{Formel (1)}$$

- Referenztemperatur $T_{ref} = 297{,}15\ K$ (24°C)
- zu untersuchende Temperatur T $[K]$
- Relaxationszeit τ_i^{ref} bei der Referenztemperatur [s]: siehe Tabelle 1
- universelle Gaskonstante R=8,314 $\frac{J}{mol \cdot K}$
- Aktivierungsenergie: $E_A = 270000 \frac{J}{mol}$

Schubmodul zum Zeitpunkt t bei der Temperatur T:

$$G(t) = G_0 \left(1 - \sum_{i=1}^{6} g_i \left(1 - e^{\frac{-t}{\tau_{i(T)}}}\right)\right) \quad [N/mm^2] \qquad \text{Formel (2)}$$

- Initialer Schubmodul G_0=36,39 N/mm2
- Normierter Schubmodul i g_i [-]: siehe Tabelle 1
- Relaxationszeit $\tau_{i(T)}$ [s] bei der Temperatur T: Formel (1)
- Belastungsdauer t [s]

Tabelle 1: Pronyparameter

Relaxationszeit τ_i^{ref}	Normierter Schubmodul
τ_1^{ref} = 1,32E+05 s	g_1= 2,00E-03
τ_2^{ref} = 3,27E+04 s	g_2= 3,10E-03
τ_3^{ref} = 1,29E+04 s	g_3= 1,02E-02
τ_4^{ref} = 1,97E+03 s	g_4= 3,79E-02
τ_5^{ref} = 1,76E+02 s	g_5= 1,26E-01
τ_6^{ref} = 7,18E+00 s	g_6= 7,87E-01

GEWE-composite Verbund-Sicherheitsglas mit Schubverbund	Anlage 1
Pronyparameter	

elektronische kopie der abz des dibt: z-70.3-240

Appendix 3.

Calculated by	Sanguk Ryu	Calculated on	9 MAY 2025	Country	Netherlands

① Stratobel Clearlite 44.2 Annealed

Glass performance data simulation

Light properties - EN 410

Light transmittance : τv [%]	89
External light reflection : ρv [%]	8
Internal light reflection : ρvi [%]	8
Colour rendering index : Ra [%]	99

Energy properties - EN 410

Total solar energy transmittance : g [%]	80
External energy reflection : ρe [%]	7
Internal energy reflection : ρei [%]	7
Direct energy transmission : τe [%]	76
Total energy absorption : αe [%]	17
Shading coefficient : SC	0.92
UV transmission : τuv [%]	0
Selectivity	1.11

Environmental properties

Cradle to Gate – Global warming potential: Module A1-A3 : [kg CO2 eq. /m²] 1	26.5

Thermal properties - EN 673

Thermal transmittance (vertical glazing) : U value [W/(m².K)]	5.5

Acoustic properties

Direct airborne sound reduction - EN 12758 : Rw (C;Ctr) [dB] 2	35 (-1;-3)

Safety properties

Resistance to fire - EN 13501-2	NPD
Reaction to fire - EN 13501-1	NPD
Bullet resistance - EN 1063	NPD
Burglar resistance - EN 356	P2A
Pendulum body impact resistance - EN 12600	1B1
Explosion resistance - EN 13541	NPD

Thickness and weight

Nominal thickness : [mm]	8.8
Weight : [kg/m²]	21

1. This value represents the global warming potential (GWP) associated with the production of the configured glass product. This value covers the entire production phase (module A1 to A3); no other stage in the product's life cycle is included in this value. This GWP value is calculated according to the modelling principles defined in EN 15804+A2:2019. A comparison of the environmental performance of construction products using EPD information must be based on the use of the products and their impact on the building, and must consider the entire life cycle (all information modules), which can be obtained via the full EPD.

2. The sound reduction indexes correspond to glazing with dimensions 1230 mm by 1480 mm according to EN ISO 10140-3 and are tested in laboratory conditions. In-situ performances may vary according to the effective glazing dimensions, supporting system, installation, environment, noise sources etc. The accuracy of the given indexes is +/- 1 dB.

Glass Configurator
Calculation software verified by INISMa
EN 410 and EN 673
Report n° 2018B COU 35741

Several AGC products are now available in Low-Carbon Glass version. The Low-Carbon Glass version does not affect the properties of the above glass configuration. For more info about the AGC Low-Carbon Glass range, please visit our YourGlass page.

The AGC Glass Configurator is a simulation tool providing a performance analysis for the limited purpose of assisting the user in evaluating the performance of the glass configuration identified in this report. The interpolated performance is only applicable for glass products manufactured or processed by AGC. It does not replace an official Declaration of Performance and therefore may contain some variations, although AGC has made every effort to verify the reliability of this simulation tool. The user assumes any risk relating to the results provided by the tool and is solely responsible for the selection of the appropriate glass configuration for the user's application.

This document is for informative purposes only and in no way implies acceptance of any order by the AGC Group. Please consult the Specific Conditions of Use https://www.agc-yourglass.com/configurator/en/specific-conditions-of-use/ for the calculation standards that are used, the INISMA test report number and the accuracy of the values.

AGC makes no express or implied warranty of any kind with respect to the Glass Configurator. There are no warranties of merchantability, non-infringement or fitness for any particular purpose and no warranty shall be implied by operation of law or otherwise. In no event shall AGC be liable for direct, indirect, consequential or incidental damages of any kind relating to or resulting from the use of the Glass Configurator.

Copyright: © 2025 – AGC Glass Europe. All rights reserved

Calculated by	Sanguk Ryu	Calculated on	9 MAY 2025	Country	Netherlands

① Stratobel Clearlite 44.2 Annealed

Visualisation

89	80	8	8	0.92	5.5
LT	SF	LR	LRint	SC	Ug



The AGC Glass Configurator is a simulation tool providing a performance analysis for the limited purpose of assisting the user in evaluating the performance of the glass configuration identified in this report. The interpolated performance is only applicable for glass products manufactured or processed by AGC. It does not replace an official Declaration of Performance and therefore may contain some variations, although AGC has made every effort to verify the reliability of this simulation tool. The user assumes any risk relating to the results provided by the tool and is solely responsible for the selection of the appropriate glass configuration for the user's application.

This document is for informative purposes only and in no way implies acceptance of any order by the AGC Group. Please consult the Specific Conditions of Use https://www.agc-yourglass.com/configurator/en/specific-conditions-of-use/ for the calculation standards that are used, the INISMA test report number and the accuracy of the values.

AGC makes no express or implied warranty of any kind with respect to the Glass Configurator. There are no warranties of merchantability, non-infringement or fitness for any particular purpose and no warranty shall be implied by operation of law or otherwise. In no event shall AGC be liable for direct, indirect, consequential or incidental damages of any kind relating to or resulting from the use of the Glass Configurator.

Copyright: © 2025 – AGC Glass Europe. All rights reserved

Appendix 4.

Experimental shear modulus data for 2K PU LOCA (time-temperature dependent)

4.2 Model:

$$G_{(t)} = \frac{G_e}{1-e^{-(\lambda t)^k}} \qquad G_{(T,t)} = G_{(T_0,t')} \cdot \frac{T_0}{T} \qquad t' = t \cdot e^{\frac{E_a}{R}\cdot\left(\frac{1}{T_0}-\frac{1}{T}\right)}$$

G_e : entropic shear modulus

k, λ : Parameters of the Weibull distribution

E_a: Arrhenius activation energy

R: universal gas constant

fitted values:

G_e	k	λ	E_a
1,97	0,1275	0,694	446,9

G [MPa]		Zeit [s]				
		1	3	60	3600	86400
Temperatur [°C]	-10	135	134	130	122	121
	0	127	127	126	113	61
	10	125	118	70	9	2,2
	23	9	5	2,0	1,9	1,9
	30	2	2,0	2,0	2,0	2,0
	40	2,1	2,1	2,1	2,1	2,1
	50	2,1	2,1	2,1	2,1	2,1
	60	2,2	2,2	2,2	2,2	2,2

The values in the green fields are within the validity range of the model covered by measurements, the gray ones are extrapolations. The influence of possible chemical creep is not covered by this model.

Appendix 5.

Prony Series Coefficients Fitting Script

```python
import numpy as np
from scipy.optimize import curve_fit
import matplotlib.pyplot as plt

# Experimental data (time [s], shear modulus [MPa])
time_data = np.array([1.0, 3.0, 60.0, 3600.0, 86400.0])
shear_modulus_data = np.array([9.0, 5.0, 2.0, 1.9, 1.9])
g_inf = 1.97  # Long-term shear modulus (equilibrium modulus)

# Define the Prony series function (both Gi and tau_i are fitting parameters)
def prony_series(t, g1, tau1, g2, tau2):
    return g_inf + g1 * np.exp(-t / tau1) + g2 * np.exp(-t / tau2)

# Initial guess for parameters
initial_guess = [shear_modulus_data[0] - g_inf, time_data[1], shear_modulus_data[1] - g_inf,
time_data[-2]]
bounds = ((0.0, 0.0, 0.0, 0.0), (np.inf, np.inf, np.inf, np.inf))  # Constraints: Gi > 0, tau_i > 0

# Fit the Prony series to the data
try:
    popt, pcov = curve_fit(prony_series, time_data, shear_modulus_data, p0=initial_guess, bounds=bounds,
maxfev=10000)

    g_fitted = popt[::2]
    tau_fitted = popt[1::2]
    num_terms = len(g_fitted)

    print("Fitted Prony series coefficients (both Gi and tau_i fitted, N=2):")
    print(f"G_inf = {g_inf} MPa")
    for i in range(num_terms):
        print(f"G_{i+1} = {g_fitted[i]:.4f} MPa, tau_{i+1} = {tau_fitted[i]:.4f} sec")

    # Generate fine time points for smooth plotting
    t_fine = np.logspace(np.log10(time_data.min()), np.log10(time_data.max()), 200)
    g_predicted = prony_series(t_fine, *popt)

    # Plotting
    plt.figure(figsize=(12, 8))
    plt.plot(t_fine, g_predicted, label=f'Fitted Prony Series (N={num_terms})', color='#202042',
linewidth=3)
    plt.scatter(time_data, shear_modulus_data, label='Experimental Data', color='#FF5000', s=100)
    plt.xlabel('Time (s)', fontsize=16)
    plt.ylabel('Shear Modulus (MPa)', fontsize=16)
    plt.xscale('log')
    plt.legend(fontsize=14)
    plt.grid(axis='both', which='major', linestyle='--', linewidth=0.8)  # Only x-axis major grid
    plt.title('Fitting Prony Series to Shear Modulus Data (G(i), tau(i) fitted)', fontsize=18)
    plt.xticks(fontsize=14)
    plt.yticks(fontsize=14)
    plt.show()

except RuntimeError:
    print("Optimal parameters could not be found. Try adjusting the initial guess or reducing the number
of terms.")
except Exception as e:
    print(f"An error occurred: {e}")
```